MITOCHONDRIAL DIVERSITY PROBED IN MOUSE CEREBELLUM ELUCIDATES CELL TYPE-SPECIFIC FINE-TUNING OF MITOCHONDRIAL BIOLOGY

CAROLINE FECHER

Graduate School of
Systemic Neurosciences
LMU Munich

Dissertation at the
Graduate School of Systemic Neurosciences
Ludwig-Maximilians-Universität München

January 2020

Supervisor
Prof. Dr. med. Thomas Misgeld
Institute of Neuronal Cell Biology
Technical University of Munich

First Reviewer:	Prof. Thomas Misgeld
Second Reviewer:	Prof. Magdalena Götz
External Reviewer	Prof. Elena I. Rugarli
Date of Submission:	January 7th, 2020
Date of Defense:	March 31st, 2020

Table of Contents

ABSTRACT **1**

CHAPTER 1: INTRODUCTION **3**

1.1. MITOCHONDRIA – A SHORT CURRICULUM VITAE 3
1.2. MITOCHONDRIAL FUNCTION 5
1.2.1. Mitochondrial bioenergetics 5
1.2.1.1. Beta-oxidation 8
1.2.2. Anabolic role of mitochondria 9
1.2.3. Mitochondrial Ca^{2+} *buffering 10*
1.2.4. Contact sites – mitochondrial association with other organelles 12
1.3. MITOCHONDRIAL PROTEOME 13
1.4. MITOCHONDRIAL DIVERSITY 17
1.4.1. Mitochondrial proteins enriched in neural cell types 20
1.4.2. Mitochondrial proteins enriched in neuronal cell compartments 22
1.5. TOOLS: AFFINITY PURIFICATION OF SUBCELLULAR ORGANELLES 23
1.6. CEREBELLUM 25
1.7. MITOCHONDRIAL DYSFUNCTION IN HUMAN DISEASES 26

CHAPTER 2: AIMS **29**

CHAPTER 3: MATERIALS AND METHODS **31**

3.1. MATERIALS 31
3.1.1. Plasmids 31
3.1.2. Buffers 31
3.1.4. Animal models 35
3.1.5. Primer sequences 35
3.1.6. Cell lines and reagents 36
3.1.7. Antibodies 36
3.1.7.1. Antibodies used for immunofluorescence staining (Chapter 3.2.14) 36
3.1.7.2. Antibodies used for western blot analysis (Chapter 3.2.11) 37
3.1.7.3. Antibodies used for flow cytometry (Chapter 3.2.13) 38
3.1.8. Kits 38
3.1.9. Western blot reagents and equipment 38
3.1.10. Mass spectrometry reagents and equipment 39
3.1.11. Microscopy reagents and equipment 39
3.1.13. Chemicals and other reagents 40
3.1.14. Other equipment 41
3.1.15. Software 41
3.2. METHODS 42
3.2.1. Molecular cloning of expression plasmids carrying GFP-OMM 42
3.2.1.1. pCMV-GFP-OMM 42
3.2.1.2. pEx-CAG-stop-GFP-OMM-bpA 43
3.2.2. Cell culture 43
3.2.3. Animal models 44
3.2.3.1. *Rosa26* GFP-OMM knock-in mice (MitoTag mouse line) 44
3.2.3.2. APP23/PS45 and $SOD1^{G93A}$ mouse model 45
3.2.3.3. Mcu^{tm1c} mouse model 45
3.2.3.4. $Rmdn3^{tm1a}$ mouse model 45
3.2.4. Genotyping of transgenic mice 47
3.2.5. Time-lapse imaging of mitochondrial transport in motor axons 47
3.2.6. Neuromuscular health assessment 48
3.2.7. Mitochondrial purification 48
3.2.7.1. Differential centrifugation 49

3.2.7.2. Immunocapture 49
3.2.8. Protein amount measurement 50
3.2.9. Oxygen consumption measurement in isolated mitochondria 50
3.2.9.1. Seahorse assay 50
3.2.9.2. OCR analysis 51
3.2.10. Mitochondrial Ca^{2+} uptake assay 51
3.2.11. Western blot analysis 52
3.2.11.1. Sample preparation 52
3.2.11.2. Western blotting and detection 52
3.2.11.3. Analysis 53
3.2.12. Mass spectrometry 53
3.2.12.1. Sample preparation 53
3.2.12.2. Data acquisition 54
3.2.12.3. Data analysis primary 54
3.2.12.4. Data analysis secondary 55
3.2.13. Fluorescence cytometry 59
3.2.14. Immunofluorescence staining 60
3.2.14.1. Mitochondrial markers in mouse tissue 60
3.2.14.2. Mitochondrial markers in human tissue 62
3.2.14.3. Double labeling of mitochondrial markers via Zenon IgG kit 63
3.2.14.4. Amyloid-β plaques and Aβ deposition 64
3.2.15. Confocal microscopy 64
3.2.16. Image processing and representation 64
3.2.17. Protein retention expansion microscopy 65
3.2.18. Electron microscopy 65
3.2.18.1. Sample preparation 65
3.2.18.2. Data acquisition 66
3.2.18.3. Analysis 66
3.2.19. Statistics 66

CHAPTER 4: RESULTS 69

4.1. VALIDATION OF THE MITOTAG MOUSE MODEL 69
4.1.1. MitoTag mice enable tagging of cell type-specific mitochondria in vivo 69
4.1.2. GFP-OMM expression does not alter mitochondrial or cellular physiology 72
4.1.3. Intact mitochondria are captured via GFP-OMM 75
4.1.4. Immunocapture separates cell type-specific mitochondria from complex tissue 80
4.2. MOLECULAR DIVERSITY OF NEURAL MITOCHONDRIA IN MOUSE CEREBELLUM 86
4.2.1. Cell type-specific profiling of mitochondria identifies similarities and differences 86
4.2.2. Candidates enriched in Purkinje cell mitochondria 92
4.2.3. Candidates enriched in granule cell mitochondria 96
4.2.4. Candidates enriched in astrocytic mitochondria 102
4.2.5. Neuronal and astrocytic candidates hint to differential pathways 105
4.3. ENHANCED LIPID OXIDATION IN ASTROCYTIC MITOCHONDRIA 108
4.4. ENHANCED CA^{2+} BUFFERING IN GRANULE CELL MITOCHONDRIA VIA MCU 113
4.5. ENHANCED ER-MITOCHONDRIA CONTACT SITES IN PURKINJE CELLS VIA RMDN3 117
4.6. MITOCHONDRIAL DIVERSITY IN HEALTH AND DISEASE 121
4.6.1. Mitochondrial markers are conserved across neural tissues and species 122
4.6.2. Cell type-specific mitochondria in AD and ALS 129

CHAPTER 5: DISCUSSION 136

5.1. TECHNICAL ADVANCES AND LIMITATIONS OF THE MITOTAG APPROACH 136
5.2. CELL TYPE-ENRICHED CANDIDATES REFLECT METABOLIC COUPLING OF NEURAL CELLS 140
5.3. FATTY ACID OXIDATION IN THE BRAIN – LOCAL ‘HOTPOTS’ IN ASTROCYTES 150
5.4. MITOCHONDRIAL CALCIUM SIGNALING IN CEREBELLAR NEURONS – ONE SIGNAL, MANY GOALS 153
5.5. FUTURE PERSPECTIVES OF CELL TYPE-SPECIFIC MITOCHONDRIA 156

CHAPTER 6: REFERENCES **158**

CHAPTER 7: APPENDIX **188**

7.1. MitoTag expression in different Cre-driver lines 188
7.2. Cell type-enriched candidates in Purkinje cells, granule cells and astrocytes 190
7.3. Immunofluorescence staining of mitochondrial candidates in cerebellum 195
7.4. Overrepresentation analysis of candidate-enriched pathways 202
7.5. Patient information related to human specimens 205
7.6. Uncropped western blots used in figures of this study 206
7.7. Comprehensive statistical information on experiments of this study 208

INDEX OF FIGURES & TABLES **214**

INDEX OF ABBREVIATIONS **217**

PUBLICATIONS **222**

COPYRIGHT INFORMATION **223**

DECLARATION OF AUTHOR CONTRIBUTIONS **225**

ACKNOWLEDGEMENTS **226**

EIDESSTATTLICHE VERSICHERUNG/AFFIDAVIT **227**

Abstract

Mitochondria house a variety of cellular functions, including catabolic and anabolic pathways, apoptosis and Ca^{2+} handling. These functions critically depend on nuclear-encoded proteins given that mitochondrial DNA only encodes for 13 proteins, which are incorporated into the respiratory chain. While mitochondria differ in morphology and functions among tissues in vivo, mitochondrial diversity among cell types is less well understood – especially in heterogeneous tissues such as the nervous system.

Here, I present an in vivo tool for the characterization of cell type-specific mitochondria in mouse. Via the MitoTag mouse model, mitochondria from the cell type of interest are tagged in a Cre recombinase-dependent manner with GFP, which is localized to the outer mitochondrial membrane (GFP-OMM). This tagging allows for the immunocapture of organelles and their subsequent investigation through functional assays and omics-based screenings.

We applied the MitoTag approach to the cerebellum and profiled the mitochondrial proteome of Purkinje cells, granule cells and astrocytes. Among these cell types, we found 196 proteins differentially enriched, of which 19 candidates were independently confirmed as cell type-enriched mitochondrial 'markers'. Further analysis revealed functional specializations that we corroborated in independent assays using immunocaptured mitochondria. Specifically, astrocytic mitochondria superiorly oxidized long-chain fatty acids, while neuronal mitochondria demonstrated enhanced Ca^{2+} uptake via the mitochondrial calcium uniporter in granule cells and enhanced contact sites with the endoplasmic reticulum via regulator of microtubule dynamics protein 3 in Purkinje cells. In studies across species, I confirmed that neural mitochondrial diversity is conserved in the nervous system of mammals, aves and amphibian. Hence, we used neuronal and astrocytic mitochondrial 'markers' to show mitochondrial pathology in mouse models and human cases of Alzheimer's disease and amyotrophic lateral sclerosis.

The MitoTag approach enables mitochondrial research in a defined cellular context in vivo. Future applications will reveal the cell type-specific fine-tuning of mitochondria in many contexts, such as development, aging and diseases, as well as their contribution to the selective vulnerability of certain cell types.

INTRODUCTION

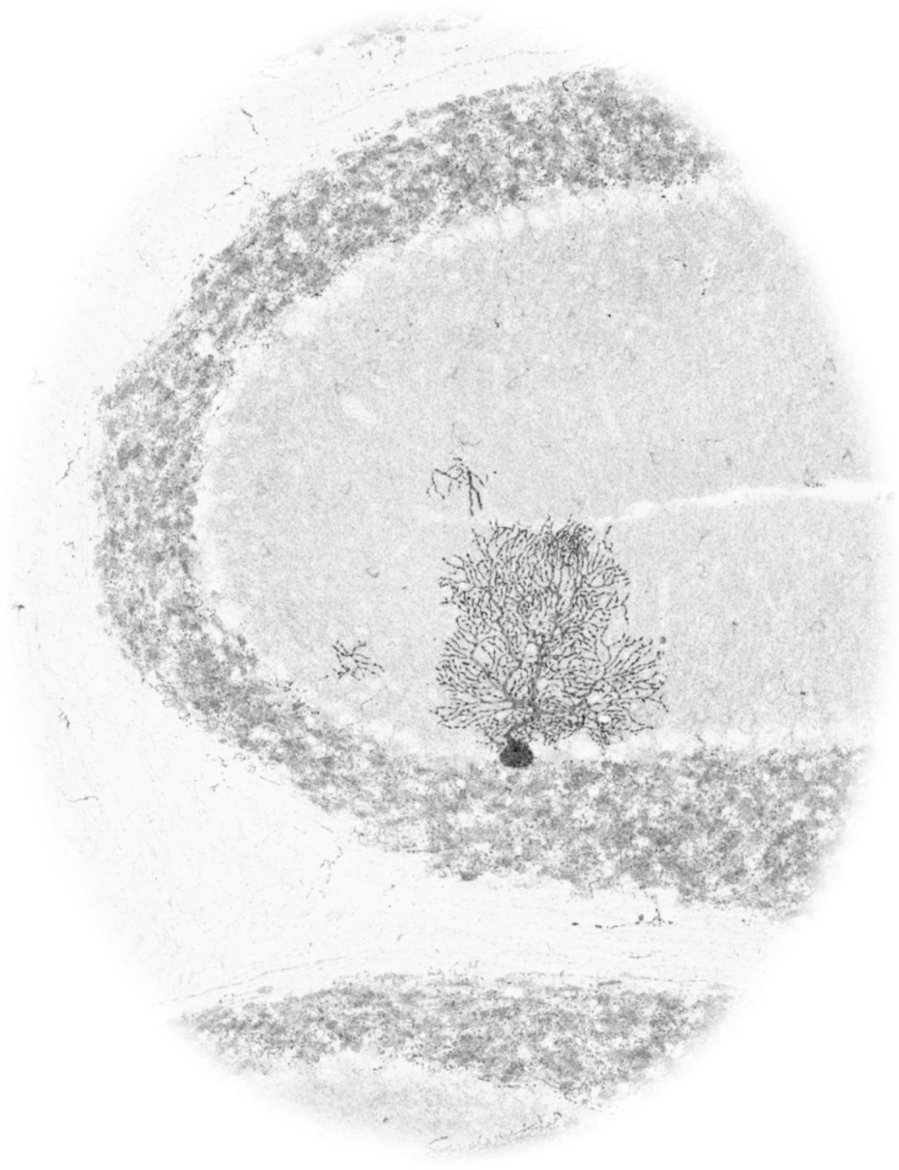

Chapter 1: Introduction

In Tasic et al. (2016) the authors state: "*The mammalian brain is likely the most complex animal organ, given the variety and scope of functions it controls, the diversity of cells it comprises, and the number of genes it expresses* […]". For example, Herculano-Houzel et al. (2006) quantified approximately 109 million cells including 71 million neurons in mouse brain. In the history of neuroscience, cells of the brain were first simply defined as neuronal and non-neuronal ('Neuron doctrine' reviewed in Shepherd, 2015; 'Nervenkitt' reviewed in Somjen, 1988). In contrast nowadays, scientists aim to define cells by their molecular, morphological and physiological properties (reviewed in Zeng and Sanes, 2017). These systematic efforts have let us to an approximate number of 100 cell types per brain area resulting in ~1,000 cell types for the total brain (Hodge et al., 2019; Koch, 2019).

Despite our acknowledgement of the cellular diversity in mammalian brain, our image of their mitochondria – the powerhouse of the cell – has remained uniform. In fact, the most acknowledged discrimination of neural mitochondria by neuroscientists is their dependency on oxidative phosphorylation to generate ATP. However, mitochondria are dynamic organelles and so are their proteome and functions that are adapting to the cellular physiology. Therefore, in principle, mitochondria should differ among neural cell types; however, a systematic approach to test this hypothesis is currently unavailable and motivated this thesis.

1.1. Mitochondria – a short curriculum vitae

The **mitochondrion** (from Greek 'mitos' for thread and 'chondrion' for granule or grain-like) is a double membrane-bound subcellular organelle (Figure 1a). It is present in most eukaryotic cells with the exception of red blood cells (Gronowicz et al., 1984). Mitochondria are composed of: (i) outer mitochondrial membrane, which is permeable for uncharged molecules ≤5 kDa (Benz, 1985); (ii) intermembrane space; (iii) inner mitochondrial membrane, which is impermeant and forms invagination into the matrix, termed cristae; and (iv) matrix (Figure 1b). In contrast to other organelles, mitochondria contain their own DNA (mtDNA; Nass and Nass, 1963), which is maternally inherited (Giles et al., 1980). In mammals, mtDNA encodes for 13 proteins, 2 ribosomal RNAs and 22 transfer RNAs, is organized as circular plasmid and lacks introns. The DNA is packed in higher-order structures, termed nucleoids, via

TFAM and other proteins (Bogenhagen et al., 2008). Mitochondria were first discovered by Albert von Kolliker in 1857 and later coined as 'mitochondrion' by Carl Benda in 1898.

According to the **endosymbiont theory** of mitochondrial origin, the organelle derives from ancestral oxidative proteobacteria that were engulfed by a glycolytic host cell (Sagan, 1967; Martijn et al., 2018). Instead of their degradation, the organelles were retained in the cell and integrated creating an evolutionary benefit by oxygen scavenging. The integration entailed several adaptations from the incorporation of novel host proteins, like the ADP/ATP translocase, to the transfer of most of the proteobacterium's genes to the nucleus (Thorsness and Fox, 1990), as well as the establishment of the protein import machinery (reviewed in Kurland and Andersson, 2000). Interestingly, the remaining protein-coding genes (*n*=13) cannot be transferred to the nucleus because such gene transfer would result in their mislocalization to the endoplasmic reticulum (von Heijne, 1986; Roger et al., 2017).

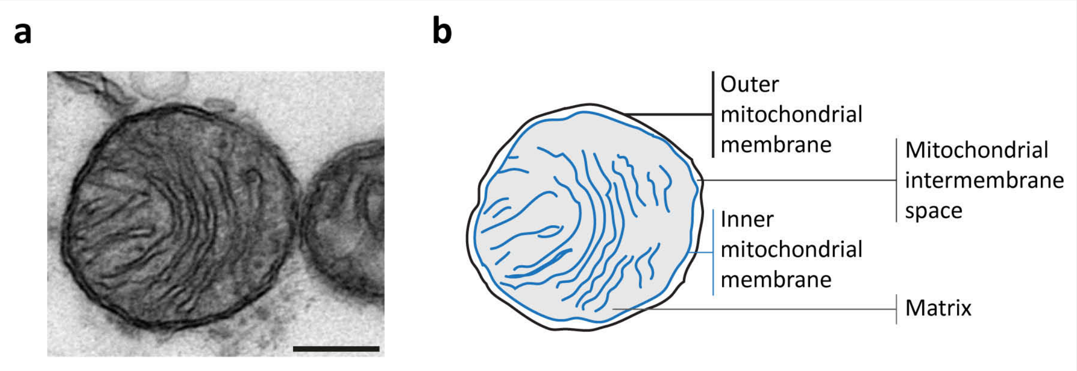
a
b
Outer mitochondrial membrane
Mitochondrial intermembrane space
Inner mitochondrial membrane
Matrix

Figure 1|Structural organization of the mitochondrion. (**a**) Electron micrograph of an isolated mitochondrion from this study. Scale bar: 100 nm. (**b**) Schema from electron micrograph shown in (a) illustrating the different compartments of this organelle. From outside to inside: outer mitochondrial membrane (black line), mitochondrial intermembrane space (white), inner mitochondrial membrane (blue line) forming cristae into the matrix (gray).

Mitochondrial **form and dynamics** vary between cell types, cells of different physiological states and among mitochondria of a single cell. Mitochondrial morphology is frequently linked to mitochondrial function (Benard et al., 2007) and analyzed in disease models and pathology (reviewed in Eisner et al., 2018). Through cycles of organelle fission and fusion mediated by distinct proteins (Drp1, Mfn1, Mfn2, Opa1; reviewed in Wai and Langer, 2016), mitochondrial content is exchanged – especially mtDNA (reviewed in Tilokani et al., 2018). For example in *Saccharomyces cerevisiae*, mitochondrial networks differ in complexity and surface area dependent on fermentable or non-fermentable growth conditions (Visser et al., 1995; Egner et al., 2002). Additionally, mitochondria are actively transported throughout the cell via cytoskeleton tracts and motor proteins (reviewed in Lin and Sheng, 2015). Adaptation of the mitochondrial network provides critical advantages for mitochondrial respiration and membrane potential, as well as organelle stress responses (Hoitzing et al., 2015; Zamponi et al., 2018).

1.2. Mitochondrial function

Mitochondria harbor a number of cellular functions, such as oxidative phosphorylation; assembly of iron-sulphur clusters (Lill et al., 2012); phospholipid, nucleotide, heme and amino acid synthesis; Ca^{2+} homeostasis and buffering; and apoptosis (Zamzami et al., 1996; Susin et al., 1999). From these, the most essential function to life is the assembly of iron-sulphur cluster, which is the only function preserved in mitosomes of microsporidia. Mitosomes are evolutionary reduced mitochondria-related structures with a simplified protein import machinery, no genome and no ATP production; however, they possess the machinery for iron-sulphur clusters synthesis (reviewed in Santos et al., 2018).

1.2.1. Mitochondrial bioenergetics

In mitochondria, metabolites of sugar, lipids and proteins are oxidized to CO_2 and energy in the form of ATP. For this, substrates are metabolized to acetyl-coenzyme A (acetyl-CoA) or other intermediates, which enter the **tricarboxylic acid cycle** (TCA or Krebs cycle; Figure 2a; Krebs, 1970). Glucose is first converted to pyruvate, which is imported into mitochondria and converted mainly to acetyl-CoA via pyruvate dehydrogenase (PDH); but also to oxaloacetate via pyruvate carboxylase (PC; Utter and Keech, 1960) to replenish TCA cycle intermediates (termed anaplerosis; Owen et al., 2002). Fatty acids are metabolized to acetyl-CoA via beta-oxidation and amino acids are converted by multiple, individual enzymes to either pyruvate, acetyl-CoA or other TCA cycle intermediates (section 23.5; Berg et al., 2002). The two-carbon acetyl group of acetyl-CoA is initially transferred to oxaloacetate creating citrate, the first intermediate of the TCA cycle. Citrate is then metabolized to oxaloacetate in seven enzymatic reactions that release two-carbon units as CO_2 and transfer the free electrons to the reduction equivalents, nicotinamide adenine dinucleotide (NADH) and flavin adenine dinucleotide ($FADH_2$). Only one reaction – succinyl-CoA to succinate plus ATP via succinyl-CoA ligase – generates nucleoside triphosphate in the TCA cycle, termed substrate level phosphorylation (Johnson et al., 1998). Interestingly, dependent on the subunits of succinyl-CoA ligase, either ATP (Sucla2) or GTP (Suclg2) are generated. While ATP is transported via the ADP/ATP

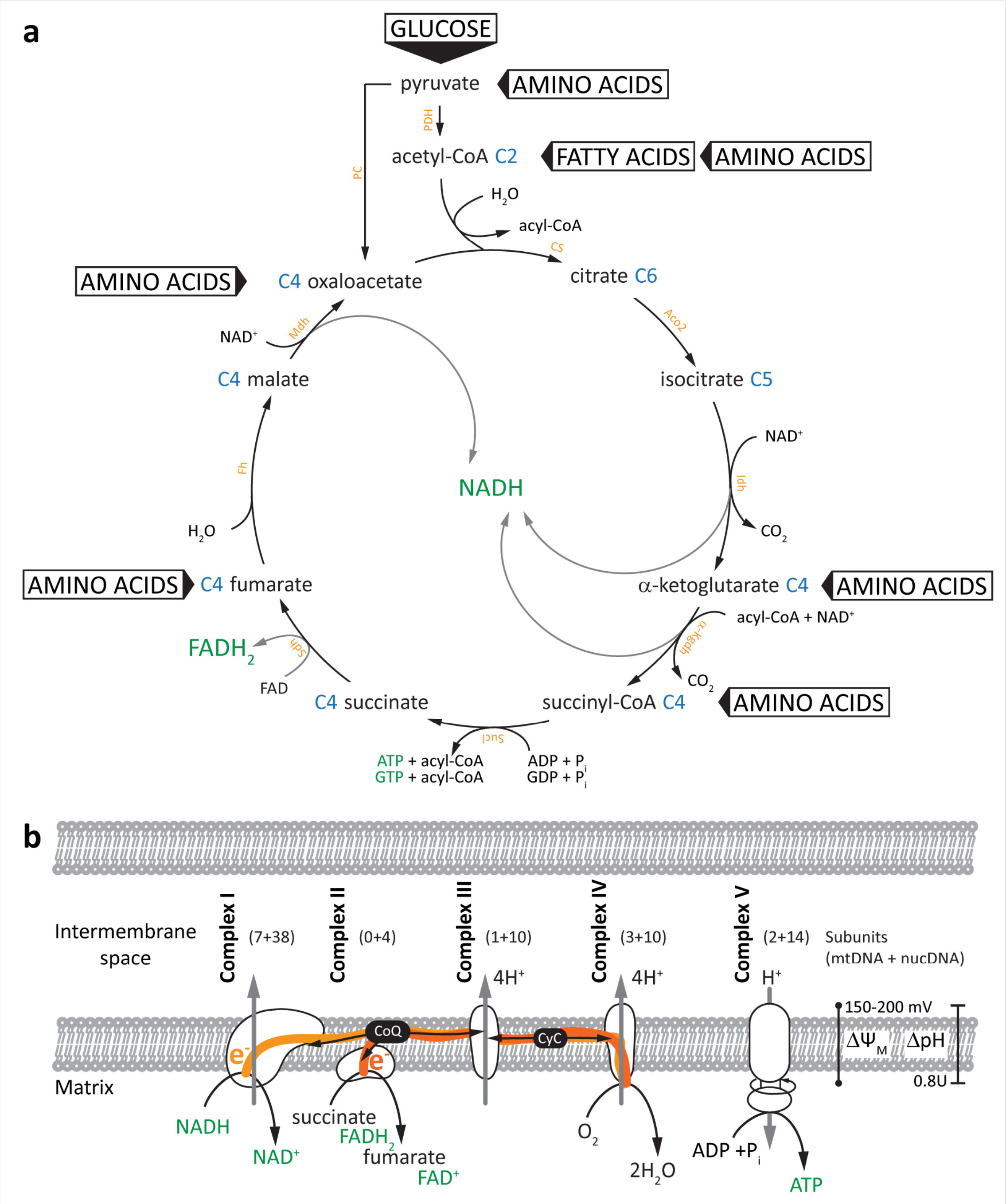
a
GLUCOSE
pyruvate
AMINO ACIDS
PDH
PC
acetyl-CoA C2
FATTY ACIDS
AMINO ACIDS
H_2O
acyl-CoA
CS
AMINO ACIDS
C4 oxaloacetate
citrate C6
Aco2
NAD+
Mdh
C4 malate
isocitrate C5
NAD+
Idh
NADH
Fh
H_2O
CO_2
AMINO ACIDS
C4 fumarate
α-ketoglutarate C4
AMINO ACIDS
acyl-CoA + NAD+
α-Kgdh
$FADH_2$
Sdh
CO_2
FAD
C4 succinate
succinyl-CoA C4
AMINO ACIDS
Sucl
ATP + acyl-CoA
GTP + acyl-CoA
ADP + P_i
GDP + P_i
b
Intermembrane space
Complex I
(7+38)
Complex II
(0+4)
Complex III
(1+10)
Complex IV
(3+10)
Complex V
(2+14)
Subunits (mtDNA + nucDNA)
4H+
4H+
H+
150-200 mV
CoQ
CyC
e-
e-
ΔΨ_M
ΔpH
0.8U
Matrix
NADH
NAD^+
succinate
$FADH_2$
fumarate
FAD^+
O_2
$2H_2O$
ADP +P_i
ATP

Figure 2│ Tricarboxylic acid cycle and electron transport chain. (**a**) Schema of TCA cycle depicting major entry routes for glucose, fatty acids and amino acids. TCA intermediates are indicated by their carbon chain length (blue) and enzymes (orange). NADH, $FADH_2$, ATP and GTP are green. Depending on Sucl subunits, substrate phosphorylation can generate ATP or GTP. PDH, pyruvate dehydrogenase; PC, pyruvate carboxylase; CS, citrate synthase; Aco2, aconitase 2; Idh, isocitrate dehydrogenase; α-Kgdh, α-ketoglutarate dehydrogenase; Sucl, succinyl-CoA ligase; Sdh, succinate dehydrogenase; Fh, fumarase; Mdh, malate dehydrogenase. (**b**) Schema of ETC depicting complex I-IV and complex V. Electrons (orange) are provided by NADH or Sdh complex via $FADH_2$, and travel via coenzyme Q (CoQ) and cytochrome c (CyC) in the inner mitochondrial membrane. Protons are pumped via complex I, III and IV into the intermembrane space (ΔpH) and thereby create the membrane potential over the inner mitochondrial membrane $\Delta\Psi_m$. At complex V, the proton gradient is used to generate ATP.

translocase complex (ANT1/2), no mitochondrial transporter for GTP exists. Therefore, the energy from GTP needs to be transferred to ATP or ADP (via nucleoside diphosphate kinase or adenylate kinases) or be used within mitochondria, e.g. by phosphoenolpyruvate carboxykinase (Pck2). The TCA cycle is regulated via substrate availability, ATP and NADH inhibition and allosteric inhibition of intermediates with three rate-limiting enzymes: citrate synthetase, isocitrate dehydrogenase and α-ketoglutarate dehydrogenase. Furthermore, Ca^{2+} stimulates the TCA cycle by activating isocitrate dehydrogenase, α-ketoglutarate dehydrogenase and pyruvate dehydrogenase phosphatase, which activates PDH (Wan et al., 1989).

NADH and $FADH_2$ are transferring the free energy in form of electrons to the **electron transport chain** (ETC) that consists of five multisubunit protein complexes (Figure 2b). All are localized in the inner mitochondrial membrane and collectively use the free energy to pump protons from the matrix into the intermembrane space thereby creating an electrochemical gradient and the membrane potential $\Delta\Psi_m$. This potential is finally used in complex V to generate ATP by chemiosmosis.

First, NADH diffuses to complex I and donates two electrons to the complex, which allows the translocation of four protons into the intermembrane space. The electrons are passed down to coenzyme Q (CoQ) that freely diffuses thought the inner mitochondrial membrane. In contrast, $FADH_2$ is directly formed on complex II (succinate dehydrogenase) and donates its electrons to CoQ. Complex II does not translocate protons over the inner mitochondrial membrane. Next on complex III, CoQ is oxidized passing two protons to the intermembrane space and its electrons to cytochrome c. The reaction enables an additional two protons to cross the inner membrane. Finally, at complex IV, electrons are transferred from cytochrome c to the complex that pumps four protons across the membrane and generated two H_2O from oxygen.

At complex V, the F_0F_1ATPase, the chemiosmotic gradient is used to phosphorylate adenosine diphosphate to ATP (Mitchell, 1961). Paul D. Boyer and John E. Walker received the Novel Prize in Chemistry in 1997 (Walker, 1998) for discovering the rotation mechanism of F_0F_1ATPase. Not all translocated protons participate in the production of ATP. Protons can leak across the mitochondrial membranes, e.g. via mitochondrial uncouplers, and generate heat (Nedergaard et al., 1977; reviewed in Kadenbach, 2003). It is estimated that a molecule NADH and a molecule FADH generate three and two molecules ATP, respectively (Watt et al., 2010).

1.2.1.1. Beta-oxidation

Mitochondria and peroxisomes metabolically cooperate in beta-oxidation of fatty acid (FA). While peroxisomes metabolize very long-chain (>C22) and branched-chain FA, mitochondria oxidize long, medium and short-chain FA (reviewed in Demarquoy and Le Borgne, 2015). In peroxisomes, FAs are shortened to acyl-CoA (C2, C3, C11), which is exported in the form of acylcarnitine and imported into mitochondria for full oxidation (Verhoeven et al., 1998; Ferdinandusse et al., 1999).

Mitochondrial beta-oxidation can be split into two steps: FA import and FA degradation to acetyl-CoA (reviewed in Eaton, 2002). For mitochondrial **FA import**, long-chain FA are imported via the carnitine shuttle system (reviewed in Qu et al., 2016) composed of carnitine o-palmitoyltransferase 1, liver isoform (Cpt1a) in the outer mitochondrial membrane (van der Leij et al., 1999) and carnitine/acylcarnitine translocase (Slc25a20) in and Cpt2 associated to the inner mitochondrial membrane (Console et al., 2014). In brief, FAs are conjugated to carnitine via Cpt1a (Yates and Garland, 1970), transported over the inner mitochondrial membrane via Slc25a20 (Iacobazzi et al., 2004) and conjugated to CoA via Cpt2 (Bonnefont et al., 2004). In contrast, medium and short-chain FA (<C12) can freely enter mitochondria. For FA catabolism, FAs are activated by conjugation to CoA that is catalyzed by acyl-CoA synthetases (Acs; reviewed in Watkins, 2008). This family is composed of several members with substrate chain length specificity (Watkins et al., 2007). FA (<C12) are activated via Acsm and Acss in the mitochondrial matrix (Williamson et al., 1968). In contrast, long-chain fatty acids are conjugated to CoA via Acsl and Acsbg in the cytosol and imported via the carnitine shuttle system with CoA conjugation via Cpt2. The mitochondrial membrane is impermeable for acyl-CoA and therefore conjugates are trapped for degradation.

For **FA degradation**, acyl-CoA is shortened to acetyl-CoA in repeated rounds of four reactions, namely oxidation-hydration-oxidation-thiolysis. These reactions are performed by chain-specific acyl-CoA dehydrogenases (Acad) and the trifunctional protein (Uchida et al., 1992; and reviewed in Houten and Wanders, 2010). The products of mitochondrial beta-oxidation are acetyl-CoA, which enters the TCA cycle, $FADH_2$ and NADH, which both transfer electrons to the ETC.

1.2.2. Anabolic role of mitochondria

Mitochondria are also **biosynthetic hubs** and participate for example in the anabolism of amino acids, fatty acids, glucose, heme and nucleotides. Several intermediates of the TCA cycle are precursors for the biosynthesis of macromolecules apart from their catabolic role in the Krebs cycle. For example in the adaptive immune system, naïve T cells are quiescent, have a catabolic metabolism and relay on oxidative phosphorylation. Upon activation, T cells become proliferative, shift to an anabolic metabolism and rely on glycolysis and glutaminolysis despite oxygen availability (reviewed in van der Windt and Pearce, 2012). In both physiological states mitochondrial metabolism and the TCA cycle are active; however, ATP is generated differently. Later on as memory T cells, metabolism is switched back to catabolism with enhanced beta-oxidation and mitochondrial biogenesis.

The biosynthesis of **amino acids** uses carbon backbones from intermediates of glycolysis, the pentose phosphate pathway and the TCA cycle. Specifically, the amino acids glutamate (Glud1), glutamine (Gs, Gls), proline (Oat, Pycr) and arginine (Ass) are derived from α-ketoglutarate; aspartate (Got2) and asparagine (Asns) from oxaloacetate; and alanine (Gpt2) from pyruvate. All other amino acids derive from intermediates of glycolysis and the pentose phosphate pathway with the exception of essential amino acids (phenylalanine, valine, threonine, tryptophan, methionine, leucine, isoleucine, lysine and histidine).

Gluconeogenesis is primarily a cytosolic process; still, its starting point originates in mitochondria, where oxaloacetate is converted to malate or aspartate for mitochondrial export. In the cytosol, phosphoenolpyruvate carboxykinase (Pck1) continuous by generating phosphoenolpyruvate that is converted to glucose-6P. This substrate can enter the pentose phosphate pathway or glycogenesis (mostly active in astrocytes; Vilchez et al., 2007). Alternatively, oxaloacetate can be converted by mitochondrial phosphoenolpyruvate carboxykinase (Pck2) to phosphoenolpyruvate and exported over the mitochondrial membrane (Drahota et al., 1983). Pck2 is GTP-dependent and uses GTP produced via substrate level phosphorylation in the TCA cycle (see Chapter 1.2.1). Interestingly, in the absence of glucose, Pck2 fuels the TCA cycle with phosphoenolpyruvate via glutamine utilization (Vincent et al., 2015).

Fatty acid synthesis is performed by two cellular systems: a cytosolic system providing triglycerides for phospholipids and a mitochondrial system (mtFAS) generating lipoic acid via octanoyl-ACP (Brody et al., 1997) and long-chain acyl carrier proteins (ACP). As such both systems have distinct roles – with mtFAS providing control over the TCA cycle and the respiratory chain dependent on acetyl-CoA availability (reviewed in Nowinski et al., 2018). Specifically, lipoic acid, which is generated from octanoyl-ACP, is an important cofactor for pyruvate dehydrogenase, α-ketoglutarate dehydrogenase, branched-chain dehydrogenase and the glycine cleavage system (Perham, 2000). However, apart from octanoyl-ACP, longer ACPs were found in mitochondria with unknown function. Recently, Van Vranken et al. (2018) demonstrated their interaction with the LYR protein family, which contains proteins important for respiratory chain assembly and iron-sulphur cluster biogenesis (Runswick et al., 1991; Van Vranken et al., 2016; reviewed in Angerer, 2015). LYR proteins are present in complex I-III and allosterically activated by acyl-ACP in a length-specific manner.

The **synthesis of heme** (porphyrin synthesis) is unique in the sense that its biosynthesis is coordinated between cytosol and mitochondria, and requires compartmentalization. Heme is incorporated in many metalloproteins, like cytochromes and catalase (Smith et al., 2011). In the mitochondrial matrix, aminolevulinate is generated from succinyl-CoA and glycine via aminolevulinate synthetase and exported via Slc25a38. In the cytosol, aminolevulinate is modified to coproporphyrinogen III that is actively imported into the intermembrane space via Abcb6. Here, it is first converted to protophyrinogen via coproporphyrinogen oxidase and then imported into the matrix, where ferrochelatase inserts ferrous iron. H_2O_2 is generated during this synthesis; hence, the confinement to a membrane-bound organelle.

1.2.3. Mitochondrial Ca^{2+} buffering

Ca^{2+} is a tightly regulated signaling molecule in cells. Its cytosolic levels are low, while the endoplasmic reticulum functions as intracellular Ca^{2+} store. Mitochondria participate in cellular Ca^{2+} homeostasis by Ca^{2+} buffering at privileged contact sites with the endoplasmic reticulum and the plasma membrane (Szymanski et al., 2017). The outer mitochondrial membrane is permeant for Ca^{2+} and therefore, cytosolic and mitochondrial intermembrane space concentrations are at equilibrium (Rizzuto et al., 1998). Free Ca^{2+} is driven into mitochondria through the negative membrane potential $\Delta\Psi_m$ and enters mainly via the mitochondrial calcium uniporter (Mcu); still, two additional Ca^{2+} currents have been measured in mitoplasts (Bondarenko et al., 2013). In the mitochondrial matrix, Ca^{2+} has been shown to stimulate key enzymes of the TCA cycle and the F_0F_1ATPase, but can also be buffered via a system with inorganic phosphate (Rossi and Lehninger, 1964; Lehninger, 1974). Here, free Ca^{2+} forms a calcium-phosphate complex (Chalmers and Nicholls, 2003). In addition, Ca^{2+} can be extruded from mitochondria via the electroneutral H^+/Ca^{2+} exchanger or the electrogenic Na^+/Ca^{2+} antiporter (NCLX; reviewed in De Stefani et al., 2016).

The ability of mitochondria to uptake Ca^{2+} was known for a long time (Deluca and Engstrom, 1961); still, its underlying molecular identity was only reported in the last decade: first with the identification of the mitochondrial calcium uptake protein 1 (Micu1; Perocchi et al., 2010), followed by Mcu (Baughman et al., 2011; De Stefani et al., 2011) and later its other complex components. The **Mcu complex** is localized to the inner mitochondrial membrane and consists of the pore-forming proteins: Mcu, McuB (Raffaello et al., 2013) and essential MCU regulator (Emre; Sancak et al., 2013). While Mcu is the Ca^{2+} permeant pore and can be reconstituted alone into lipid bilayers (De Stefani et al., 2011), its function in cells requires co-expression of Emre (Kovacs-Bogdan et al., 2014). Mcu forms homodimers and heterodimers with McuB and their distribution is heterogeneous across tissue (Fieni et al., 2012). Raffaello et al. (2013) showed that Ca^{2+} flux through McuB is impaired. In fact, McuB acts as dominant-negative Mcu homolog and its presence is proposed as regulatory mechanism for mitochondrial Ca^{2+} regulation across tissues and during stress conditions (reviewed in De Stefani et al., 2016; Lambert et al., 2019).

The Mcu complex further consists of Micu 1-3 that regulate the sigmoid opening of the channel and are localized to the intermembrane space. Both Micu1 and Micu2 (Plovanich et al., 2013) have gatekeeper function for Mcu with Micu1 controlling the Ca^{2+} threshold and opening of the channel at high Ca^{2+} concentrations (Mallilankaraman et al., 2012b; Csordas et al., 2013) and Micu2 controlling the channel closure at low Ca^{2+} concentrations (Patron et al., 2014). Additionally, Tomar et al. (2019b) identified MIC60 and CHCHD2 as novel Ca^{2+}-independent interactors of Micu1 – thus, indicating Micu1 function in cristae organization. Micu3 is predominantly expressed in the central nervous system (Plovanich et al., 2013), where it interacts with Micu1 to regulate Mcu opening. In contrast to Micu2, Micu3 increases Ca^{2+} uptake of the Mcu complex and is an activator of the channel (Patron et al., 2019).

Finally, Mallilankaraman et al. (2012a) identified another interactor of the Mcu complex, McuR1. Its function in the complex is currently still controversial (reviewed in Paupe et al., 2015; Raffaello et al., 2016).

Regulation of the Mcu complex has been shown at multiple levels: (i) via expression levels of Mcu/McuB (Fieni et al., 2012); (ii) via expression levels of Micu1/Mcu (Paillard et al., 2017); and (iii) via posttranslational modification of Micu1 (Madreiter-Sokolowski et al., 2016; Marchi et al., 2019). Interestingly, mice on a mixed CD1-C57BL/6 background can compensate Mcu deletion (Pan et al., 2013), while Mcu^{ko} mice are embryonal lethal on a C57BL/6 inbreed strain (Murphy et al., 2014). The underlying cause is currently under investigation. Furthermore, deletion of Mcu is not detrimental in multiple cell types apart from their metabolic adaptation (Luongo et al., 2015; Nichols et al., 2018; Gherardi et al., 2019; Tomar et al., 2019a). In contrast, Micu1 deletion in mouse leads to a high perinatal lethality and surviving animals develop severe neurological defects and myopathy (Liu et al., 2016; Antony et al., 2016).

1.2.4. Contact sites – mitochondrial association with other organelles

Mitochondria are not simply 'rocks in the sea of cytoplasm' – but are tightly interconnected with other organelles (Valm et al., 2017). Classically a contact site between organelles is the close apposition of their membranes. Such sites of interaction allow for the exchange of molecules for shared biochemical pathways and signaling. An increasing number of molecules that establish these contact sites have been identified between most organelles (Eisenberg-Bord et al., 2016). These molecules can be categorized into tether and spacer (Fernandez-Busnadiego et al., 2015) depending on the phenotype of their loss/enhancement. As defined in Scorrano et al. (2019), contact sites are mediated by a protein-protein or protein-lipid interaction, can range from 10 – 80 nm in distance (but also might span >300 nm; Klecker et al., 2013), should convey a function and can be static or dynamic (Raiborg et al., 2015).

In the case of mitochondria, a number of organelle-specific **tethers** have been described. For example, mitochondria form contact sites with: the endoplasmic reticulum via Mfn2 (de Brito and Scorrano, 2008) or VAPB-Rmdn3 (De Vos et al., 2012); lipid droplets via Plin5 (Wang et al., 2011a); the plasma membrane via Num1 (Ping et al., 2016); lysosomes via Rab7 (Wong et al., 2018); and with peroxisomes via Pex34 (Shai et al., 2018).

Amongst them, the contact to the **endoplasmic reticulum** (ER) is best studied in the context of Ca^{2+} homeostasis (Rizzuto et al., 1998), phospholipid synthesis (Vance, 1990) and its role in mitochondrial fission (Friedman et al., 2011).

Peroxisomes and mitochondria share an intimate relationship via their functional interplay in beta-oxidation (reviewed in Wanders et al., 2016), reactive oxygen species handling (reviewed in Lismont et al., 2015) and anti-viral signaling (Dixit et al., 2010). While the molecular identity of their contact sites is less clear than with the ER, a frequent placing of peroxisomes at sites of ER-mitochondria contacts was reported by Cohen et al. (2014).

1.3. Mitochondrial proteome

The mitochondrial proteome is estimated to contain ~**1,200 – 1,500 proteins**. Of these, 13 proteins are encoded by mtDNA in mammals, while >99% of mitochondrial proteins are transcript from genes in the nucleus. Consequently, mitochondria are shaped by the cellular translatome. Related to the endosymbiont origin of mitochondria, the engulfed proteobacteria had to adapt to their host cell on different levels and this process has shaped the current mitochondrial proteome by: (i) incorporation of host proteins; (ii) transfer of genes to the less mutagenesis-prone nucleus; (iii) loss of proteobacterial proteins or their relocation to other subcellular compartments; and (iv) adaption of an import machinery for novel and own proteins. Gabaldon and Huynen (2007) calculated that ~15% of mitochondrial proteins have orthologs in α-proteobacteria with an additional 28% originating from other proteobacteria and the rest deriving from prokaryotes (~16%) and eukaryotes (~40%; reviewed in Szklarczyk and Huynen, 2010).

As >99% of proteins are encoded by nuclear DNA, an essential element of mitochondrial adaptation was the **targeting of proteins** to the organelle and their selective **import**. Currently, at least six mechanisms are known that target proteins for the import into mitochondria (reviewed in Chacinska et al., 2009). They can be divided into cleavable and non-cleavable target sequences, and present as: (i) positively charged amphipathic α-helix; (ii) β signal for β-barrel proteins; (iii) α-helical transmembrane segment for the outer mitochondrial membrane (via signal anchor, tail anchor or internal signal); (iv) multiple internal transmembrane signals; (v) an internal presequence-like signal; or (vi) as cysteine-containing signal. Via these motives, proteins are directed to the mitochondrial matrix, inner and outer mitochondrial membrane or the intermembrane space. Signal recognition is mediated through several complexes that sort proteins, namely the translocase of the outer membrane (TOM complex; van Wilpe et al., 1999; Abe et al., 2000) with the sorting and

Table 1. Experimental studies defining the mitochondrial proteome.

Mitochondrial proteome

Study	*Species*	*Sample*	*Isolation method*	*Proteins*
Rabilloud et al. (1998)	Hu	Placenta	CMF	46
Taylor et al. (2003)	Hu	Heart	Sucrose density centrifugation	615
Mootha et al. (2003)	Ms	Heart, kidney, liver, brain	Percoll density centrifugation	399
Kislinger et al. (2006)	Ms	Heart, kidney, liver, brain, lung, placenta	CMF	2,533
Forner et al. (2006)	Ms	Heart, liver, muscle	Sucrose density centrifugation,	689
Foster et al. (2006)	Ms	Liver	Density gradient centrifugation, protein correlation profiling	297
Adachi et al. (2007)	Ms	3T3-L1 adipocytes	Sucrose density centrifugation	1,130
Johnson et al. (2007)	Rat	Heart, kidney, liver, brain	CMF	1,162
Pagliarini et al. (2008)	Ms	14 tissues	CMF *vs* Percoll density centrifugation	1,098
Lotz et al. (2014)	Hu	Heart	CMF	419
	Ms	Heart, liver		
	Dmel	total		
Calvo et al. (2016)	Hu Ms	update from Pagliarini et al. (2008)	CMF *vs* Percoll density centrifugation	1,158
Itzhak et al. (2016)	Hu	HeLa endocervical adenocarcinoma cells	Density gradient centrifugation with SILAC	658
Morgenstern et al. (2017)	Yeast	total	CMF *vs* Percoll density centrifugation, subcompartments	901

Mitochondrial subcompartment proteome

Study	*Species*	*Sample*	*Isolation method*	*Proteins*
Rhee et al. (2013)	Hu	HEK 293T embryonic kidney cells	APEX-labeling, matrix	495
Hung et al. (2014)	Hu	HEK 293T embryonic kidney cells	APEX-labeling, intermembrane space with SILAC	127
Hung et al. (2017)	Hu	HEK 293T embryonic kidney cells	APEX-labeling, outer mitochondrial membrane with SILAC	137

Mitochondrial proteomes in the central nervous system

Study	*Species*	*Sample*	*Isolation method*	*Proteins*
Stauch et al. (2014)	Ms	Brain, synaptosomes	Percoll gradient for synaptosomal and non-syn. mitochondria then IC Tom22; SILAC mix from cell culture	1,629 (2,260)
Graham et al. (2017)	Rat Sheep	Forebrain, synaptosomes	Fiscoll-sucrose density centrifugation for synaptosomal and non-syn. mitochondria	1,511
Stauch et al. (2019)	Ms	Forebrain, midbrain, synaptosomes	Percoll gradient for synaptosomal mitochondria then IC Tom22; SILAC mix from cell culture	750 (1,293)

Hu, human; Ms, mouse; Dmel, *Drosophila melanogaster*; CMF, crude mitochondrial fraction. X (Y), mitochondrial annotated proteins (total proteins).

assembly machinery (SAM) for the outer mitochondrial membrane, the mitochondrial import 1 (Mim1) also for the outer mitochondrial membrane, the mitochondrial intermembrane space assembly (MIA), the presequence translocase of the inner membrane (TIM23 complex; Yamamoto et al., 2002) with presequence translocase-associated motor (PAM) for the matrix and insertase/export machinery of the inner membrane (OXA) for the inner mitochondrial membrane, and the carrier translocase of the inner membrane (TIM22 complex) for carrier proteins of the inner mitochondrial membrane. In the mitochondrial matrix, target sequences are cleaved off via the mitochondrial processing peptidase and proteins can be further modified via other peptidases in matrix and intermembrane space (Vogtle et al., 2009; reviewed in Schmidt et al., 2010).

Targeting sequences have been used by Calvo et al. (2017) and others to define the mitochondrial proteome using experimental data, genomic sequencing data and bioinformatics tools (reviewed in Gaston et al., 2009). Still, targeting sequences alone are not powerful in detecting the mitochondrial proteome as a whole due to our limitation in sequence knowledge and a high false-positive rate from prediction studies (reviewed in Calvo and Mootha, 2010). In addition, proteomics of purified mitochondrial fractions via tandem mass spectrometry has been successful in identifying the core mitochondrial proteome (see Table 1).

The most conclusive study today – the **MitoCarta** – combined the experimental evidence of mitochondrial proteins across 14 mouse tissues by mass spectrometry with six other data sources, including yeast homology, Pfam domains and N-terminal targeting signals, and integrated them via Bayesian integration (Figure 3a; Pagliarini et al., 2008; Calvo et al., 2016). The initial mass spectrometry discovery phase included Percoll gradient isolated mitochondria from cerebrum, cerebellum, brainstem, spinal cord, kidney, liver, heart, skeletal muscle, white adipose tissue stomach, small intestine, large intestine, testis, and placenta, and identified 3,881 proteins by LS-MS/MS. In a second phase, crude mitochondria and Percoll gradient isolated mitochondria from ten tissues were analyzed and 2,565 proteins were identified with 1,022 and 709 enriched in the crude and pure fractions, respectively. Based on subtractive proteomics and protein abundance, the authors calculated a likelihood ratio for each protein taking into account several other data sources via a Maestro naïve Bayes framework integration (Calvo et al., 2006). This predicted 951 proteins under a corrected false discovery rate of 10%. Further complementation by microscopy and literature search defined a total of

1,098 proteins in mouse and 1,013 in human as mitochondrial. In 2016, the study was updated to MitoCarta 2.0 – now containing 1,158 proteins in mouse and human. Interestingly, the authors noticed several features of mitochondria across tissues: (i) mitochondrial abundance can vary up to 30 times between tissues (Figure 3b); (ii) ~one-third of proteins represent a common core across tissue proteomes; and (iii) pairs of tissues share 63 – 88% of their mitochondrial proteome (Figure 3c).

The MitoCarta is currently the 'gold standard' for defining mitochondrial proteins; still, ~30% of its entries are orphan proteins without functional annotation. Here, advances are made by

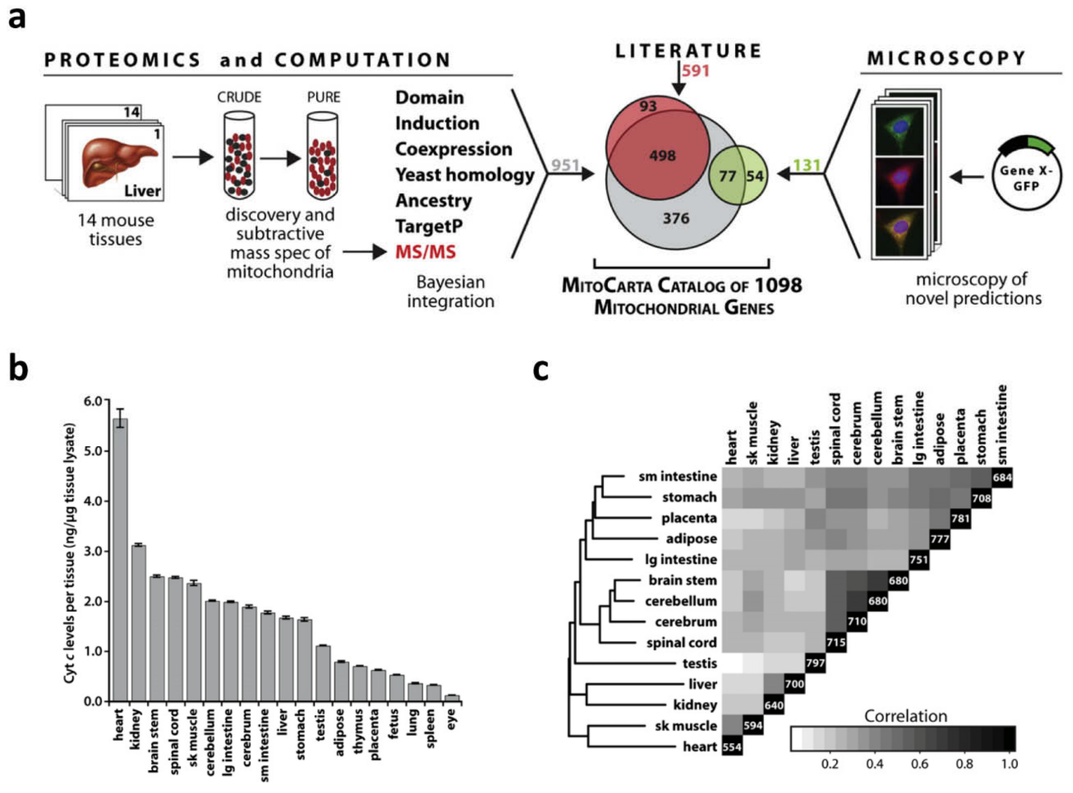

Reprinted from Cell, 134/1, Pagliarini, DJ et al., A mitochondrial protein compendium elucidates complex I disease biology, p.112-123, Copyright (2008), with permission from Elsevier.

Figure 3| MitoCarta catalog of 1,098 mitochondrial genes. (**a**) Building a compendium of mitochondrial proteins by an integrated analysis of seven genome-scale data sets (gray circle), a large-scale GFP tagging and microscopy study (green circle), and prior experimental support from focused studies (red circle). Reprinted from Pagliarini et al. (2008), Figure 1 and figure legend. (**b**-**c**) Mitochondrial proteins expression across 14 mouse tissues. (**b**) Mitochondrial quantity per tissue, assessed by ELISA measurements of cytochrome c from whole-tissue lysates. Error bars represent the range of duplicate measurements. (**c**) Correlation matrix of MitoCarta proteins detected by MS/MS in each tissue, clustered hierarchically. Counts on the diagonal indicate number of MitoCarta proteins identified by MS/MS. Reprinted from Pagliarini et al. (2008), Figure 4c and 4d, and figure legend. Reprinted from Cell, 134/1, Pagliarini et al. (2008), with permission from Elsevier. DOI: 10.1016/j.cell.2008.06.016.

the collection of big data sets, their integration via bioinformatics and the deciphering of co-regulated proteins. For example, Stefely et al. (2016a) used **multi-omic profiling** of proteome, lipidome and metabolome in mitochondrial deletion strains in *Saccharomyces cerevisiae* and hereby identified novel members of the CoQ pathway. Recently, Kustatscher et al. (2019) generated a co-regulation map of the entire human proteome and thereby, identified co-regulation of Pex11β with subunits of the mitochondrial ETC. They further showed that Pex11β established contact sites between peroxisomes and mitochondria, likely for the exchange of metabolites. Related to the nervous system, Sharma et al. (2015) generated a high-resolution proteome of 10 defined brain tissue areas, four FACSorted cell types and five primary cell types in culture and identified 12,934 proteins of the ~20,000 genes in mammals. Interestingly, 144 MitoCarta proteins were not identified by this study implying their absence in the nervous system or molecular restrictions that prevent their identification by mass spectrometry.

In addition, several **databases** have been created (Smith and Robinson, 2016; Godin and Eichler, 2017; Yim et al., 2020) that collected experimental data from a variety of experiments and assays and integrated them for further processing by users.

Overall, our understanding of the molecular composition of mitochondria has been broadened by the identification of estimated >85% of its proteins. Still, as mitochondria are made by the translatome of their host cells, **not every mitochondrion will be the same**, but rather is adapted by the cell depending on tissue, cell type and physiological state. As proteomes cannot easily be inferred from transcriptomes (Ghazalpour et al., 2011) and the profiling from nuclear mRNA does not necessarily reflect local translation – especially in complex cells such as neurons, we are still far from understanding the mitochondrial proteome in its heterogeneity and complexity in different cells.

1.4. Mitochondrial diversity

Through proteomics studies like the MitoCarta (Pagliarini et al., 2008) and many others (see Table 1), it is widely accepted that mitochondrial populations from **different tissues** contain subsets of differential proteins (12-33% of proteins; Figure 3c) and hence are specialized in certain mitochondrial functions. In addition, mitochondrial ultrastructure varies among tissues linking form to function (reviewed in Zick et al., 2009; Vafai and Mootha, 2012). Interestingly, given that all mtDNA-encoded proteins are essential for the respiratory chain, only nuclear-encoded proteins contribute to this heterogeneity. Still, mitochondrial diversity is particularly discussed on the level of inter- and intracellular mtDNA heteroplasmy (reviewed in Aryaman et al., 2018) – likely due to its context in mitochondrial diseases (see Chapter 1.7). While cells contain up to several thousand copies of mtDNA (D'Erchia et al., 2015), mtDNA is more prone to mutations than nuclear DNA – particularly for age-related deletions and replication errors (Kennedy et al., 2013). Dependent on time of occurrence, mutations might propagate along the lineage of a cell type and influence a whole organ system; or accumulate over time through the mtDNA life cycle of degradation and biogenesis in even non-proliferative cells, e.g. neurons (Aryaman et al., 2018; and references herein). However, only mutations that cross a certain threshold, result in a phenotype (reviewed in Rossignol et al., 2003). This threshold is tissue- and cell type-dependent and partially causative for the heterogeneity of symptoms in humans with mtDNA mutations and deletions (reviewed in Moggio et al., 2014). Morris et al. (2017) analyzed three high-confidence single-nucleotide variances in individual mitochondria from neurons and astrocytes and confirmed their heteroplasmy across single cells and individuals in mice and humans.

In contrast to mitochondrial proteome heterogeneity among tissues, the distribution of this diversity among its resident **cell types** is less well known. Similarly, we are limited in our knowledge of organelle variation **within cells**. One reason for this is the limitation to probe for such origin-specific organelles in vivo.

For example, in skeletal muscle fibers, mitochondria are present as distinct intracellular populations dependent on localization, namely subsarcolemmal and intermyofibrillar mitochondria (reviewed in Hollander et al., 2014). These mitochondrial populations differ in ultrastructure and function – particularly respiration and Ca^{2+} handling (Palmer et al., 1977; McMillin-Wood et al., 1980; Shimada et al., 1984; Cogswell et al., 1993). Murgia et al. (2015) performed mass spectrometry on single muscle fibers and identified distinct fiber specialization in TCA cycle, beta-oxidation and redox metabolism – for example in isocitrate dehydrogenase 2 and 3 expression. Further analysis strengthened their conclusion of a fiber-tuned TCA cycle (reviewed in Schiaffino et al., 2015).

This situation is more complex in neurons, which in some cases can have an axon length of ~0.46 m in mouse and ~100 m in humans (Matsuda et al., 2009; Wu et al., 2014), and face an extraordinary challenge in maintaining organelles throughout their entire geometry. While in other cells mitochondrial content can be easily exchanged via mitochondrial dynamics and biogenesis, these processes are spatially limited in neurons due to an increasing distance to the nucleus and a limited local organelle pool. Specifically, the interplay of selective and directional transport, local translation, organelle dynamics and protein degradation as well as bulk biogenesis and autophagy form the neuronal “[…] mitostasis […]” (Misgeld and Schwarz, 2017). Hence, mitochondria differ between dendrites, soma, axon and synapse. For example, Lewis et al. (2018) quantified mitochondria in cortical pyramidal neurons of layer 2/3 in vivo and observed a length gradient of 1.3 – 13.3 µm in dendrites and 0.5 – 1.1 µm in axons. Independent confirmation of these size differences comes from ultrastructure analysis across brain regions (Delgado et al., 2019). Furthermore, scientists have particularly focused on mitochondria at the synapse. These mitochondrial populations can be enriched via gradient density centrifugation (Lai et al., 1977) and are traditionally compared to non-synaptic mitochondria. Early studies by Dennis et al. (1977) demonstrated respiratory differences between these organelle populations. Further, McKenna et al. (2000) showed enrichment of glutamate metabolism at the synapse and recent proteomics studies identified molecular differences (Stauch et al., 2014; Graham et al., 2017). Consensus of these studies is that oxidative phosphorylation, mitochondrial dynamics and Ca^{2+} handling are major contributors to mitochondrial specialization at the synapse.

Still, these studies have to face two major criticisms: (i) the contamination of glial mitochondria; and (ii) the multisubtype-specific origin of synaptic mitochondria. Synaptosomes, which are the starting material for synaptic mitochondria, usually contain material from pre-, postsynapse, and glial processes. While glial processes might be removed or pre- and postsynapse separated via sophisticated protocols, the presence of glial mitochondria within the non-synaptic fraction cannot be denied. Hence, the comparison of synaptic *vs* non-synaptic mitochondria is to a large degree a comparison of neuronal to brain mitochondria including all non-neuronal cell types. Secondly, even within the synaptic fraction, mitochondria originate from different neuronal subtypes, e.g. excitatory and inhibitory neurons (reviewed in Wang and Savas, 2018 with focus on the synapse in general). This mixing of mitochondrial origin either in the non-synaptic or synaptic fraction is masking the true mitochondrial heterogeneity among neural cell types and their specialization at synapses. Thus, novel purification approaches are needed for a cell type-resolved interpretation of synaptic mitochondria.

Nevertheless, a number of studies have uncovered profound functional specializations of neural mitochondria – even within neuronal compartments (see the following Chapters).

1.4.1. Mitochondrial proteins enriched in neural cell types

Mitochondrial calcium uptake protein 3 (Micu3) is a paralog to Micu1 and Micu2 and microarray data from 21 mouse tissues showed its strong enrichment in the nervous system (Plovanich et al., 2013). This was independently confirmed in fly and humans (Tufi et al., 2019; Patron et al., 2019). Micu2 and Micu3 are interacting with Micu1 and recently, Xing et al. (2019) reported their similarity in structure based on their Ca^{2+}-bound and unbound crystal structure. In contrast, Patron et al. (2019) reported that Micu1-Micu3 interaction leads to an increased Ca^{2+} uptake of Mcu and therefore proposed Micu3 as Mcu activator. Thus, Micu2 and Micu3 seem to have opposing roles in the Mcu complex, while their structural mechanism is similar. In agreement with this report, Ashrafi et al. (2020) demonstrated that neuronal mitochondria uptake stimulus-evoked Ca^{2+} in an ER-independent manner in axons and that this is possible due to the lower Ca^{2+} threshold of Micu3-containing Mcu complex.

Adck3 (Coq8a) and Adck4 (Coq8b) are orthologues of the yeast *Coq8* gene. Both have been shown to be part of the coenzyme Q_{10} complex and to stabilize it (Floyd et al., 2016). Their function is non-redundant given that Stefely et al. (2016b) demonstrated that Adck3 has ATPase activity, while its protein kinase activity is structurally blocked (Stefely et al., 2015). In contrast, Adck4 functions as protein kinase (Stefely and Pagliarini, 2017). Strikingly, deficiency in Adck3 clinically presents as ataxia and cerebellar atrophy (Lagier-Tourenne et al., 2008), while Adck4 deficiency leads to nephrotic syndrome (Ashraf et al., 2013). In an Adck3 deficient mouse model, Stefely et al. (2016b) observed dark and shrunken Purkinje cells with ~10% neuronal degeneration and altered peacemaking activity implicating a cell type-specific vulnerability in Adck3.

4-nitrophenylphosphatase domain and non-neuronal SNAP25-like protein homolog 1 (**Nipsnap1**) is localized to the mitochondrial matrix and Nautiyal et al. (2010) reported its exclusive expression in neurons in the nervous system. Functionally, Nipsnap1 was shown to interact with components of the branched-chain α-keto acid dehydrogenase enzyme complex (Nautiyal et al., 2010) and the amyloid precursor protein (APP) in mitochondria via the C-terminal region of APP (Tummala et al., 2010). Recently, two reports provided evidence for Nipsnap1 accumulation on the outer mitochondrial membrane of damaged mitochondria, where it served as an autophagy recruitment signal (Abudu et al., 2019; Princely Abudu et al., 2019). Interestingly, while Nipsnap1 is also expressed in non-neuronal tissues, like kidney and liver, its deletion in zebrafish leads to Parkinsonism and neuronal loss (Princely Abudu et al., 2019).

Pyruvate can enter the TCA cycle via the **pyruvate dehydrogenase complex** (PDH) or via **pyruvate carboxylase** (PC), which are both differentially regulated in neuronal and non-neuronal cells. PDH contains three units, E1, E2 and E3, and complex activity is modulated by protein expression levels, phosphorylation by pyruvate dehydrogenase kinases (Pdk1 - 4) and dephosphorylation by pyruvate dehydrogenase phosphatases (Pdp1/2), as well as acetylation and succinylation (reviewed in Patel and Korotchkina, 2001). Halim et al. (2010) showed that all PDH components are expressed in neurons and astrocytes; however, in astrocytes PDH is inactivated via phosphorylation through PDK2 and PDK4. Itoh et al. (2003) reported that inhibition of PDK4 by dichloroacetate increased pyruvate respiration in astrocytes at the cost of lactate production.

In contrast, PC levels are regulated on the protein level with high expression in astrocytes and neglectable levels in neurons (Yu et al., 1983; Shank et al., 1985; Waagepetersen et al., 2001). PC converts pyruvate to oxaloacetate to replenish this TCA intermediate. This process is termed anaplerosis and in total mediated by four carboxylating enzymes, namely PC, phosphoenolpyruvate carboxykinase (Pck2), malic enzymes (Me2, Me3) and propionyl-CoA carboxylase (PCC; Hassel, 2000), which can provide oxaloacetate from pyruvate, phosphoenolpyruvate from oxaloacetate, pyruvate from malate or methyl-malonyl-CoA from propionyl-CoA.

Carnitine o-palmitoyltransferase 1, liver isoform (**Cpt1a**) is part of the carnitine shuttle system that imports long-chain fatty acids (FA) into mitochondria for their oxidation. While the catabolism of FA is debated in the nervous system (reviewed in Schonfeld and Reiser, 2013; and answered in Panov et al., 2014), Knobloch et al. (2017) showed that neural stem/progenitor cells depend on FA metabolism and remodel its use during proliferation and differentiation in the developing and adult brain. Specifically, neural progenitor cells rely on FA oxidation during their quiescent state, while their proliferation is dependent on *de novo* lipogenesis and FA oxidation blocked by malonyl-CoA (Knobloch et al., 2013). Repression of Cpt1a reduces the pool of neural stem cells by enhancing symmetric differentiating divisions

(Xie et al., 2016). Finally, Cpt1a expression is reduced during neurogenesis and FA oxidation repressed in differentiated neurons.

Lopez-Fabuel et al. (2016) observed in neurons and astrocytes in culture that **complex I** of the respiratory chain is preferentially **assembled into supercomplexes** in neurons. In contrast, more free complex I was found in astrocytes correlating with a lower oxygen consumption ratio and higher reactive oxygen species (ROS) production (Maranzana et al., 2013; Hernansanz-Agustin et al., 2017). The functional purpose of supercomplex assembly of the respiratory chain is currently still debated (Blaza et al., 2014), while cristae shape regulates supercomplex assembly (Cogliati et al., 2013). However, through analysis of complex I subunits in free or supercomplex formation, Lopez-Fabuel et al. (2016) found that the subunit Ndufs1 is enriched in neurons – especially in supercomplexes. They further corroborated that Ndufs1 stimulates supercomplex assembly of complex I by neuronal knockdown and astrocytic overexpression. Hence, the authors concluded that metabolic differences between neurons and astrocytes arise in part from structural difference of complex I assembly.

1.4.2. Mitochondrial proteins enriched in neuronal cell compartments

Syntaphilin (Snph) was first described as SNAP25 competitor for the interaction with syntaxin-1, and Snph/syntaxin-1 interaction blocks SNARE complex formation (Lao et al., 2000). In a later study, Kang et al. (2008) demonstrated that Snph localizes to the outer mitochondrial membrane via its C-terminal transmembrane domain. In neuronal cultures, Snph was enriched in axons and sparse in MAP2-positive dendrites. Specifically, Kang et al. (2008) identified an axon-sorting domain in residues 381-469 of Snph and deletion of this region abolished axon targeting and distributed Snph equally throughout the cell. Functionally, Snph contains a microtubule-binding domain (AA 130-203) and via this domain arrests mitochondrial transport. While Snph function seems most relevant in neurons, it is also expressed in non-neuronal tissues (Snph via HPA049393 in the Human Protein Atlas; Uhlen et al., 2015).

Mitochondrial fission factor (Mff) is an outer mitochondrial membrane protein that recruits – like Fis1 (James et al., 2003; Yoon et al., 2003) - mitochondrial dynamin protein 1 (Drp1) to mitochondria and enables mitochondrial fission (Gandre-Babbe and van der Bliek, 2008; Loson et al., 2013; Liu and Chan, 2015). Mff and Fis1 are dually localized to mitochondria and peroxisomes (Koch and Brocard, 2012). In neurons, Mff is present in dendrites, soma and axon; however, Mff selectively regulates mitochondrial size in axons and prior to axon entry, while it does not affect dendritic mitochondria (Lewis et al., 2018). In this study, knockdown of Mff increased the length of axon-entering mitochondria by fourfold, while mitochondrial flux was reduced by half. In the axon, increased mitochondrial size resulted in enhanced mitochondrial Ca^{2+} uptake without altering axonal transport, membrane potential or ATP levels. Still, altered mitochondrial morphology decreased neurotransmitter release and resulted in reduced axon branching in cortical pyramidal neurons in vivo. The authors hypothesized that compartment-specific regulation of Mff and/or Drp1 underlie the dominant axonal effect of Mff function.

1.5. Tools: Affinity purification of subcellular organelles

Traditionally, subcellular organelles, like the nucleus, mitochondria or synaptosomes, are isolated via centrifugation (reviewed in Satori et al., 2012). Here, separation is achieved via differential centrifugation, i.e. sequential centrifugation at different speeds, and density gradient centrifugation in different media. While these methods sufficiently enrich organelles from cells, current application methods often require purer or faster isolation approaches. Some of which are: fluorescence-activated organelle sorting (Luquet et al., 2017), laser capture microdissection (Pflugradt et al., 2011) and affinity purification. In particular, affinity purification has been applied to enrich peroxisomes (Luers et al., 1998), plasma membrane (Lawson et al., 2006), synaptic vesicles (Burre et al., 2007; Morciano et al., 2005), mitochondria (Hornig-Do et al., 2009) and lysosomes (Nylandsted et al., 2011) by using endogenous proteins as organelle 'handles'.

Recently, this approach has been refined by modifying organelle-specific proteins with epitope 'handles' in cells in culture and transgenic organisms. Importantly, the epitope is accessible from the outside of the intact structure, i.e. present on the surface of organelles.

Truernit and Hibberd (2007) described the isolation of cell type-specific **chloroplasts** via the expression of YFP-labeled chloroplast envelop protein 14. Transgene expression in distinct cell types was achieved via enhancer trap lines of *Arabidopsis* using the Gal4-UAS system and organelles purified via magnetic beads with anti-GFP antibody. Chloroplasts were further analyzed for their mRNA content depending on cell type.

Heiman et al. (2008) developed a rapid, affinity purification method to isolate translating mRNAs from defined cell types in vivo. This method – termed translating ribosome affinity purification (**TRAP**) – allowed the cell type-specific expression of the EGFP-tagged 60S ribosomal subunit L10a. EGFP-RPL10a incorporates into polysomes and provides an isolation ‘handle’ on translating ribosomes and their bound mRNA via immunoprecipitation against GFP. In vivo profiles were first derived from 24 distinct cell types via 16 transgenic bacTRAP mouse lines (Doyle et al., 2008). Later, Sanz et al. (2009) reported a different mouse model – termed **RiboTag mouse**. Here, the endogenous Rpl22 gene was targeted, of which exon 4 is in-frame tagged with double HA in a Cre recombinase-dependent manner. These mice then express endogenous levels of HA-Rpl22 protein after Cre recombination. Similar to TRAP, the tagged protein is incorporated in polysomes and enables the isolation of actively translated mRNA via immunoprecipitation against HA.

Chen et al. (2016) reported the rapid isolation of mitochondria – termed **HA-MITO IP** – from cells in culture. Here, the C-terminus of OMP25 is triple HA tagged (3xHA-EGFP-OMP25) and introduced into cells. Affinity purification of mitochondria is performed by using magnetic beads with anti-HA antibody in as little as 12 minutes and organelle content used for metabolomics.

Abu-Remaileh et al. (2017) presented a rapid isolation method for lysosomes – termed **LysoIP** – from cells in culture. Here, the authors overexpressed the transmembrane protein 192 tagged with triple HA. Lysosomes were affinity purified by using magnetic beads with anti-HA antibody in as little as 10 minutes and profiled for their metabolome.

Roh et al. (2017) introduced the **NuTRAP mouse** to isolated cell type-specific nuclei and mRNA in vivo. Here, *Rosa26* knock-in mice were created with a cassette containing a floxed ‘stop’ sequence, a biotin ligase, a dual tagged RanGAP1 protein with biotin ligase recognition peptide and mCherry, and EGFP-RPL10a. The transgenes are expressed in a Cre recombinase dependent manner and allow the tagging of the nuclear envelop via tagged RanGAP1 protein together with the tagging of polysomes via EGFP-RPL10a. The authors chose two tags on the RanGAP1 protein to enable isolation by biotin immunocapture and by mCherry fluorescence-activated sorting. NuTRAP allows for the correlated analysis of transcriptome and epigenome in defined cell types.

1.6. Cerebellum

The cerebellum coordinates the planning and execution of motor behavior (Ito and Itō, 1984), but also non-motor functions, such as cognition and emotions via polysynaptic circuits between the cerebellum – thalamus – cerebral cortex (Buckner, 2013; Sathyanesan et al., 2019). Furthermore, Carta et al. (2019) recently demonstrated cerebellar involvement in reward learning and social behavior via cerebello-ventral tegmental area projections.

Structurally, the cerebellum is organized as two hemispheres with the central vermis; each hemisphere can be divided into 10 lobules (Figure 4a) and all connection from and to other parts of the brain travel through the pons. **Cells** of the cerebellar cortex are present in three layers (Figure 4b): the molecular layer (ML) containing Bergmann glia, basket and stellate cells as well as Purkinje cell dendrites and granule cell axons; the Purkinje cell layer (PCL) containing Purkinje cell perikarya and candelabrum cells (Laine and Axelrad, 1994); and the granule cell layer (GCL) containing granule cells, unipolar brush, Golgi and Lugaro cells, Purkinje cell axons and other glial cells. The Purkinje cell axon run in fiber tracts to the four cerebellar nuclei: dentate, emboliform, globose and fastigii.

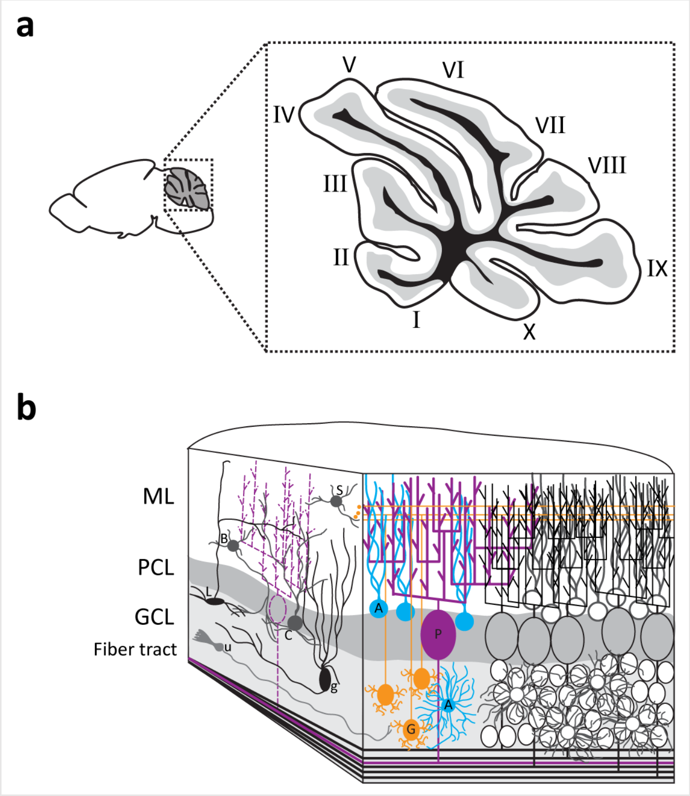

Figure 4| Organization of mouse cerebellum. (**a**) Schemata of sagittal mouse brain and detail of cerebellum with its 10 lobules I – X. Fiber tract, black; granule cell layer, gray; molecular layer, white. (**b**) Schema depicting the cellular architecture of the cerebellum: molecular layer (ML, white), Purkinje cell layer (PCL, dark gray), granule cell layer (GCL, light gray) and fiber tract. Shown cell types in ML are: A, astrocytes (blue); S, stellate cell; B, basket cell. Shown cell types in PCL are: P, Purkinje cell (magenta); C, candelabrum cell. Shown cell types in GCL are: G: granule cell (orange); g, Golgi cell; A, astrocyte (blue); L, Lugaro cell; u, unipolar brush cell. Due to complexity, not all cell types are depicted.

While the cellular architecture of the cerebellum is uniform, additional parasagittal zones contribute to its complexity. These zones are based on multiple molecular markers in Purkinje cells, namely zebrin II (Hawkes and Leclerc, 1987), EAAT4 (Dehnes et al., 1998), mGluR1β (Mateos et al., 2001), PLCβ3/4 (Sarna et al., 2006) and D3 dopamine receptor, dopamine transporter and synaptic vesicular monoamine transporter (Kim et al., 2009). This molecular diversity further correlated with functional heterogeneity across Purkinje cell populations obtained by electrophysiology (reviewed in Gill and Sillitoe, 2019).

1.7. Mitochondrial dysfunction in human diseases

Mitochondrial disorders represent a class of genetic diseases that are primarily defined by oxidative phosphorylation defects. Mutated genes are encoded either by nuclear DNA or mtDNA (15-20% of patients). In the case of mtDNA, it is important to consider that mutations can occur as homoplasmy or heteroplasmy and that the age of onset, severity of symptoms and involved organ systems depend on mutation load. Amongst nuclear encoded mitochondrial proteins, mitochondrial DNA polymerase γ (*POLG*) mutations are most common among mitochondrial diseases. *POLG* mutations can cause a spectrum of disorders like childhood myocerebrohepatopathy spectrum disorders (MCHS), Alpers-Huttenlocher syndrome, myoclonic epilepsy myopathy sensory ataxia (MEMSA), ataxia neuropathy spectrum (ANS) or progressive external ophthalmoplegia (PEO) with or without sensory ataxic neuropathy and dysarthria (SANDO). Affected organ systems are in the majority the musculoskeletal, gastrointestinal and central/peripheral nervous systems (Saneto and Naviaux, 2010). For example, patients frequently present with cerebellar ataxia with reports of Purkinje cell vulnerability, synaptic disorganization and loss (Lax et al., 2012b), profound neuronal loss of complex I (Hakonen et al., 2008), microinfarcts in cerebellar cortex (Tzoulis et al., 2010) and myelinopathy (Lax et al., 2012a). Mitochondrial disease may also cause severe cerebellar atrophy (Scaglia et al., 2005; Inbar-Feigenberg et al., 2018; Finsterer and Zarrouk-Mahjoub, 2018). Additionally, *POLG* mutation have been described for recessive Charcot-Marie Tooth disease (Harrower et al., 2008) and idiopathic Parkinson’s disease (Hsieh et al., 2019). In fact, mitochondrial disorders frequently present as neuropathy and neurodegeneration (reviewed in Lax et al., 2017), which gives reason to the hypothesis that the nervous system is more susceptible to mitochondrial dysfunction than other organ systems.

Vis versa mitochondrial dysfunction is implicated in many **neurodegenerative diseases**, such as Alzheimer’s disease, Parkinson’s disease, and amyotrophic lateral sclerosis. Specifically, mitochondrial alterations in ATP production, oxidative stress, Ca^{2+} homeostasis, mitophagy and axonal transport have been reported (reviewed in Cabral-Costa and Kowaltowski, 2020).

Alzheimer’s disease (AD; Alzheimer, 1907) is a form of dementia with the hallmarks of intraneuronal neurofibrillary tangles generated by hyperphosphorylated tau and extraneuronal plaques made of amyloid-β (Aβ), the cleavage product of amyloid precursor protein (APP; reviewed in Polanco et al., 2018; Hardy and Allsop, 1991; Hardy and Higgins, 1992). A number of dysfunction have been ascribed to AD pathology, such as synaptic failure, oxidative stress, axonal injury, microglia and mitochondria dysfunction (reviewed in Swerdlow, 2018; and Cenini and Voos, 2019). Hirai et al. (2001) and Baloyannis (2006) have reported ultrastructural alteration in mitochondria from AD patients. Additionally, others have reported Aβ-related alterations in mitochondrial enzymes and metabolism (Casley et al., 2002; Gibson et al., 2010), decreased cytochrome c oxidase activity (Parker et al., 1990; Canevari et al., 1999), decrease Ca^{2+} extrusion via NCLX (Jadiya et al., 2019), as well as altered mitochondrial dynamics (Mandelkow et al., 2003; Wang et al., 2008) and mitophagy via tau (Cummins et al., 2019). Cardoso et al. (2001) demonstrated Aβ-induced apoptosis in a mtDNA-dependent manner. Interestingly, APP and Aβ have been reported to localize to mitochondria (reviewed in Pagani and Eckert, 2011) as well as the specific interaction of Aβ with mitochondrial proteins: 3-hydroxyacyl-CoA dehydrogenase type 2 (Hsd17b10; Lustbader et al., 2004), the TOM complex (Hansson Petersen et al., 2008; Cabodevilla et al., 2013) and its clogging via Aβ (Anandatheerthavarada et al., 2003), mitochondrial ATP synthase subunit O (Atp5po; Beck et al., 2016) and cyclophilin F (CypD; Du et al., 2008). Additionally, APP processing is affected by mitochondrial dysfunction (Gabuzda et al., 1994; Webster et al., 1998) and mtDNA polymorphism (Scheffler et al., 2012). All this evidence has led to the formulation of a ‘mitochondrial cascade hypothesis’ in addition to the leading paradigm, the ‘amyloid cascade hypothesis’ (Swerdlow and Khan, 2004).

Amyotrophic lateral sclerosis (ALS; Charcot, 1881) is characterized by the selective loss of upper and lower motor neurons in spinal cord, which leads to progressive muscle denervation, motor dysfunction, speech problems, paralysis and respiratory failure (reviewed in Chio et al., 2013). ALS pathology has been linked mechanistically to the aggregation of protein in cytosol, increased oxidative stress, axonal transport deficits, deregulation of mRNA metabolism, dysfunction in glial cells and mitochondrial dysfunction (reviewed in Carri et al., 2017). Ultrastructural alterations in mitochondria from ALS patients and mouse models have been reported for example by Okamoto et al. (1990), Sasaki and Iwata (2007), Xu et al. (2010) and Genin et al. (2016). Furthermore, several reports document reduced respiration and complex I and IV activity (Wiedemann et al., 1998; Borthwick et al., 1999; Vielhaber et al., 2000; Straub et al., 2018) as well as increased mtDNA mutations (Wiedemann et al., 2002) and abnormal mitochondrial transport (Magrane et al., 2014; Marinkovic et al., 2012). Specifically, cupper/zinc superoxide dismutase 1 (SOD1) is found mutated in one fifth of familiar ALS cases (Banci et al., 2008), but is also observed in sporadic cases (Pare et al., 2018). Mouse models of mutant SOD1, like SOD1^{G93A} and SOD1^{G37R}, recapitulate features of the disease in mice (Gurney et al., 1994; Wong et al., 1995). In SOD1^{G93A}, misfolded protein is found in the inner mitochondrial membrane (Ahtoniemi et al., 2008), impairs voltage-dependent anion-selective channel (VDAC) function (Israelson et al., 2010), increases oxidative stress (Andrus et al., 1998; reviewed in Barber and Shaw, 2010) and leads to apoptosis (Pasinelli et al., 2004; Pedrini et al., 2010).

Chapter 2:

AIMS OF THIS THESIS

Mitochondrial biology is intimately intertwined with essential cellular functions – as one would expect from an organelle that integrated as a proteobacterium into a host cell more than 1.5 billion year ago. The transfer of essential genes to the host nucleus as well as the incorporation of novel host proteins into mitochondria give current day cells the opportunity to equip and fine-tune mitochondria according to their physiological state.
Hence, mitochondria across tissues, cell types and even within cells differ in their molecular composition and function. Surprisingly, our knowledge of most mitochondrial proteins is poor (Pagliarini and Rutter, 2013) and particularly the contribution of mitochondrial proteins to the physiology of specific cell types, e.g. neuronal subtypes, unknown.

In the strong believe that such cell type-resolved information will elucidate the function of mitochondrial proteins, i.e. the cellular context of an enriched protein can inform about its function and help generating related hypotheses, the present thesis aims to:

1. Introduce a **method** for the molecular and functional characterization of cell type-specific mitochondria from mouse tissue (Chapter 4.1).

2. Demonstrate the extant of **mitochondrial diversity** in the context of mouse cerebellum by probing mitochondria from Purkinje cells, granule cells and astrocytes (Chapter 4.2).

3. Follow up on the **mitochondrial biology** of each probed cell types and thereby consolidating the findings of *Aim 2* (Chapter 4.3 – 4.5).

4. Provide evidence for the conservation of cerebellar mitochondrial diversity **across species** and the utilization of cell type-enriched mitochondrial 'markers' to investigate **neurodegeneration** (Chapter 4.6).

MATERIALS & METHODS

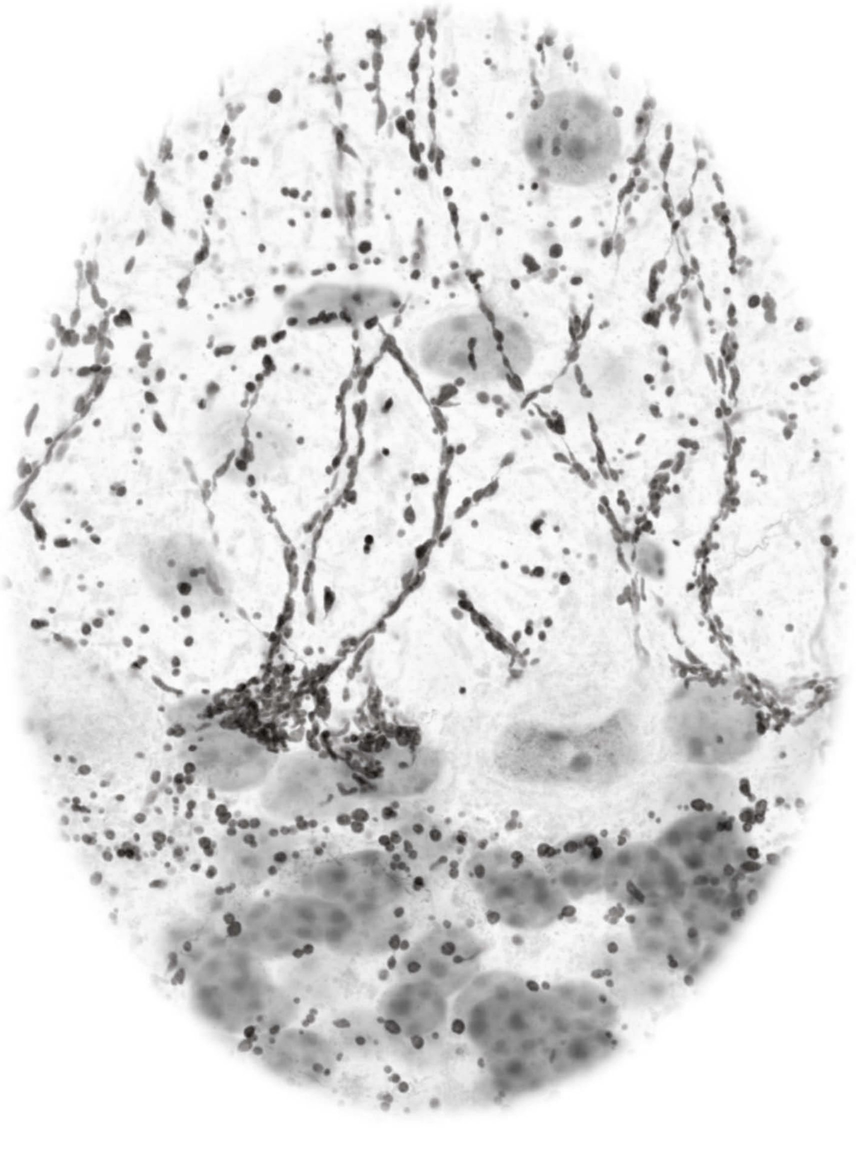

Chapter 3: Materials and Methods

3.1. Materials

3.1.1. Plasmids

Name	*#*	*Reference*
pMXs-IP GFP-Omp25	Addgene #38249	Yoshii et al. (2011)
pEx-CAG-stop-bpA	-	Hitz et al. (2007)
pDsRed2-Mito	632421	Clontech Laboratories
pEx-CAG-Stop-GFP-OMM-bpA	-	This study
pCMV-GFP-OMM	-	This study

3.1.2. Buffers

Gitocher buffer pH 8.8, 10x			
Tris Base	670 mM	T1503	Sigma
Ammonium sulfate	166 mM	A4418	Sigma
Magnesium chloride hexahydrate	65 mM	630628	Sigma
Gelatin	0.1%	48723	Sigma

Ringer's solution, 1x			
Sodium chloride	125 mM	3957.1	Roth
Potassium chloride	2.5 mM	7447-40-7	Merck
Sodium phosphate monobasic dihydrate	1.25 mM	71505	Sigma
Sodium bicarbonate	26 mM	S5761	Sigma
Calcium chloride dihydrate	2 mM	C7902	Sigma
Magnesium chloride hexahydrate	1 mM	630628	Sigma
D-(+)-Glucose	20 mM	G7021	Sigma

oxygenate with carbogen (95% O_2/5% CO_2)

PBS pH 7.4, 10x			
Sodium phosphate monobasic dihydrate	18.6 mM	71505	Sigma
Sodium phosphate dibasic	84.1 mM	S5136	Sigma
Sodium chloride	1.75 M	3957.1	Roth

4% Paraformaldehyde in PBS			
Paraformaldehyde	4%	158127	Sigma
PBS, pH 7.4 (10x)	1x	-	-

heat paraformaldehyde in water to 50°C, add two drops of NaOH until clear; filter solution, add PBS and adjust pH

TBSt pH 7.6, 10x			
Tris HCl	158 mM	T5941	Sigma
Tris Base	46 mM	T1503	Sigma
Sodium chloride	1.5 M	3957.1	Roth
Tween20	10%	P1379	Sigma

Isolation buffer (IB) pH 7.4			
Mannitol	220 mM	M9546	Sigma
Sucrose	80 mM	S7903	Sigma
HEPES	10 mM	15630056	Thermo Fisher Scientific
EDTA	1 mM	E9884	Sigma
BSA, fatty acid-free	1%	A7030	Sigma
cOmplete, EDTA-free Protease Inhibitor	1x	11873580001	Sigma

Immunocapture buffer (ICB) pH 7.4			
Potassium chloride	137 mM	P9333	Sigma
Magnesium chloride hexahydrate	2.5 mM	630628	Sigma
Potassium phosphate monobasic	3 mM	P5655	Sigma
HEPES	10 mM	15630056	Thermo Fisher Scientific
EDTA	1 mM	E9884	Sigma
BSA, fatty acid-free	1%	A7030	Sigma
cOmplete, EDTA-free Protease Inhibitor	0.5x	11873580001	Sigma

MAS-1X pH 7.4			
Mannitol	220 mM	M9546	Sigma
Sucrose	70 mM	S7903	Sigma
Potassium phosphate monobasic	10 mM	P5655	Sigma
Magnesium chloride hexahydrate	5 mM	630628	Sigma
HEPES	2 mM	15630056	Thermo Fisher Scientific
EGTA	1 mM	E3889	Sigma
BSA, fatty acid-free	0.2%	A7030	Sigma

Respiration buffer pH 7.4			
Potassium chloride	137 mM	P9333	Sigma
Magnesium chloride hexahydrate	2.5 mM	630628	Sigma
Potassium phosphate monobasic	3 mM	P5655	Sigma
HEPES	10 mM	15630056	Thermo Fisher Scientific
Succinic acid	5 mM	S9512	Sigma
L-Malic acid	5 mM	M1000	Sigma
L-Glutamic acid	5 mM	49449	Sigma
BSA, fatty acid-free	0.2%	A7030	Sigma

RIPA buffer pH 8.0			
Tris HCl	50 mM	T5941	Sigma
Sodium chloride	150 mM	3957.1	Roth
EDTA	0.1 mM	E9884	Sigma
Triton X100	1%	T9284	Sigma
NP-40	0.25%	I3021	Sigma
SDS	0.1%	05030	Sigma
cOmplete, EDTA-free Protease Inhibitor	1x	11873580001	Sigma

RIPA buffer 2 pH 8.0

Tris HCl	50 mM	T5941	Sigma
Sodium chloride	150 mM	3957.1	Roth
EDTA	5 mM	E6758	Sigma
Sodium deoxycholate	0.5%	D6750	Sigma
Triton X100	1%	T9284	Sigma
SDS	0.1%	05030	Sigma

Tris-Glycine SDS buffer

Tris Base	25 mM	T1503	Sigma
Glycine	192 mM	G8898	Sigma
SDS	0.1%	05030	Sigma

TWOBIN buffer

Tris Base	25 mM	T1503	Sigma
Glycine	192 mM	G8898	Sigma
Methanol	20%	20846.326	Merck

SDT lysis buffer pH 7.6

Tris HCl	100 mM	T5941	Sigma
DTT	100 mM	43816	Sigma
SDS	4%	05030	Sigma

Blocking solution

Fish gelatin	2%	G7765	Sigma
FBS	2%	10100147	Thermo Fisher Scientific
BSA, fatty acid-free	2%	A7030	Sigma
PBS pH 7.4, 10x	1x	-	-

Heat-induced antigen retrieval buffer (HIER) 1-7

Sodium citrate buffer pH 6.0; **HIER1**

Tri-sodium citrate	10 mM	4088.3	Roth
Tween20	0.05%	P1379	Sigma

Citrate buffer pH 6.0; **HIER2**

Citric acid	10 mM	X863.1	Roth
Tween20	0.05%	P1379	Sigma

Citrate-EDTA buffer pH 6.2; **HIER3**

Citric acid	10 mM	X863.1	Roth
EDTA	2 mM	E6758	Sigma
Tween20	0.05%	P1379	Sigma

EDTA buffer pH 8.0; **HIER4**

EDTA	1 mM	E6758	Sigma
Tween20	0.05%	P1379	Sigma

Tris-EDTA buffer pH 9.0; **HIER5**

Tris base	10 mM	T1503	Sigma
EDTA	1 mM	E6758	Sigma
Tween20	0.05%	P1379	Sigma

Tris buffered saline (TBS) pH 9.0; **HIER6**

Tris base	50 mM	T1503	Sigma
Sodium chloride	150 mM	3957.1	Roth
Tween20	0.05%	P1379	Sigma

Tris buffer pH 10.0; **HIER7**

Tris base	10 mM	T1503	Sigma
Tween20	0.05%	P1379	Sigma

Monomer solution (for expansion microscopy)

Sodium acrylate	8.6%	408220	Sigma
Acrylamide	2.5%	1610140	BioRad
N,N’-Methylenebisacrylamide	0.15%	M7279	Sigma
Sodium chloride	11.7%	3957.1	Roth
PBS pH 7.4, 10x	1x	-	-
Add 4-Hydroxy-TEMPO	0.01%	176141	Sigma
TEMED	0.2%	T7024	Sigma
Ammonium persulfate	0.2%	A3678	Sigma

Digestion buffer

Tris Base	50 mM	T1503	Sigma
EDTA	1 mM	E6758	Sigma
Sodium chloride	740 mM	3957.1	Roth
Triton X100	0.5%	T9284	Sigma
Proteinase K	8 U/ml	V3021	Promega

EM fixative pH 7.2

Glutaraldehyde	2.5%	16300	Electron Microscopy Sciences
Paraformaldehyde	4%	15700	Electron Microscopy Sciences
Sodium cacodylate buffer	0.1 M	11654	Electron Microscopy Sciences

EPON

2-Dodecenylsuccinic acid anhydride	115.0g	20755.02	Serva
Glycid ether 100	171.3g	21045.02	Serva
Methylnadic anhydride pract.	89.0g	29452.03	Serva
2,4,6-Tris(dimethylaminomethyl)phenol	6.5ml	36975.01	Serva

3.1.4. Animal models

Mouse line	*ID*	*MGI*	*Reference*
B6N.Cg-Tg(ACTFLPe)$^{9205Dym/CjDswJ}$	#019100	5473808	Rodriguez et al. (2000)
B6N.Cg-Gt(ROSA)26Sor$^{tm1(CAG-EGFP^*)Thm}$/J	#032675	6296994	This study (*MitoTag*)
Thy1:mito-RFP	-	-	Breckwoldt et al. (2014)
C57BL/6N^{Crl}	027	2683688	Charles River
B6.129S2-*Emx1*$^{tm1(cre)Krj}$/J	#005628	3617405	Gorski et al. (2002)
B6;129S6-*Chat*$^{tm2(cre)Lowl}$/J	#006410	3699161	Rossi et al. (2011)
B6.Cg-Tg(Gabra6-cre)B1Lfr/Mmucd		4358481	Fünfschilling and Reichardt (2002)
B6.129-Tg(Pcp2-cre)$^{2Mpin/J}$	#004146	2174502	Barski et al. (2000)
B6.Cg-Tg(Gfap-cre)$^{77.6Mvs/2J}$	#024098	5554256	Gregorian et al. (2009)
STOCK Tg(Rbp4-cre)$^{KL100Gsat/Mmucd}$	031125-UCD	4367068	Gong et al. (2007); Gong et al. (2003)
B6.Cg-Tg(SOD1*G93A)$^{1Gur/J}$	#004435	2181028	Gurney et al. (1994)
APP23/PS45 : Tg(Thy1-APP)3Somm Tg(Thy1-PSEN1*G384A)45Jckr	- #030504 -	- 2447146 4819105	Busche et al. (2008); (Sturchler-Pierrat et al., 1997); (Herzig et al., 2004)
C57BL/6N-Mcu$^{tm1a(EUCOMM)Hmgu/H}$	07445	5557399	MMRRC
Mcu^{tm1c}	-	6122827	This study
C57BL/6N-Rmdn3$^{tm1a(KOMP)Wtsi/MbpMmucd}$	049471	6347157	MMRRC
B6;129-*Gt(ROSA)26Sor*$^{tm4(CAG-EGFP^*)Nat}$/J	021429	5571611	Jeremy Nathans, Johns Hopkins University
Tg(Pvalb-EGFP)1Mony	-	6117392	Meyer et al. (2002)

3.1.5. Primer sequences

Primer	*Sequence 5′ ⟶ 3′*	*Product (bp)*
ACTB-FLPe	TGC CGG TCC TAT TTA CTC GT TAC TTC TTT AGC GCA AGG GGT AG	100
APP23	GAATTCCGACATGACTCAGG GTTCTGCTGCATCTTGGACA	246
Cre	GCCGAAATTGCCAGGATCAG AGCCACCAGCTTGCATGATC	650
Gabra6:Cre (ctr)	CCCTGCAAGCAGAGATTGTT GCCTAGAGTCTGCCAGGTCA	217
Gabra6:Cre (mut)	CCCTGCAAGCAGAGATTGTT TGCCGCCTTTGCAGGTGTGTCTTAC	586
GFP	CACGCTTCAAAAGCGCACGTCTG GTTGTGCCCAGTCATAGCCGAATAG	280
GFP-OMM (mut)	CAAGATCCGCCACAACATCG TATCTCACGAAGGCCCAAAC	324
GFP-OMM (WT)	GCACTTGCTCTCCCAAAGT CATAGTCTAACTCGCGACACTG	600
Mcu (mut)	TGGGTGTTGATTACAAAGTTTTCA GGTTGTCCTCTGACCTCCAC	462/118

Primer	*Sequence 5′ → 3′*	*Product (bp)*
Mcu (WT)	TGGGTGTTGATTACAAAGTTTTCA GAACTTCGGAATAGGAACTTCG	300
PS45	CAGGTGCTATAAGGTCATCC ATCACAGCCAAGATGAGCCA	291
Rbp4-Cre	GGGCGGCCTCGGTCCTC CCCCAGAAATGCCAGATTACGTAT	600
Rmdn3 (mut)	GGGATCTCATGCTGGAGTTCTTCG GGTCTATGTAACTCCAGCCGTCTGG	546
Rmdn3 (WT)	GCCTCAGCAGCGAGTACTTTTACCC GCCCCTAGGCTGAAGAGATGGC	231
Mito-GFP (mut)	GCA CTT GCT CTC CCA AAG TC GTT ATG TAA CGC GGA ACT CC	300
Mito-GFP (WT)	GCA CTT GCT CTC CCA AAG TC CAT AGT CTA ACT CGC GAC ACT G	557
SOD1	CATCAGCCCTAATCCATCTGA CGCGACTAACAATCAAAGTGA	236
Thy1:mito-RFP	CGCCAAGATCCATTCGTT TTCTGCTGCCGTACATGAAG	254

3.1.6. Cell lines and reagents

Item	*#*	*Company*
U-2 OS cell line	ATCC HTB-96	ATCC
IDG 3.2 murine hybrid ES cell line (129S6/SvEv/Tac x C57Bl/6)	-	Ralf Kühn
DMEM, high glucose, GlutaMax	61965059	ThermoFisher Scientific
Fetal Bovine serum, FBS	10100147	ThermoFisher Scientific
G418	10131027	ThermoFisher Scientific
PBS pH7.4	10010015	ThermoFisher Scientific
TrypLE Express Enzyme, no phenol red	12604013	ThermoFisher Scientific
X-treme GENE 9 DNA reagent	06365779001	Roche

3.1.7. Antibodies

3.1.7.1. Antibodies used for immunofluorescence staining (Chapter 3.2.14)

Antigen	*Species*	*#*	*Dilution*	*Company*
Acads	Rabbit	ab156571	1:200	Abcam
Ak3	Mouse IgG_1	sc-398571	1:100	Santa Cruz
Ak4	Mouse IgG_1	sc-271161	1:100	Santa Cruz
Amyloid-β (1-16) 6E10	Mouse IgG_1	803020	1:500	BioLegend
Amyloid-β (17-24) 4G8	Mouse IgG_{2b}	800712	1:1,000	BioLegend
Amyloid-β (8-17) 6F/3D	Mouse IgG_1	M0872	1:100	Dako
Catalase	Rabbit	100-4151	1:200	Rockland
Calbindin	Chicken	CPCA-Calb	1:1000	EnCor Biotechnology Inc.
ChAT	Goat	AB144P	1:500	Sigma
Cox4i1	Rabbit	AP22111a	1:200	Abgent

Antigen	*Species*	*#*	*Dilution*	*Company*
Cpt1a	Rabbit	15184-1-AP	1:50	ProteinTech
Gfap	Chicken	ab4674	1:2,000	Abcam
GFP	Chicken	ab13970	1:1,000	Abcam
Gldc	Rabbit	HPA002318	1:400	Sigma
Gls (KGA)	Rabbit	20170-1-AP	1:200	ProteinTech
Gls2	Rabbit	AP6650d	1:400	Abgent
Got2	Rabbit	ab171739	1:400	Abcam
Ldhd	Rabbit	ab182146	1:100	Abcam
MaoB	Mouse IgG$_1$	sc-515354	1:100	Santa Cruz
Mavs	Rabbit	#4983	1:200	Cell Signaling
Mcu	Rabbit	HPA016480	1:400	Sigma
NeuN	Rabbit	MAB377	1:100	Sigma
NeuN-Alexa Fluor 488	Rabbit	ab190195	1:50	Abcam
Nipsnap1	Rabbit	#13226	1:200	Cell Signaling
Ociad2	Rabbit	HPA040979	1:200	Sigma
Ociad2	Rabbit	ab91576	1:200	Abcam
Pex14	Rabbit	-	1:1,000	Gift from Denis Crane
Pptc7	Rabbit	ab122548	1:200	Abcam
Rmdn3	Rabbit	ab189845	1:400	Abcam
Slc25a20	Rabbit	19363-1-AP	1:400	ProteinTech
Sfxn5	Rabbit	ab172971	1:500	Abcam
Snph 1-100	Rabbit	ab192605	1:400	Abcam
Snph 225-428	Rabbit	-	1:400	Gift from Zu-Hang Sheng
Tst	Rabbit	ab166625	1:500	Abcam
Tubulin βIII-AF 555	Mouse IgG$_{2a}$	560339	1:200	BD Bioscience
α-chicken IgY-AF 488	Goat	A-11039	1:1,000	ThermoFisher Scientific
α-chicken IgY-AF 647	Goat	A-21449	1:1,000	ThermoFisher Scientific
α-goat IgG-AF 594	Donkey	A-32758	1:1,000	ThermoFisher Scientific
α-mouse IgG Fab	Goat	115-007-003	1:100	Jackson Immunoresearch
α-mouse IgG$_1$-AF 594	Goat	A-21125	1:1,000	ThermoFisher Scientific
α-mouse IgG-AF 647	Donkey	715-605-151	1:2,000	Jackson Immunoresearch
α-rabbit IgG-AF 555	Donkey	A-31572	1:2,000	ThermoFisher Scientific
α-rabbit IgG-AF 568	Goat	A-11011	1:1,000	ThermoFisher Scientific
α-rabbit IgG-AF 594	Goat	A-11012	1:1,000	ThermoFisher Scientific

3.1.7.2. Antibodies used for western blot analysis (Chapter 3.2.11)

Antigen	*Species*	*#*	*Dilution*	*Company*
Ak4	Mouse IgG$_1$	sc-271161	1:100	Santa Cruz
ATP5a	Mouse IgG$_1$	ab14748	1:10,000	Abcam
Cox4i1	Rabbit	AP22111a	1:1,000	Abgent
CypD	Mouse IgG$_1$	ab110324	1:5,000	Abcam
Emre	Rabbit	sc-86337	1:500	Santa Cruz

Antigen	*Species*	*#*	*Dilution*	*Company*
GFP	Mouse IgG_{2b}	sc-9996	1:500	Santa Cruz
Gldc	Rabbit	HPA002318	1:1,000	Sigma
Got2	Rabbit	ab171739	1:1,000	Abcam
Mcu	Rabbit	HPA016480	1:1,000	Sigma
Ociad2	Rabbit	HPA040979	1:1,000	Sigma
Rmdn3	Rabbit	ab189845	1:2,000	Abcam
Sfxn5	Rabbit	ab172971	1:2,000	Abcam
Tomm20	Rabbit	ab78547	1:1,000	Abcam
tRFP	Rabbit	AB234	1:5,000	Evrogen
α-mouse IgG-HRP	Goat	1706516	1:5,000	BioRad
α-rabbit IgG-HRP	Goat	1706515	1:5,000	BioRad

3.1.7.3. Antibodies used for flow cytometry (Chapter 3.2.13)

Antigen	*Species*	*#*	*Dilution*	*Company*
Mouse IgG-APC	Mouse IgG_1	130-113-758	1:25	Miltenyi Biotec
Tom22-APC	Mouse IgG_1	130-107-733	1:25	Miltenyi Biotec

3.1.8. Kits

Item	*#*	*Company*
ImmPRESS® HRP Anti-Rabbit IgG (Peroxidase) Polymer Detection Kit	MP-7451	Vector Lab
Mitochondria Isolation kit, mouse tissue	130-096-946	Miltenyi Biotec
Pierce 660 nm Protein Assay kit	22660	ThermoFisher Scientific
Pierce BCA Protein Assay kit	23225	ThermoFisher Scientific
QIAquick Gel Extraction Kit	28706	QIAGEN
QIAQuick PCR Purification Kit	28106	QIAGEN
Zenon Alexa Fluor 647 Rabbit IgG Labeling Kit	Z25308	ThermoFisher Scientific
μMACS GFP Isolation kit	130-091-125	Miltenyi Biotec

3.1.9. Western blot reagents and equipment

Item	*#*	*Company*
DL-Dithiothreitol solution (DDT)	43816	Sigma
ECL Prime Western Blotting Detection Reagent	RPN2232SK	GE Healthcare Life Sciences
Fusion FX7	-	Vilber Lourmat
Mini-PROTEAN Tetra Vertical Electrophoresis Cell	1658004	BioRad
PowerPac™ Basic Power Supply	1645050	BioRad
PVDF membrane, 0.2 μm	1620177	BioRad
SDS polyacrylamide gel, 12%; AnyKDa; 4-20%	4561096 4569036 4561043	BioRad
Skim milk	70166	Sigma

Item	#	*Company*
Sodium azide	S8032	Sigma
SYPRO™ Ruby Protein Blot Stain	S11791	ThermoFisher Scientific
Trans-Blot Turbo Transfer System	1704150	BioRad
TruPAGE LDS sample buffer	PCG3009	Sigma
WYPAL*X60	115-2058	Kimberly Clark

3.1.10. Mass spectrometry reagents and equipment

Item	#	*Company*
Acetonitrile	1.00017	Supelco
Benzonase	E8263	Sigma
Column oven	-	Sonation
Easy nLC-1,000 nano UHPLC	-	Thermo Fisher Scientific
LysC	V1671	Promega
Nanospray Flex electrospray ion source	-	Thermo Fisher Scientific
Q-Exactive HF mass spectrometer	-	Thermo Fisher Scientific
Q-Exactive mass spectrometer	-	Thermo Fisher Scientific
Trypsin	V5111	Promega
Urea	U4883	Sigma
VialTweeter, sonication	-	Hielscher Ultrasonics
Vivacon filter	VN01H02	Sartorius

3.1.11. Microscopy reagents and equipment

Item	#	*Company*
BX51WI	-	Olympus
Retiga EXi	-	Qimaging
FV1000	-	Olympus
20xO/N.A. 0.85	UPlanSApo	Olympus
FV3000	-	Olympus
20x/N.A. 0.75	UPlanSApo	Olympus
40x/N.A. 0.95	UApo N340	Olympus
JEM-1400	-	Jeol Tokyo
60xO/N.A. 1.42	PlanApo	Olympus
100xW/N.A. 1.0	LumPlanFL	Olympus
10x/N.A. 0.4	UPlanSApo	Olympus
20xW/N.A. 0.5	LumPlanFL	Olympus
Lambda 10-3	LB10-NWIQ	Sutter
4x/N.A. 0.16	UPlanFL N	Olympus
4x/N.A. 0.28	XLFluor 4x/340	Olympus

3.1.13. Chemicals and other reagents

Item	*#*	*Company*
Acryloyl-X, SE, 6-((acryloyl)amino)hexanoic Acid, Succinimidyl Ester (Acryloyl-X SE)	A20770	Thermo Fisher Scientific
ADP	01905	Sigma
Antimycin A	8674	Sigma
Autofluorescence Eliminator Reagent	2160	Merck
BglI	R0143	New England BioLabs
Calcium chloride	C1016	Sigma
CalciumGreen-5N, hexapotassium salt	C3737	Thermo Fisher Scientific
Calf intestinal phosphatase	M0289	New England BioLabs
CCCP	C2759	Sigma
Dako Diluent	52022	Dako
Dako REAL Peroxidase-Blocking Solution	S202386-2	Dako
DAPI	D9542	Sigma
DNA polymerase I	M0209	New England BioLabs
Ferrocyanide	-	Science Services
Fluoromount Mounting Medium	F4680	Sigma
GoTaq(R) G2 Hot Start Green Master Mix	M7423	Promega
HBSS, calcium, magnesium	14025092	Thermo Fisher Scientific
Heparin sodium salt	H3149	Sigma
HindIII	R3104	New England BioLabs
Hoechst 33342	H3570	Molecular Probes
Ultro stain (lead citrate)	16707235	Leica
anti-CD4 microbeads, human (mouse IgG_1)	130-045-101	Miltenyi Biotec
NEB 5-α *E.coli*	C2988J	New England BioLabs
NotI	R3189	New England BioLabs
Oligomycin A	75351	Sigma
OsO_4	E19130	Science Services
L-palmitoylcarnitine	61251	Sigma
Phalloidin-Alexa Fluor 647	A30107	Thermo Fisher Scientific
Proteinase K	351100902	Biozym
Pyruvic acid	107360	Sigma
Quick-Load® 2-Log DNA Ladder	N0469S	New England BioLabs
Rotenone	557368	Calbiochem
Ru360	557440	Sigma
SeaKem LE Agarose Lonzo	733-0829	VWR
Streptavidin-Alexa Fluor 405	S32351	Thermo Fisher Scientific
T4 ligase	M0202	New England BioLabs
TAE buffer 50x	CL86.1	Roth
TSA	FP1170	Perkin Elmer
Uranyl acetate	E22400	Science Services
Vectashield Mounting medium	H-1,000	Vector Laboratories
Wash Buffer	53006	Dako

Item	*#*	*Company*
XbaI	R0145	New England BioLabs
α-bungarotoxin-biotin	B1196	Thermo Fisher Scientific
β-Mercaptoethanol	M6250	Sigma

3.1.14. Other equipment

Item	*#*	*Company*
35x10 mm petri dish	351008	Corning, FALCON
CLARIOstar	-	BMG Labtech
CyAn ADP 9 flow cytometer	-	Beckman Coulter
KIMBLE Dounce tissue grinder set	D9063	Sigma
Leica UltraCut2	-	Leica
LS column	130-042-401	Miltenyi Biotec
Parr bombe disruption vessel	4635-39	Parr Instrument Company
Pre-separation filter, 30 µm	130-041-407	Miltenyi Biotec
QuadroMACS separator	130-090-976	Miltenyi Biotec
Seahorse XFe96 Extracellular Flux Analyzer	-	Agilent
Vibratome	VT1200	Leica

3.1.15. Software

Software	*Version*	*Company*
FlowJo	10.5.3	TreeStar
GenoPlex	7.12.09.0	BiHELab
GraphPad Prism	8.2.1	GraphPad Software
Illustrator CS5	15.0.2	Adobe
Image Studio Lite	5.2.5	Licor
ImageJ/Fiji	1.52f	Schindelin et al. (2012)
MaxQuant	1.5.4.1 1.5.5.1	Cox et al. (2014)
Microsoft Excel	2016	Microsoft Office
Perseus	1.6.1.1.	Tyanova et al. (2016)
Photoshop	12.0.4	Adobe
Seahorse XFe96 Wave	2.3.0.19.	Agilent
µManager	1.48v	www.micro-manager.org

3.2. Methods

The methods described in this thesis are partially published in the related article Fecher et al. (2019) and I have written this part with input from all co-authors.

3.2.1. Molecular cloning of expression plasmids carrying GFP-OMM

We generated expression plasmids via site-specific restriction enzyme digest and blunt-end cloning. In brief, 4 µg of parent plasmid containing insert or vector were cut with the described restriction enzymes overnight at 37°C. The reaction was stopped by heat inactivation, the ends of DNA fragments blunted by DNA polymerase I at 24°C for 15 minutes and reaction stopped by addition of 10 mM EDTA and heating at 75°C for 20 minutes. The products were run on a 1% agarose/TAE gel to separate product from remaining parent plasmid, and purified using the QIAQuick Gel Extraction Kit. The vector plasmid was further dephosphorylated using 0.5 unit calf intestinal phosphatase per µg DNA at 37°C for one hour and cleaned using the QIAQuick PCR Purification Kit. For ligation, a vector to insert ratio of 1:5 was mixed to the following reaction and incubated overnight at 16°C:

DNA vector	50 ng
DNA insert	10 x (insert size/vector size) ng
Ligase buffer, 10x	1 µl
T4 ligase	1 µl
	ad 10 µl water

5 µl reaction were used to transform chemically-competent NEB 5-α *E.coli*. DNA from positive clones was purified and controlled for proper integration via restriction enzyme digest. Finally, we transiently transfected cells in culture for functional validation.

3.2.1.1. pCMV-GFP-OMM

GFP-OMM is a fusion protein consisting of green fluorescent protein (GFP) and the C-terminal anchor of OMP25/Synj2bp (37 amino acids; Figure 5a) and was characterized by Nemoto and De Camilli (1999) and Horie et al. (2002). I generated the pCMV-GFP-OMM plasmid via NotI digestion of the plasmid pMXs-IP GFP-Omp25 (Yoshii et al., 2011) to obtain the GFP-OMM insert, and via HindIII and XbaI digest of the vector plasmid pDsRed2-Mito. Vector and insert were combined via blunt-end cloning (Figure 5b) and tested in cell culture (Figure 5c).

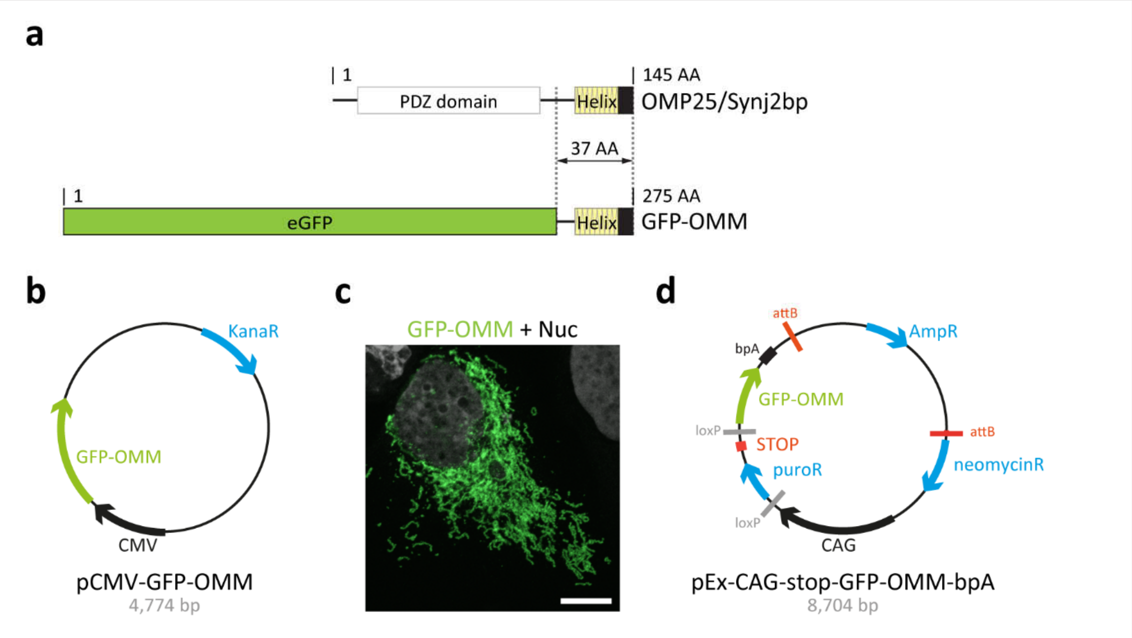
a
1
PDZ domain
Helix
145 AA
OMP25/Synj2bp
37 AA
1
eGFP
Helix
275 AA
GFP-OMM
b
KanaR
GFP-OMM
CMV
pCMV-GFP-OMM
4,774 bp
c
GFP-OMM + Nuc
d
attB
AmpR
bpA
GFP-OMM
loxP
STOP
attB
puroR
neomycinR
loxP
CAG
pEx-CAG-stop-GFP-OMM-bpA
8,704 bp

Figure 5| GFP-OMM fusion protein, its vectors for expression and transfection in cells. (**a**) Amino acid (AA) sequence map of OMP25/Synj2bp and GFP-OMM. The C-terminal 37 amino acids facilitate localization to the outer mitochondrial membrane (OMM). Protein domains: PDZ, Helix, transmembrane (black), eGFP. (**b**) Vector map of CMV-driven GFP-OMM for the transient transfection of cells in culture. KanaR, kanamycin resistance. (**c**) Transient expression of GFP-OMM in U-2 OS cells. Nuc, nuclear counter stain. Scale bar: 10 µm. (**d**) Vector map of CAG-driven, stopped GFP-OMM for the generation of MitoTag mice. AmpR, ampicillin resistance; attB, phiC31 integrase recognition site; loxP, Cre recombinase recognition site; puroR, puromycin resistance; STOP, multiple stop codons; bpA, bovine growth hormone polyadenylation site.

3.2.1.2. pEx-CAG-stop-GFP-OMM-bpA

Laura Trovò (L.T.; Institute of Neuronal Cell Biology, TUM) obtained the GFP-OMM sequence consisting of 848 base pairs via NotI digestion of the plasmid pMXs-IP GFP-Omp25 (Yoshii et al., 2011). Next, L.T. opened the expression vector pEx-CAG-stop-bpA via BglI digest and inserted the GFP-OMM DNA fragment via blunt-end cloning (Figure 5d).

3.2.2. Cell culture

U-2 OS cells were cultured in DMEM with GlutaMax and 10% FBS at 37°C, 5% CO_2. At 70% confluence, cells were sub-cultured by de-attachment with TrypLE Express Enzyme for 1 minute, washing cells with medium and plating them 1:5 in fresh medium.

I transiently transfected U-2 OS cells with plasmids using X-treme GENE 9 DNA transfection reagent according to the manufacturer’s instructions. Briefly, a ratio of 1 µg DNA to 3 µl reagent in 100 µl serum-free medium was used for transfection. Cells were used for experiments two days post transfection.

3.2.3. Animal models

All animal experiments were approved by the responsible regulatory agencies. Mice of mixed C57BL/6 N and J background were kept in ventilated IVC racks on a 12/12 light/dark cycle with standard chow diet and water supply. Transgenic mice were genotypes through PCR of tail biopsies, which were performed by animal caretakers and laboratory technicians using standard protocols. If not mentioned differently in the text, experimental animals were from both sexes and within the age range of 1.5 to 6 months.

3.2.3.1. *Rosa26* GFP-OMM knock-in mice (MitoTag mouse line)

MitoTag mice harboring GFP-OMM under control of the cytomegalovirus early enhancer element, chicken β-actin promoter, rabbit β-globin splice acceptor, in short CAG promoter and Cre recombinase (Cre) and were generated as previously described (Hitz et al., 2009; Ortiz et al., 2013). The knock-in was established via recombinase-mediated cassette exchange into the *Rosa26* locus of mouse embryonic stem cells and was performed and planned by Oskar Ortiz and Ralf Kühn (Institute of Developmental Genetics, Helmholtz Zentrum München). First, the donor vector (pEx-CAG-stop-GFP-OMM-bpA) was co-electroporated together with the C31-integrase expression vector into ID G3.2 embryonic stem cells. Cassette exchange is mediated by phiC31 integrase *attB* recognition sites in the donor vector (Figure 5d, red) and phiC31 integrase *attP* recognition sites in one allele of the *Rosa26* locus of the embryonic stem cells. This allows for integration of a single copy of the GFP-OMM cassette. Secondly, selection of positive embryonic stem cells was confirmed via neomycin resistance upstream of the CMV early enhancer/chicken β-actin promoter (Figure 5d, neomycinR). Cells were cultured with 140 μg/ml G418 for one week. Resistant colonies were isolated and screened for vector orientation by southern blot analysis (Hitz et al., 2007; Hitz et al., 2009). Thirdly, confirmed clones were injected into C57BL/6 blastocysts to obtain chimeric animals, which were screened by PCR probing for GFP. We further bred positive chimaera with C57BL/6 mice to obtain founder animals. These heterozygous mice were crossed to C57BL/6 mice for 8 generations before generating the homozygous colony of MitoTag mice.

We further genotyped MitoTag mice with four primers to distinguish homozygous (PCR product: 604 bp) and heterozygous (PCR products: 604 bp, 324 bp) animals. The MitoTag mouse line is transferred to *The Jackson Laboratory* and available as JAX#032675 (Rosa26-CAG-LSL-GFP-OMM).

3.2.3.2. APP23/PS45 and SOD1^{G93A} mouse model

I obtained transgenic APP23/PS45 mice (Busche et al., 2008) as model for Alzheimer's disease (AD) from Arthur Konnerth (Institute of Neuroscience, TUM) and SOD1^{G93A} mice (Gurney et al., 1994) as model for amyotrophic lateral sclerosis (ALS) to visualize mitochondrial morphology changes in disease models. Animals at the age of 9 month and within the age range of 2-5 month were examined for AD and SOD, respectively. Transgenic APP23/PS45 mice express mutant amyloid precursor protein (APP) KM670/671NL (Swedish double mutation, APPSwe Sturchler-Pierrat et al., 1997) and mutant presenilin 1 G384A (PS45 Herzig et al., 2004) from human driven by the Thy1 promoter.

3.2.3.3. Mcu^{tm1c} mouse model

We obtained the Mcu^{tm1a} knockout-first allele (C57BL/6N-Mcu$^{tm1a(EUCOMM)Hmgu/H}$; Figure 6) from the MMRRC. As previously described (Harrington and Murphy, 2015), no homozygous Mcu^{tm1a} mice were born due to embryonal lethality on C57BL/6 background. To generate conditional Mcu^{tm1c} mice (Figure 6b), I crossed Mcu^{tm1a} mice with ACTB-FLPe mice (Rodriguez et al., 2000) and tested the cassette removal of lacZ reporter and neomycin selection by PCR (products: 462 bp, 118 bp). Granule cell-specific Mcu deletion was achieved by breeding Mcu^{tm1c} with Gabra6:Cre-driver mice (Fünfschilling and Reichardt, 2002). I confirmed successful deletion by immunofluorescence staining and western blot analysis (Figure 38a and b). Mcu$^{GC:ko}$ mice were viable and normal in behavior. Mice of the age 1 to 5 month were used for experiments.

3.2.3.4. Rmdn3^{tm1a} mouse model

We obtained the Rmdn3 knockout-first allele (C57BL/6N-Rmdn3$^{tm1a(KOMP)Wtsi/MbpMmucd}$; Figure 7) from the KOMP Repository (project: 3U01HG004080; www.komp.org) where it was generated together with the Wellcome Trust Sanger Institute and the Children's Hospital Oakland Research Institute as part of the Knockout Mouse Project (Skarnes et al., 2011). The embryonic stem cell clone EPD0131_4_D01 was used for generation. Rmdn3^{tm1a} mice are born in normal Mendelian ratios, are fertile and normal in behavior. The mutant allele was identified by PCR (product: 546 bp) and I confirmed deletion of Rmdn3 protein by immunofluorescence staining and western blot analysis (Figure 40a and b).

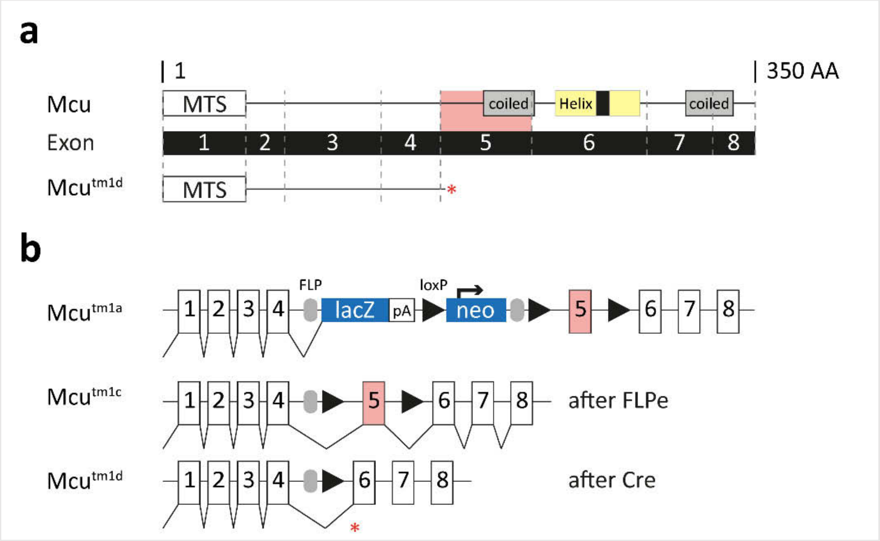

a
1
350 AA
Mcu
MTS
coiled
Helix
coiled
Exon
1
2
3
4
5
6
7
8
Mcutm1d
MTS
*
b
Mcutm1a
FLP
loxP
lacZ
pA
neo
Mcutm1c
after FLPe
Mcutm1d
after Cre
*

Figure 6│ Knockout-first allele of the murine Mcu locus. (**a**) The Mcu protein consists of eight exons coding for a 350 amino acid (AA) long protein. The Mcu^{tm1d} allele disrupts the Mcu locus creating a truncated 167 AA long protein. MTS, mitochondrial translocation signal; coiled, coiled domain; Helix, helical structure prior to transmembrane domain; *, stop. (**b**) Genetic modifications of the knockout-first allele of Mcu, Mcu^{tm1a} : insertion of the lacZ and neomycinR cassette prior to the critical exon 5 (red) and loxP site flanking of exon 5. Here, Mcu expression is disrupted. After FLP site recombination, the conditional allele Mcu^{tm1c} is generated without disruption of Mcu expression. After crossing with Cre-driver lines, the cell type-specific Mcu deletion is generated (Mcu^{tm1d}), which generates a non-functional, truncated 167 AA long protein. *, stop. Modified from documentation of the MMRRC (www.mmrrc.org).

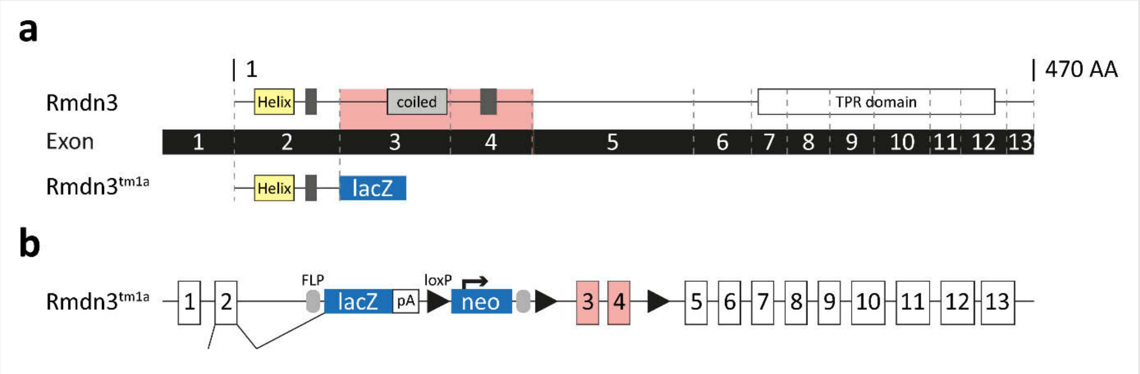

a
1
470 AA
Rmdn3
Helix
coiled
TPR domain
Exon
1
2
3
4
5
6
7
8
9
10
11
12
13
Rmdn3tm1a
Helix
lacZ
b
Rmdn3tm1a
FLP
loxP
lacZ
pA
neo

Figure 7│ Knockout-first allele of the murine Rmdn3 locus. (**a**) Rmdn3 protein consists of 13 exons coding for a 470 amino acid (AA) long protein. The Rmdn3^{tm1a} allele disrupts the Rmdn3 locus creating a lacZ-exon 2 fusion protein. AA, amino acid; coiled, coiled domain; Helix, helical structure prior to transmembrane domain; TPR domain, tetratricopeptide repeat domain. (**b**) Genetic modifications of the knockout-first allele of Rmdn3: insertion of the lacZ and neomycinR cassette prior to the critical exon 3 and 4 (red) and loxP site flanking of this critical region. Here, Rmdn3 expression is disrupted. Modified from documentation of the KOMP Repository (www.komp.org).

3.2.4. Genotyping of transgenic mice

Animal caretakers obtained tail biopsies and laboratory technicians performed DNA extraction, PCR and gel electrophoresis using standard protocols. DNA was isolated via proteinase K extraction using:

Proteinase K	0.5 μg/ml	
Triton X100	0.5%	55°C for 5 hours;
β-Mercaptoethanol	1%	95°C for 5 minutes;
Gitocher buffer	1x	4°C ∞
	ad 150 μl water	

PCR products were amplified using:

GoTaq	1x	95°C for 2 minutes; 32 cycles: 95°C, 15s 58°C, 30s 72°C, 15s; 72°C for 5 minutes; 4°C ∞
Primers	10 pmol	
DNA	1 μl	
	ad 20 μl water	

Products and 1K DNA ladder were separated on a 1.5% agarose/TAE gel via electrophoresis at 180 V, 30 minutes. DNA bands were visualized under 312 nm UV light and documented with GenoPlex software.

3.2.5. Time-lapse imaging of mitochondrial transport in motor axons

Laura Trovò (L.T.; Institute of Neuronal Cell Biology, TUM) probed mitochondrial transport ex vivo in nerve-muscle explants of transgenic mice as previously described (Kerschensteiner et al., 2008). Briefly, the rib cage including the triangularis sterni muscle and its innervating intercostal nerves was excised post mortem and transferred to a dish with oxygenated Ringer's solution. Extraneous tissue and fat were removed and the explant pinned down with insect pins into a Sylgard-coated 35 mm dish. During the entire experiment, the explant was super-fused with oxygenated Ringer's solution at 33°C to 35°C. Time-lapse imaging was performed using an Olympus BX51WI upright down, epifluorescence microscope equipped with a 20xW/0.5 and a 100xW/1.0 water immersion objective, an automated filter wheel, neutral density filters and a cooled CCD camera (Retiga EXi). The acquisition was controlled by μManager.

To asses mitochondrial transport in MitoTag mice, we crossed Rosa26-GFP-OMM mice to ChAT:Cre$^+$-driver mice (Rossi et al., 2011) and Thy1:mito-RFP mice (Breckwoldt et al., 2014). Because GFP-OMM in motor neurons was dimmer than observations made by Rosa26-mitoGFP, L.T. evaluated transport based on mito-RFP signals – a transgenic mouse line with matrix localized, bright RFP. Comparisons were made between ChAT:Cre$^-$/GFP-OMMxThy1:mito-RFP and ChAT:Cre$^+$/GFP-OMMxThy1:mito-RFP litter mates.

3.2.6. Neuromuscular health assessment

Laura Trovò (L.T.; Institute of Neuronal Cell Biology, TUM) performed the assessment of neuromuscular junction (NMJ) area and acetylcholine receptor density at NMJs in motor neurons expressing GFP-OMM ex vivo. For this, triangularis sterni muscles were fixed with 4% paraformaldehyde in PBS on ice for one hour. Thereafter, the muscle was dissected from the rib cage and stained with α-bungarotoxin-biotin (10 mg/μl) and phalloidin conjugated to Alexa Fluor 647 (4 U/ml) at 4°C overnight. Next, the samples were washed with PBS and incubated with streptavidin-Alexa Fluor 405 (1:500) in PBS at room temperature for one hour. Muscles were mounted with Vectashield Mounting medium and flattened by magnets at 4°C overnight.

Comparisons were made between tissues from ChAT:Cre$^-$/GFP-OMMxThy1:mito-RFP and ChAT:Cre$^+$/GFP-OMMxThy1:mito-RFP litter mates. The α-bungarotoxin staining was thresholded with the Otsu algorithm in ImageJ/Fiji (Schindelin et al., 2012) to obtain the area of neuromuscular junction. Next, within this area the intensity of α-bungarotoxin staining was measured and background subtracted.

3.2.7. Mitochondrial purification

I isolated mitochondria from freshly collected mouse tissue as described in Wettmarshausen and Perocchi (2017). In brief, mice were anesthetized with a lethal dose of isoflurane and transcardially perfused with heparin (19.5 U/ml) in PBS. The tissue of interest was dissected, weighed and minced with a Dounce glass homogenizer using three complete up and down cycles of an A-type pestle in isolation buffer (IB). During all steps, I kept the sample on ice or at 4°C. Next, cells were opened by nitrogen cavitation using a cell disruption vessel (model 4635-39) at 800 psi and under stirring at 60 rpm for 10 minutes. Upon release from the disruption vessel, protease inhibitor was added to the resulting total tissue fraction. Nuclei and debris were removed by centrifugation at 600 g for 10 minutes. The supernatant was transferred and centrifuged again. The resulting post-nuclear tissue fraction was filtered through a 30 µm pre-separation filter.

3.2.7.1. Differential centrifugation

To obtain the crude mitochondrial fraction (CMF) from the post-nuclear tissue fraction, a volume equivalent to 20 mg initial tissue was centrifuged at 12,000 g for 3 minutes. The pellet washed twice with IB without BSA. For respiratory measurements, I gently resuspended the final CMF in 30 µl IB with 0.2% BSA. For western blot analysis, I immediately stored the pellet at -20°C.

3.2.7.2. Immunocapture

For immunocapture (IC) against Tom22 (Franko et al., 2013; Hornig-Do et al., 2009) or GFP-OMM, the post-nuclear tissue fraction was diluted to a concentration of maximal 2 mg tissue/ml in immunocapture buffer (ICB). 50 µl microbeads coated with mouse IgG_1 subtype antibodies (Miltenyi Biotec) against Tom22, GFP or CD4 were added and incubated on a shaker (60 rpm) at 4°C for 30 to 90 minutes. Incubation was dependent on cell type abundance within the tissue and was adjusted accordingly, e.g. 30 minutes for $Emx:Cre^+$/GFP-OMM and 90 minutes for $ChAT:Cre^+$/GFP-OMM. To separate microbeads-coated mitochondria from the solution, I placed LS columns in a magnetic QuadroMACS Separator and equilibrated them with 3 ml ICB. The IC was applied to the column in 3-ml-steps, followed by three 3-ml-wash-steps with ICB. I removed the column from the magnet and gently flushed out mitochondria in 4 ml ICB using the plunger. Isolated mitochondria were pelleted by centrifugation at 12,000 g for 3 minutes and washed twice with IB without BSA. For respiratory measurements, I gently resuspended the final pellet in 30 µl IB with 0.2% BSA. For western blot analysis, I immediately stored samples at -20°C.

We deliberately avoided the use of an additional Percoll gradient for further purification (Sims and Anderson, 2008) in order to preserve organelle interactions and mitochondrial integrity (Wang et al., 2011b). This results in some level of commonly known contaminations with non-mitochondrial proteins; however, this is in the analysis largely eliminated by normalization to IC Tom, where it is equally present. Still, if one desires purity over organelle viability, yield and time, cell type-specific mitochondria can be further purified via a Percoll gradient.

3.2.8. Protein amount measurement

I determined protein amount concentration in samples by using the Pierce BCA Protein assay kit according to the manufacturer’s instructions with BSA as standard. Assay dependent sample buffers were used to correct for alterations due to detergent or BSA.

3.2.9. Oxygen consumption measurement in isolated mitochondria

3.2.9.1. Seahorse assay

Laura Trovò (L.T.; Institute of Neuronal Cell Biology, TUM) performed oxygen consumption measurements in isolated mitochondria, which were isolated by myself (Figure 13 and 15) and by L.T. (Figure 36).

Mitochondrial oxygen consumption rate (OCR) was measured in the assay solution MAS-1X using a Seahorse XFe96 Extracellular Flux Analyzer with typical mix (1 minute) and measurement cycle times (3 minutes). CMF or immunocaptured mitochondria (Table 2) were added in a volume of 10 µl per well of a 96-well plate and centrifuged at 2,000 g, 4°C for 20 minutes to attach mitochondria. Substrate mixtures (Table 3) were added and the plate was equilibrated at 37°C.

Table 2. Amounts of mitochondria per substrate and tissue origin.

		Complex I		Complex II		Beta-oxidation	
Tissue	Isolation	µg	CCCP (µM)	µg	CCCP (µM)	µg	CCCP (µM)
Cortex	CMF	2	10	2	10	-	-
	IC	2	10	1	10	-	-
Cerebellum	IC	3	7.5	2	7.5	8	3

Table 3. Substrates and inhibitors used for testing mitochondrial respiration.

		Complex I		Complex II		Beta-oxidation	
state 2	Substrates	Pyruvate Malate	10 mM 2 mM	Succinate Rotenone	10 mM 2 µM	L-Palmitoylcarnitine Malate	50 µM 2 mM
state 3	ADP	4 mM					
state 4o	Oligomycin	1.5 µM					
state 3u	CCCP	(see Table 2)					
non-mito OCR	Antimycin A Rotenone	4 µM 2 µM					

Mitochondrial respiration was determined for complex I in the presence of pyruvate+malate, complex II with succinate+rotenone and beta-oxidation with L-palmitoylcarnitine+malate (Watkins et al., 1991; Demarquoy and Le Borgne, 2015). With a series of injection oxygen consumption was measured under basal conditions (*state 2*), after the addition of ADP (*state 3*, ADP-uncoupled respiration), after oligomycin injection (*state 4o*, proton leak), with CCCP (*state 3u*, maximal respiration) and finally upon antimycin A and rotenone application to disrupt mitochondrial respiration (non-mitochondrial residual oxygen consumption).

Per sample, eight technical replicates were run, of which at least three successful replicates were necessary for inclusion in the analysis. L.T. excluded measurements that showed no response to an injection and in which mitochondria had deattached during the assay.

3.2.9.2. OCR analysis

Analysis was performed with the Agilent Seahorse XFe96 Wave software and Microsoft Excel 2016 by calculating coupling efficiency (CE), respiratory control ratio (RCR) and spare respiration capacity (SRC):

$$\text{CE}=\frac{(state\ 2-state\ 4o)}{state\ 2};\qquad \text{RCR}=\frac{(state\ 3-state\ 4o)}{state\ 4o};\qquad \text{SRC}=\frac{state\ 3u}{state\ 2}.$$

Prior to these calculations, all measurements were corrected for non-mitochondrial residual oxygen consumption by subtracting the OCR with antimycin A and rotenone (mean of the last four measurements). To illustrate OCR dynamics of individual experiments across substrates, I generated OCR graphs normalized to basal respiration values (mean of first five measurements) from representative experiments showing the mean of technical replicates with s.e.m. (for example see Figure 13b).

3.2.10. Mitochondrial Ca^{2+} uptake assay

Ca^{2+} uptake of immunocaptured mitochondria was performed as described in Wettmarshausen and Perocchi (2017) with the following modifications: I resuspended 50 µg mitochondria in respiration buffer (RB) supplemented with 100 nM CalciumGreen-5N and in the absence or presence of 10 µM Ru360. Fluorescence (ex.485/em.530) was measured via a microplate reader (CLARIOstar) in 2 seconds intervals for a total of 24 minutes with the injection of 20 µM $CaCl_2$ in assay buffer every 3 minutes at 25°C. I used animals within the age range of 2 to 4 months.

I calculated the Ca^{2+} uptake capacity as the differential area under the curve (∆AUC) between the presence and absence of Mcu inhibitor Ru360. In Brief, the first $CaCl_2$ injection was ignored due to residual EDTA from immunocapture. Traces were background corrected, normalized to the injection time point and AUC was calculated. Finally, the difference between AUC_{-Ru360} and AUC_{+Ru360} per sample (∆AUC) is shown as percentage of AUC_{+Ru360}.

3.2.11. Western blot analysis

3.2.11.1. Sample preparation

For western blot analysis, I first lysed material in RIPA buffer supplemented with protease inhibitor (cOMPLETe, EDTA-free) on ice for 30 minutes with frequent vortexing. Protein concentration was determined via BCA assay, samples were mixed with 1x LDS sample buffer supplemented with 50 mM DDT and boiled at 70°C for 10 minutes.

3.2.11.2. Western blotting and detection

Per sample 10 µg protein was used in the case of mitochondrial isolations and whole tissue comparison; 20 µg was used in the case of total cerebellum lysates to evaluate Rmdn3 expression. Using SDS polyacrylamide gels (12% or 4-20%), samples were separated via electrophoresis with Tris-Glycine buffer and transferred on PVDF membrane (0.2 µm pore size) with TWOBIN buffer using the TurboBlot semi-dry system with the following settings: 20 V max., 1.3 A, 12 minutes.

After transfer, membranes were washed with water and air dried, followed by SyproRuby staining for total protein quantification according to the manufacturer’s instructions. SyproRuby signals were acquired using UV light on the Fusion FX7 machine. To remove total protein staining, membranes were incubated in 3% skim milk in TBSt at room temperature for 30 minutes and blocked for further 30 minutes in fresh solution.

Incubation with primary antibody was performed overnight under agitation at 4°C in 3% skim milk in TBSt using antibodies listed in Chapter 3.1.7.2. Membranes were washed three times in TBSt at room temperature under agitation for 10 minutes, followed by a 2 hours incubation with HRP-conjugated secondary antibody in 3% skim milk in TBSt under agitation at room temperature. After washing, membranes were incubated with ECL Prime according to the manufacturer’s instructions and signals were acquired using the Fusion FX7 machine. A second round of antibody probing was performed for antibodies from a different species. After extensive washing in TBSt with 0.8% sodium azide at room temperature, membranes were blocked again and incubated overnight with primary antibody. Cross-reactivity of antibodies from different species was excluded in prior experiments.

3.2.11.3. Analysis

For quantification, samples were run as technical triplicates on one membrane and the mean was further used for graphs and statistics – with the exception of Figure 17, where sample amounts limited the analysis to one per experiment and Figure 37 and 38, where samples were run as duplicates. I used only non-saturated images and calculated relative dosimetry with Image Studio Lite software and Microsoft Excel 2016. Signals per lane were background subtracted, normalized with total protein signals (SyproRuby) and results expressed as fold change to a given sample on the same membrane. I further used mitochondrial content (evaluated by ATP5a, CypD, Tomm20) for normalization between different isolations. Uncropped western blots for all depicted blots in figures are shown in the Appendix 7.6.

3.2.12. Mass spectrometry

Stephan Müller (S.M.; Lichtenthaler laboratory, German Center for Neurodegenerative Diseases) prepared mass spectrometry samples, acquired them and performed the first analysis in MaxQuant and Microsoft Excel.

3.2.12.1. Sample preparation

I generated mass spectrometry samples from 8- to 9-week-old, male mice. Mitochondria were immunocaptured from cerebellum according to the described protocol (see Chapter 3.2.7.2) with the alteration that the final mitochondrial pellet was washed twice in IB without EDTA and BSA. S.M. lysed samples in 100 µL SDT lysis buffer by heating at 95°C for 5 minutes and ultrasonication (Vialtweeter: 6 times for 30 s, 100% Amplitude, 50% cycle, max. power). Debris and non-dissolved material was removed by centrifugation at 20,000 g for 10 minutes. Protein concentrations were estimated using the Pierce 660 nm Protein assay supplemented with the ionic detergent compatibility reagent with a dilution series of BSA in SDT buffer for calibration. An amount of 15 µg was subjected to protein digestion using the filter-aided sample preparation (FASP) with small modifications (Wisniewski et al., 2009). Briefly, 30 kDa Vivacon filters were used. The alkylation step was followed by incubation with 50 U benzonase in 50 mM Tris HCl, pH 8 and 1 mM magnesium chloride. Afterwards, three washing steps with 100 µl of 8M urea in 100 mM Tris HCl, pH 8 were implemented. Proteins were digested with 0.3 µg of LysC for 16 h followed by 4 h incubation with 0.15 µg of trypsin. Peptides were eluted into collection tubes and desalted using C18 stop-and-go extraction (Rappsilber et al., 2003). Samples were dried after elution by vacuum centrifugation.

Whole cerebellum samples were lysed in RIPA buffer 2. Cell debris and undissolved material was removed by centrifugation at 16,000 g, 4°C for 10 minutes. A protein amount of 20 µg was further dilute 1:2 with water and 10 mM magnesium chloride was added. Afterwards, 25 U benzonase were added and the DNA digestion was performed for 30 minutes at 37°C. Protein digestion was performed using FASP as described above without addition of benzonase.

3.2.12.2. Data acquisition

S.M. analyzed samples on an Easy nLC-1,000 nano UHPLC coupled online via a Nanospray Flex electrospray ion source equipped with a column oven to either a Q-Exactive or a Q-Exactive HF mass spectrometer. An amount of 1.3 µg peptides was separated on self-packed C18 columns (300 µm × 75 µm, ReproSil-Pur 120 C18-AQ, 1.9 µm; Dr. Maisch) using a binary gradient of water (A) and acetonitrile (B) supplemented with 0.1% FA (0 minutes, 2% B; 5 minutes, 5% B; 185 minutes, 25% B; 230 minutes, 35% B; 250 minutes, 60% B).

The dataset from Purkinje cell mitochondria was analyzed on a Q-Exactive mass spectrometer. Full mass spectrometry spectra were acquired at a resolution of 70,000 (AGC target: 3E+6). The ten most intense peptide ions were chosen for fragmentation by higher-energy collisional dissociation (resolution: 17.5 k, isolation width: 2 m/z, AGC target: 1E+5, NCE: 25%). A dynamic exclusion of 120 s was applied for fragment ion spectra acquisition.

The datasets from cerebellum, granule cell mitochondria and astrocytic mitochondria were analyzed on a Q-Exactive HF mass spectrometer with slightly adjusted settings. For full mass spectrometry spectra, a resolution of 120,000 was applied. The 15 most intense ions were chosen for fragmentation (resolution: 15 k, isolation width: 1.6 m/z, AGC target: 1E+5, NCE: 26%).

3.2.12.3. Data analysis primary

S.M. performed peptide identification, label-free quantification (LFQ) and intensity-based absolute quantification (iBAQ) of proteins in MaxQuant for each dataset separately (version 1.5.4.1 for the Purkinje cell mitochondria dataset; 1.5.5.1 for the dataset from cerebellum, granule cell mitochondria and astrocytic mitochondria) using default settings (Cox et al., 2014). In brief, a canonical database of the reviewed reference mouse proteome (UniProt, 2019; download: June 8th, 2016; 16,798 entries) was used for database search. The astrocytic mitochondria dataset from cerebellum was analyzed together with data from astrocytic mitochondria from cortex because both dataset (cerebellum and cortex) were generated in parallel from the same biological replicate. As increased sample numbers increase the number of peptide identifications, this part was done together – however, all further data analysis steps were exclusively performed on cerebellar mitochondria. The false discovery rate (FDR) for both peptides and proteins was adjusted to less than 1% using a target and decoy approach (concatenated forward/reverse database). The 'match between runs' option was enabled using a time window of 2 minutes. LFQ required at least two ratio counts of unique peptides. The data sets are available in the ProteomeXchange Consortium via the PRIDE partner repository (Vizcaino et al., 2016): mitochondria from Purkinje cells (PXD010772), mitochondria from granule cells (PXD010774) and mitochondria from astrocytes (PXD010781); whole cerebellum (PXD013380).

3.2.12.4. Data analysis secondary

I further analyzed and compared protein intensities in Perseus (Tyanova et al., 2016; Cox and Mann, 2012). The bioinformatics analysis is depicted in Figure 8. First protein IDs from the three mass spectrometry experiments were merged against the reviewed reference mouse proteome including annotation from MitoCarta (Calvo et al., 2016) and LocTree3 (Goldberg et al., 2014) for subcellular localization. Only proteins with at least two unique peptides were further considered for relative quantification. Protein LFQ intensities were $\log_2$ transformed. Second, for relative quantification, the protein $\log_2$ LFQ ratios were calculated by subtracting the $\log_2$ value of IC Tom from IC GFP separately for each biological replicate. Next, proteins which were relatively quantified in less than three biological replicates, were removed, leading to a group of 3,130 protein which were consistently quantified in all three datasets from Purkinje cells, granule cells and astrocytes. Finally, the $\log_2$ fold change of each protein between cell types (comparisons: PC/GC, PC/A and GC/A) was analyzed by a two-sided, unpaired *t*-test (with ≥3 biological replicates, randomizations: 500, permutation-based FDR≤0.05). Proteins with $\log_2$ fold changes that passed the permutation-based FDR criterion are marked as blue, filled circles (see Figure 23a). The scatter plot summarizing changes in PC/A *vs* GC/A is depicted in Figure 23b by showing proteins that passed the FDR criterion in at

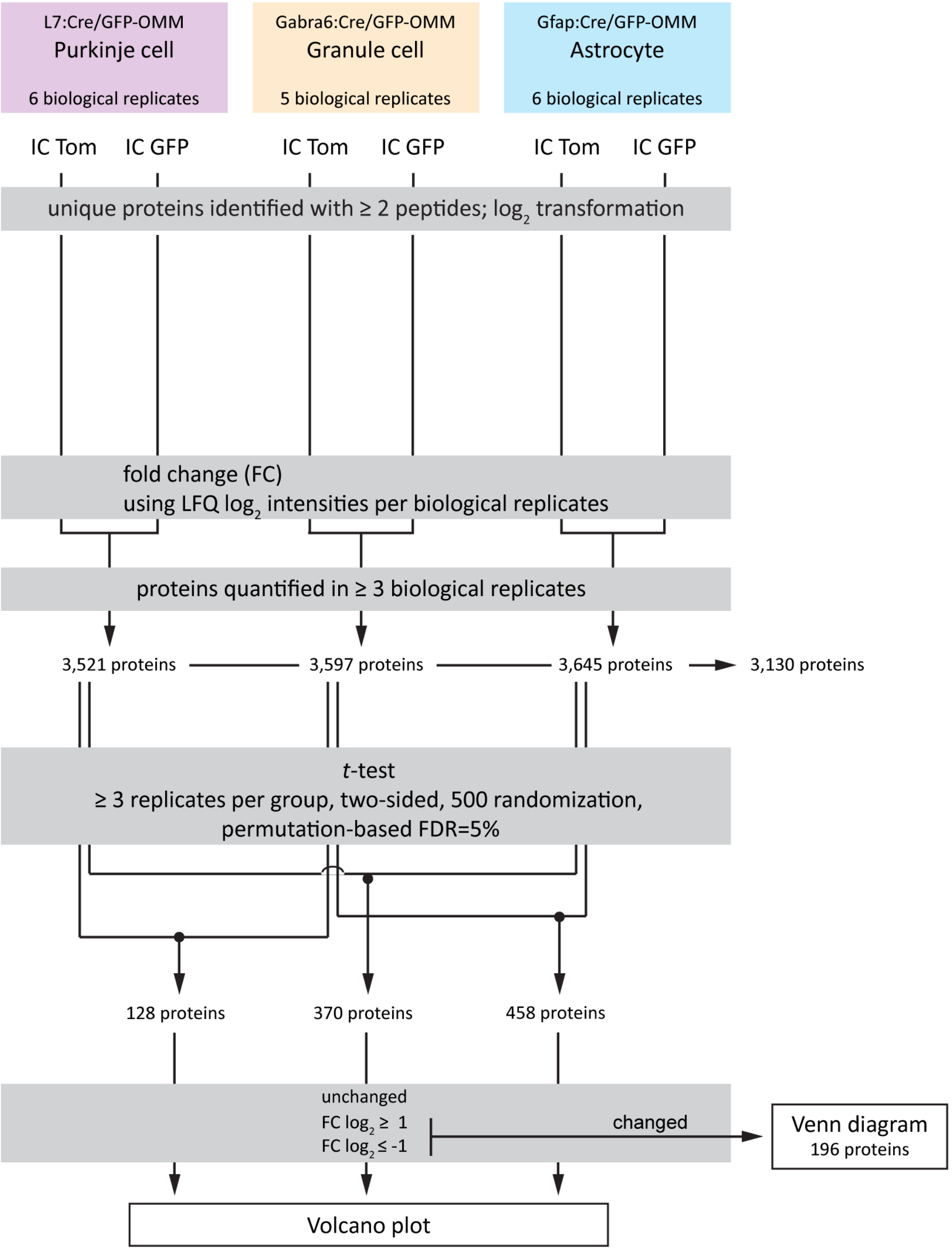
L7:Cre/GFP-OMM
Purkinje cell
6 biological replicates
Gabra6:Cre/GFP-OMM
Granule cell
5 biological replicates
Gfap:Cre/GFP-OMM
Astrocyte
6 biological replicates
IC Tom
IC GFP
IC Tom
IC GFP
IC Tom
IC GFP
unique proteins identified with ≥ 2 peptides; log2 transformation
fold change (FC)
using LFQ log2 intensities per biological replicates
proteins quantified in ≥ 3 biological replicates
3,521 proteins
3,597 proteins
3,645 proteins
3,130 proteins
t-test
≥ 3 replicates per group, two-sided, 500 randomization,
permutation-based FDR=5%
128 proteins
370 proteins
458 proteins
unchanged
FC log2 ≥ 1
FC log2 ≤ -1
changed
Venn diagram
196 proteins
Volcano plot

Figure 8│ Flow chart depicting secondary analysis of mass spectrometry data comparing mitochondrial proteomes from Purkinje cells, granule cells and astrocytes. IC, immunocapture; LFQ, label free quantification; FC, fold change. Modified from Fecher et al. (2019), Supplementary Figure 6.

least one of the two *t*-tests. In the text, mass spectrometry statistics are called out as, e.g. for Cox4i1, two-tailed, unpaired *t*-test with permutation-adjusted q-value: PC *vs* A: *0.554, 0.0268; GC *vs* A: *0.496, 0.0002; PC *vs* GC: 0.058, 0.9085. (*) indicates a significant result with the first following value being the fold change and the second value the permutation-adjusted q-value for multiple comparison.

From the pairwise *t*-tests between cell types, proteins were considered as changed, if their $\log_2$ fold change ≥|1|. Thus, they were further analyzed for their enrichment in a specific cell type by using the online Venn diagram tool (http://bioinformatics.psb.ugent.be/webtools/Venn/). Here, 18, 51 and 114 proteins were identified to be enriched in Purkinje cells, granule cells and astrocytes, respectively (Figure 24a); using the following definitions for cell type-specificity:

Table 4. Criteria for cell type enrichment.

PC-enriched	FC≥1 in PC/A combination A (FC≥1 in PC/A & PC/GC) combination B (FC≥1 in PC/GC only)
GC-enriched	FC≥1 in GC/A combination A (FC≤-1 in PC/A & PC/GC, FC≥1 in GC/A) combination B (FC≥1 in GC/A, FC≤-1 in PC/GC) combination C (FC≤-1 in PC/GC only)
A-enriched	FC ≤ -1 in PC/A and/or GC/A

I color-coded these groups in the scatter plot in Figure 24 comparing PC/A *vs* GC/A.

For Over-Representation Analysis (ORA) of the ‘biological process’ category of gene ontology processes (GOTerm; Figure 31b, top) and KEGG pathways (Figure 31b, bottom), the WEB-based GEne SeT AnaLysis Toolkit (WebGestalt 2019; Liao et al., 2019) I used with the following data sets:

- reference set: genome_protein-coding, mmusculus as background (n=27,331);
- candidates enriched in astrocytes (n=114);
- candidates enriched in neurons (GC-enriched, PC-enriched, GC & PC-enriched; n=74).

Standard parameters for the enrichment analysis were used with the following settings: Minimum number of Entrez Gene IDs in the category: 5; Maximum number of Entrez Gene IDs in the category: 2,000; FDR Method: BH (Multiple Test Adjustment); Significance Level:

FDR≤0.05. In Appendix 7.4, the full results are documented, whereas in Figure 31b the top 10 hits per category are listed for KEGG and the clustered gene sets for GOTerms.

For heat map generation of mitochondrial functions, the following KEGG and GOTerm annotations (AmiGO version 2.5; Ashburner et al., 2000; The Gene Ontology, 2019) were used:

Table 5. Annotation list for core mitochondrial functions.

Beta-oxidation	mmu00071, fatty acid degradation; Adeva-Andany et al. (2019); Pei et al. (2003); Iacobazzi et al. (2004); He et al. (2011)
mtRibosome	GO:0005762, mitochondrial large ribosomal subunit; GO:0005763, mitochondrial small ribosomal subunit
Complex I	GO:0005747, mitochondrial respiratory chain complex I
Complex II	GO:0005749, mitochondrial respiratory chain complex II, succinate dehydrogenase complex (ubiquinone)
Complex III	GO:0005750, mitochondrial respiratory chain complex III
Complex IV	GO:0005751, mitochondrial respiratory chain complex IV
Complex V	GO:0000276, mitochondrial proton-transporting ATP synthase complex, coupling factor F(o); GO:0005753, mitochondrial proton-transporting ATP synthase complex
CoQ synthesis	Acosta et al. (2016)
TCA cycle	GO:0006099, tricarboxylic acid cycle

The lists were further curated for mitochondrial annotation of proteins and additional information provided on the UniProt profile (update: October 16th, 2019, UniProt, 2019) and from previous reports.

Enrichment of mitochondrial protein abundance was calculated based on iBAQ values (Shin et al., 2013). First, I calculated the average $\log_{10} iBAQ$ value per protein per group of biological replicates for immunocaptures (IC Tom, IC GFP). Second, I generated the average over all proteins annotated as mitochondrial as well as non-mitochondrial based on MitoCarta (Calvo et al., 2016) and LocTree3 (Goldberg et al., 2014) annotations. Finally, the difference between these two groups was transformed to fold change (linear). Similar calculations were performed on the proteomics datasets from whole cerebellum and the reference dataset of Percoll purified mitochondria from Pagliarini et al. (2008).

To compare the immunocapture approach to recent studies, I generated Venn diagrams with the online Venn diagram tool (http://bioinformatics.psb.ugent.be/webtools/Venn/) comparing IC Tom from cerebellum to the proteomic dataset from cerebellar mitochondria published by Pagliarini et al. (2008), from whole cerebellum published by Sharma et al. (2015) and MitoCarta (Figure 20). For this comparison, proteins found in ≥9 biological replicates of IC Tom were considered.

3.2.13. Fluorescence cytometry

After mitochondrial isolation (see Chapter 3.2.7.1), I resuspended the crude mitochondrial fraction (CMF) of 20 mg cortex samples in 100 µl 4% paraformaldehyde in PBS and incubated it in the dark at room temperature for 5 minutes. Samples were washed three times with PBS and resuspended in 100 µl 0.5% BSA in PBS. 20 µl fixed mitochondria were used per staining. First, I washed the sample with 0.5% BSA in PBS. Then the sample was incubated with APC-conjugated mouse IgG$_1$ or mouse Tom22 (1:25) in the dark, at 4°C, 60 rpm for 60 minutes. Samples were washed three times with 0.5% BSA in PBS and finally resuspended in 100 µl PBS. For flow cytometry, Sylvia Heink (Experimental Neuroimmunology, Klinikum rechts der Isar, TUM) acquired samples on a CyAn ADP 9 flow cytometer (equipped with 405 nm, 488 nm and 642 nm lasers) and was consulted for analysis. We diluted sampled 1:20 with PBS. To allow for optimal identification and separation of small particles, the flow rate was adjusted accordingly and optical parameters (forward scatter, FSC, and sideward scatter, SSC) were scaled

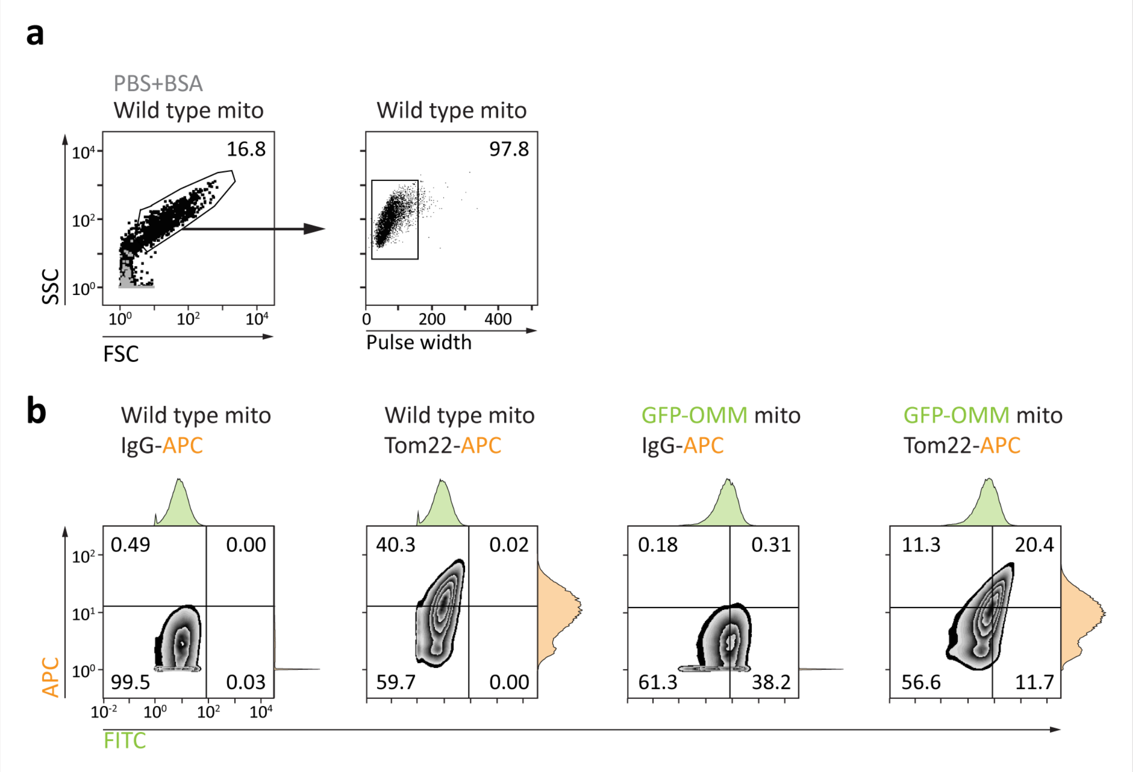

Figure 9| Gating strategy to quantify cell type-specific mitochondria in Cre$^+$/GFP-OMM mouse lines. Crude mitochondria from cortex of Emx1:Cre$^-$/GFP-OMM and Emx1:Cre$^+$/GFP-OMM mice were labeled with Tom22-APC or IgG$_1$-APC. (**a**) First gating step: forward and sideward scatter, and pulse width of wild type mitochondria. (**b**) Zebra plots and histograms of FITC and APC intensity shown for wild type mitochondria with IgG$_1$-APC and Tom22-APC, as well as for Emx1:Cre$^+$/GFP-OMM mitochondria. Taken from Fecher et al. (2019), Supplementary Figure 4.

logarithmically. Based on light-scattering properties (FSC-log *vs* SSC-log), 100,000 events were acquired per sample.

Using FlowJo software, I gated mitochondria by FSC and SSC, as well as pulse width to discriminate doublets. Then Tom22-APC staining (APC, Em. 665/20) intensities were manually gated against mouse IgG_1-APC control samples to define mitochondria. From this, individual gates for GFP-OMM (FITC, Em. 530/40) and mito-RFP (PE, Em. 575/25) were gated according the wild type mitochondria (Figure 9). In Figures, the histogram of the samples closest to mean is shown with IgG_1 control (gray histogram) as well as the mean±s.e.m. of $n \geq 4$ biological replicates.

3.2.14. Immunofluorescence staining

Mice were killed with isoflurane and transcardially perfused first with heparin (19.5 U/ml) in PBS followed by 4% paraformaldehyde in PBS. Tissues were kept in 4% paraformaldehyde in PBS at 4 °C overnight. Similarly, fixation of rat and zebra finch tissue was performed, while tissue from embryonal day 19 chicken and Cuban tree frog were fixed by immersion fixation in 4% paraformaldehyde in PBS at 4°C overnight. All tissues were subsequently cut using a vibratome. Tissue from rat, zebra finch, chicken and Cuban tree frog were kindly provided by Grass Fellows, Marine Biological Laboratory, Woods Hole 2019.

3.2.14.1. Mitochondrial markers in mouse tissue

If not mentioned differently, I performed all steps at room temperature under agitation (100 rpm). First, I tested antibodies against candidates with a series of antigen retrieval conditions including Triton X100 and different heat-induced antigen retrieval buffer (HIER 1-7; Figure 10). From this test, the best condition was further used for experiments. Depending on epitope, tissue sections were permeabilized with different conditions (Table 6), extensively washed and blocked using blocking solution for one hour. For primary antibodies produced in mouse, sections were incubated with goat anti-mouse Fab fragments (1:100 in PBS) for one hour. Incubation with primary antibody (see Chapter 3.1.7.1) was performed in 10% blocking solution in PBS at 4°C overnight. After extensive washing, secondary antibodies were applied in 10% blocking solution in PBS for two hours. Tissue section were further stained with Hoechst (Hoechst 33342; 100 µg/ml in PBS) for 10 minutes and mounted using Vectashield Mounting medium.

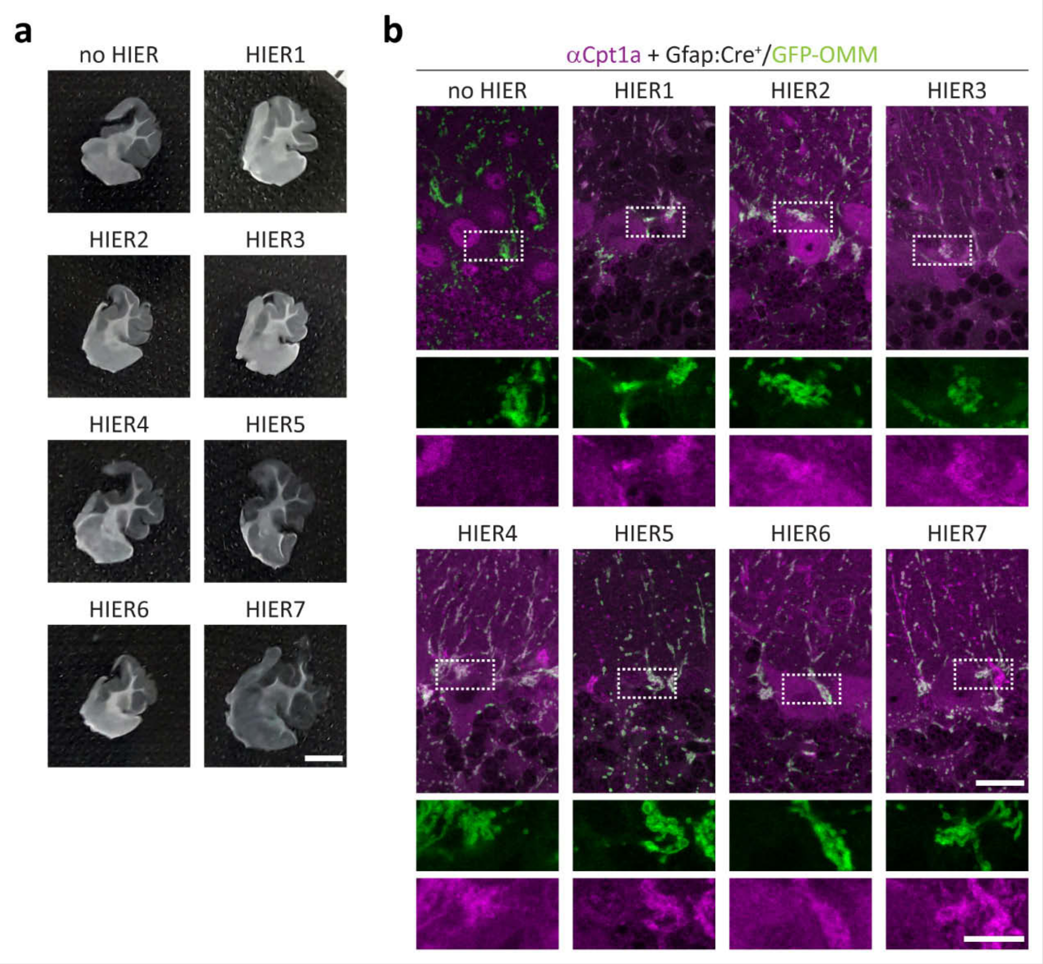

Figure 10| Detection of candidates via heat-induced antigen retrieval. Sagittal cerebellum sections (50 μm) from Gfap:Cre^{+}/GFP-OMM mice were pretreated with 0.1% Triton X100 and subsequent treated with PBS at room temperature (no HIER) or different buffers at 90°C for 30 minutes (HIER 1-7). (**a**) Tissue morphology after heat-induced antigen retrieval. Note that some conditions partially clear the tissue und lead to expansion. Scale bar: 2 mm. (**b**) Following blocking, immunofluorescence staining against GFP (green, 1:1000) and Cpt1a (magenta, 1:200) was performed. While with 'no HIER' I observed nuclear localization of Cpt1a as previously reported (Mazzarelli et al., 2007), HIER5 and HIER7 performed best with low background and mitochondrial localization of Cpt1a. Scale bars: 20 μm (detail 10 μm).

Table 6. Details for immunofluorescence staining of mitochondrial markers in mouse tissue. Modified from Fecher et al. (2019), Supplementary Table 1.

Epitope	*#*	*Species*	*Dilution*	*Treatment*
Acads	ab156571	Rabbit	1:200	Tris pH 10
Ak3	sc-398571	Mouse IgG$_1$	1:100	Tris-EDTA pH 9
Ak4	sc-271161	Mouse IgG$_1$	1:100	Tris-EDTA pH 9
Catalase	100-4151	Rabbit serum	1:200	Tris pH 10
Cox4i1	AP22111a	Rabbit	1:200	Citrate-EDTA pH 6.2
Cpt1a	15184-1-AP	Rabbit	1:200	Tris-EDTA pH 9

Epitope	*#*	*Species*	*Dilution*	*Treatment*
Gldc	HPA002318	Rabbit	1:400	Tris pH 10
Gls	20170-1-AP	Rabbit	1:200	Tris-EDTA pH 9
Gls2	AP6650D	Rabbit	1:400	Tris-EDTA pH 9
Got2	ab171739	Rabbit	1:400	Tris pH 10
Ldhd	ab182146	Rabbit	1:100	Tris pH 10
MaoB	sc-515354	Mouse IgG_1	1:100	Tris pH 10
Mavs	#4983	Rabbit	1:200	EDTA pH 8
Mcu	HPA016480	Rabbit	1:400	EDTA pH 8
Nipsnap1	#13226	Rabbit	1:200	Tris-EDTA pH 9
Ociad2	HPA040979	Rabbit	1:200	Tris-EDTA pH 9
Ociad2	ab91576	Rabbit	1:200	Tris-EDTA pH 9
Pex14	-	Rabbit	1:1,000	0.2% Tx100/PBS
Pptc7	ab122548	Rabbit	1:200	TBS pH 9
Rmdn3	ab189845	Rabbit	1:400	Tris-EDTA pH 9
Sfxn5	ab172971	Rabbit	1:500	0.2% Tx100/PBS
Slc25a20	19363-1-AP	Rabbit	1:400	Tris-EDTA pH 9
Snph 1-100	ab192605	Rabbit	1:400	Tris pH 10
Snph 225-428	-	Rabbit	1:400	Tris pH 10
Tst	ab166625	Rabbit	1:500	0.2% Tx100/PBS

3.2.14.2. Mitochondrial markers in human tissue

Human sample were provided by Doron Merkler (Department of Pathology and Immunology, University of Geneva, Switzerland) and Ingrid Wagner (I.W.; Department of Pathology and Immunology, University of Geneva, Switzerland) performed immunofluorescence staining in human tissue with assistance from me regarding antibody dilutions. I performed acquisition of the samples at the Institute of Neuronal Cell Biology, Munich.

For human tissue sections (4 µm thickness), the following changes for immunohistochemical staining were applied (see Table 7 for details): after de-paraffination, I.W. performed heat-induced antigen-retrieval on paraformaldehyde fixed tissue. Following blocking with 10% FCS in PBS, sections were incubated with primary antibodies in Dako Diluent (Dako) at 4°C overnight. After extensive washing with Wash Buffer (Dako) and autofluorescence removal treatment (Merck), secondary antibodies and DAPI (1:2,000) were diluted in PBS and incubated at room temperature for one hour. Slides were cover slipped with Fluoromount Mounting Medium.

For sections requiring Tyramide Signal Amplification (TSA), endogenous peroxidase blockade with Dako REAL Peroxidase-Blocking solution was performed prior to addition of 10% FCS in PBS. Following primary antibodies incubation, slides were incubated with anti-rabbit HRP at room temperature for 30 minutes, followed by incubation with TSA (FP1170, Perkin Elmer) at room temperature for 10 minutes as a secondary system. Autofluorescence removal treatment was performed prior to DAPI staining.

Table 7. Details for immunofluorescence staining of mitochondrial markers in human tissue. Taken from Fecher et al. (2019), Supplementary Table 2.

Epitope	*#*	*Species*	*Dilution*	*Treatment*	*Detection*
Amyloid β (8-17)	M0872	Mouse	1:100	Tris-EDTA pH 9	Alexa Fluor
Cox4i1	Ap22111a	Rabbit	1:200		HRP/TSA
Cpt1a	15184-1-AP	Rabbit	1:50		Alexa Fluor
Gfap	ab4674	Rabbit	1:2,000		Alexa Fluor
Got2	ab171739	Rabbit	1:2,000		Alexa Fluor
Mcu	HPA016480	Rabbit	1:200		HRP/TSA
NeuN-AF 488	ab190195	Rabbit	1:50		-
NeuN	MAB377	Mouse	1:100		Alexa Fluor
Nipsnap1	#13226	Rabbit	1:200		Alexa Fluor
Ociad2	HPA040979	Rabbit	1:500		HRP/TSA
Rmdn3	ab189845	Rabbit	1:2,000		Alexa Fluor
Sfxn5	ab172971	Rabbit	1:2,000		Alexa Fluor

Use of human samples was in accordance with institutional ethical guidelines and approved by the ethics committee of the University of Geneva (Switzerland). Written informed consent to use autopsy samples for research purposes were obtained for all samples with exceptions for autopsies that were performed more than 20 years ago. In all cases, no samples were used from patients that refused for being involved in research projects. Patient information are listed in Appendix 7.5. The data from human cerebellum is representative for one experiment; data from human cortex and spinal cord is representative for one experiment performed on at least three different cases.

3.2.14.3. Double labeling of mitochondrial markers via Zenon IgG kit

To perform double labeling of mitochondrial markers with antibodies raised in the same species, I used the Zenon™ Alexa Fluor™ 647 Rabbit IgG Labeling kit according to the manufacturer's instructions. Briefly, 1 µg rabbit anti-Sfxn5 antibody was linked to 10 µl component A and incubated for 5 minutes at room temperature. I added 10 µl of component B and waited further 10 minutes. After incubation of secondary antibody and extensive washing, sections were incubated with Zenon complex and Hoechst for two hours. The sections were washed three times with PBS for 5 minutes. Importantly, to stabilize staining for longer storage, I further incubated sections with 1:100 Acryloyl-X SE in PBS at 4°C for four hours and mounted them using Vectashield Mounting medium.

3.2.14.4. Amyloid-β plaques and Aβ deposition

To visualize amyloid-β plaques and Aβ deposition in APP23/PS45 animals, I used the Hoechst which superiorly detected the amyloid-β plaque– a feature previously reported for AD mouse models by Uchida and Takahashi (2008). I further confirmed Aβ detection using the antibody clones 4G8 and 6E10 conjugated to Alexa Fluor-647, which however penetrated less well in our staining conditions. For human tissue, I.W. used the amyloid-β (8-17) antibody (clone 6F/3D).

3.2.15. Confocal microscopy

We scanned tissue sections either on an upright FV1000 confocal microscopy system (Olympus) equipped with 4x/0.28, 10x/0.4, 20xO/0.85, 40xO/1.35 and 60xO/1.42 objectives or on an inverted FV3000 confocal microscopy system (Olympus) equipped with 4x/0.16, 20x/0.75 and 40x/0.95 objectives. Images were acquired using standard filter sets and intensity projections were generated using the open source software ImageJ/Fiji (Schindelin et al., 2012) and Adobe Photoshop.

3.2.16. Image processing and representation

For figure representation, we combined different channels of confocal image series in pseudo-color using the 'screen' function in Adobe Photoshop. We equally adjusted contrast and brightness in the entire image. In Appendix 7.3, I acquired immunofluorescence staining on Cre^- tissue and control (omission of primary antibody) with the same settings and adjusted images with the same processing parameters. In non-quantitative panels, I adjusted gamma non-linearly to enhance visibility of low-intensity objects. We assembled figures in Adobe Illustrator.

3.2.17. Protein retention expansion microscopy

I performed expansion microscopy on mouse cortical tissue sections as previously described (Tillberg et al., 2016). In brief, the cerebrum of Emx1:Cre$^+$/GFP-OMMxThy1:mito-RFP mice was fixed using 4% paraformaldehyde in PBS and sectioned in 100 µm thick, sagittal section using a vibratome. To enhance GFP-OMM signals, sections were stained against GFP as described before using 0.2% Triton X100 in PBS for permeabilization. Next, samples were cross-linked with 1:100 Acryloyl-X SE in PBS at 4°C for 6 hours and gelled with freshly prepared monomer solution at 37°C. Next, samples were digested with proteinase K (8 U/ml) in Digestion buffer at 37°C overnight. For expansion, I first incubated digested samples in PBS, then in distilled water. An expansion factor of ~2-3 fold was estimated from the sample. Data in Figure 11e is representative for n=2 independent experiments.

3.2.18. Electron microscopy

3.2.18.1. Sample preparation

Nicolas Snaidero (N.S.; Institute of Neuronal Cell Biology, TUM) and I performed sample preparation for electron microscopy. N.S. further cut samples, contrasted them and acquired images. I performed data analysis as blinded investigator.

Isolated mitochondria (as CMF or IC) were incubated in electron microscopy (EM) fixative for 10 minutes before being centrifuged and after supernatant removal, resuspended in 2% low melting point agarose. The agarose mitochondria pellets were then embedded for electron microscopy using 2% OsO_4 for four hours followed by ethanol/acetone dehydration and Epon embedding.

To analyze mitochondrial morphology in cerebellar cells in situ, I perfused 2- to 3-month-old animals with 5 mL HBSS with heparin (19.5 U/ml), followed by 30 mL EM fixative. The brain was extracted and further post-fixed in EM fixative at 4°C for 8 hours. N.S. dissected cerebella and sectioned them in thin slices, below 1 mm. Sections were further dissected in piece of two to three lobes and post-fixed with 2% OsO_4 and 1.5% ferrocyanide, dehydrated by ethanol/acetone and Epon embedded. Epon blocks were further trimmed and 50 nm thick sections (Leica UltraCut2) were obtained from the thickest part of the sample. The section were post stained with 4% uranyl acetate for 30 minutes followed by lead citrate for 5 minutes.

3.2.18.2. Data acquisition

For isolated mitochondria, N.S. acquired images approximately 20-50 µm away from the pellet edge with a JEM-1400 Transmission Electron Microscope using 20,000x magnification. Quantification for mitochondria morphology in cerebellum was done at 6,000x – 20,000x magnification.

3.2.18.3. Analysis

For data analysis, I was blinded for the genetic background of samples. The open source software ImageJ/Fiji (Schindelin et al., 2012) was used to define total mitochondrial perimeter and percent mitochondrial perimeter in ≤30 nm distance to the endoplasmic reticulum (ER). Contact frequency in percent is shown as box plot over cell numbers and over mitochondria per genetic background. In the case of granule cells, a larger number of cells had to be analyzed due to cellular morphology (see Figure 39b). Granule cell perikarya are densely packed in the granule cell layer with a small region of cytoplasm around the nucleus giving space to only 1-4 mitochondria per 50 nm section. Therefore, statistical analysis was performed on mitochondria as unit (see Figure 39c). For orientation, I color-coded electron micrographs in figures for organelle content: mitochondria, magenta; ER, light orange; contact sites, red.

3.2.19. Statistics

All data sets are shown as box plots consisting of median, box spanning quartile 1 to 3 (Q1-Q3) and whiskers to the maximum and minimum (max./min. value) as well as the underlying individual values. To see overlapping data points, individual points have an opacity of 30% (EM data: 10%). Values used throughout the text represent mean±s.e.m. and if used in Figures, are defined in the figure legend. Within the text, mass spectrometry data is represented as: "[…] two-tailed, unpaired *t*-test with permutation-adjusted q-value: PC *vs* A: *FC, q-value […]"and statistical significance of *P* ≤0.05 indicated with (*).

We tested data distribution for normality using the Shapiro-Wilk normality test to determine statistical tests. Exclusion of data points was only performed in oxygen consumption measurements for technical replicates, in which one of the multiple injections failed during the experiment; no other data points were excluded. The statistical details for each experiments can be found in the figure legend and further information (sample size, n of independent experiments, testing and *P* values) is provided in Appendix 7.7. A *P* ≤0.05 was considered statistically significant and indicated by (*); *P* ≤0.01 (**); *P* ≤0.001 (***). I performed statistical analyses using Microsoft Excel 2016 and GraphPad Prism software. No statistical methods were used to pre-determine sample sizes but the chosen sample sizes are similar to those reported in previous publications (e.g. Brill et al. (2016), Baughman et al. (2011), Pagliarini et al. (2008)). Samples were not randomized during data collection and animals assigned to experimental groups according to genotype. Randomization was not possible due to constraints in animal availability, and determination of experiment by given genotype. Data collection and analysis were performed blinded to the conditions in the following experiments: Figure 13b, 15b, 39c and 40c. In all other experiments, the experimenters were not blinded.

RESULTS

Chapter 4: Results

The experiments and conclusions of this section have been published as Fecher et al. (2019) in Nature Neuroscience and parts of this article were prior published as a preprint (Fecher et al., 2018). Similarities might arise to these manuscripts that are authored by Laura Trovò (L.T.), Thomas Misgeld (T.M.) and myself. In this chapter, content stated with '*I*' reflects my own opinion and work, while statements with '*We*' reflect the collaborative work product of the article Fecher et al. (2019) by L.T., T.M., myself and our collaborators.

4.1. Validation of the MitoTag mouse model

Recently the isolation and profiling of subcellular structures, such as ribosomes (Heiman et al., 2008; Doyle et al., 2008), mitochondria (Chen et al., 2016), nuclei (Roh et al., 2017) and lysosomes (Abu-Remaileh et al., 2017) enabled the analysis of compartmentalized transcriptomes, proteomes and metabolomes, as well as the cell type-specific analysis of transcriptomes and epigenomes (see Chapter 1.5). For example, the RiboTag mouse has provided us with a cell type-specific, in vivo tool to characterization actively translated mRNA from polysomes (Sanz et al., 2009); however, such an approach remained unavailable for mitochondria. We therefore generated in analogy MitoTag mice to enable cell type-defined mitochondrial research by probing functional organelles from their in situ context.

4.1.1. MitoTag mice enable tagging of cell type-specific mitochondria in vivo

In collaboration with Wolfgang Wurst's laboratory (Oskar Ortiz and Ralf Kühn; Institute of Developmental Genetics, Helmholtz Zentrum München), *Rosa26* knock-in mice were generated that harbor an expression cassette generated by Laura Trovò (Institute of Neuronal Cell Biology, TUM). This cassette (Figure 11a) contains a ubiquitous promoter – CAG – followed by a 'stop' sequence flanked with loxP sites and GFP localized to the outer mitochondrial membrane (GFP-OMM). We named this mouse line 'MitoTag' in the style of RiboTag mice and I crossed them to a variety of Cre-recombinase (Cre) diver lines to test faithful, cell type-specific expression. While I observed no GFP-OMM expression in 'stopped' mice (Figure 11b), robust GFP-OMM signals were detected in a cell type- and cell lineage-specific manner with a number of Cre lines (see Appendix 7.1).

For example, using the *empty spiracles homeobox 1* gene promoter – Emx1-IRES-Cre line (Emx1:Cre; Gorski et al., 2002) – GFP-OMM tagged mitochondria are present in olfactory bulb,

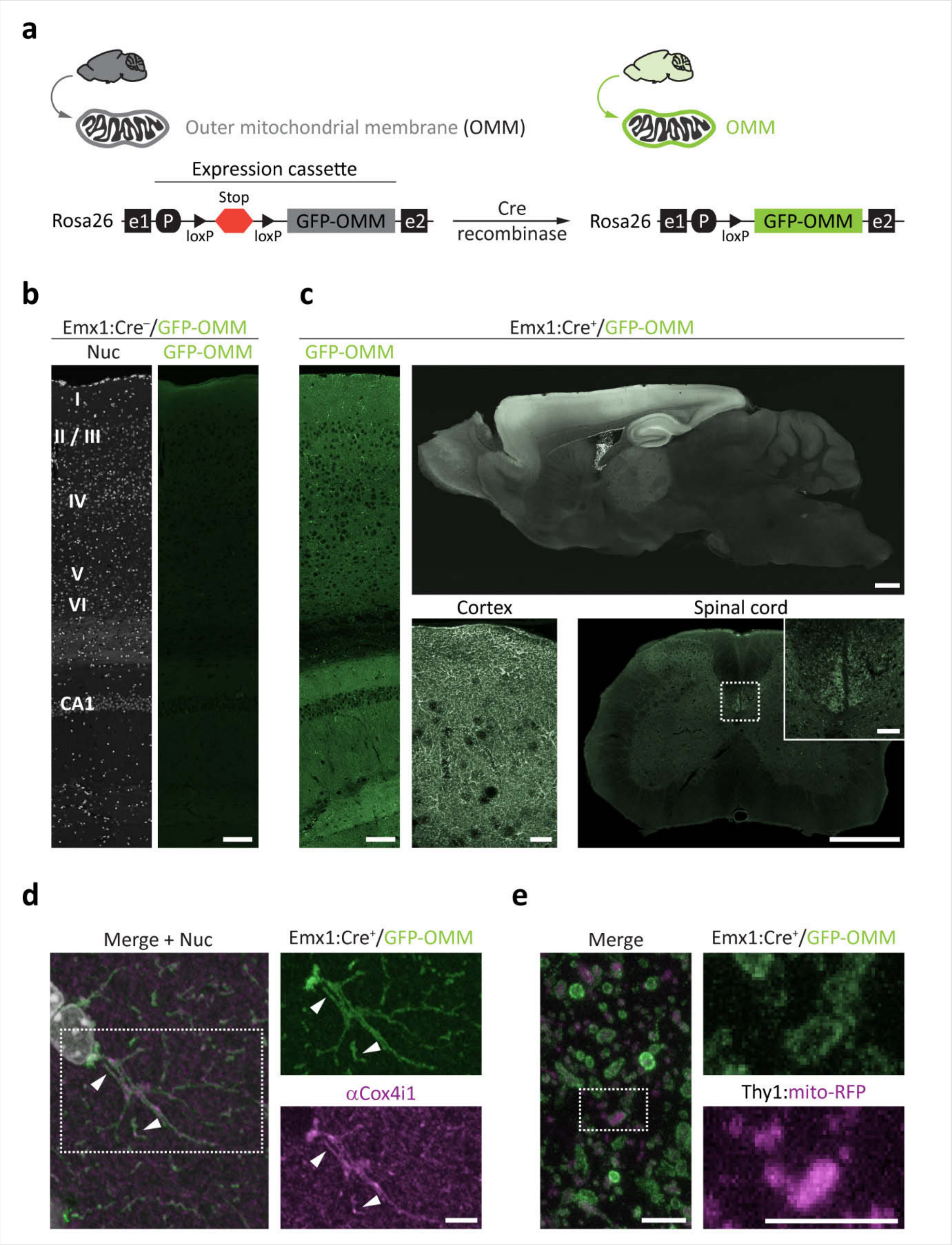
a
Outer mitochondrial membrane (OMM)
OMM
Expression cassette
Stop
Rosa26
e1
P
loxP
loxP
GFP-OMM
e2
Cre
recombinase
Rosa26
e1
P
loxP
GFP-OMM
e2
b
Emx1:Cre⁻/GFP-OMM
Nuc
GFP-OMM
I
II / III
IV
V
VI
CA1
c
Emx1:Cre⁺/GFP-OMM
GFP-OMM
Cortex
Spinal cord
d
Merge + Nuc
Emx1:Cre⁺/GFP-OMM
αCox4i1
e
Merge
Emx1:Cre⁺/GFP-OMM
Thy1:mito-RFP

Figure 11| MitoTag mice enable the cell type-specific expression of outer mitochondrial membrane targeted GFP (see next page for legend).

neocortex and hippocampus, as well as in the corticospinal tract (Figure 11c). As described by Gorski et al. (2002), DNA recombination at loxP sites takes place in astrocytes and excitatory neurons. I further confirmed mitochondrial localization of GFP-OMM in Emx1:Cre$^+$/GFP-OMM cortex by immunofluorescence staining of the endogenous protein cytochrome c oxidase subunit 4 isoform 1 (Cox4i1; Figure 11d). This nuclear encoded protein is localized to the mitochondrial inner membrane, where it contributes to cytochrome c oxidase of the electron transport chain. Using confocal microscopy, I detected substantial overlap of Cox4i1 with GFP-OMM. Interestingly, in some cases GFP-OMM signals enclosed Cox4i1 puncta as one would predict from their localization in outer and inner mitochondrial membrane. However, due to the diffraction limit of light, confocal microscopy cannot resolve objects below a XY resolution of 180 – 250 nm (Schermelleh et al., 2010). I therefore used expansion microscopy, a super-resolution microscopy technique, to further address GFP-OMM localization in mitochondria. In expansion microscopy, proteins are cross-linked to an expandable matrix. Upon trypsin digestion of the tissue, the matrix isotropically expands in water creating a magnified version of the specimen. Trypsin cleaves peptides after lysine and arginine; however, beta barrel structures – as present in fluorescence proteins – are protected from cleavage and therefore can be imaged after digest. I compared GFP-OMM localization to a mitochondrial matrix localized red fluorescent protein (mito-RFP) in mouse cortex. For this, Emx1:Cre$^+$/GFP-OMM mice were crossed to Thy1:mito-RFP mice, in which the majority of neurons express the transgene (Breckwoldt et al., 2014). Hence, I observed the presence of both transgenes in most excitatory neurons in cortex. I confirmed spatial separation of the transgenes using expansion microscopy with GFP-OMM surrounding bright mito-RFP signals (Figure 11e).

Figure 11 | MitoTag mice enable the cell type-specific expression of outer mitochondrial membrane targeted GFP. (**a**) Genetic *Rosa26* locus describing the expression cassette of MitoTag mice. Upon Cre recombinase mediated excision of the loxP site flanked 'stop' element, GFP-OMM is expressed. e1/e2, exon 1 and 2; P, promoter. (**b**) In Cre$^-$/GFP-OMM no GFP fluorescence is detected. Shown is mouse cortex with layer I to VI and CA1 region of the hippocampus. Nuc, nuclear counter stain. Scale bar: 100 μm. (**c**) In Emx1:Cre$^+$/GFP-OMM, GFP-OMM signals are observed in cortex and hippocampus (same orientation as in b), and in corticospinal projections of the spinal cord (detail). Scale bars: 100 μm (cortex/hippocampus orientation); 1 mm (brain overview); 50 μm (cortex, spinal cord detail); 500 μm (spinal cord). (**d**) Confocal image of Emx1:Cre$^+$/GFP-OMM cortex immunostained for Cox4i1 and GFP. Scale bar: 5 μm. (**e**) Confocal image after expansion microscopy of Emx1:Cre$^+$/GFP-OMMxThy1:mito-RFP cortex. GFP signals were enhanced with anti-GFP staining prior to digestion. Expansion is estimated to be 2-3 fold. Scale bar: 5 μm. Modified from Fecher et al. (2019), Figure 1 and Supplementary Figure 1.

4.1.2. GFP-OMM expression does not alter mitochondrial or cellular physiology

Because GFP-OMM is an artificially introduced protein, we asked if its presence in the outer mitochondrial membrane interferes with mitochondrial or cellular health. The Misgeld laboratory has generated a number of transgenic mouse lines, which express mitochondrial targeted fluorescent proteins or biosensors in neurons via elements of the Thy1.2 promoter (Vidal et al., 1990; Caroni, 1997). For the validation of these lines, neuronal and mitochondrial health is regularly analyzed in motor neurons, and axonal transport rates have been proven to be sensitive measurements for transgene effects (Misgeld et al., 2007; Marinkovic et al., 2012; Breckwoldt et al., 2014). For this assay, we crossed ChAT:Cre$^+$/GFP-OMM mice with the Thy1:mito-RFP line to avoid phototoxicity during widefield imaging, because I observed weaker GFP signals with the OMM localization than with a matrix localized GFP (ChAT:Cre$^+$/mito-GFP). Laura Trovò (L.T.; Institute of Neuronal Cell Biology, TUM) performed time-lapse, widefield imaging of mitochondrial transport in a nerve-muscle explants of the thin triangularis sterni muscle, which is localized at the thorax inside. Once the thorax is flattened and kept in physiological state, superficial axons of the intercostal nerve are accessible. L.T. quantified normal mitochondrial transport rates of 4.2±0.3 *vs* 4.1±0.2 organelles per minute in anterograde direction and 2.5±0.3 *vs* 2.9±0.2 organelles per minute in retrograde direction (mean±s.e.m.; ChAT:Cre$^-$ *vs* ChAT:Cre$^+$; Figure 12a). Statistical testing indicated no difference between groups. From these images, L.T. determined the length and width of mitochondria with no statistical difference between groups (length: 23.0±0.7 *vs* 22.4±0.6 μm; width: 3.3±0.1 *vs* 3.2±0.05 μm; Figure 12b). Next, L.T. analyzed synaptic size and receptor density at the neuromuscular junction (NMJ; Figure 12c). α-bungarotoxin binds to the nicotinic acetylcholine receptor (AChR) at the postsynaptic site of the NMJ and is used to define NMJ area and receptor density. Again, neither synapse size nor AChR density were changed between groups (size: 396±16 *vs* 418±16 μm^2; receptor density: 937±37 *vs* 883±52 AU; Figure 12d). This indicated that GFP-OMM expression in motor neurons is not interfering with mitochondrial function and synaptic physiology as tested by our assays. However, we further questioned whether other neural cells might handle transgene expression differently. We therefore tested a basic mitochondrial function – oxidative phosphorylation – in Emx1:Cre$^+$/GFP-OMM mice. For this experiment, I isolated mitochondria from cortex of Emx1:Cre$^-$/GFP-OMM and Emx1:Cre$^+$/GFP-OMM mice via differential centrifugation and obtained the crude mitochondrial fraction (CMF; Figure 13a). These

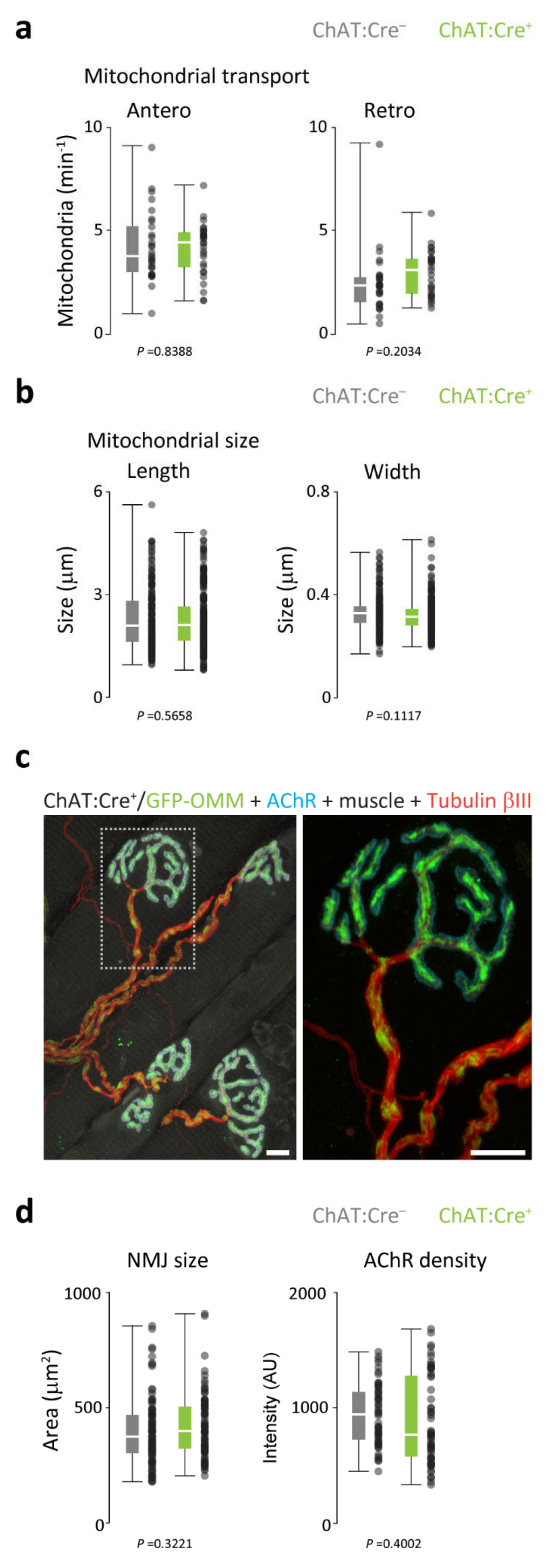

Figure 12| Axonal transport, mitochondrial shape and NMJ area are normal in ChAT:Cre$^+$/GFP-OMM mice. (**a**) Antero- and retrograde mitochondrial transport quantified in the intercostal nerve of the triangularis sterni muscle. Mitochondria are time-lapse imaged via Thy1:mito-RFP in ChAT:Cre$^-$/GFP-OMM or ChAT:Cre$^+$/ GFP-OMM mice using an ex vivo nerve-muscle explant. n≥29 axons from five mice. (**b**) Mitochondrial length and width quantified from data generated in a. n≥170 mitochondria from five mice. (**c**) Confocal image of ChAT:Cre$^+$/GFP-OMM triangularis sterni muscle immunostained for neuron-specific tubulin βIII (red) and for the acetylcholine receptor (AChR) via α-bungarotoxin (blue). Muscle signals are background from AChR channel and reduced in detail by gamma adjustment. Scale bars: 10 µm. (**d**) Quantification of NMJ size and AChR density via α-bungarotoxin staining from samples in a. n≥83 for NMJ size; n≥54 for AChR density from five mice. Box plot: median, quartile 1-3 and whisker from min./max. value, and individual data points; *P* values from statistical testing are shown. Modified from Fecher et al. (2019), Supplementary Figure 2.

mitochondrial preparations were further tested in oxygen consumption assays by L.T. in collaboration with Fabiana Perocchi's laboratory (Gene Center, LMU). Mitochondria respired normal under either pyruvate+malate (complex I; Figure 13b) or succinate+rotenone (complex II; Figure 13c). Interestingly, under pyruvate+malate ADP-stimulated oxygen consumption

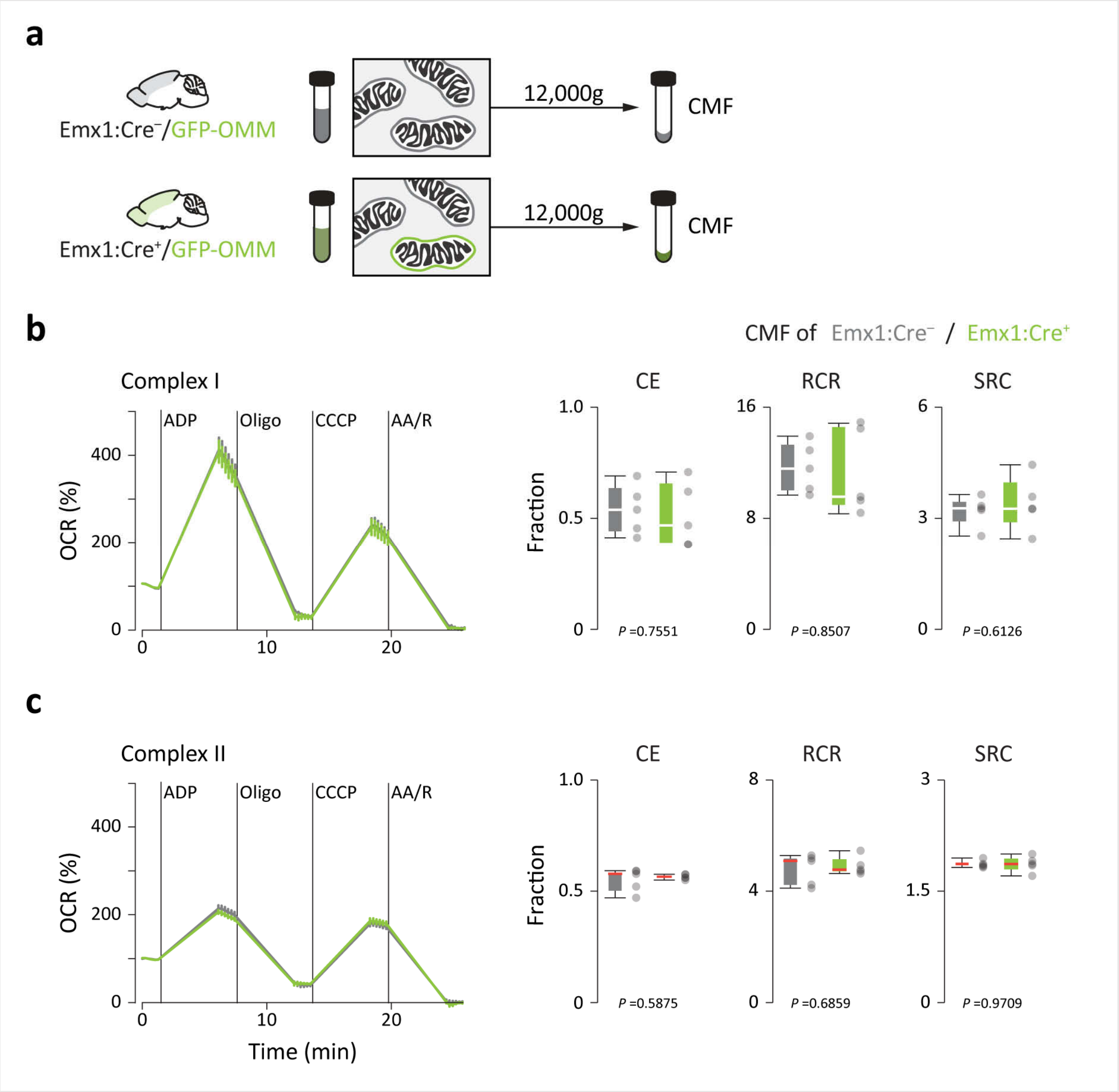

Figure 13| Mitochondrial respiration is normal in GFP-OMM tagged mitochondria from cortex. (**a**) Isolation of mitochondria via differential centrifugation from the cortex of Emx1:Cre$^-$/GFP-OMM and Emx1:Cre$^+$/GFP-OMM mice. CMF, crude mitochondrial fraction. (**b**, **c**) Oxygen consumption rate (OCR) as percentage of basal respiration with indicated injections, and calculated parameters: coupling efficiency (CE), respiratory control ratio (RCR) and spare respiratory capacity (SRC). Left side: representative data from one experiment; right side: n=5 mice from three independent experiments. Mitochondrial respiration was probed using (**b**) pyruvate+malate (complex I) and (**c**) succinate+rotenone (complex II) as substrates. Line graph: mean±s.e.m.; box plot: median, quartile 1-3, whisker from min./max. value, and individual data points; *P* values from statistical testing are shown. Modified from Fecher et al. (2019), Supplementary Figure 2.

rates (state 3) approximately doubled compared with state 3 under succinate+rotenone, while uncoupled respirations rates (state 3u) were comparable (Figure 13b and 13c – left side, OCR line graphs normalized to basal respiration). These differences can be explained by a differential net proton force pumped per mole of pyruvate+malate and succinate+rotenone (see calculation by Mookerjee et al. (2017) and Chapter 1.2.1). L.T. calculated coupling efficiency (CE), respiratory control ratio (RCR) and spare respiration capacity (SRC) to compare genetic groups, and none of the parameters were significantly changed. While the CMF of Emx1:Cre^{+}/GFP-OMM cortex contains a mixture of tagged and untagged mitochondria, I confirmed by flow cytometry that 74±5% of mitochondria (gated as Tom22^{+} events) are GFP-OMM positive. Hence, GFP-OMM tagged mitochondria represent a significant population in the analyzed tissue and any effect of transgene expression would have been detected in oxygen consumption assays, if present.

We concluded from these experiments that GFP-OMM tagged mitochondria are functional in terms of their transport rates in neurons and their respiratory activity. Furthermore, neuronal health is normal as analyzed at the NMJ. Thus, any differences observed among cell type-specific mitochondrial populations should arise from their biological diversity and not from an effect of our MitoTag model.

4.1.3. Intact mitochondria are captured via GFP-OMM

The cell type-specific expression of a mitochondrial localized fluorescent protein is not novel – in fact, Jeremy Nathans (Johns Hopkins University) donated a *Rosa26* CAG-stop-mito-GFP mouse line to the JAX repository a decade ago (Agarwal et al., 2017). However, the major difference between existing ‘mito lines’ and our MitoTag line is the localization of the tag: in previous mouse models, the tag is localized to the mitochondrial matrix and inaccessible for isolation via immunoprecipitation, while in the MitoTag line the tag is accessible on the outer mitochondrial membrane. Although it might be argued for the first case that mitochondria could be isolated via fluorescence activated cell sorting, Laura Trovò (Institute of Neuronal Cell Biology, TUM) initially performed such experiments and was unsuccessfully in isolating healthy mitochondria. Only recently, MacDonald et al. (2019) reported a costume-made nanoscale flow cytometry-based method that achieves the isolation of intact mitochondria, termed fluorescence-activated mitochondria sorting (FAMS). Thus, our model allows the visualization of cell type-specific mitochondria, but also provides a ‘handle’ for these organelles. I therefore tested different approaches to immunoprecipitate GFP-OMM tagged mitochondria while preserving their integrity and function.

Initial experiments included standard immunoprecipitation protocols using: (i) agarose beads or magnetic beads; (ii) different buffer systems to keep mitochondria healthy and intact; and (iii) different antibodies against GFP. I tested these conditions in a mitochondrial mixing experiment with the starting material consisting of GFP-OMM tissue and mito-RFP tissue in a ~1:1 ratio. Conditions were evaluated via western blot analysis probing for GFP-OMM and mito-RFP content with the goal of GFP-OMM enrichment and mito-RFP depletion. To my surprise, none of the initially tested conditions could deplete mito-RFP (data not shown). While I enriched mitochondria with GFP antibodies from the tissue lysate, tagged mitochondria always co-purified with a significant amount of mito-RFP mitochondria. This outcome indicated a clumping of mitochondria and/or the formation of intermediate fusion events (Meeusen et al., 2004). While OMM fusion cannot be complete under the isolation conditions (Brandt et al., 2016), OMM attachment through close proximity of mitochondria, e.g. via centrifugation or transient association on beads (data not shown), could lead to co-purification of mitochondria. Consequently, I optimized the purification protocol to prevent mitochondria attachment via proximity. To this end, two modifications were made that significantly improved the isolation process that we termed immunocapture (IC):

(1) Starting material for immunocapture:

    While a fast separation of mitochondria from cytosol and other organelles might be favored for mitochondrial purification, the generation of a mitochondrial pellet via high-speed centrifugation impairs organelle separation. Therefore, the post-nuclear lysate was used for immunocapture and further diluted to a concentration of ≤2 mg tissue per ml buffer during bead incubation.

(2) Immunocapture via paramagnetic microbeads:

    Standard agarose or magnetic beads have a diameter of 150 – 40 μm and 4 – 1 μm, respectively; and trap simultaneously multiple mitochondria on their surface. This facilitates attachment of neighboring mitochondria. In contrast, the used microbeads have a diameter of 50 nm and accumulate on the mitochondrial surface via epitope-antibody binding. Several beads are necessary to trap a mitochondrion in the magnetic field and allow for its purification.

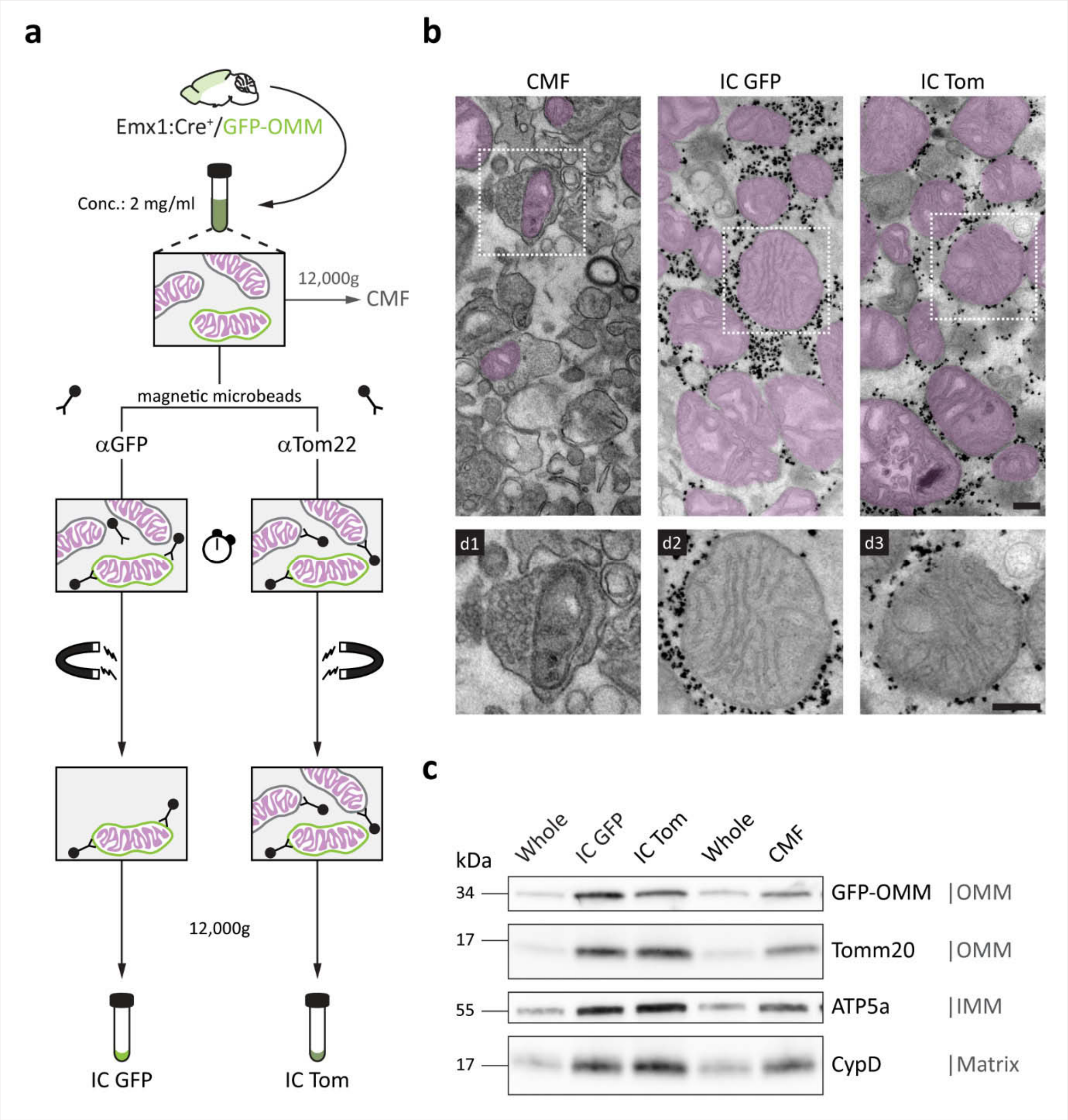
a
Emx1:Cre+/GFP-OMM
Conc.: 2 mg/ml
12,000g
CMF
magnetic microbeads
αGFP
αTom22
12,000g
IC GFP
IC Tom
b
CMF
IC GFP
IC Tom
d1
d2
d3
c
kDa
Whole
IC GFP
IC Tom
Whole
CMF
34
17
55
17
GFP-OMM
|OMM
Tomm20
|OMM
ATP5a
|IMM
CypD
|Matrix

Figure 14| Immunocapture enriches mitochondria. (**a**) Mitochondria are enriched via the optimized immunocapture (IC) protocol starting with the post-nuclear tissue lysate (conc. 2 mg/ml). Mitochondria can be isolated via centrifugation (12,000 g; CMF) and IC against GFP or Tom22. Following microbeads incubation, mitochondria are separated on a magnetic stand and the final elution pelleted by centrifugation. (**b**) Electron micrographs of isolated mitochondria from Emx1:Cre$^+$/GFP-OMM cortex using centrifugation or immunocapture. Mitochondria are highlighted in magenta. Details 1-3 below. Scale bars: 250 nm. (**c**) Western blot analysis of mitochondrial preparation probing for different mitochondrial compartments and GFP-OMM. Whole, whole tissue lysate; CMF, crude mitochondrial fraction; OMM, outer mitochondrial membrane; IMM, inner mitochondrial membrane; Tomm20, mitochondrial import receptor subunit TOM20 homolog; ATP5a, ATP synthase subunit alpha; CypD, cyclophilin D; kDa, molecular weight in kilo Dalton. Modified from Fecher et al. (2019), Figure 1 and Supplementary Figure 3.

Magnetic microbeads cross-linked with anti-Tom22 antibody were previously used by Franko et al. (2013) to isolate mitochondria from tissue. Mitochondrial import receptor subunit TOM22 homolog (Tom22) is a ubiquitously expressed outer mitochondrial membrane protein and part of the protein import machinery. In this report, the authors used 5-10 mg tissue per ml buffer to incubate microbeads with mitochondria and separated them via a magnetic column. I used these conditions with magnetic microbeads cross-linked to anti-GFP antibody and observed significant mito-RFP contamination. Therefore, I tested different tissue-to-buffer ratios and achieved mito-RFP depletion at a concentration of 2 mg tissue per ml buffer and below.

To demonstrate mitochondrial enrichment with immunocapture, I used Emx1:Cre$^+$/GFP-OMM cortex, generated the post-nuclear tissue lysate and purified mitochondria using differential centrifugation, immunocapture with Tom22 as bait (IC Tom) and with GFP-OMM as bait (IC GFP; Figure 14a). In collaboration with Nicolas Snaidero (N.S.; Institute of Neuronal Cell Biology, TUM), I prepared these samples for electron microscopy and N.S. performed image acquisition. In the crude mitochondrial fraction (CMF), I observed that mitochondria were frequently enclosed in membranes, presumably synaptosomes (Figure 14b, d1) and that the majority of objects could not be identified as mitochondria. In contrast, the majority of objects in IC Tom and IC GFP were free mitochondria. Furthermore, mitochondrial cristae structure was well preserved after immunocapture (Figure 14b, d2 and d3). Next, I evaluated mitochondrial enrichment between CMF and immunocapture by western blot analysis (Figure 14c). Compared to the whole tissue lysate, all conditions enriched the probed mitochondrial proteins localized to OMM, inner mitochondrial membrane (IMM) and matrix. However, immunocaptures enriched these proteins more than CMF. GFP-OMM was only slightly higher enriched in IC GFP compared with IC Tom because the majority of mitochondria are GFP-OMM tagged in the tissue lysate (Emx1:Cre$^+$/GFP-OMM: 74±5%).

To validate that immunocaptured mitochondria are functional, we tested isolated organelles in oxygen consumption assays. I enriched mitochondria with the described protocol from either Emx1:Cre$^-$/GFP-OMM cortex using IC Tom or Emx1:Cre$^+$/GFP-OMM cortex using IC Tom and IC GFP (Figure 15a), and Laura Trovò (Institute of Neuronal Cell Biology, TUM) performed oxygen consumption assays. While we observed a higher degree of variability among the immunocapture samples than the CMF samples, no significant difference was detected among groups using pyruvate+malate or succinate+rotenone as substrate (Figure 15b).

This confirmed that immunocaptured mitochondria via GFP-OMM and Tom22 are intact (Figure 14b and c) and functionally indistinguishable between Emx1:Cre$^-$/GFP-OMM and Emx1:Cre$^+$/GFP-OMM tissue (Figure 15b).

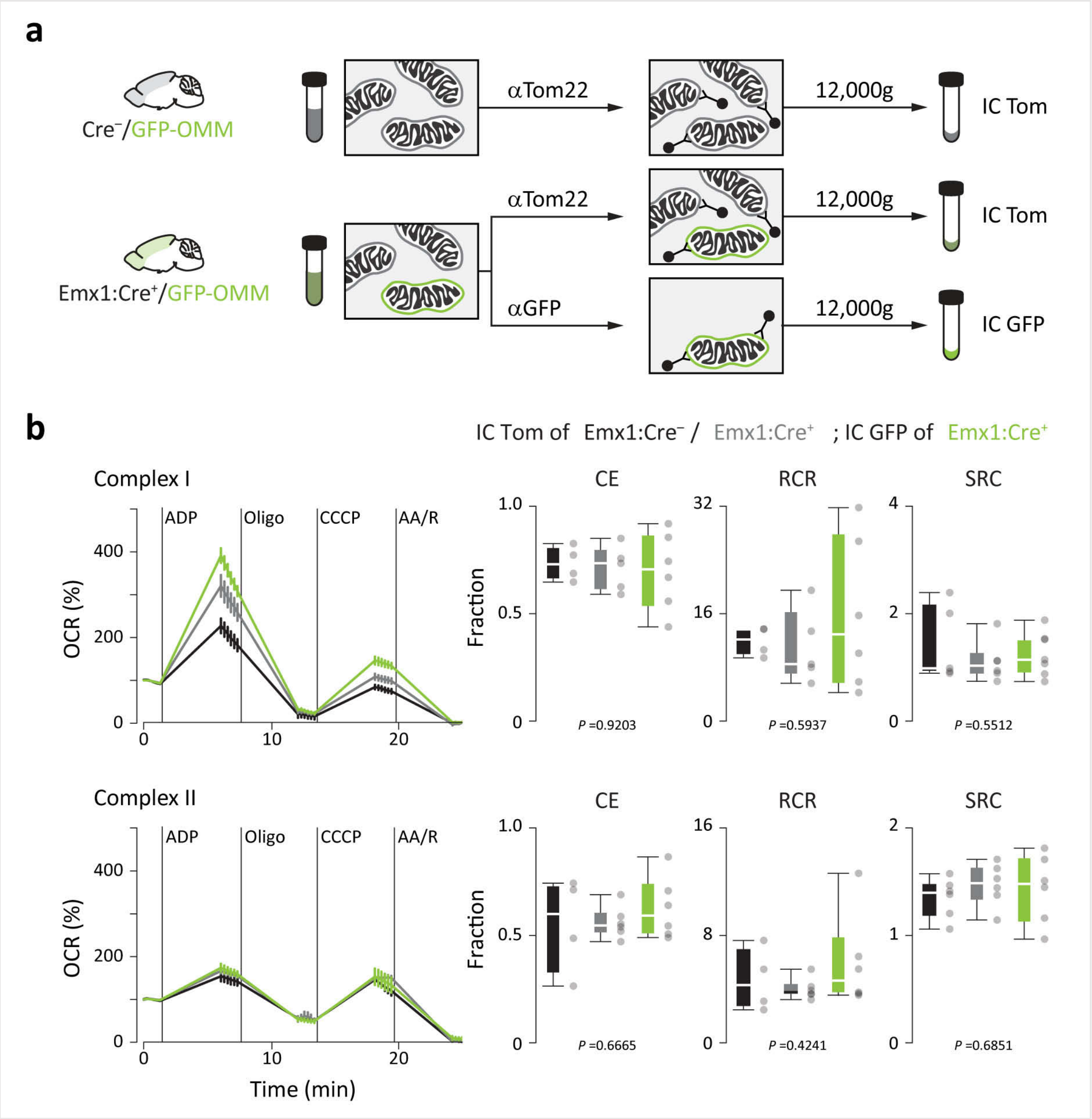

Figure 15| Mitochondrial respiration is unaltered between GFP-OMM tagged and untagged organelles after immunocapture. (**a**) Isolation of mitochondria via immunocapture from Emx1:Cre$^-$/GFP-OMM cortex and Emx1:Cre$^+$/GFP-OMM cortex. (**b**) Oxygen consumption rate (OCR) as percentage of basal respiration with indicated injections and calculated parameters: coupling efficiency (CE), respiratory control ratio (RCR) and spare respiratory capacity (SRC). Left side: representative data from one experiment; right side: n≥4 mice from three to four independent experiments. Mitochondrial respiration was probed using pyruvate+malate (complex I; upper graph) and succinate+rotenone (complex II; lower graph) as substrates. Line graph: mean±s.e.m.; box plot: median, quartile 1-3, whisker from min./max. value, and individual data points; *P* values from statistical testing are shown. Modified from Fecher et al. (2019), Figure 1.

4.1.4. Immunocapture separates cell type-specific mitochondria from complex tissue

With the immunocapture protocol at hand, I further ask what the remaining level of untagged mitochondria is. For this, I used the introduced mitochondrial mixing experiment with a starting lysate containing Emx1:Cre$^+$/GFP-OMM cortex and Thy1:mito-RFP cortex in a ~1:1 tissue mix (Figure 16a). This generated an initial ratio of approximately 54% GFP-OMM to 46% mito-RFP tagged mitochondria as determined by flow cytometry (Figure 16b) and by excluding non-fluorescent mitochondria. Using 20 mg tissue lysate as input, I purified mitochondria and analyzed them by western blot analysis probing for GFP-OMM and mito-RFP as well as endogenous mitochondrial proteins localized to OMM, IMM and matrix. With IC Tom, I recovered similar GFP-OMM to mito-RFP ratios as with the CMF, which represents the initial ratio of mitochondria (Figure 16c). When using microbeads cross-linked with anti-CD4 antibody as negative control, no mitochondria were purified. Only IC GFP enriched GFP-OMM tagged mitochondria and reduced mito-RFP signals. No mitochondria could be isolated with IC GFP from a pure mito-RFP lysate or wild type lysate. I observed with IC GFP an enrichment of 4.6±0.38-fold for GFP-OMM and a reduction to 0.2±0.07-fold for mito-RFP compared to CMF, while IC Tom recovered 0.98±0.14-fold GFP-OMM and 0.79±0.18-fold mito-RFP (Figure 16d). GFP-OMM enrichment and mito-RFP reduction were significantly changed between IC Tom and IC GFP (one-tailed, ratio-paired *t*-test: GFP-OMM, *P*=0.002; mito-RFP, *P*=0.0368; n=5 experiments).

From this result, we further asked if small populations of GFP-OMM tagged mitochondria, i.e. from rare cell types, can be purified as efficiently as big populations. To test this hypothesis, I modified the mitochondrial mixing experiment by creating different GFP-OMM to mito-RFP ratios ranging from 100% to 5% GFP-OMM content (Figure 17a). While in Figure 16a similar amounts of tissue were mixed prior to lysate generation, the mixing in this experiment is performed with post-nuclear lysate. Using western blot analysis (Figure 17b), I observed with IC GFP in the presence of GFP-OMM tagged mitochondria (content of 100% to 5% GFP-OMM) an average enrichment of 5.1±0.21-fold for GFP-OMM and an average reduction to 0.03±0.03-fold for mito-RFP compared to the 50:50 CMF condition (Figure 17c). Statistical testing provided no evidence for a significant difference among these conditions in either GFP-OMM enrichment or mito-RFP reduction (one-way Friedman test with post hoc testing: GFP-OMM, *P*=0.0720; mito-RFP, *P*=0.1211; n=4 experiments). However, total protein amounts

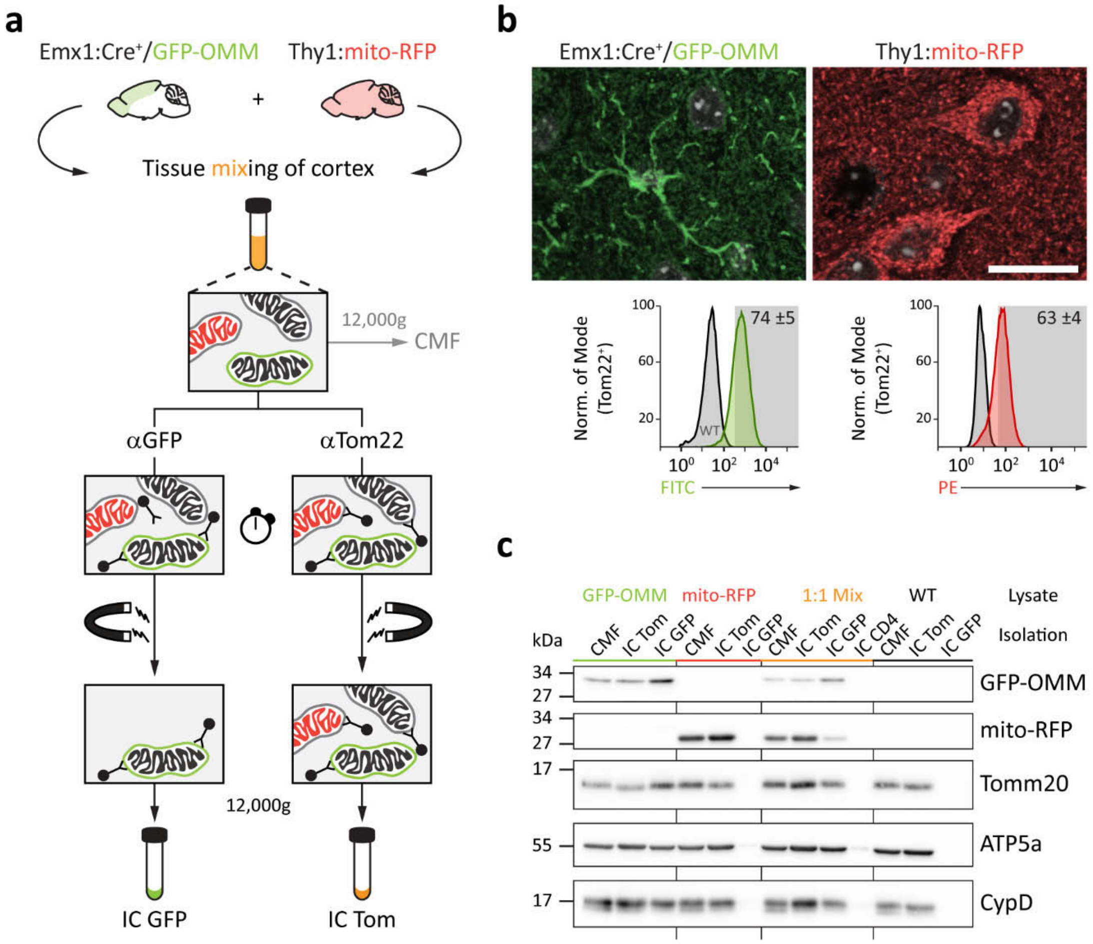
a
Emx1:Cre+/GFP-OMM
+
Thy1:mito-RFP
Tissue mixing of cortex
12,000g
CMF
αGFP
αTom22
12,000g
IC GFP
IC Tom
b
Emx1:Cre+/GFP-OMM
Thy1:mito-RFP
Norm. of Mode (Tom22+)
100
60
20
74 ±5
WT
10^0
10^2
10^4
FITC
63 ±4
PE
c
GFP-OMM
mito-RFP
1:1 Mix
WT
Lysate
Isolation
kDa
CMF
IC Tom
IC GFP
IC CD4
34
27
17
55
GFP-OMM
mito-RFP
Tomm20
ATP5a
CypD

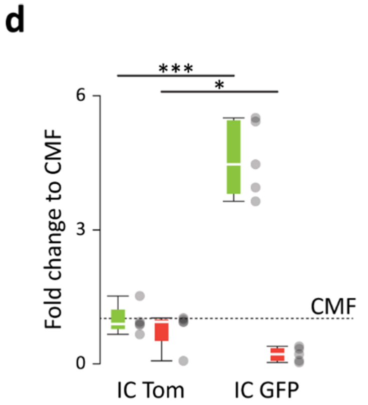

Figure 16| Immunocapture enriches GFP-OMM tagged mitochondria and separates them from other mitochondria. (**a**) Immunocapture workflow starting with the mixed tissue lysate and depicting the possible isolation via centrifugation (CMF) and IC against GFP-OMM or Tom22. (**b**) Confocal images of Emx1:Cre$^+$/GFP-OMM cortex and Thy1:mito-RFP cortex and histograms of flow cytometry experiments showing the percentage of labeled mitochondria in cortex samples. Mitochondria are gated according to Tom22-APC. The mean±s.e.m. for n=5 mice is indicated. Nuclei are visualized by nuclear counter stain. FITC, GFP-OMM channel; PE, mito-RFP channel. Scale bar: 20 μm. (**c**) Western blot analysis of mitochondrial isolations using different starting lysates (GFP-OMM, mito-RFP, 1:1 Mix and wild type) and isolation conditions (CMF, IC Tom, IC GFP and IC CD4). The blot is probed for GFP-OMM, mito-RFP and different mitochondrial compartments: OMM, Tomm20; IMM, ATP5a; matrix, CypD; kDa, molecular weight in kilo Dalton. (**d**) Quantification of the 1:1 Mix condition shown as fold change to CMF and normalized to total protein amount and mitochondrial content. Box plot: median, quartile 1-3, whisker from min./max. value, and individual data points; n=5 experiments quantified as technical triplicates; statistical testing is indicated. Modified from Fecher et al. (2019), Figure 2 and Supplementary Figure 4.

from IC GFP-recovered mitochondria were depended on GFP-OMM abundance in the lysate and proportionally decreased among the conditions.

In summary, small populations of GFP-OMM tagged mitochondria can be purified as efficiently as big populations using the immunocapture protocol. However, for small populations an upscaling of column numbers and animals might be necessary dependent on the downstream application of isolated mitochondria.

Finally, we asked if the observed separation efficiency of our protocol is altered in vivo where mitochondrial populations are directly present in neighboring cells. To test this hypothesis, I crossed Gfap:Cre$^+$/GFP-OMM mice to the Thy1:mito-RFP line and generated animals that have GFP-OMM tagged mitochondria in astrocytes and mito-RFP labeled mitochondria in neurons (Figure 18a). In cortex from these mice, approximately 29% of mitochondria are GFP-OMM tagged, while mito-RFP is present in 63% of organelles. When excluding unlabeled mitochondria from the calculation, this creates a ratio of 32% GFP-OMM to 68% mito-RFP mitochondria in the post-nuclear tissue lysate. Using western blot analysis, I observed with IC GFP an enrichment of 6.7±1.7-fold for GFP-OMM and a reduction to 0.8±0.13-fold of mito-RFP compared to CMF, while IC Tom recovered 0.91±0.1-fold GFP-OMM and 1.24±0.16-fold mito-RFP (Figure 18b). GFP-OMM enrichment was significantly changes between IC Tom and IC GFP (one-tailed, ratio-paired *t*-test: GFP-OMM, *P*=0.0002; mito-RFP, *P*=0.0677; n=5 experiments). In contrast to the previous experiments, I observed no significant reduction of mito-RFP in the one-tissue mixing experiment. Furthermore, IC Tom enriched mito-RFP compared with CMF. In Thy1:mito-RFP mice, the transgene is highly abundant and likely not fully imported into mitochondria due to expression levels. This would leave a small amount of

Figure 17│ Immunocapture performance persists even for small populations of GFP-OMM tagged mitochondria. (**a**) Immunocapture workflow starting with the mixing of tissue lysate from Emx1:Cre$^+$/GFP-OMM cortex and Thy1:mito-RFP cortex (confocal images) in descending ratios from 100% to 0% GFP-OMM lysate. Mitochondria are isolated by centrifugation (CMF) and IC against GFP-OMM or Tom22. In confocal images, nuclei are visualized by nuclear counter stain. Scale bar: 20 µm. (**b**) Representative western blot from quantification probed for GFP-OMM and mito-RFP as well as mitochondrial proteins localized to OMM, IMM and matrix. Note that due to protein amount limitation different amounts of total protein are probed (see mitochondrial markers for IC GFP of 25-0%). To visualized mito-RFP contamination, the second mito-RFP blot lane has been adjusted to saturation. kDa, molecular weight in kilo Dalton. (**c**) Quantification of GFP-OMM (upper graph) and mito-RFP (lower graph) in the different conditions shown as fold change to CMF 50:50 and normalized to total protein amount and mitochondrial content. Box plot: median, quartile 1-3, whisker from min./max. value, and individual data points; n=5 mice quantified as technical triplicates; *P* values from statistical testing are shown. Modified from Fecher et al. (2019), Supplementary Figure 5.

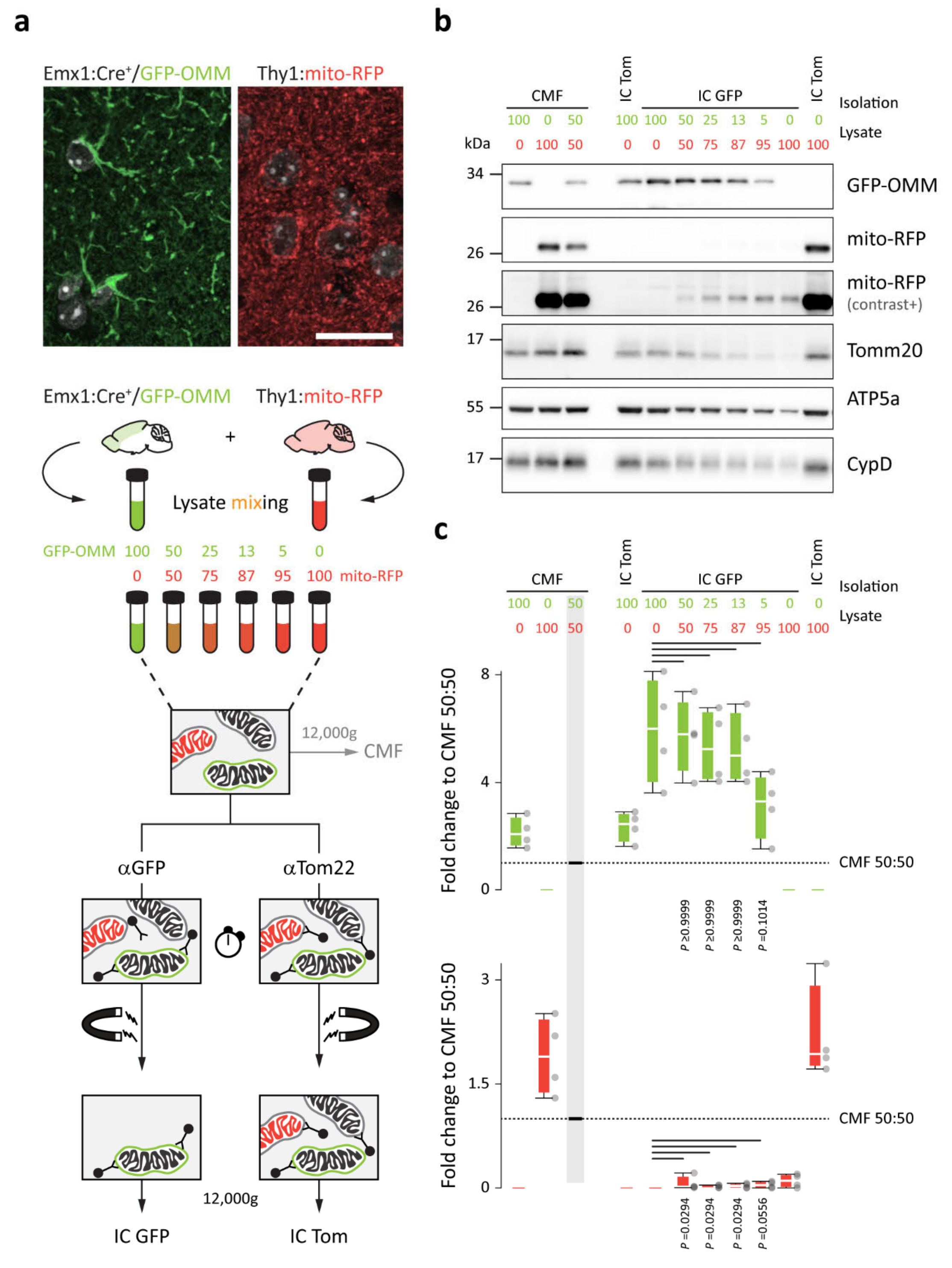

Figure 17│ Immunocapture performance persists even for small populations of GFP-OMM tagged mitochondria (see previous page for legend).

mito-RFP precursor protein in the cytosol, where it could be attached and/or imported to other mitochondria during the incubation period of ~60 minutes. In this experiment, the CMF was generated immediately after starting the microbeads incubation, i.e. approximately 90 minutes earlier than IC Tom, giving a possible explanation for this result. Still, in this experiment the mitochondrial content of IC GFP is massively changed compared to IC Tom. Thus, this experiment confirms that the immunocapture enriches GFP-OMM tagged mitochondria from complex tissue. However, the level of contamination from other mitochondrial populations needs to be carefully evaluated for the tissue of interest and the downstream application. A source of contamination might be abundant mitochondrial proteins (like mito-RFP in our experiment), which cross-contaminate during the immunocapture; however, these proteins are likely non-specific for cell types.

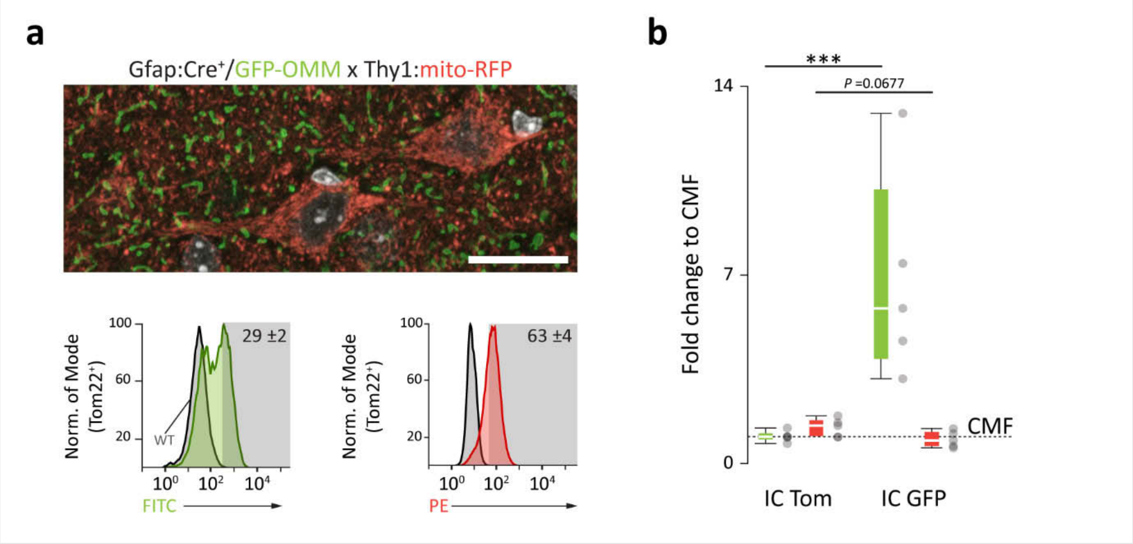

Figure 18│ Immunocapture separates directly adjacent mitochondrial populations from one tissue. (**a**) Confocal image of Gfap:Cre$^+$/GFP-OMMxThy1:mito-RFP cortex and histograms of flow cytometry experiments determining the percentage of labeled mitochondria in this crossing. Mitochondria are gated according to Tom22-APC. The mean±s.e.m. for n≥4 mice is indicated. Nuclei are visualized by nuclear counter stain. FITC, GFP-OMM channel; PE, mito-RFP channel. Scale bar: 20 µm. (**b**) Quantification from western blot analysis of immunocaptures from Gfap:Cre$^+$/GFP-OMMxThy1:mito-RFP cortex shown as fold change to CMF and normalized to total protein amount and mitochondrial content. Box plot: median, quartile 1-3, whisker from min./max. value, and individual data points; n=5 experiments quantified as technical triplicates; statistical testing is indicated. Modified from Fecher et al. (2019), Figure 2 and Supplementary Figure 4.

The results of Chapter 4.1 demonstrated that cell type-specific mitochondria can be tagged via the MitoTag mouse model and that this mitochondrial population can be enriched from a mixture with non-tagged mitochondria. This is possible even if the tagged population of mitochondria represents 13% or less. Additionally, mitochondria do not fuse during immunocapture; nonetheless, a small amount of contaminating, untagged mitochondria is to be expected.

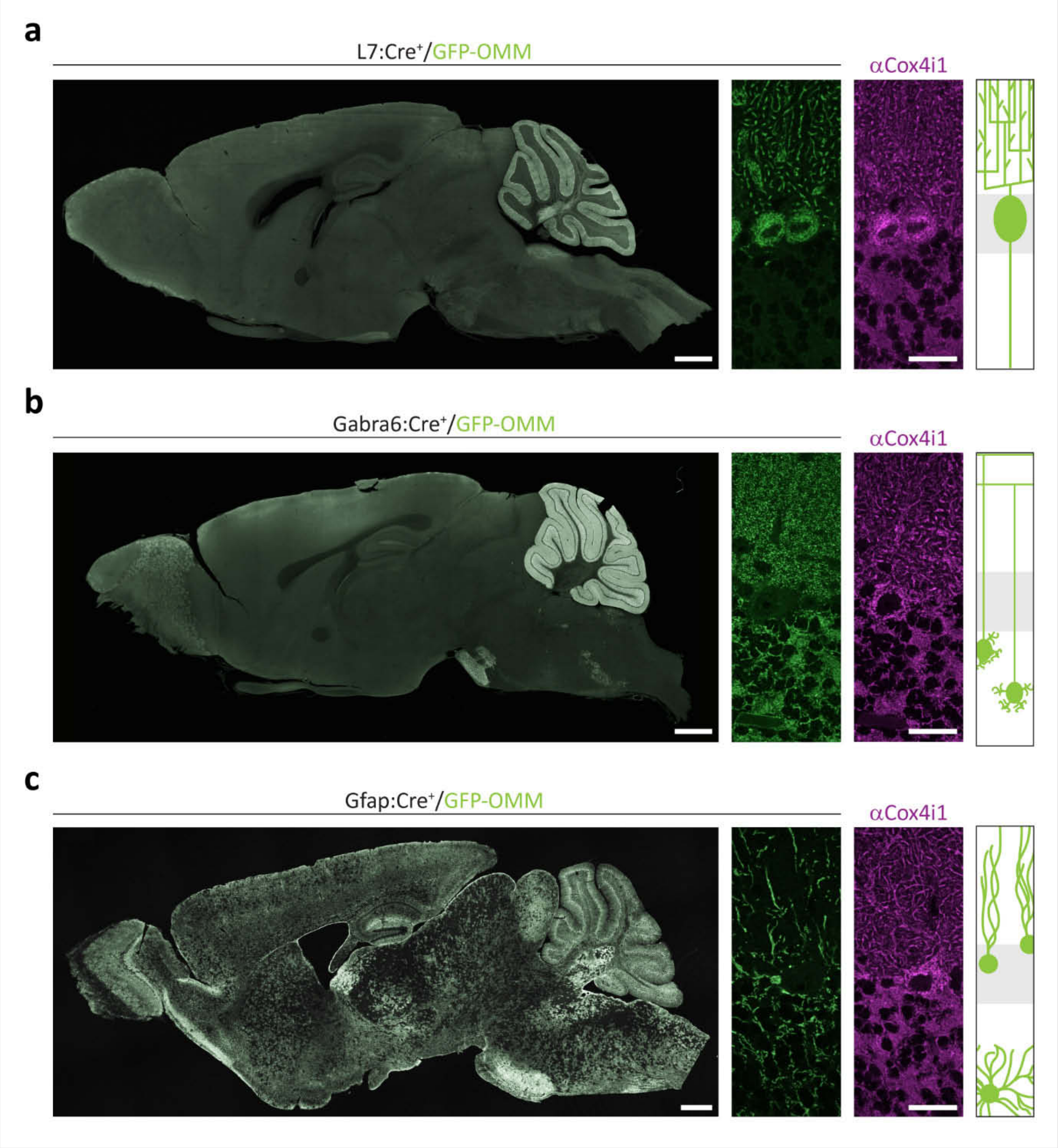

Figure 19| Cre-driver lines crossed to the MitoTag mouse line to tag mitochondria in Purkinje cells, granule cells and astrocytes. Brain overview shows general expression pattern and detail shows the pattern in cerebellum as well as the distribution of cerebellar mitochondria via immunofluorescence staining against Cox4i1 (magenta). The schema gives information about the cellular position in cerebellar cortex. Grey box, Purkinje cell layer; above, molecular layer; below, granule cell layer. (**a**) Purkinje cells are labeled via L7:Cre; (**b**) granule cells are labeled via Gabra6:Cre; and (**c**) astrocytes, including Bergmann glia, are labeled via Gfap:Cre. Scale bars: 1 mm (brain); 25 μm (cerebellum detail). Modified from Fecher et al. (2019), Figure 3 and Supplementary

4.2. Molecular diversity of neural mitochondria in mouse cerebellum

To explore mitochondrial diversity in vivo, we focused on cell types in mouse cerebellum as proof-of-concept model. The cerebellum – like the retina – is a layered structure with well-characterized cell types (see Chapter 1.6). The position of a cell as well as its geometry informs well about the cell's identity, which was an important feature for our validation. In addition, Cre-driver lines are available to investigate most cerebellar cell types. Cerebellar atrophy and ataxia are frequently observed in patients with mitochondrial disorders (see Chapter 1.7; Peng et al., 2019) implicating a unique dependence on or specialization of mitochondrial function in cerebellar cell types, for example Purkinje cells.

4.2.1. Cell type-specific profiling of mitochondria identifies similarities and differences

To profile mitochondrial heterogeneity in an unbiased way, we performed label-free mass spectrometry to screen for enriched proteins from cell type-specific mitochondria. I generated MitoTag mouse lines for three cerebellar cell types, namely: Purkinje cells, an inhibitory neuron (L7:Cre$^+$/GFP-OMM, Figure 19a); granule cells, a highly abundant excitatory neuron (Gabra6:Cre$^+$/GFP-OMM, Figure 19b); and astrocytes, a glial cell type (Gfap:Cre$^+$/GFP-OMM, Figure 19c). Mice at the age of 2 month were sacrificed and I immunocapture mitochondria from the cerebellum via IC Tom and IC GFP per biological replicate (n≥5 mice, Figure 8). Stephan Müller (S.M.; Lichtenthaler laboratory, German Center for Neurodegenerative Diseases) further processed samples for mass spectrometry and label-free quantification (LFQ) in MaxQuant (see Chapter 3.2.12.3). IC Tom represented the control sample in this experiment by providing the average mitochondrial proteome from the cerebellum, in contrast to the cell type-specific mitochondrial proteome obtained with IC GFP.

Intensity-based absolute quantification (iBAQ) showed that immunocaptures in general contained a high abundance of mitochondrial proteins when compared to the quantification of a whole tissue sample (Δmean ($\text{iBAQ}_{\text{mitochondrial peptides}}$-$\text{iBAQ}_{\text{non-mitochondrial peptides}}$): 6.51-fold (immunocapture) *vs* 2.64-fold (cerebellum). IC Tom consistently contained 3,718 proteins of which 821 were annotated in MitoCarta (coverage 70.9%; Calvo et al., 2016). This MitoCarta coverage is similar to previous mass spectrometry studies using Percoll gradient isolated mitochondria (Pagliarini et al., 2008) or an in-depth analysis of mouse brain via high-resolution mass spectrometry (12,934 proteins identified by mass spectrometry, Sharma et al., 2015; Figure 20).

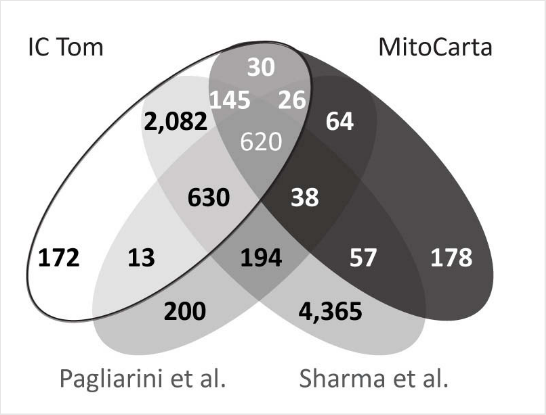

Figure 20│ Proteomic comparison among IC Tom, mitochondria in Pagliarini et al. (2008) and whole tissue in Sharma et al. (2015) to MitoCarta (Calvo et al., 2016). Venn diagram depicting the number of proteins consistently found in the studies. MitoCarta includes 1,158 high confidence candidates found in mitochondria. 620 of these are shared among the three studies, while 30, 64 and 57 are only found in IC Tom, Pagliarini et al. and Sharma et al., respectively. All studies cover ≥64% of MitoCarta. Taken from Fecher et al. (2019), Supplementary Figure 3.

By comparing IC GFP to IC Tom per biological sample, we eliminated technical variation among experiments and biological variability among mouse cohorts. First, I calculated the cell type-specific $\log_2$ fold change per protein for each biological samples ($\log_2$ FC (IC GFP *vs* IC Tom)) and generated the mean per cell type for proteins found in ≥3 biological replicates. With these values, we then asked if core mitochondrial processes were enriched in a cell type-specific manner (Figure 21 and 22). Most proteins were unchanged arguing for a conserved core of mitochondrial functions and a successful normalization of our data. Still, individual proteins (n=7) were cell type-enriched among these core mitochondrial functions.

For example, mitochondrial inner membrane protein like 2 (Mpv17L2) was significantly enriched in the proteome of astrocytic mitochondria (Figure 22a; two-tailed, unpaired *t*-test with permutation-adjusted q-value: PC *vs* A: *-0.745, 0.0468; GC *vs* A: *-1.699, <0.0001; PC *vs* GC: 0.954, 0.0759). Dalla Rosa et al. (2014) showed that Mpv17L2 is necessary for mitochondrial ribosome assembly and the generation of mitochondrial encoded proteins. It co-sediments with the large ribosome subunit and monosomes and Mpv17L2 depletion causes mitochondrial swelling, nucleoid aggregation and a halt of protein synthesis in mitochondria.

Likewise, several components of the coenzyme Q_{10} biosynthesis pathway (CoQ) were enriched in Purkinje cell mitochondria (Coq6, Coq3, Pptc7; Figure 22b). Not surprisingly, mutations in CoQ enzymes manifest in patients with ataxia and cerebellar atrophy (Alcazar-Fabra et al., 2018) and Coq8a deficiency has been shown to cause Purkinje cell dysfunction in mice (Stefely et al., 2016b). Surprisingly, AarF domain-containing kinase 1 (Adck1; Figure 22b) was significantly enriched in astrocytic mitochondria, while being proposed to participate in CoQ synthesis (Stefely et al., 2016b; Acosta et al., 2016). Recently, however, Yoon et al. (2019) reported the functional interaction of Adck1 with the protease Yme1L1 to instruct MIC60 and

Opa1 in cristae formation and mitochondrial dynamics; thereby given the first experimental evidence for CoQ-independent Adck1 function.

Additionally, two enzymes of the tricarboxylic acid cycle (TCA cycle; Figure 22c) were enriched in astrocytic mitochondria, namely: mitochondrial [NADP] isocitrate dehydrogenase (Idh2; two-tailed, unpaired *t*-test with permutation-adjusted q-value: PC *vs* A: *-2.208, <0.001; GC *vs* A: *-1.437, <0.0001; *PC *vs* GC: -0.771, 0.0029); and succinate-CoA ligase (GTP-forming) subunit beta (Suclg2; two-tailed, unpaired *t*-test with permutation-adjusted q-value: PC *vs* A: *-2.665, <0.0001; GC *vs* A: *-2.708, <0.0001; PC *vs* GC: 0.043, 0.9376). Idh2 catalyzes the reversible reaction of $isocitrate \xleftrightarrow{Idh2} \alpha\text{-ketoglutarate} + \text{NADPH}$ in the TCA cycle. While Idh2 is proposed to not contribute to the TCA cycle flux by reverse direction, Hartong et al. (2008) reported that Idh2 compensates for Idh3 loss in most tissues except for the retina.

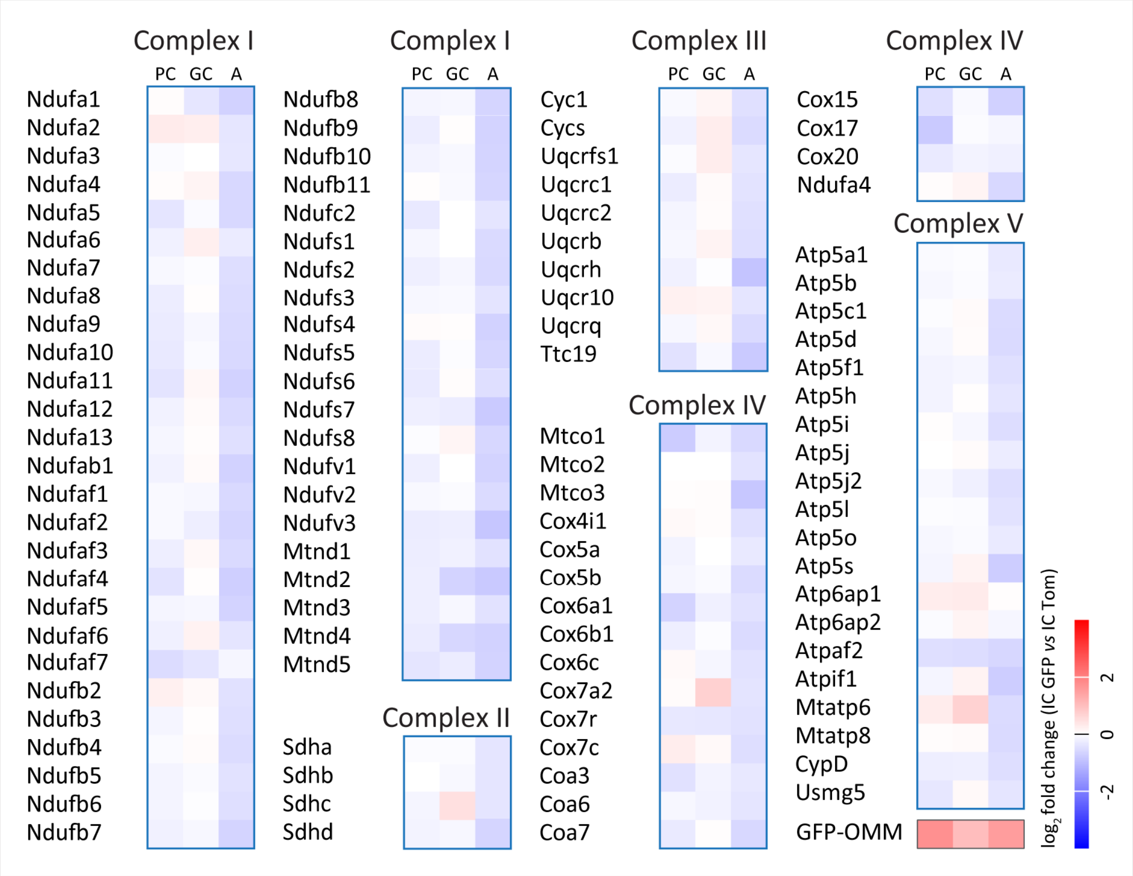

Figure 21| Proteomic composition of the electron transport chain in cell type-specific mitochondria. The average fold change ($\log_2$ fold change (IC GFP *vs* IC Tom)) of LFQ intensity per protein (n≥3 biological replicates) was calculated for mitochondria from Purkinje cells (PC), granule cells (GC) and astrocytes (A), and is shown as heat map ranging from -4 (blue) to 4 (red). The fold change for GFP-OMM per cell type is shown in the right lower corner. Modified from Fecher et al. (2019), Supplementary Figure 8.

Besides controlling the TCA cycle (Sazanov and Jackson, 1994), Idh2 also plays a key role in oxidative stress and ROS defense by providing NADPH for thioredoxin reductase 2 (White et al., 2018) and glutathione reductase (Kong et al., 2018). Here, Idh2 together with nicotinamide nucleotide transhydrogenase (Nnt; Hojeberg and Rydstrom, 1977) provide NADPH for the regeneration of reduced glutathione and thioredoxins (Vogel et al., 1999). Interestingly, Nnt was also enriched in the proteome of astrocytic mitochondria (Nnt; two-tailed, unpaired *t*-test with permutation-adjusted q-value: PC *vs* A: *-1.062, 0.0007; GC *vs* A: *-1.151, 0.0002; PC *vs* GC: -0.089, 0.8621). Disruption of Idh2 function has been linked to grade II-IV glioma

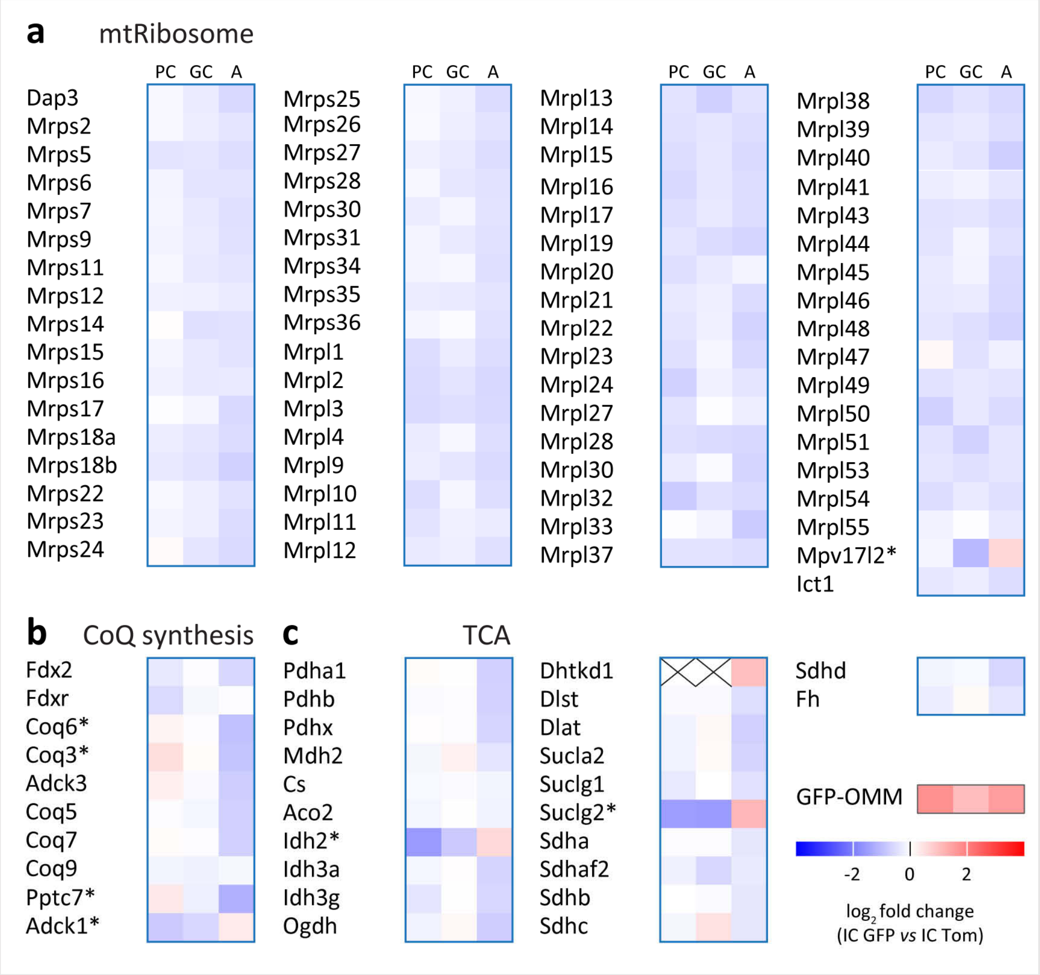

Figure 22| Proteomic composition of core mitochondrial processes in cell type-specific mitochondria. The average fold change (log$_2$ fold change (IC GFP *vs* IC Tom)) of LFQ intensity per protein (n≥3 biological replicates) was calculated for mitochondria from Purkinje cells (PC), granule cells (GC) and astrocytes (A). Proteins are shown as heat map ranging from -4 (blue) to 4 (red) for (**a**) the mitochondrial ribosome; (**b**) the coenzyme Q_{10} synthesis pathway (CoQ); and (**c**) the tricarboxylic acid cycle (TCA). Significantly enriched candidates (*) are: Mpv17L2 (in a); Coq3, Coq6, Pptc7, Adck1 (in b); and Idh2, Suclg2 (in c). The fold change for GFP-OMM per cell type is shown in the right lower corner. Crossed field, no value. Modified from Fecher et al. (2019), Supplementary Figure 8.

(Huang et al., 2019). Suclg2 forms a heterodimer complex with Suclg1, named succinyl-CoA ligase (Sucl), and catalyzes the reversible reaction of $\text{succinyl-CoA} \xleftrightarrow{Sucl} succinate + CoA + GTP$, known as substrate level phosphorylation in the TCA cycle (see Chapter 1.2.1). This reaction is an important intersection for multiple metabolic pathways (reviewed in Tretter et al., 2016) and together with the mitochondrial nucleoside diphosphate kinase (Nme3) provides phosphorylated deoxyribonucleotides to maintain mitochondrial DNA (Kadrmas et

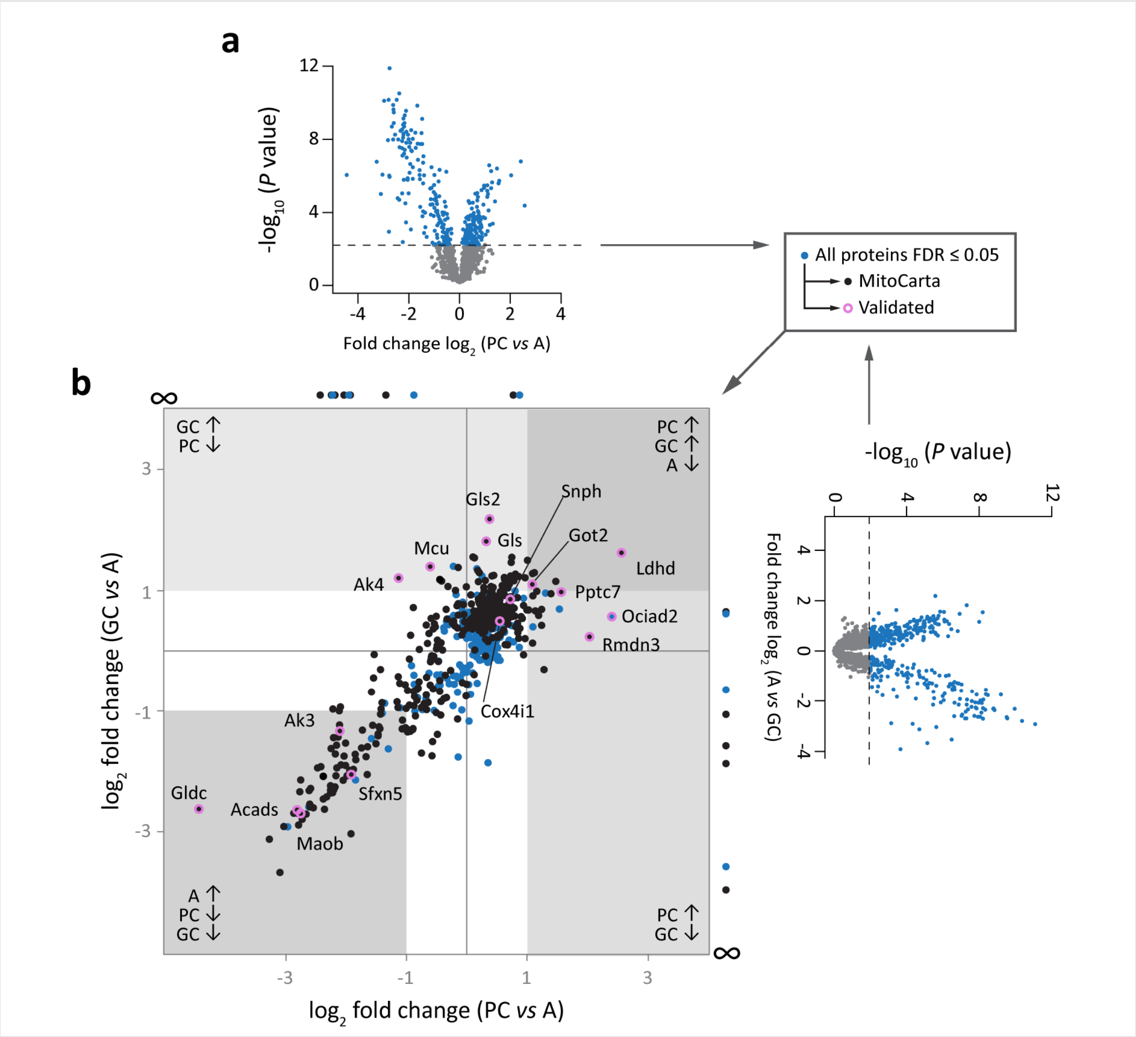

Figure 23| Comparison of cell type-specific mitochondrial proteomes among Purkinje cells, granule cells and astrocytes. (**a**) Volcano plot testing for significant proteins between the mitochondrial proteome from Purkinje cells (PC) and astrocytes (A). Proteins passing the FDR≤0.05 are marked in blue and further considered for b. Right site, volcano plot comparing the mitochondrial proteome from granule cells (GC) with astrocytes (A). (**b**) Scatter plot depicting the fold changes per protein between the two volcano plots in a with (PC *vs* A) on the x-axis and (GC *vs* A) on the y-axis. Only proteins prior passing the FDR in one test are considered (blue filled circles) and proteins with only one fold change between cell types are depicted at the axis with ∞ for the missing value. Black filled circles, MitoCarta annotated proteins; magenta outlined circles, validated candidates with gene name annotation. Modified from Fecher et al. (2019), Figure 3 and Supplementary Figure 7.

al., 1991; Tokarska-Schlattner et al., 2008). Mutations in Suclg1 and Sucla2 cause severe encephalomyopathy with mitochondrial DNA depletion (Ostergaard, 2008); Suclg2 mutations are presumed lethal (Kacso et al., 2016).

Next, I performed statistical testing in Perseus (Tyanova et al., 2016) to identify cell type-enriched candidates. First, I tested for significantly found proteins between mitochondria from Purkinje cells and astrocytes; and between mitochondria from granule cells and astrocytes (blue filled circles; two-tailed, unpaired *t*-test, FDR≤0.05, 500 randomization, n≥3 quantifications per group; Figure 23a). Next, all proteins that passed the applied FDR≤0.05 in one comparison were included in the scatter plot comparing all three cell types (Figure 23b). Here, proteins are annotated by MitoCarta (black filled circles; Calvo et al., 2016) and as validated candidates in this study (magenta outline). I considered proteins as cell type-enriched candidates, if their fold change was ≥|1| in one comparison. 196 proteins met this criterion, of which 18, 51 and 114 proteins were enriched in Purkinje cells, granule cells and astrocytes, respectively (Figure 24a). 13 candidates were shared between cell types.

I used MitoCarta (Calvo et al., 2016) and LocTree3 prediction (Goldberg et al., 2014) to annotate subcellular localization of candidates (Figure 24b). 89.8% of candidates were predicted to be mitochondrial. Only 10.2% of candidates were annotated to another subcellular compartment – with 8 candidates predicted to be peroxisomal and exclusively enriched in the proteome of astrocytic mitochondria.

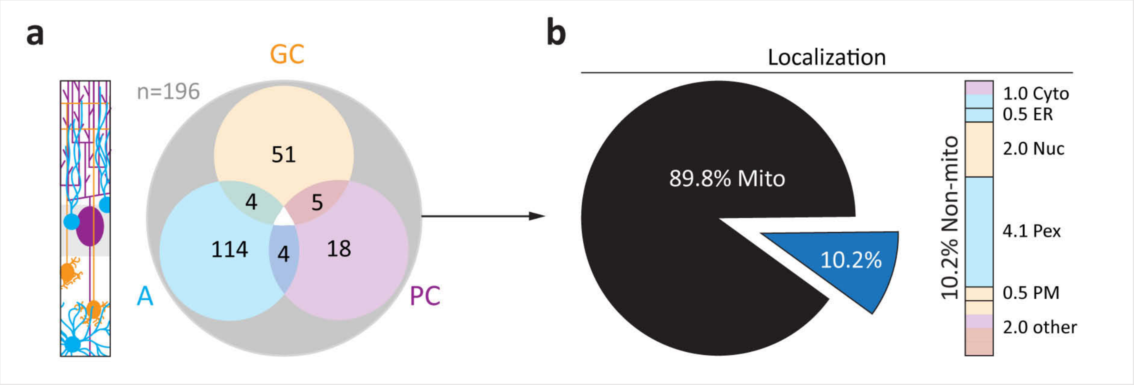

Figure 24| Cell type-enriched candidates and their predicted localization in cells. (**a**) Venn diagram depicting the enriched candidates (n=196) found in mitochondrial proteomes from Purkinje cells (PC, magenta), granule cells (GC, orange) and astrocytes (A, blue). 13 candidates are shared between two cell types. Schema depicts cellular position in cerebellum. (**b**) Pie chart illustrating the predicted subcellular localization of candidates according to MitoCarta and LocTree3 prediction. Distribution of non-mitochondrial proteins is further annotated by cell type (PC, magenta; GC, orange; A, blue) and categorized in: Cyto, cytosol; Nuc, nuclear; ER, endoplasmic reticulum; Pex, peroxisomal; PM, plasma membrane; and other. Modified from Fecher et al. (2019), Figure 3 and Supplementary Figure 3.

Finally, I selected 28 candidates for further validation based on antibody availability and prior literature regarding protein function, mitochondrial localization and abundance in the central nervous system. Using immunofluorescence staining, I confirmed the predicted cell type-enrichment in 21 cases in mouse cerebellum (Figure 25, 27 and 30). For the other 7 cases, no validation could be achieved due to antibody performance (Table A3). Additionally, I stained for Cox4i1 as a ubiquitously expressed mitochondrial protein that did not pass our criteria for being cell type-enriched (two-tailed, unpaired *t*-test with permutation-adjusted q-value: PC *vs* A: *0.554, 0.0268; GC *vs* A: *0.496, 0.0002; PC *vs* GC: 0.058, 0.9085).

4.2.2. Candidates enriched in Purkinje cell mitochondria

In Purkinje cells, all selected candidates colocalized with the genetic GFP-OMM label in L7:Cre$^+$/GFP-OMM tissue confirming their mitochondrial localization (Figure 25b). Specifically, I confirmed that regulator of microtubule dynamics protein 3 (Rmdn3; two-tailed, unpaired *t*-test with permutation-adjusted q-value: PC *vs* A: *2.042, <0.0001; GC *vs* A: 0.238, 0.3951; PC *vs* GC: *1.803, 0.0023) – also known as protein tyrosine phosphatase-interacting protein 51 (PTPIP51) or cerebral protein 10 – is highly abundant in Purkinje cells. Rmdn3 is a C-tail anchored outer mitochondrial protein (Lv et al., 2006) and has been shown to mediate contact sites between the endoplasmic reticulum and mitochondria in vitro (via VAPB, De Vos et al., 2012; via ORP5, ORP8, Galmes et al., 2016).

Secondly, ovarian carcinoma immunoreactive antigen domain–containing protein 2 (Ociad2; two-tailed, unpaired *t*-test with permutation-adjusted q-value: PC *vs* A: *2.413, <0.0001; GC *vs* A: 0.587, 0.082; PC *vs* GC: *1.825, 0.0015) was not included in MitoCarta (Calvo et al., 2016) and further annotated as localized to endosomes (Q9D8W7, version 104; UniProt, 2019). Its paralog Ociad1/Asrij has been reported to localize to endocytic vesicles (Kulkarni et al., 2011) and mitochondria (Shetty et al., 2018) via the two helix-motifs in the OCIA domain (Sinha et al., 2018). I validated Ociad2 with two distinct antibodies recognizing epitopes in the N- or C-terminus. The N-terminus of Ociad2 contains the OCIA domain and its two helix-motifs and is to a low degree conserved with Ociad1/Asrij; the C-terminus is Ociad2-specific. In both cases, I confirmed colocalization with mitochondria, which were genetically marked by GFP-OMM (Figure 26a). However, while the C-terminal antibody confirmed Purkinje cell enrichment, the N-terminal antibody colocalized with granule cell mitochondria. Sinha et al. (2018) reported partial endosomal localization of Ociad2, which could not be determined in these experiments. I then aligned the reported mouse Ociad2 isoform sequences (four isoforms, version 104; UniProt, 2019) with the mass spectrometry-identified peptides in Purkinje cell and granule cell mitochondria (Figure 26b). Both antibodies recognized the full-length Ociad2 protein; however, also react to different isoforms. Therefore, differential expression of Ociad2 isoforms might a reason for my results obtained with epitope-specific antibodies. Functionally, Ociad2 is no well characterized. Han et al. (2014) reported nicastrin interaction with Ociad2 via its C-terminus (residues 132-142). Presumably, this leads to

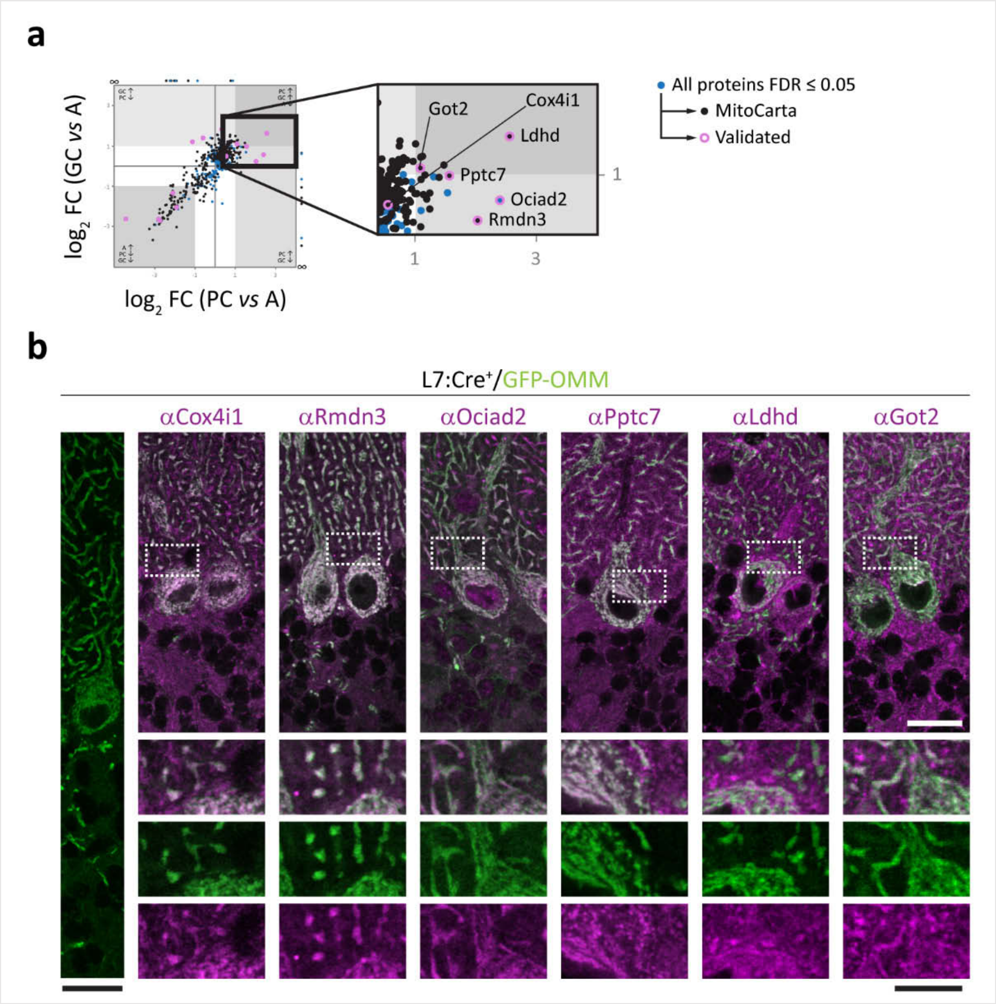
a
log$_2$ FC (GC *vs* A)
log$_2$ FC (PC *vs* A)
Got2
Cox4i1
Ldhd
Pptc7
Ociad2
Rmdn3
1
1
3
● All proteins FDR ≤ 0.05
● MitoCarta
○ Validated
b
L7:Cre$^+$/GFP-OMM
αCox4i1
αRmdn3
αOciad2
αPptc7
αLdhd
αGot2

Figure 25│ Candidates enriched in Purkinje cells mitochondria. (**a**) Scatter plot summarizing the fold changes of proteins from the pairwise comparison of cell type-specific mitochondrial proteomes (see Figure 23b). Detail illustrates the enriched proteins in Purkinje cell mitochondria with annotation of validated candidates in b. FC, fold change. (**b**) Immunofluorescence staining of candidates in cerebellum from L7:Cre$^+$/GFP-OMM mice. Cox4i1 is a ubiquitous mitochondrial protein, while ldhd and Got2 are predicted as neuronal. Rmdn3, Ociad2 and Pptc7 are predicted as Purkinje cell enriched. All proteins localize to mitochondria. Details show the merge channel and the single channels for GFP-OMM (green) and the candidate (magenta). Scale bars: 20 μm (detail 10 μm). Modified from Fecher et al. (2019), Figure 3.

pre-assembly of the γ-secretase complex and in an increase in amyloid-β production. Further involvement of Ociad2 in Alzheimer's disease is not reported in humans.

Thirdly, I confirmed enrichment of protein phosphatase PTC7 homolog (Pptc7; two-tailed, unpaired *t*-test with permutation-adjusted q-value: PC *vs* A: *1.571, <0.001; GC *vs* A: *0.984, 0.0089; PC *vs* GC: 0.587, 0.1569) in Purkinje cell mitochondria. Pptc7 is localized to the mitochondrial matrix (Ramos et al., 2000) and I observed punctuated immunofluorescence signals surrounded by continuous GFP-OMM signals (Figure 25b, Pptc7 detail). Recently, Niemi et al. (2019) showed that Pptc7 is essential for postnatal survival via mitochondrial protein import and biogenesis. Additionally, Pptc7 activity modulates the TCA cycle via dephosphorylation of citrate synthase (CS; Guo et al., 2017).

Next, probable mitochondrial D-lactate dehydrogenase (Ldhd) was predicated as neuronal candidate, i.e. significantly enriched in mitochondria from Purkinje cells and granule cells (two-tailed, unpaired *t*-test with permutation-adjusted q-value: PC *vs* A: *2.571, 0.0007; GC *vs* A: *1.633, 0.0026; PC *vs* GC: 0.938, 0.2091). In agreement with our mass spectrometry data, I confirmed enrichment of Ldhd in Purkinje cells, but also robust signals in other mitochondria, presumably from granule cell (Figure 25b; note that lack of recombination in neighboring Purkinje cell accounts for Ldhd signals without GFP-OMM colocalization). In mammals, D-lactate cannot be converted into L-lactate and its reaction to pyruvate was questioned due to the lack of a D-lactate dehydrogenase. D-lactate is primarily produced via the glyoxalase system to detoxify methylglyoxal, which is a metabolic by-product of glycolysis and neurotoxic (reviewed in Allaman et al., 2015; and in the context of neurodegeneration in Munch et al., 2012). Ldhd was first reported by de Bari et al. (2002) and Flick and Konieczny (2002); still, its function in vivo was not supported in the past. Recently, however, Ldhd function was confirmed in vivo in patients with Ldhd mutations (Monroe et al., 2019).

Finally, I validated mitochondrial aspartate aminotransferase (also known as glutamate oxaloacetate transaminase 2, Got2; or fatty acid-binding protein, FABP-1) as significantly enriched in Purkinje cells (Figure 25b) and granule cells (Figure 27b; two-tailed, unpaired *t*-test with permutation-adjusted q-value: PC *vs* A: *1.093, <0.0001; GC *vs* A: *1.109, 0.0001; PC *vs* GC: -0.016, 0.9701). Got2 is localized to the mitochondrial matrix (Katunuma et al., 1962) and catalyzes the reaction of $oxaloacetate \xrightarrow{Got2} aspartate + \alpha\text{-ketoglutarate}$ or $glutamate \xrightarrow{Got2} \alpha\text{-ketoglutarate}$. These reactions represent the fastest steps of the TCA cycle and facilitates ATP production based on amino acids without the use of acetyl-CoA, termed

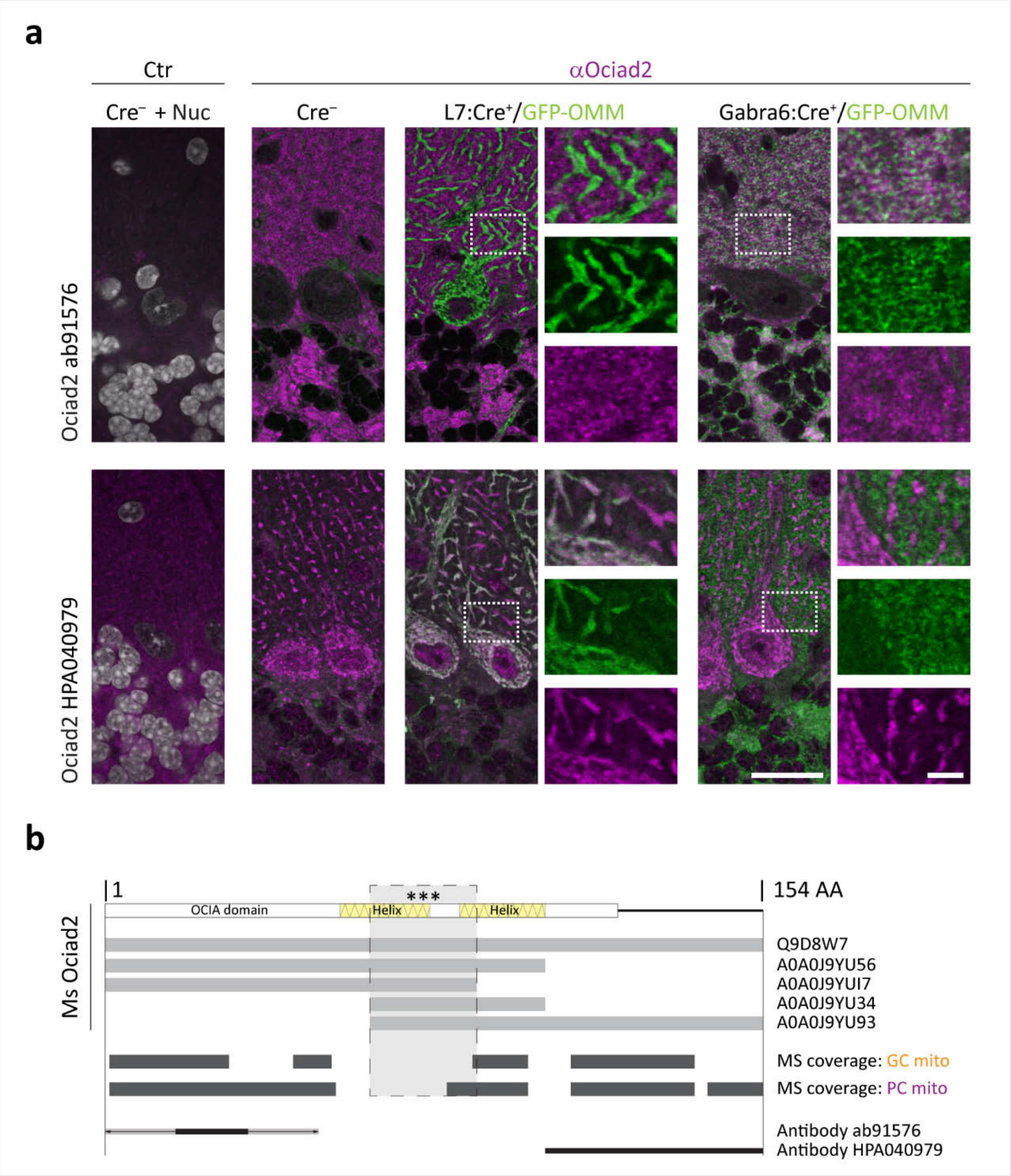
a
Ctr
αOciad2
Cre$^-$ + Nuc
Cre$^-$
L7:Cre$^+$/GFP-OMM
Gabra6:Cre$^+$/GFP-OMM
Ociad2 ab91576
Ociad2 HPA040979
b
1
154 AA
***
OCIA domain
Helix
Helix
Ms Ociad2
Q9D8W7
A0A0J9YU56
A0A0J9YUI7
A0A0J9YU34
A0A0J9YU93
MS coverage: GC mito
MS coverage: PC mito
Antibody ab91576
Antibody HPA040979

Figure 26│ Ociad2 isoforms are localized to mitochondria in Purkinje cells and granule cells. (**a**) Immunofluorescence staining of Ociad2 using two epitope-specific antibodies (N-terminal: ab91576; C-terminal: HPA040979) in cerebellum from Cre$^-$/GFP-OMM, L7:Cre$^+$/GFP-OMM and Gabra6:Cre$^+$/GFP-OMM mice. Details show the merge channel and the single channels for GFP-OMM (green) and the antibody staining (magenta). Ctr, omission of primary antibody; Nuc, nuclear counter stain. Scale bars: 25 µm (detail 5 µm). (**b**) Alignment of protein sequences for full-length murine Ociad2 (154 AA), its shorter isoforms (light gray), peptides identified by mass spectrometry in Purkinje cell (PC) and granule cell (GC) mitochondria (dark gray) and epitopes of antibodies (black). Note the exact epitope of ab91576 is proprietary and declared as 17 amino acid long and within the N-terminus of human Ociad2. ***, the conserved region within Ociad2 isoforms; MS, mass spectrometry. Modified from Fecher et al. (2019), Supplementary Figure 11.

‘mini TCA cycle’ (Yudkoff et al., 1994). On the one hand, α-ketoglutarate enters the TCA cycle, on the other hand, aspartate plus acetyl-CoA forms N-acetylaspartate, which is important for N-acetylaspartylglutamate synthesis, neuronal metabolism and myelin synthesis (Moffett et al., 2007). Additionally, Got2 has been reported to function as kynurenine aminotransferase producing kynurenic acid, the only endogenous antagonist of NMDA receptors and α7-nicotinic acetylcholine receptors (Han et al., 2011; Guidetti et al., 2007); and as fatty acid-binding protein for the uptake of long-chain fatty acids at the plasma membrane (Stump et al., 1993; Bradbury et al., 2011). In these experiments, I could not determine the proposed partial localization of Got2 on the plasma membrane.

4.2.3. Candidates enriched in granule cell mitochondria

In granule cells, all selected candidates colocalized with the genetic GFP-OMM label in Gabra6:Cre$^+$/GFP-OMM tissue confirming their mitochondrial localization (Figure 27b). First, I verified cell type-enrichment of mitochondrial adenylate kinase 4 (Ak4) in granule cell mitochondria, with absence of signal in Purkinje cells (Figure 27b; two-tailed, unpaired *t*-test with permutation-adjusted q-value: PC *vs* A: *-1.127, 0.0004; GC *vs* A: *1.211, 0.0004; *PC *vs* GC: -2.338, 0.0007). The family of adenylate kinases maintains nucleotide homeostasis by interconversion of nucleoside phosphates. Ak4 and Ak3 are localized to the mitochondrial matrix and Ak2 is present in the intermembrane space (Nakazawa et al., 1990; Yoneda et al., 1998). While Ak3 converts $\mathrm{Mg^{2+}GTP} + AMP \xrightarrow{Ak3} \mathrm{Mg^{2+}GDP} + ADP$, Ak4 binds GTP but surprisingly lacks phosphotransferase activity (Noma et al., 2001). In contrast to its family members, Ak4 plays a role in stress signaling by interacting with the ADP/ATP translocase complex (ANT1 or Slc25a4; Liu et al., 2009). In this report, Ak4 binds to ANT upon oxidative stress and prevents permeability transition pore opening, cytochrome c release and apoptosis. Under normal conditions, Ak4 modulates ANT1 activity by sensing GTP levels in the mitochondrial matrix. Controversially, Miyoshi et al. (2009) reported high levels of Ak4 protein in Bergmann glia; in contrast to a study by Yoneda et al. (1998) that confirms our result of Ak4 enrichment in granule cells. I also validated Ak3 as candidate enriched in astrocytic mitochondria (Figure 30b; two-tailed, unpaired *t*-test with permutation-adjusted q-value: PC *vs* A: *-2.1, <0.0001; GC *vs* A: *-1.335, <0.0001; PC *vs* GC: *-0.765, 0.0147) and believe that the observation from Miyoshi et al. (2009) is related to this paralog, Ak3. Interestingly, GTP cannot leave mitochondria, but is generated during substrate phosphorylation in the TCA cycle

(Johnson et al., 1998). Here, Ak3 functions as a GTP scavenger and transfers the energy from GTP to ADP (Heldt and Schwalbach, 1967; Noma et al., 2001). Importantly, also GTP-forming Sucl was significantly enriched in astrocytic mitochondria (Figure 22c).

Secondly, we were surprised to find the mitochondrial calcium uniporter (Mcu) as well as its interactors mitochondrial calcium uptake protein 1 and 3 (Micu1, Micu3) enriched in granule cell mitochondria (Figure 27b; Mcu; two-tailed, unpaired *t*-test with permutation-adjusted q-value: PC *vs* A: *-0.602, 0.0345; GC *vs* A: *1.404, <0.0001; PC *vs* GC: *-2.0006, 0.0005). Given

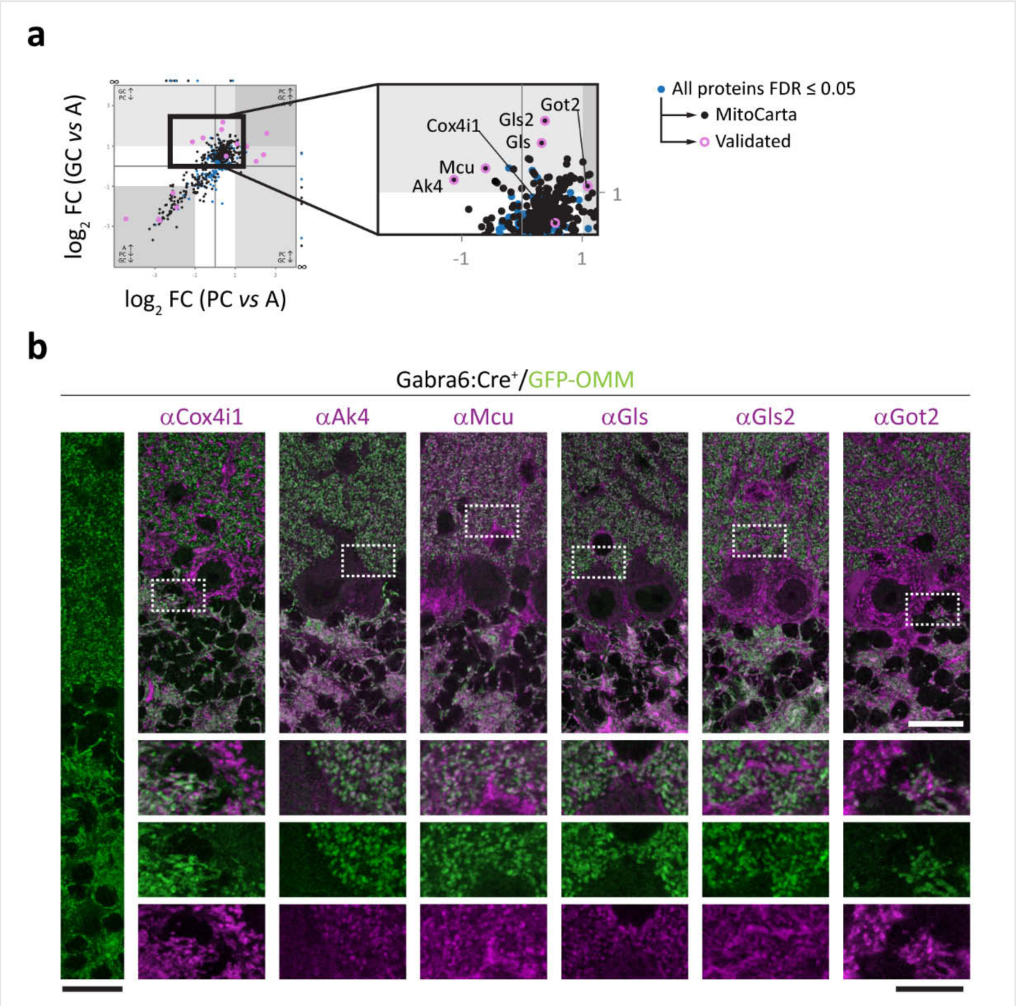
a
log2 FC (GC vs A)
log2 FC (PC vs A)
∞
∞
Cox4i1
Gls2
Got2
Gls
Mcu
Ak4
1
-1
1
All proteins FDR ≤ 0.05
MitoCarta
Validated
b
Gabra6:Cre+/GFP-OMM
αCox4i1
αAk4
αMcu
αGls
αGls2
αGot2

Figure 27| Candidates enriched in granule cell mitochondria. (**a**) Scatter plot summarizing the fold changes of proteins from the pairwise comparison of cell type-specific mitochondrial proteomes (see Figure 23b). Detail illustrates the enriched proteins in granule cell mitochondria with annotation of validated candidates in b. FC, fold change. (**b**) Immunofluorescence staining of candidates in cerebellum from Gabra6:Cre$^+$/GFP-OMM mice. Cox4i1 is a ubiquitous mitochondrial protein, while Got2 is predicted as neuronal. Ak4, Mcu, Gls and Gls2 are predicted as granule cell enriched. All proteins localize to mitochondria. Details show the merge channel and the single channels for GFP-OMM (green) and the candidate (magenta). Scale bars: 20 μm (detail 10 μm). Modified from Fecher et al. (2019), Figure 3.

the importance of mitochondrial Ca^{2+} buffering in neurons (Devine and Kittler, 2018), we expected Mcu to be uniformly expressed, while complex regulation via McuB, Micu1 and posttranslational modification has been reported (see Chapter 1.2.3).

Next, I confirmed enrichment of mitochondrial glutaminase kidney isoform (Gls; two-tailed, unpaired t-test with permutation-adjusted q-value: PC *vs* A: 0.328, 0.0832; GC *vs* A: *1.823, <0.0001; PC *vs* GC: *-1.495, 0.0003) in granule cells (Figure 27b), which is in agreement with the glutamatergic nature of these neurons. The glutamine-glutamate cycle is compartmentalized between neurons and astrocytes (Daikhin and Yudkoff, 2000). Upon glutamate release from excitatory neurons, astrocytic endfeet at the synapse uptake glutamate via transporters, convert it to glutamine via glutamine synthetase and export it. Glutamine is taken up by neurons and metabolized via the reaction $glutamine \xrightarrow{Gls} glutamate + ammonia$. Apart from being used as neurotransmitter, glutamate also enters the TCA cycle via Got2 (enriched in neurons; Figure 25b and 27b) or mitochondrial glutamate dehydrogenase 1 (Glud1; enriched in astrocytes, two-tailed, unpaired t-test with permutation-adjusted q-value: PC *vs* A: *-1.743, <0.0001; GC *vs* A: *-1.616, <0.0001; PC *vs* GC: -0.127, 0.6226). Gls was first discovered by Krebs (1935) and two isoforms are generated via alternative splicing: KGA and GAC (Elgadi et al., 1999). Both are activated by phosphate (Kvamme et al., 1970) and allosterically inhibited by glutamate, and localized exclusively to mitochondria (Laake et al., 1999). The antibody used in this study is specific for KGA, which is most abundant in mouse brain (Martin-Rufian et al., 2012).

Interestingly, Gls has a paralog, mitochondrial glutaminase liver isoform (Gls2; two-tailed, unpaired t-test with permutation-adjusted q-value: PC *vs* A: 0.385, 0.2687; GC *vs* A: *2.19, 0.0001; PC *vs* GC: *-1.805, 0.0008), which was predicted to be enriched in granule cell mitochondria. However, immunofluorescence staining confirmed presence of Gls2 in granule cell mitochondria and Purkinje cell mitochondria (Figure 27b and A1c). Purkinje cells are GABAergic interneurons and GABA is generated via glutamate. Furthermore, Gls and Gls2 are commonly co-expressed in cells raising the question about their redundancy (Campos-Sandoval et al., 2015). In fact, while these paralogs arose from gene duplication, Gls2 has evolved different properties and Gls deficiency is not compensated by Gls2 in mice (Masson et al., 2006). From the *Gls2* gene two isoforms are generated via alternative transcription initiation: GAB and LGA (Martin-Rufian et al., 2012). In contrast to Gls, Gls2 is not activated by phosphate and can translocate to the nucleus via interaction motifs (Olalla et al., 2002).

Therefore, presumably Gls2 plays a multifunctional signaling role in cells and is less involved in glutamate metabolism (Marquez et al., 2006; Marquez et al., 2009).

In addition to the qualitative validation via immunofluorescence staining, I quantified candidate enrichment via western blot analysis by comparing mitochondrial lysates from Purkinje cells with granule cells. I chose four unchanged proteins: Cox4i1 as ubiquitous mitochondrial protein, Got2 as neuronal protein, and sideroflexin-5 (Sfxn5) and mitochondrial glycine dehydrogenase (Gldc) as astrocyte-enriched proteins; as well as two granule cell-

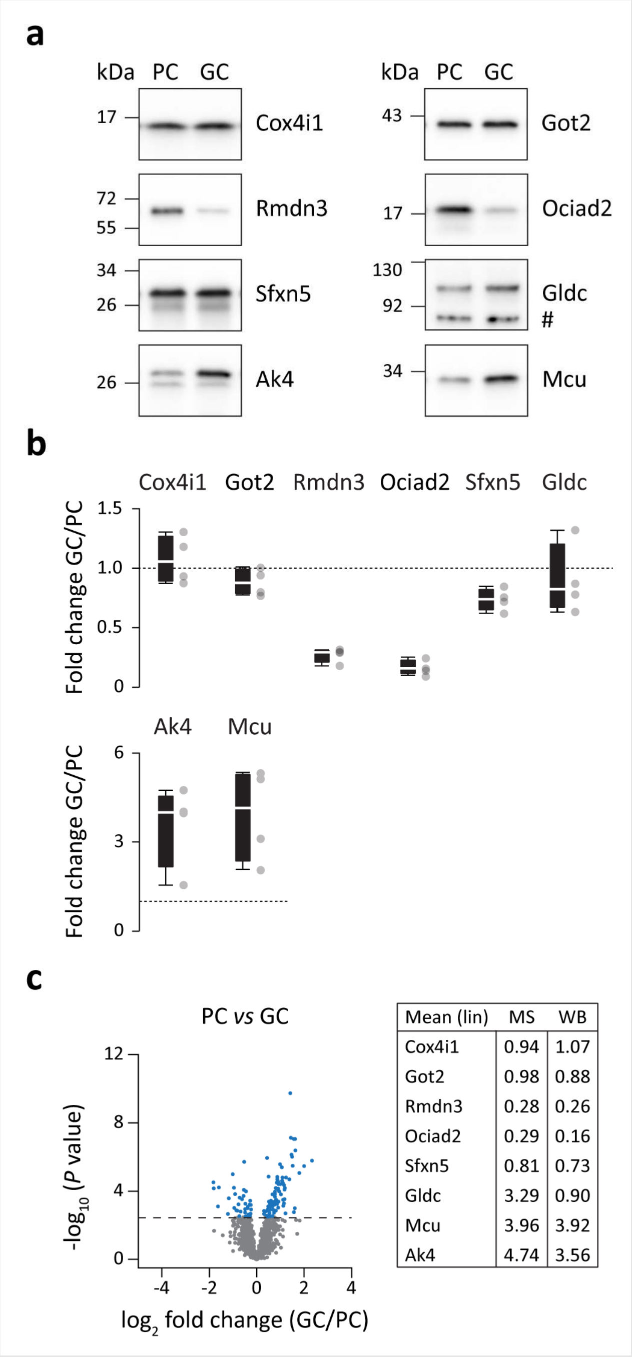

Mean (lin)	MS	WB
Cox4i1	0.94	1.07
Got2	0.98	0.88
Rmdn3	0.28	0.26
Ociad2	0.29	0.16
Sfxn5	0.81	0.73
Gldc	3.29	0.90
Mcu	3.96	3.92
Ak4	4.74	3.56

Figure 28| Western blot analysis of mitochondrial proteins found in cell type-specific mitochondria from Purkinje cells and granule cells by mass spectrometry. (**a**) Representative western blot of cell type-specific mitochondrial lysates from Purkinje cells (PC) and granule cells (GC) probing for mitochondrial proteins: Cox4i1 (pan-mitochondrial), Got2 (neuronal), Rmdn3 and Ociad2 (PC-enriched), Sfxn5 and Gldc (astrocyte-enriched), Ak4 and Mcu (GC-enriched). Differences are quantified in **b**. #, unspecific band not quantified; kDa, molecular weight in kilo Dalton. (**b**) Quantification of mitochondrial proteins shown as fold change to PC mitochondria and normalized to total protein amount and mitochondrial content. Box plot: median, quartile 1-3, whisker from min./max. value, and individual data points; n=4 mice quantified as technical triplicates. (**c**) Volcano plot testing for significant proteins between the mitochondrial proteome from granule cells (GC) and Purkinje cells (PC). Table inset shows average fold change obtained by mass spectrometry (MS) and western blot analysis (WB) for selected proteins. Proteins passing the FDR≤0.05, blue filled circles. Modified from Fecher et al. (2019), Supplementary Figure 10.

enriched (Ak4 and Mcu) and two Purkinje cell-enriched (Rmdn3 and Ociad2) proteins (Figure 28a). This analysis confirmed the mass spectrometry-predicated fold changes (Figure 28b; Figure 28c, Table inset) with the exception of Gldc quantification. In contrast to the enrichment of Gldc in granule cell mitochondria over Purkinje cell mitochondria by mass spectrometry, I confirmed a rather uniform Gldc present in neurons. This difference could be due to antibody specificity in western blot application (Figure 28a, #); however, Gldc signals were also undetectable in neurons by immunofluorescence staining (Figure 30b and A1b) while strongly enriched in astrocytic mitochondria; hence, confirming the direction of our mass spectrometry prediction.

Prior to our study, a group of mitochondrial proteins had been shown to be expressed in a cell type- and/or localized in a cell compartment-specific manner (see Chapter 1.4.1 and 1.4.2). Syntaphilin (Snph) is one of these proteins, which we had hoped to find as positive neuronal candidate in our mitochondrial profiling. Snph localizes to the outer mitochondrial membrane via its C-terminal transmembrane domain and it pauses mitochondrial transport along the axon (Kang et al., 2008). In our proteomic profiling, Snph was quantified in neuronal and astrocytic mitochondria (two-tailed, unpaired *t*-test with permutation-adjusted q-value: PC *vs* A: *0.722, 0.0035; GC *vs* A: *0.886, 0.0008; PC *vs* GC: -0.164, 0.4703); however, its fold change did not pass our enrichment criterion (FC≥|1|). Still, I performed immunofluorescence staining of Snph in mouse cerebellum to understand this divergence between its literature annotation and our proteomic quantification. Supporting our data, Snph signals did not

Figure 29| Syntaphilin is enriched in cerebellar basket cells and their axons forming the pinceau organization. (**a**) Immunofluorescence staining of syntaphilin (Snph) in cerebellum from wild type (Cre^{-}), L7:Cre^{+}/GFP-OMM, Gabra6:Cre^{+}/GFP-OMM and Gfap:Cre^{+}/GFP-OMM mice. Details show the merge channel with GFP-OMM (green) and the single Snph channels (magenta). Scale bars: 25 μm (detail 10 μm). (**b**) Schema depicting basket cell (Bs) position in molecular layer and relationship to Purkinje cell (PC). Bs form pericellular baskets on to PC soma and hillock with specialized terminals, termed pinceau. Confocal image showing Bs (green; GFP driven by parvalbumin promoter, Pvalb:GFP) and PC (blue; immunofluorescence staining against calbindin, αCalb) in mouse cerebellum. Note also stellate cells are labeled in Pvalb:GFP mouse line; however, their axons terminate on smooth shafts of PC dendrites. Scale bar: 25 μm. (**c**) Single confocal planes of a Z-stack illustrating basket (green, GFP) surrounding PC soma (blue, αCalb) and enrichment of syntaphilin labeling (Snph, magenta). Scale bar: 25 μm. (**d**) Comparison of two antibodies for Snph showing similar enrichment of Snph in Bs axons forming pinceau organization. ab192605 is raised against human Snph 1-100 AA; the second antibody (Kang et al., 2008) is raised against 225-428 AA. Here, Snph signals are more pronounced in PC – still, Snph is enriched in Bs axon. Ctr, immunofluorescence staining with omission of primary antibody; AA, amino acids; GFP, Pvalb:GFP; Calb, calbindin. Nuc, nuclear counter stain. Scale bars: 25 μm. Modified from Fecher et al. (2019), Supplementary Figure 9.

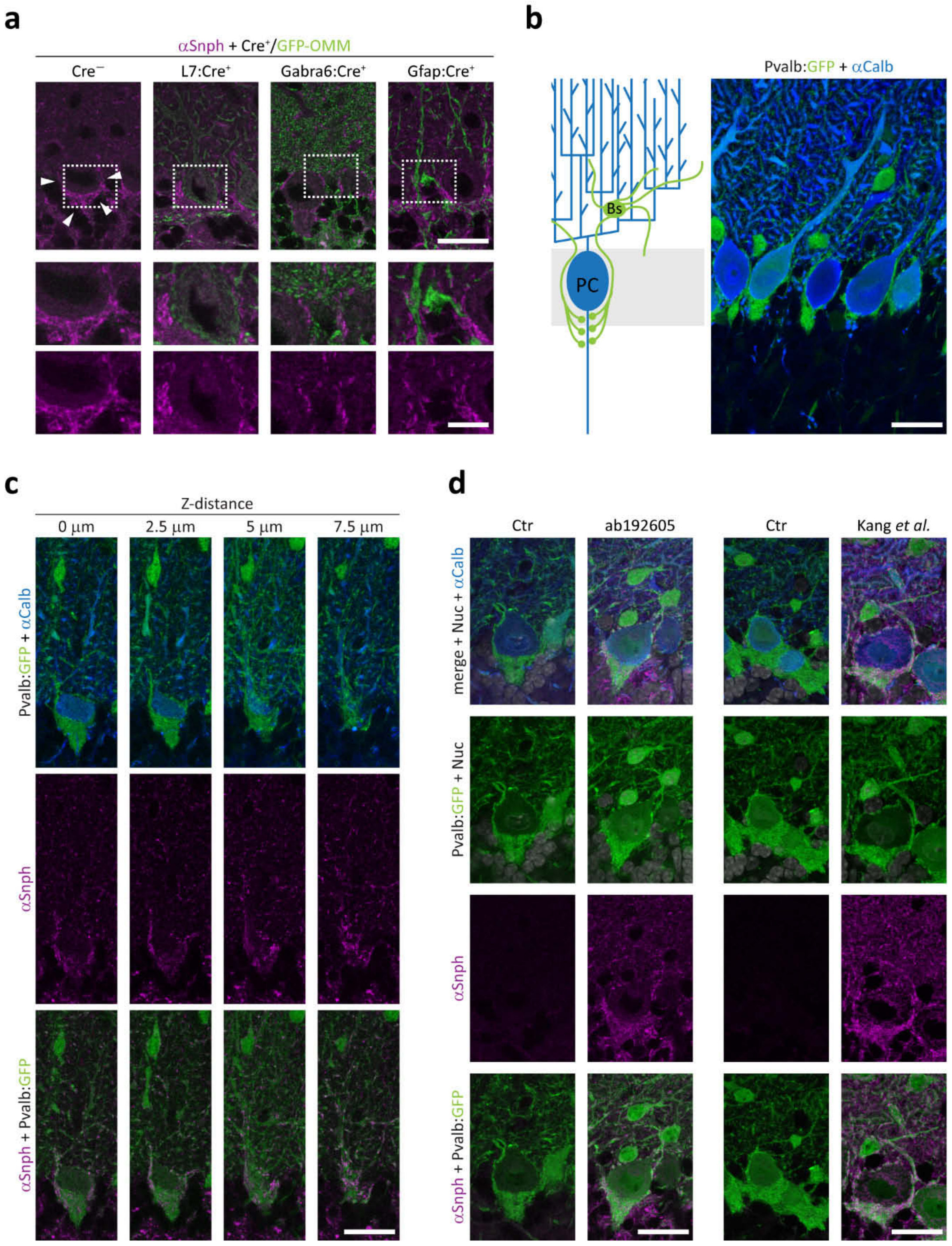
a
αSnph + Cre⁺/GFP-OMM
Cre⁻
L7:Cre⁺
Gabra6:Cre⁺
Gfap:Cre⁺
b
Pvalb:GFP + αCalb
Bs
PC
c
Z-distance
0 μm
2.5 μm
5 μm
7.5 μm
Pvalb:GFP + αCalb
αSnph
αSnph + Pvalb:GFP
d
Ctr
ab192605
Ctr
Kang et al.
merge + Nuc + αCalb
Pvalb:GFP + Nuc
αSnph
αSnph + Pvalb:GFP

Figure 29| Syntaphilin is enriched in cerebellar basket cells and their axons forming the pinceau organization (see previous page for legend).

colocalize with cell type-specific mitochondria visualized by MitoTag (Figure 29a). Still, intense Snph signals without GFP-OMM signal were localized at the soma of Purkinje cells (Figure 29a, arrowheads). This localization is characteristic for projections from basket cells, inhibitory neurons of the molecular layer (Pvalb:GFP, Figure 29b). To evaluate the hypothesis of Snph enrichment in basket cell axons, I performed immunofluorescence staining of Snph and calbindin in the cerebellum from Pvalb:GFP mice (provided by Arthur Konnerth, Institute of Neuroscience, TUM) to distinguish basket cells from Purkinje cells (Figure 29c). Indeed, Snph signals colocalized with the pericellular basket formation from basket cells (Buttermore et al., 2012) and surrounded Purkinje cell somas. I further corroborated this result with another Snph antibody produced by Kang et al. (2008; Figure 29d), with which I additional observed weak Snph signals in Purkinje cells. Given that Snph is enriched in another, yet not profiled cerebellar cell type and is present in IC Tom, our normalization strategy, i.e. the fold change of IC GFP to IC Tom per sample, weakens the cell type-specific contrast for this candidate among the profiled cell types.

4.2.4. Candidates enriched in astrocytic mitochondria

Finally in astrocytes, all selected candidates colocalized with the genetic GFP-OMM label in Gfap:Cre$^+$/GFP-OMM tissue confirming their mitochondrial localization (Figure 30b). Here, the strongest enrichment was calculated for mitochondrial glycine dehydrogenase (Gldc; two-tailed, unpaired *t*-test with permutation-adjusted q-value: PC *vs* A: *-4.443, <0.0001; GC *vs* A: *-2.625, <0.0001; PC *vs* GC: -1.818, 0.0653). Previous work established that Gldc is enriched in astrocytes, Bergmann glia and Müller cells (Sato et al., 1991), which I confirmed. However, surprisingly Gldc has not been used as astrocyte-specific mitochondrial protein since this report. Gldc is localized to the mitochondrial matrix and associated with the inner mitochondrial membrane (Motokawa and Kikuchi, 1971). While Gldc alone can breakdown glycine, it is more efficient in a multienzyme complex with three other protein, termed the glycine cleavage system (GCS; Bruin et al., 1973). It catabolizes $glycine + THF + NAD^+ \xrightarrow{Gcs} \mathrm{CH_2\text{-}THF} + \mathrm{CO_2} + ammonia + NADH$ (as part of the 1C metabolism; Lamers et al., 2009). As such, this system supplies cells with 1C units for nucleotide synthesis and DNA methylation (Tibbetts and Appling, 2010), but also degrades glycine, an inhibitory neurotransmitter and excitatory modulator of NMDA receptors dependent on brain region (Aprison and Daly, 1978; Johnson and Ascher, 1987). Astrocytes recycle glycine via uptake from the synaptic cleft through the Na$^+$/Cl$^-$-dependent glycine transporter 1 (Slc6a9), and thereby terminate neurotransmission (Verleysdonk et al., 1999). Patients with Gldc mutations present with nonketotic hyperglycinemia causing neuronal dysfunction in neonates (Kure et al., 2006; Bravo-Alonso et al., 2017).

Secondly, I confirmed the enrichment of mitochondrial short-chain specific acyl-CoA dehydrogenase in astrocytic mitochondria (Acads; two-tailed, unpaired *t*-test with permutation-adjusted q-value: PC *vs* A: *-2.814, <0.0001; GC *vs* A: *-2.638, <0.0001; PC *vs* GC:

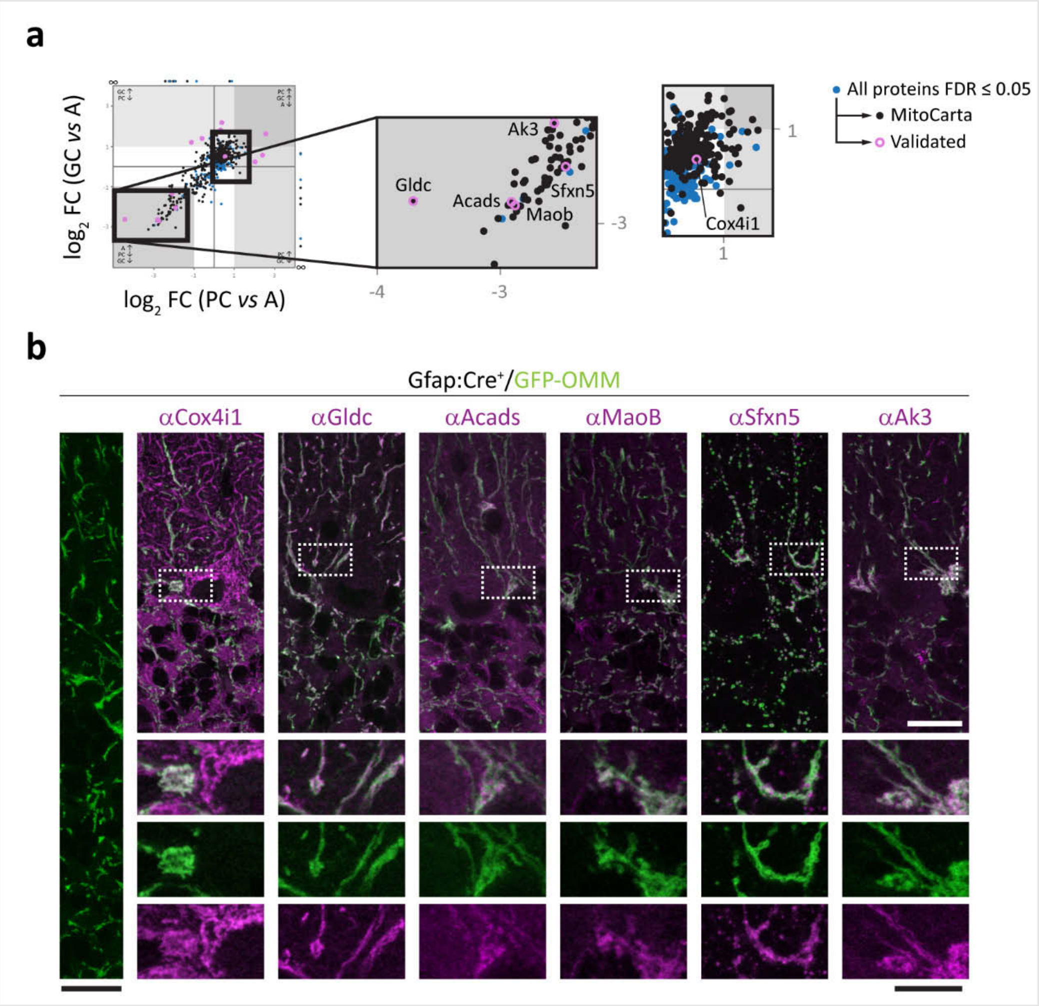

Figure 30| Candidates enriched in astrocytic mitochondria. (**a**) Scatter plot summarizing the fold changes of proteins from the pairwise comparison of cell type-specific mitochondrial proteomes (see Figure 23b). Details illustrate the enriched proteins in astrocytic mitochondria as well as pan-mitochondrial protein Cox4i1 with annotation of validated candidates in b. FC, fold change. (**b**) Immunofluorescence staining of candidates in cerebellum from Gfap:Cre$^+$/GFP-OMM mice. Cox4i1 is a ubiquitous mitochondrial protein. Gldc, Acads, MaoB, Sfxn5 and Ak3 are predicted as astrocyte enriched. All proteins localize to mitochondria. Details show the merge channel and the single channels for GFP-OMM (green) and the candidate (magenta). Scale bars: 20 µm (detail 10 µm). Modified from Fecher et al. (2019), Figure 3.

-0.176, 0.705; Figure 30b). Acads catalyzes the breakdown of short-chain FA (C4 – C6) in mitochondrial beta-oxidation and is localized to the mitochondrial matrix (Ikeda et al., 1983). Transcriptome analysis in mouse and human predicted the presence of FA oxidation in brain, and specifically an enrichment in astrocytes (Eraso-Pichot et al., 2018). Additionally, multiple reports provide strong evidence that neurons do not use FA as fuel (Schonfeld and Reiser, 2017). Acads deficiency in humans causes a spectrum of phenotypes from metabolic acidosis to developmental delay and epilepsy (Jethva et al., 2008).

Next, I confirmed monoamine oxidase type B enrichment in astrocytes (MaoB; two-tailed, unpaired *t*-test with permutation-adjusted q-value: PC *vs* A: *-2.75, <0.0001; GC *vs* A: *-2.696, <0.0001; PC *vs* GC: -0.054, 0.9121; Figure 30b) as previously reported by Luque et al. (1995). MaoB is localized to the outer mitochondrial membrane (Cotzias and Dole, 1951; Schnaitman et al., 1967) and inactivates biogenic amines like dopamine, octopamine, tyramine, but also benzylamine and phenylethylamine (Waldmeier, 1987). In positron emission tomography, MaoB is used to visualize human brain activity (Fowler et al., 2002).

Finally, I found the inner mitochondrial membrane protein sideroflexin-5 (Sfxn5; two-tailed, unpaired *t*-test with permutation-adjusted q-value: PC *vs* A: *1.91, <0.0001; GC *vs* A: *-2.054, <0.0001; PC *vs* GC: 0.144, 0.7328) enriched in astrocytes (Figure 30b). First, sideroflexins were believed to transport iron (specifically Sfxn1; Fleming et al., 2001), later citrate as tricarboxylate carrier (Azzi et al., 1993), and currently only Sfxn1 and 3 function has been confirmed as serine transporters (Kory et al., 2018). In contrast, Sfxn4 has been associated with iron-sulfur cluster biogenesis (Paul et al., 2019). Miyake et al. (2002) reported neuronal localization of TCC, likely Sfxn3, and BBG-TCC enrichment in Bergmann glia, likely Sfxn5 (Rivell et al., 2019). I confirm Sfxn5 enrichment in Bergman glia and extend it to astrocytes in brain, retina and spinal cord.

In summary, these examples of confirmed cell type-specific candidates demonstrate how mitochondrial biology is fine-tuned within the nervous system. While in many cases prior scientific reports documented cell type-enrichment for mitochondrial proteins, this knowledge has not surfaced further functional validation or protein relevance in the described cell types.

4.2.5. Neuronal and astrocytic candidates hint to differential pathways

One reason for the lack in our understanding of cell type-enriched mitochondrial proteins might be their case-by-case description, from which further pathway analysis is needed to draw functional conclusions. I therefore performed pathway enrichment analysis probing for functional differences between neuronal (n=74) and astrocytic (n=114) candidates (Figure 31a). I subgrouped the analysis in gene ontology terms, specifically biological process (GOTerm), and the pathway database of Kyoto encyclopedia of genes and genomes (KEGG), and compared the over-representation enrichment ratio between candidates and the mouse protein-encoding genome using WebGestalt (Liao et al., 2019; Figure 31b). Neuronal candidates grouped to the following significant terms: for GOTerm – mitochondrial transport

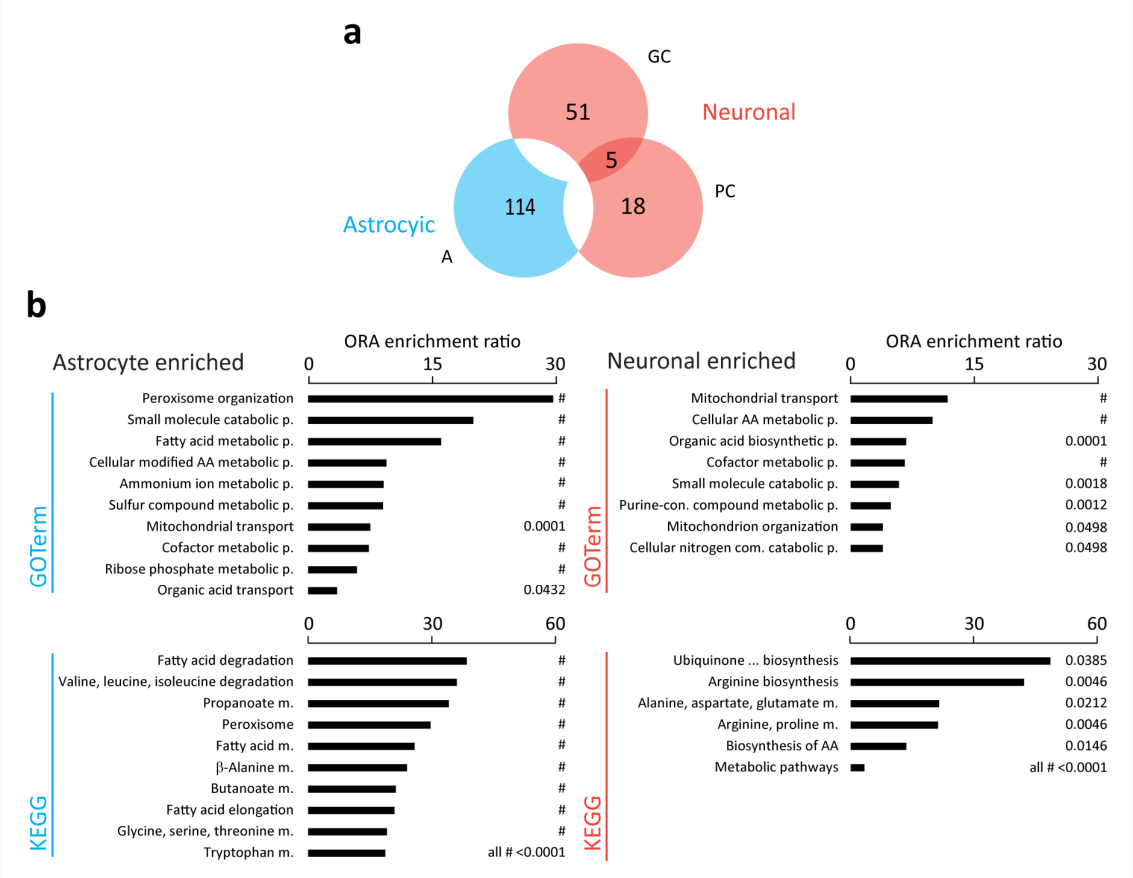

Figure 31 | Pathway analysis of enriched candidates in mitochondria from astrocytes and cerebellar neurons. (**a**) Venn diagram depicting distribution of candidates among cell types. Neuronal candidates are grouped to n=74; astrocytic candidates to n=114. (**b**) Gene sets found via over-representation analysis (ORA) of candidates against the coding mouse genome. Depicted terms are all significantly enriched (FDR<0.05, multiple testing corrected) and q-values are indicated per term. GOTerm was probed via biological process category and top gene sets were further clustered for maximal gene coverage. Individual gene sets can be found in Appendix 7.4. M., metabolism; p., process. Modified from Fecher et al. (2019), Supplementary Figure 8.

(e.g. Mfn2, Mcu, Slc25a22), cellular amino acid metabolism (e.g. Gls, Got2, Aars2), and organic acid biosynthetic process (e.g. Gls2, Got2, Hk1); for KEGG – ubiquinone biosynthesis (e.g. Coq3, Coq6) and arginine biosynthesis (e.g. Gls, Got2, Gls2). Astrocytic candidates significantly grouped to the terms: for GOTerm – peroxisome organization (e.g. Acox1, Pex14, Mavs), fatty acid metabolism (e.g. Acads, Acadm, Cpt1a), and small molecule metabolism (e.g. Oat, Gldc, Eci2); for KEGG – fatty acid degradation (e.g. Cpt1a, Cpt2, Acads), valine, leucine, isoleucine degradation (e.g. Echs1, Mut, Acads) and peroxisome (e.g. Cat, Dao, Pex14). Several gene sets recapitulated the previously described functions of validated candidates, for example the metabolic role of Got2, Gls and Acads.

Surprisingly, the term 'peroxisome' appeared among the top enrichment ratios of astrocytic candidates in GOTerm and KEGG analysis. In addition, peroxisomal proteins were also among candidates as the biggest group of non-mitochondrial proteins (8 out of 20; Figure 24b). I therefore chose two proteins, peroxisomal membrane protein PEX14 (Pex14; two-tailed, unpaired *t*-test with permutation-adjusted q-value: PC *vs* A: *-1.359, 0.0021; GC *vs* A: -0.872, 0.0543; PC *vs* GC: -0.487, 0.3165; Figure 32) and catalase (Cat; two-tailed, unpaired *t*-test with permutation-adjusted q-value: PC *vs* A: *-2.255, <0.0001; GC *vs* A: *-2.237, <0.0001; PC *vs* GC: -0.018, 0.9694; Figure 32) for further investigation via immunofluorescence staining. Pex14 is

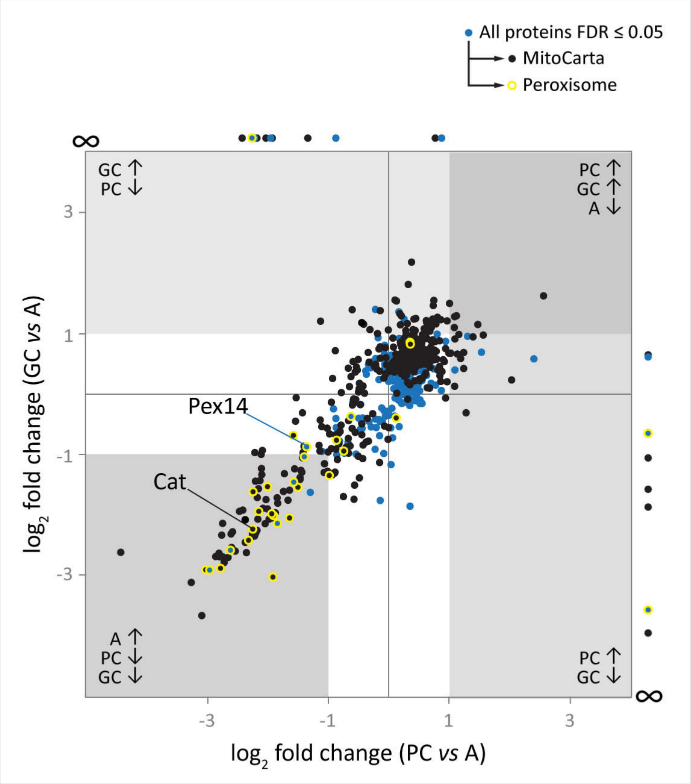

Figure 32| Peroxisomal proteins among mitochondrial proteomes from cell type-specific mitochondria. Scatter plot from Figure 23b depicting the fold changes per protein between the two volcano plots with (PC *vs* A) on the x-axis and (GC *vs* A) on the y-axis. Pex14 and Cat are among cell type-enriched candidates. Proteins with only one fold change between cell types are depicted at the axis with ∞ for the missing value. Blue filled circles, proteins passing at least one *t*-test between cell types; black filled circles, MitoCarta annotation; yellow outlined circles, peroxisomal annotation in LocTree3; PC, Purkinje cell; GC, granule cell; A, astrocyte. Note several peroxisomal proteins are included in MitoCarta. Modified from Fecher et al. (2019), Figure 3

localized to the peroxisomal membrane and is an essential part of the protein import machinery as well as responsible for organelle movement via tubulin interaction (Fransen et al., 1998; Bharti et al., 2011). In mouse cerebellum, I observed small puncta with Pex14 antibody that are characteristic for peroxisomes. Punctate signals were equally distributed among cerebellar cell type, thereby excluding an enrichment due to overall peroxisomal enrichment in astrocytes (Figure 33a). While GFP-OMM signals were closely associated with Pex14 signals in all three cell types, I could not observed strict colocalization of signals as one would predicted for mitochondrial localization of Pex14 (Figure 33a, details in black box). This was in contrast to Cat immunofluorescence staining. Here, I observed intense, punctate staining in astrocytes – especially in Bergmann glia – as well as moderate signals that colocalized with GFP-OMM (Figure 33b, details in black box). Previously, Nagase et al. (2004) reported a similar distribution of Cat and Pex14 in mouse cerebellum. Cat detoxifies hydrogen peroxide in the lumen of peroxisomes. However, under respiratory conditions in

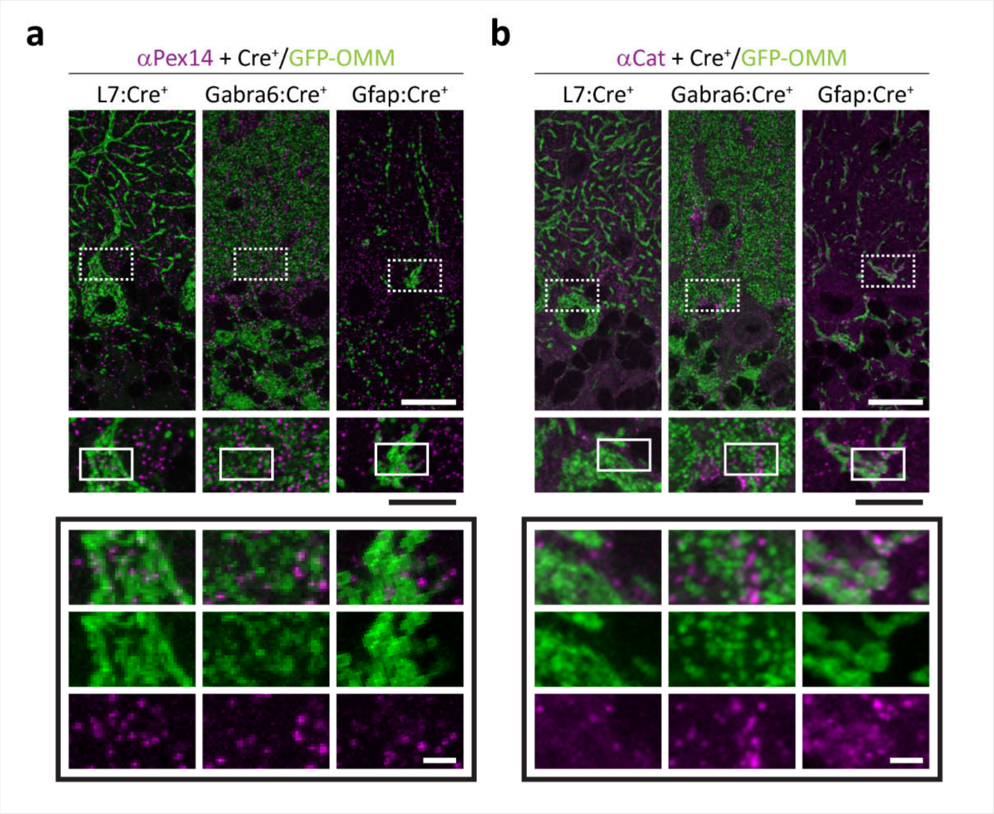

Figure 33| Peroxisomal Pex14 and catalase mainly localize to peroxisomes. Immunofluorescence staining of Pex14 (**a**) and catalase (Cat; **b**) in cerebellum from L7:Cre$^+$/GFP-OMM, Gabra6:Cre$^+$/GFP-OMM and Gfap:Cre$^+$/GFP-OMM mice. Details show the merge channel with GFP-OMM (green) and single channels of GFP-OMM and the candidate (magenta). Scale bars: 20 μm (detail 10 μm); 2 μm (detail in black box). Modified from Fecher et al. (2019), Supplementary Figure 9c.

Saccharomyces cerevisiae, Petrova et al. (2004) showed that Cat relocalizes to mitochondria despite the lack of an import signal. This study is in agreement with an earlier report of Cat activity in rat heart mitochondria (Radi et al., 1991). In fact, peroxisomes and mitochondria share an intimate relationship in cells: Sugiura et al. (2017) demonstrated that peroxisome de-novo biogenesis involves membrane recruitment from the endoplasmic reticulum and mitochondria; several proteins are localized to both organelles (see Figure 32, black filled circles with yellow outline; Costello et al., 2017; Costello et al., 2018); and in peroxisome disorders, like the Zellweger syndrome (Braverman et al., 2016), proteins are mislocalized to mitochondria due to the absence of peroxisomes (Sacksteder et al., 2000; Sugiura et al., 2017). Therefore in astrocytes, the significant enrichment of peroxisomal proteins with astrocytic mitochondria could point to a functional coupling of these organelles in vivo, e.g. for beta-oxidation – a function shared between mitochondria and peroxisomes (Lazarow and De Duve, 1976); and here predicted to be enriched in astrocytic mitochondria (Figure 31b).

4.3. Enhanced lipid oxidation in astrocytic mitochondria

To expand our investigation of mitochondrial diversity on the functional level, we focused on the catabolic role of mitochondria to produce ATP via oxidative phosphorylation. In my initial selection process of cell type-specific candidates (see Chapter 4.2.1), I already noticed an abundance of enzymes involved in beta-oxidation among astrocytic candidates. This was further confirmed by our pathway analysis naming ‘fatty acid degradation’ (mmu00071;

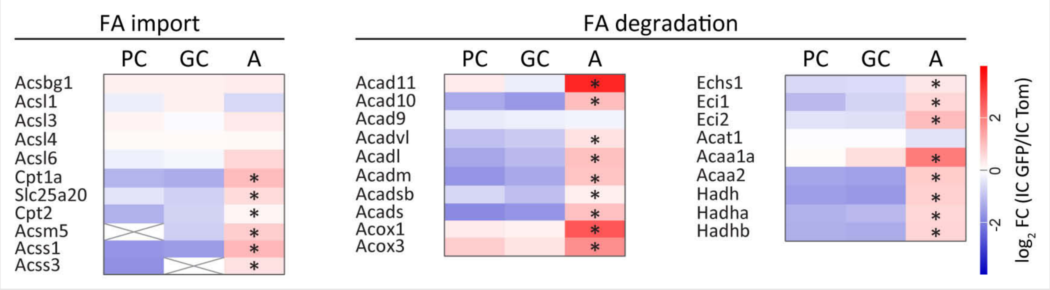

Figure 34| Proteins involved in beta-oxidation are enriched in astrocytic mitochondria. Heat map depicting the average fold change ($\log_2$ FC (IC GFP *vs* IC Tom)) of LFQ intensity per protein involved in fatty acid (FA) degradation (related to mmu:00071). Proteins are grouped in FA import and FA degradation in the mitochondria matrix, and were curated according to localization in mitochondria (MitoCarta and previous reports). Values are obtained from Purkinje cell (PC), granule cell (GC) and astrocytic (A) mitochondria via mass spectrometry. * indicates a significant difference of FC ≥ |1| to the other values (one-tailed, unpaired t-test with FDR≤0.005) ; crossed field, no data; heat map ranges from -4 (blue) to 4 (red). Modified from Fecher et al. (2019), Figure 5a.

Table A5) as most enriched gene set among astrocytic candidates. While astrocytes (Edmond et al., 1987; Sayre et al., 2017) and hypothalamic neurons (McFadden et al., 2014) in culture respire on fatty acids (FA), the use of long-chain FA (≥C14) is debated in the central nervous system (reviewed in Schonfeld and Reiser, 2013; and Panov et al., 2014). In support of neural FA oxidation, Ebert et al. (2003) calculated that 20% of steady state cerebral energy is generated by mitochondrial beta-oxidation based on octanoic acid metabolism in rats. Furthermore, neural stem/progenitor cells depend on FA oxidation in their quiescent state (Knobloch et al., 2017; see Chapter 1.4.2). We therefore further corroborated beta-oxidation in immunocaptured mitochondria from the adult mouse cerebellum.

For mitochondrial beta-oxidation, FA are first imported over the mitochondrial membranes and then metabolized to acetyl-CoA (see Chapter 1.2.1.1). The majority of proteins involved in these two steps were significantly enriched in our mitochondrial proteome from cerebellar astrocytes compared to Purkinje cell and granule cell mitochondria (Figure 34, *; Table A2). For FA metabolism, FA need to be converted to their active acyl-CoA form via a family of acyl-CoA synthetases (Acs; reviewed in Watkins, 2008). Of these, medium-chain (Acsm5) and short-chain (Acss1, Acss3) Acs were significantly enriched in astrocytic mitochondria (Figure 34, *, FA import). In contrast to long-chain FA, FA ≤C12 can cross mitochondrial membranes and are

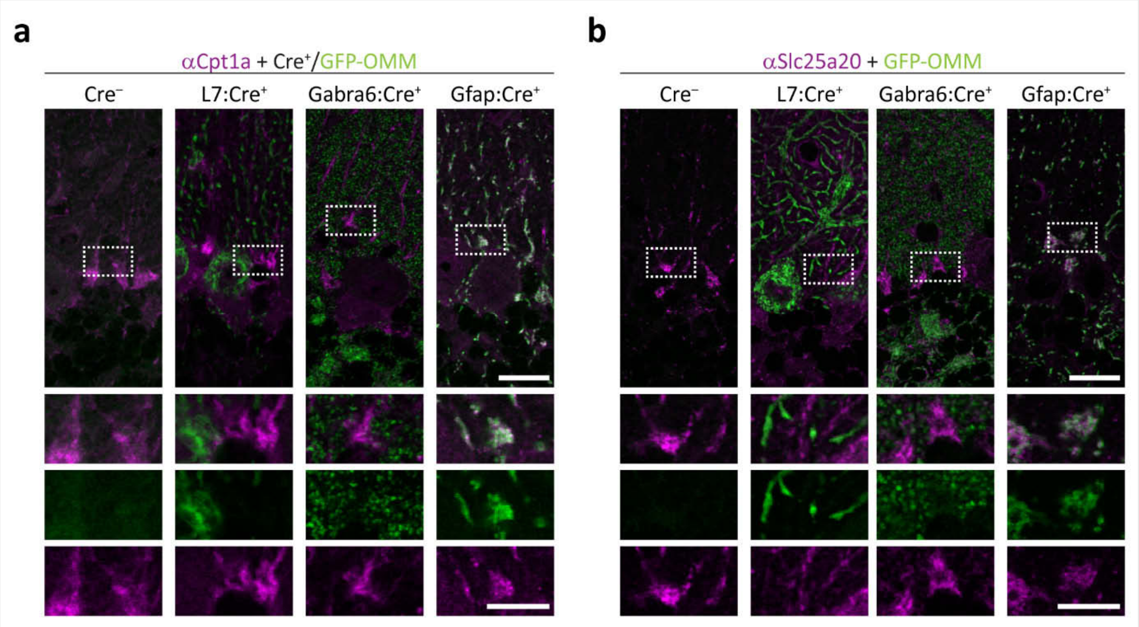

Figure 35│ Import machinery for long-chain fatty acids is enriched in astrocytic mitochondria. Immunofluorescence staining of (**a**) Cpt1a and (**b**) Slc25a20 in cerebellum from wild type (Cre$^-$), L7:Cre$^+$/GFP-OMM, Gabra6:Cre$^+$/GFP-OMM and Gfap:Cre$^+$/GFP-OMM mice. Details show the merge channel with GFP-OMM (green) and the single channels. Scale bars: 25 μm (detail 10 μm).

conjugated to CoA in the mitochondrial matrix (Williamson et al., 1968). Long-chain FA are activated via CoA conjugation in the cytosol, which were not enriched in our proteomic profiling, and imported via the carnitine shuttle system into mitochondria. Here, Cpt1a conjugates $\text{acyl-CoA} + \text{L-carnitine} \xrightarrow{Cpt1a} acylcarnitine + CoA$, which was reported to be rate-limiting in astrocytes (Blazquez et al., 1998). Acylcarnitine is transported over the inner mitochondrial membrane via Slc25a20 (Iacobazzi et al., 2004) and Cpt2 converts $acylcarnitine + CoA \xrightarrow{Cpt2} \text{acyl-CoA} + \text{L-carnitine}$ (Bonnefont et al., 2004).

To verify our proteomics data, we first performed immunofluorescence staining of proteins involved in FA import in mouse cerebellum. Laura Trovò (L.T.; Institute of Neuronal Cell Biology, TUM) optimized Cpt1a immunofluorescence staining and I performed the experiment shown in Figure 35a confirming enrichment of Cpt1a in astrocytes, including Bergmann glia. Cpt1a signals colocalized with cell type-specific GFP-OMM confirming its mitochondrial localization. Similar cell type enrichment of Cpt1a was previously reported by Jernberg et al. (2017). Secondly, I optimized and confirmed Slc25a20 enrichment in astrocytic mitochondria (Figure 35b). Again, signals colocalized with GFP-OMM confirming mitochondrial localization. For FA degradation, imported acyl-CoA is shortened to acetyl-CoA via Acads and the trifunctional protein in repeated cycles. The majority of proteins involved in this process were enriched in astrocytic mitochondria (Figure 34, *, FA degradation). We therefore thought to determine the ability of astrocytic mitochondria to respire on long-chain fatty acids in comparison to neuronal mitochondria. For this, L.T. immunocaptured mitochondria from mouse cerebellum using L7:Cre$^+$/GFP-OMM or Gfap:Cre$^+$/GFP-OMM mice (Figure 36a). To normalize experimental and genetic variabilities between groups, mitochondria were isolated

Figure 36| Astrocytic mitochondria respire better on long-chain fatty acids than neuronal mitochondria. (**a**) Isolation of mitochondria via immunocapture from L7:Cre$^+$/GFP-OMM cerebellum and Gfap:Cre$^+$/GFP-OMM cerebellum. (**b**-**d**) Oxygen consumption rate (OCR) of immunocapture mitochondria from L7:Cre$^+$/GFP-OMM (PC, magenta) and Gfap:Cre$^+$/GFP-OMM (A, blue) mice. OCR is shown as percentage of basal respiration with indicated injections and calculated parameters: coupling efficiency (CE), respiratory control ratio (RCR) and spare respiratory capacity (SRC). For comparison, calculated parameters are normalized to corresponding IC Tom value (dashed line). Left side: representative data from one experiment per genotype; right side: quantification. Mitochondrial respiration was probed using (**b**) L-palmitoylcarnitine+malate (beta-oxidation; n≥9 mice from 12 independent experiments); (**c**) pyruvate+malate (complex I; n≥6 mice from 9 independent experiments) and (**d**) succinate+rotenone (complex II; n≥6 mice from 9 independent experiments) as substrates. Line graph: mean±s.e.m.; box plot: median, quartile 1-3, whisker from min./max. value, and individual data points; *P* values from statistical testing are shown. Modified from Fecher et al. (2019), Figure 5.

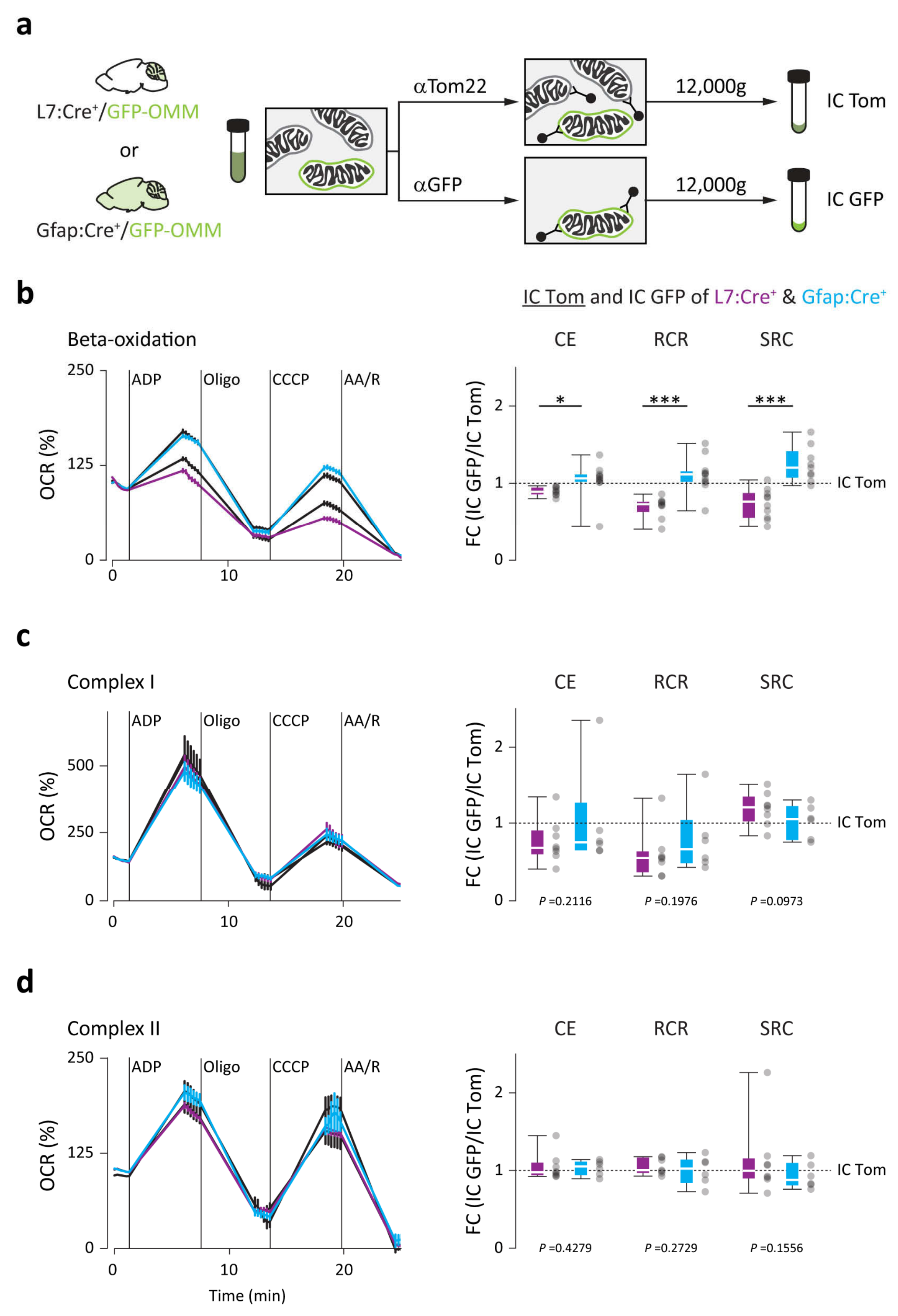

Figure 36| Astrocytic mitochondria respire better on long-chain fatty acids than neuronal mitochondria (see previous page for legend).

via IC Tom and IC GFP, and results normalized to IC Tom, which represents the average cerebellar mitochondrion. First, L.T. analyzed oxygen consumption measurements in the presence of L-palmitoylcarnitine+malate (Figure 36b). Prior evidence suggested that astrocytic mitochondria could be coupled to peroxisomes in a cell type-specific manner (see Chapter 4.2.5). We therefore used the pre-conjugate of L-palmitate (C16:0), given that its carbon chain length and carnitine-conjugate are prerequisites for beta-oxidation in mitochondria, but not peroxisomes (Wanders et al., 2016). Astrocytic mitochondria oxidized significantly more L-palmitoylcarnitine than Purkinje cell mitochondria and performed in all calculated parameters better than neuronal organelles (one-tailed, unpaired Welch's test: CE, 1.18-fold, $P=0.0297$; RCR, 1.60-fold, $P<0.0001$; SRC, 1.74-fold, $P<0.0001$; $n \geq 9$ mice). This was in stark contrast to their respiration on pyruvate+malate (complex I, Figure 36c) and succinate+rotenone (complex II, Figure 36d), where we found no significant difference between cell type-specific mitochondria. Still, comparing the oxygen consumption ratios of astrocytic mitochondria across substrates indicated that for beta-oxidation, four times more mitochondrial mass was necessary to achieve respiration rates close to complex II respiration (8 *vs* 2 μg; see Table 2).

In summary, these experiments independently confirmed our prediction of enhanced beta-oxidation in astrocytic mitochondria and their superior performance on L-palmitoylcarnitine compared to Purkinje cell mitochondria. However, in comparison to other probed substrates, beta-oxidation seemed rather inefficient even in astrocytes, which is in agreement with other reports comparing beta-oxidation capacity of brain mitochondria to liver and heart (Bird et al., 1985; Yang et al., 1987).

4.4. Enhanced Ca^{2+} buffering in granule cell mitochondria via Mcu

We were initially intrigued by our profiling result revealing enrichment of Mcu (Figure 27b) and to a similar degree of its interactors: Micu1 (two-tailed, unpaired *t*-test with permutation-adjusted q-value: PC *vs* A: -0.137, 0.5076; GC *vs* A: *1.385, 0.0001; PC *vs* GC: *-1.522, 0.0005) and Micu3 (two-tailed, unpaired *t*-test with permutation-adjusted q-value: PC *vs* A: -0.216, 0.2469; GC *vs* A: *1.406, <0.0001; PC *vs* GC: *-1.622, 0.0007) in granule cell mitochondria. The finding of robust differences in Mcu complex between neuronal subtypes was unexpected given the known regulation of the Mcu complex via Micu1-3, its modification depending on McuB incorporation (see Chapter 1.2.3) and its long half-life (De Stefani et al., 2016).

I therefore verified Mcu enrichment qualitatively via immunofluorescence staining in mouse cerebellum and confirmed its enrichment in granule cell mitochondria (Figure 37a). Whereas I observed no Mcu signals in Purkinje cell mitochondria, astrocytic mitochondria colocalized with dim Mcu signals and granule cell mitochondria with intense signals. To quantitatively corroborate this data, I performed western blot analysis using cell type-specific mitochondria from cerebellum (Figure 37b). While Mcu levels between granule cell and astrocytic mitochondria were not significantly different and only showed a trend towards lower levels in astrocytes (A: 45.4±12.0% compared to GC), Mcu protein levels were significantly reduced to 31.7±5.7% in Purkinje cell mitochondria (one-way Friedman test with post hoc testing: PC *vs* GC, *P*=0.0047; n=5 isolations). As previously reported (Sancak et al., 2013), protein levels of mitochondrial essential MCU regulator (Emre) correlate with Mcu levels and were also reduced in Purkinje cell and astrocytic mitochondria.

Next, I explored the capacity of cell type-specific mitochondria to uptake extramitochondrial Ca^{2+} and confirmed Mcu enrichment on the functional level in granule cells. In this in vitro assay, isolated mitochondria are spiked with Ca^{2+} injections and Ca^{2+} uptake is indirectly measured via the low-affinity Ca^{2+} indicator CalciumGreen-5N, which is impermeant. I isolated cell type-specific mitochondria from Purkinje cells, granule cells and astrocytes and probed their Ca^{2+} uptake in the absence or presence of Ru360, a Mcu inhibitor (Figure 37c). While mitochondria from granule cells (69.5±7.3%) and astrocytes (43.9±9.6%) buffered the Ca^{2+} pulse compared to the '+Ru360' condition, Purkinje cell mitochondria demonstrated a significantly reduced capacity (Figure 37d; 20.5±5.9%; one-way ANOVA with post hoc testing:

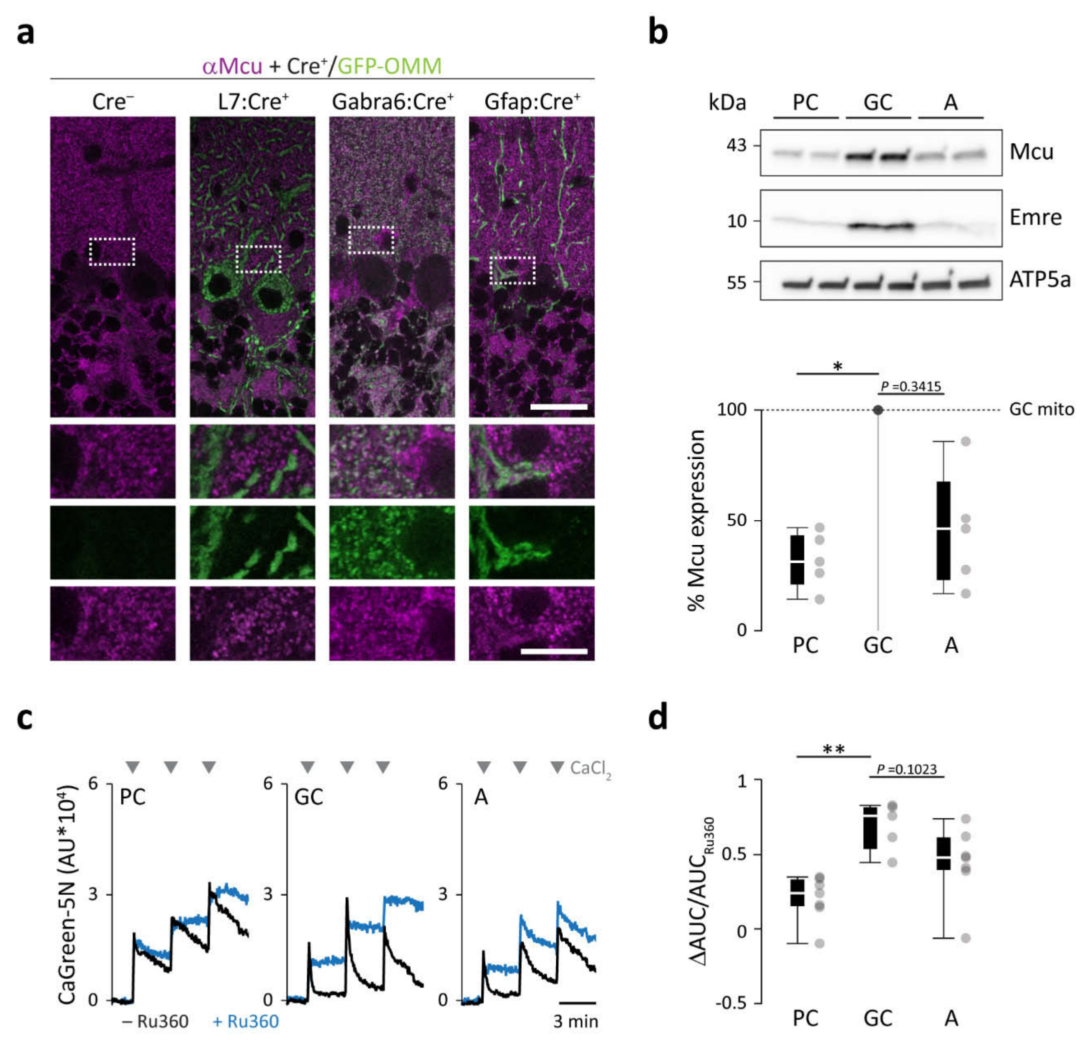

Figure 37│ Mcu is enriched in granule cell mitochondria and enables their Ca^{2+} uptake capacity. (**a**) Immunofluorescence staining of Mcu in cerebellum from wild type (Cre^{-}), L7:Cre^{+}/GFP-OMM, Gabra6:Cre^{+}/GFP-OMM and Gfap:Cre^{+}/GFP-OMM mice. Details show the merged channel with GFP-OMM (green) and single channels. Scale bars: 25 µm (detail 10 µm). (**b**) Western blot analysis of Mcu levels in cell type-specific mitochondria. Top: representative western blot of mitochondrial lysates from Purkinje cells (PC), granule cells (GC) and astrocytes (A) probing for Mcu, Emre and ATP5a. Bottom: quantification of Mcu shown as fold change to GC mitochondria and normalized to total protein amount and mitochondrial content. kDa, molecular weight in kilo Dalton; n=5 isolations quantified as technical duplicates. (**c**-**d**) Ca^{2+} uptake assay in cell type-specific mitochondria. (**c**) Representative experiment of immunocaptured mitochondria in the absence (black line) or presence of Ru360 (blue line). Ca^{2+} uptake is reflected by a decrease of extramitochondrial CaGreen-5N fluorescence after 20 µM CaCl$_2$ pulse (triangle). (**d**) Quantification of Ca^{2+} uptake related to the first CaCl$_2$ pulse and is shown as ΔAUC/AUC$_{Ru360}$. n≥5 isolations; box plot: median, quartile 1-3, whisker from min./max. value, and individual data points; *P* values from statistical testing are shown. Modified from Fecher et al. (2019), Figure 6.

PC *vs* GC, *P*=0.0018; n≥5 isolations). Again, astrocytic mitochondria showed a tendency towards a lower Ca^{2+} uptake capacity (GC *vs* A, *P*=0.1023; n≥5 isolations).

To further verify that Mcu expression was responsible for the observed Ca^{2+} uptake in granule cells, I generated a granule cell-specific Mcu knockout mouse model (see Chapter 3.2.3.3). For this, Gabra6:Cre^{+}/GFP-OMM mice were crossed to Mcu^{tm1c} mice, which harbor loxP sites around exon 5 of the murine *Mcu* locus. First, I confirmed Mcu deletion in granule cells by immunofluorescence staining (Figure 38a). While in Mcu$^{GC:WT}$ mice GFP-OMM colocalized with Mcu signals, this colocalization was absent in Mcu$^{GC:ko}$ mice and Mcu signals were most prominent in neural cells of the molecular layer, likely interneurons or Bergmann glia. Secondly, I immunocaptured granule cell mitochondria from Mcu^{tm1c} crossings and quantified Mcu deletion by western blot analysis (Figure 38b). Here, Mcu protein levels were significantly reduced to 54.7±4.4% in Mcu$^{GC:+/-}$ and 6.1±0.8% in Mcu$^{GC:ko}$ animals (one-way REML with Geisser-Greenhouse correction and post hoc testing: *P*<0.0001; n≥6 mice). Additionally, Emre was undetectable in Mcu$^{GC:ko}$ mitochondria.

Finally, I tested these mitochondria in Ca^{2+} uptake assays and confirmed that Mcu deletion abolishes the observed Ca^{2+} uptake in granule cell mitochondria (Figure 38c). While immunocaptured mitochondria from Mcu$^{GC:WT}$ (69.5±7.3%) and Mcu$^{GC:+/-}$ animals (54.9±6.2%) buffered Ca^{2+} compared to the '+Ru360' condition, mitochondria from Mcu$^{GC:ko}$ failed in this assay (Figure 38d; -0.14±6.7%; one-way ANOVA with post hoc testing: GC:WT *vs* GC:*ko* and GC:+/− *vs* GC:*ko*, *P*<0.0001; n≥5 mice). Interestingly, despite the reduction of Mcu to 54.7% in heterozygous Mcu$^{GC:+/-}$ animals, mitochondrial Ca^{2+} uptake was not significantly different compared to Mcu$^{GC:WT}$ (GC:WT *vs* GC:+/−, *P*=0.3344; n≥5 mice). I observed similar results in astrocytic mitochondria, where Mcu is reduced to 45.4% compared to granule cell mitochondria; also, here, no significant difference was noticed in Ca^{2+} uptake capacity (Figure 37d).

In summary, these experiments functionally corroborated our finding of the enhanced expression of the Mcu complex in granule cell mitochondria and their related superior ability to buffer Ca^{2+} compared to other cerebellar cell types. Interestingly, while neuronal mitochondria from Purkinje cells were unable to uptake Ca^{2+} in vitro, astrocytic mitochondria performed well in this task despite lower Mcu expression. Surprisingly, granule cell-specific ablation of Mcu did not cause behavioral alterations or neuronal death up to 6 month of age.

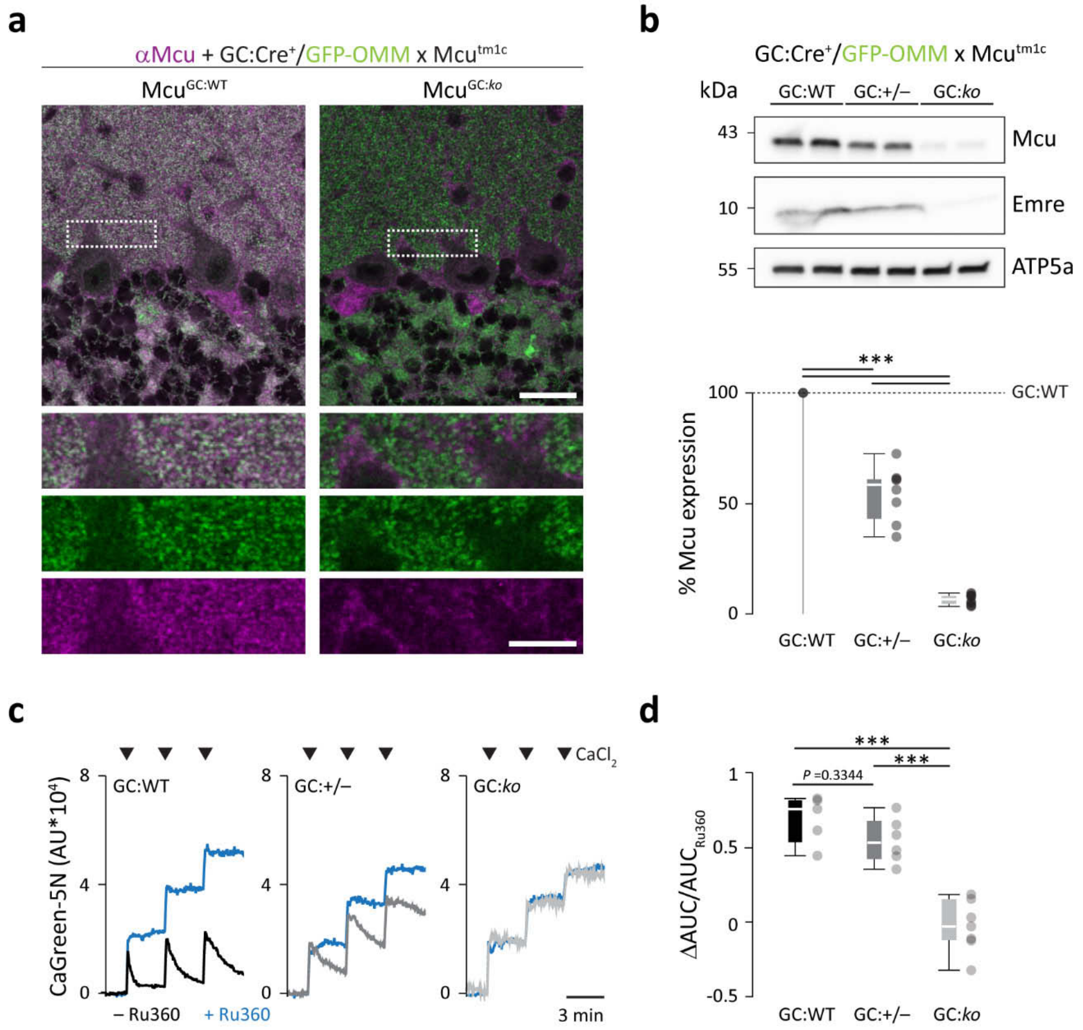

Figure 38│ Ablation of Mcu in granule cells disrupts Ca^{2+} uptake capacity. Granule cell-specific ablation of Mcu was generated by breeding Gabra6:Cre^{+} mice (GC:Cre^{+}) with Mcu^{tm1c} mice. (**a**-**b**) Validation of Mcu depletion in granule cells. (**a**) Mcu staining in cerebellum from GC:Cre^{+}/GFP-OMMx$Mcu^{GC:WT}$ and GC:Cre^{+}/GFP-OMMx$Mcu^{GC:\mathit{ko}}$ mice. Details show the merged channel with GFP-OMM (green) and single channels. Scale bars: 25 µm (detail 10 µm). (**b**) Western blot analysis of Mcu levels in granule cell mitochondria with $Mcu^{GC:WT}$, $Mcu^{GC:+/-}$ and $Mcu^{GC:\mathit{ko}}$ background. Top: representative western blot of mitochondrial lysates from $Mcu^{GC:WT}$ (GC:WT, black), $Mcu^{GC:+/-}$ (GC:+/–, dark gray) and $Mcu^{GC:\mathit{ko}}$ (GC:*ko*, light gray) probing for Mcu, Emre and ATP5a. Bottom: quantification of Mcu shown as fold change to WT mitochondria and normalized to total protein amount and mitochondrial content. kDa, molecular weight in kilo Dalton; n≥6 mice quantified as technical duplicates. (**c**-**d**) Ca^{2+} uptake assay in Mcu-deficient granule cell mitochondria. (**c**) Representative experiment of immunocaptured granule cell mitochondria with $Mcu^{GC:WT}$, $Mcu^{GC:+/-}$ and $Mcu^{GC:\mathit{ko}}$ background in the absence or presence of Ru360 (blue line). Ca^{2+} uptake is reflected as a decrease of extramitochondrial CaGreen-5N fluorescence after 20 µM $CaCl_2$ pulse (triangle). (**d**) Quantification of Ca^{2+} uptake related to the first $CaCl_2$ pulse and is shown as $\Delta AUC/AUC_{Ru360}$. n≥5 mice; box plot: median, quartile 1-3, whisker from min./max. value, and individual data points; *P* values from statistical testing are shown. Modified from Fecher et al. (2019), Figure 6.

4.5. Enhanced ER-mitochondria contact sites in Purkinje cells via Rmdn3

Mitochondria form privileged sites of contact with a number of other cellular organelles. These sites are established via tether and spacer proteins (reviewed in Scorrano et al., 2019) and establish cellular communication and signaling (see Chapter 1.2.4). Given the importance of these organelle contact sites, we were especially interested in Rmdn3 among the candidates enriched in Purkinje cells. This outer mitochondrial membrane protein (Lv et al., 2006) has been described as tether between the endoplasmic reticulum (ER) and mitochondria (Stoica et al., 2014) via the interaction with ER-resident proteins, like VAPB (De Vos et al., 2012) and ORP5/8 (Galmes et al., 2016). Koch et al. (2009) previously reported neuronal expression of Rmdn3 and specifically its enrichment in a subpopulation of Purkinje cells with strong signals in dendrites. I therefore optimized immunofluorescence staining of Rmdn3 in mouse tissue and validated its abundance in Purkinje cells (Figure 39a). In contrast to Koch et al. (2009), I detected Rmdn3 uniformly in all Purkinje cells and throughout their cellular geometry. Penetration issues often hinder axonal labeling of mitochondria; however, frequently Purkinje cell axons were positive for Rmdn3 – especially in recurrent axon branches to neighboring Purkinje cells. Furthermore, our Rmdn3 antibody recognized the full-length isoform of 51 kDa and additional higher molecular weight forms (Figure A5b), while the antibody by Koch et al. (2009) mainly detected a smaller, 30-34 kDa band in cerebellum. Rmdn3 signals colocalized with GFP-OMM signals in L7:Cre$^+$/GFP-OMM tissue further confirming its mitochondrial localization, while mitochondria in granule cells and astrocytes were devoid of Rmdn3 signals.

Related to the abundant in vitro literature of Rmdn3 and VAPB as tether between the ER and mitochondria, we hypothesized that Rmdn3 abundance in Purkinje cells might be linked to an increased ER-mitochondria contact in vivo. To test this theory, we performed ultrastructural analysis of organelle contacts in wild type cerebellum. Nicolas Snaidero (N.S.; Institute of Neuronal Cell Biology, TUM) performed tissue preparation for electron microscopy and acquired images, which were further quantified by me in a blinded manner. I quantified contact sites within a distance of ≤30 nm between mitochondrial perimeter and ER using images from Purkinje cell and granule cell perikarya as well as from areas around the nucleus of astrocytes, which adjoined Purkinje cell perikarya (Figure 39b). While the cellular organization of Purkinje cell and adjoined astrocyte was similar in terms of organelle composition and space, the cytoplasm of granule cells was thin due to the dense packing of

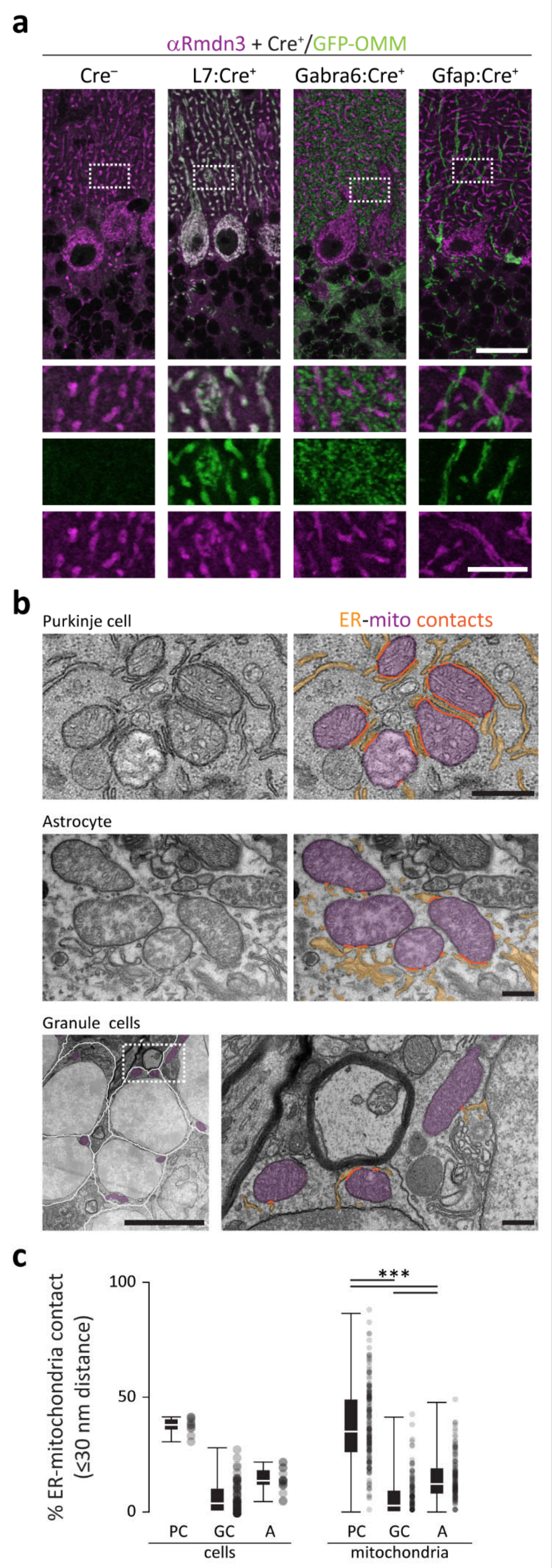
a
αRmdn3 + Cre+/GFP-OMM
Cre−
L7:Cre+
Gabra6:Cre+
Gfap:Cre+
b
Purkinje cell
ER-mito contacts
Astrocyte
Granule cells
c
% ER-mitochondria contact (≤30 nm distance)
100
50
0
***
PC
GC
A
cells
PC
GC
A
mitochondria

Figure 39| Rmdn3 and ER-mitochondria contact sites are enriched in Purkinje cells. (**a**) Immunofluorescence staining of Rmdn3 in cerebellum from wild type (Cre⁻), L7:Cre⁺/GFP-OMM, Gabra6:Cre⁺/GFP-OMM and Gfap:Cre⁺/GFP-OMM mice. Details show the merged channel with GFP-OMM (green) and single channels. Scale bars: 25 µm (detail 10 µm). (**b**) Electron micrographs from wild type cerebellum depicting intracellular organelles in Purkinje cell (PC), astrocyte (A) and granule cell (GC). For granule cells, an overview with multiple cells in the granule cell layer is shown (cell outline, white) and detail. Right side: organelles are color-coded: mitochondria, magenta; ER, yellow; contact sites ≤ 30 nm, orange. Scale bars: 400 nm (GC overview 5 µm). (**c**) Ultrastructural analysis of ER-mitochondria contact sites shown as % mitochondrial perimeter in ≤30 nm distance to the ER. Per cell type, the quantification is shown with cells (left side; n≥10 cells from two animals) and mitochondria (right side; n≥120 mitochondria from two mice) as entities. Box plot: median, quartile 1-3, whisker from min./max. value, and individual data points; *P* values from statistical testing are shown and were performed based on mitochondria as entities due to differences in cell geometry. Modified from Fecher et al. (2019), Figure 7.

cells in the granule cell layer (Figure 39b, granule cells overview). In contrast, mitochondrial size was similar between granule cells and astrocytes, while Purkinje cell mitochondria were smaller (see scale bar difference, Figure 39b). Quantification of ER-mitochondria contact sites revealed a significant increase in Purkinje cells (37.7±1.3%) compared to either granule cells (6.1±0.7%) or astrocytes (14.5±0.9%; one-way Kruskal-Wallis test with post hoc testing: in all cases, $P<0.0001$; n≥120 mitochondria from two mice; Figure 39c).

Still, the observations so far represented a correlation between high abundance of Rmdn3 and high frequency of ER-mitochondria contact sites in Purkinje cells, which might be unrelated to Rmdn3 itself. To demonstrate that Rmdn3 directly mediates organelle contacts in vivo, we obtained a knockout-first allele of Rmdn3 from the KOMP Repository (Rmdn3$^{\mathrm{tm1a}}$; see Chapter 3.2.3.4). These mice harbor an expression cassette between exon 2 and 5 of the murine *Rmdn3* locus, which disturbs normal expression. First, I confirmed Rmdn3 deletion in Rmdn3^{ko} mice by immunofluorescence staining (Figure 40a). While I observed strong Rmdn3 signals in Purkinje cells of Rmdn3$^{\mathrm{WT}}$ cerebellum, these signals were absent in the cerebellum from Rmdn3^{ko} mice. Here, weak signals in Bergmann glia were observed, which are likely unspecific and caused by antibody binding in the absence of target. Secondly, I quantified Rmdn3 protein levels by western blot analysis (Figure 40b). I probed total cerebellum with Rmdn3 antibody and confirmed a significant reduction of full-length Rmdn3 protein and its higher molecular weight forms in Rmdn3^{ko} tissue (11.4±3.5%; RM one-way ANOVA with post hoc testing: all conditions, P<0.001; n=4 animals). No smaller molecular weight bands were detected with our antibody in Rmdn3$^{\mathrm{ko}}$ tissue (Figure A5b). Additionally, the mouse model reduced Rmdn3 levels in a gene dose-dependent manner with Rmdn3 protein levels of 46.5±3.3% in Rmdn3$^{+/-}$ tissue when compared to Rmdn3$^{\mathrm{WT}}$.

Finally, we characterized ER-mitochondria contact sites in Rmdn3$^{\mathrm{ko}}$ tissue. For this, N.S. performed sample preparation and image acquisition in perikarya of Purkinje cells and adjoined astrocytes, and I quantified the frequency of organelle contacts within a distance of ≤30 nm in a blinded manner. While the frequency of ER-mitochondria contact sites was unchanged in astrocytes upon Rmdn3 depletion (Figure 40c, right side; one-way ANOVA with post hoc testing: $P=0.0935$; n≥10 cells from 2-3 mice), organelle contacts were significantly reduced in Purkinje cells in a gene dose-dependent manner: Rmdn3$^{\mathrm{WT}}$, 37.1±1.8%; Rmdn3$^{+/-}$, 28.3±1.3%; Rmdn3^{ko}, 19.6±1.3% (Figure 40c, left side; one-way ANOVA with post hoc testing: WT *vs* +/−, $P=0.0022$; WT *vs ko*, $P<0.0001$; +/− *vs ko*, $P=0.0016$; n≥8 cells from 2-3 mice).

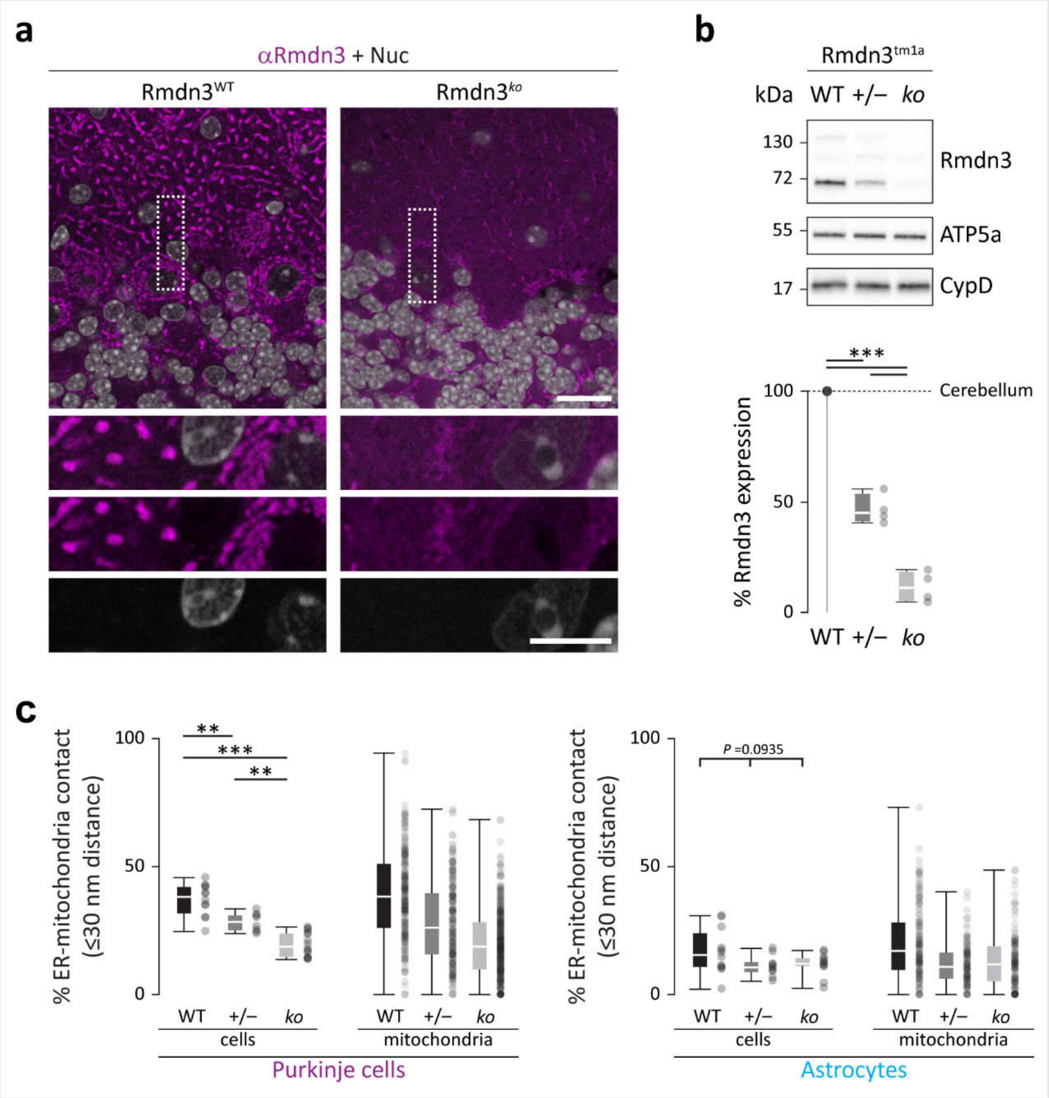

Figure 40| Rmdn3 mediates ER-mitochondria contact sites in Purkinje cells in vivo. (**a**-**b**) Validation of Rmdn3 depletion in cerebellum of Rmdn3^{tm1a} mice. (**a**) Immunofluorescence staining of Rmdn3 in cerebellum from wild type (Rmdn3^{WT}) and Rmdn3^{tm1a} (Rmdn3^{ko}) mice. Details show the merged channel with nuclear counter stain (Nuc) and single channels. Note defuse antibody signals in Rmdn3^{ko} tissue likely due to antibody specificity. Scale bars: 25 μm (detail 10 μm). (**b**) Western blot analysis of Rmdn3 levels in mouse cerebellum from Rmdn3^{WT} (black), Rmdn3$^{+/-}$ (dark gray) and Rmdn3^{ko} (light gray) mice. Top: representative western blot of total cerebellum lysate probing for Rmdn3, ATP5a and CypD. Bottom: quantification of Rmdn3 (51-130 kDa) shown as fold change to Rmdn3^{WT} and normalized to total protein amount and mitochondrial content. kDa, molecular weight in kilo Dalton; n=4 mice quantified as technical triplicates. (**c**) Ultrastructural analysis of ER-mitochondria contact sites in Purkinje cells (left side, magenta) and astrocytes (right side, blue) from Rmdn3^{WT}, Rmdn3$^{+/-}$ and Rmdn3^{ko} mice. Quantification is shown as % mitochondrial perimeter in ≤30 nm distance to the ER and per cell type. Either cells (PC, n≥8 cells; A, n≥10 cells from 2-3 mice) or mitochondria (PC, n≥189 mitochondria; A, n≥105 cells from 2-3 mice) were used as entities. Box plot: median, quartile 1-3, whisker from min./max. value, and individual data points; *P* values from statistical testing are shown and were performed based on cells as entities for the comparison among genotypes. Modified from Fecher et al. (2019), Figure 7.

In summary, we demonstrated that Rmdn3 is highly enriched in Purkinje cells as predicted by our cell type-specific profiling of mitochondria. In Purkinje cells, it participates in approximately half of the established contact sites between the ER and mitochondria given that the organelle contact frequency drops in Rmdn3^{ko} Purkinje cells from 37.1% to 19.6%. Interestingly, on the one hand, other tether proteins are not compensating for the loss of Rmdn3, which speaks for the specificity of its tethering function and interaction partners. On the other hand, Rmdn3^{ko} mice behave normal without Purkinje cell loss up to an age of one year, which might hint to compensation by other pathways unrelated to ER-mitochondria contact sites.

4.6. Mitochondrial diversity in health and disease

Our profiling of cell type-specific mitochondria in mouse cerebellum has led us to the discovery of a number of unique specializations among neural mitochondria. In Chapter 4.2, I have linked the validation of selected candidates by immunofluorescence staining to their so far reported biological function, which in many cases is incomplete and not studied with regard to the here reported cell type-enrichment. In the case of beta-oxidation in astrocytes, mitochondrial Ca^{2+} uptake in granule cells and ER-mitochondrial contact sites in Purkinje cells, we have confirmed our profiling prediction and further corroborated the cell type-specific enrichment of these mitochondrial functions in the respective cell types.

However, apart from characterizing individual candidates in their function and contribution to cellular physiology, these proteins also represent cell type-specific ‘markers’ of mitochondria in neural tissue – with the current validation in mouse cerebellum. Mitochondrial form is frequently used for the analysis of disease models and pathology (reviewed in Eisner et al., 2018; Friedman and Nunnari, 2014) and it is intimately related to mitochondrial function (Benard et al., 2007; reviewed in Zick et al., 2009). Therefore, the application of cell type-specific mitochondrial markers in the central nervous system might be a powerful tool to investigate mitochondrial contribution to development, health and disease.

4.6.1. Mitochondrial markers are conserved across neural tissues and species

To establish cell type-specific mitochondrial 'markers' as tool to characterize mitochondrial involvement in development, health and disease, further validation was necessary in other neural tissues and potential species of interest.

First, I confirmed the presence of mitochondrial markers in mouse cortex (Figure 41) and spinal cord (Figure 42). Here, GFP-OMM was used to confirm mitochondrial localization using the Cre-driver lines Rbp4:Cre for excitatory neurons of layer 5 (Figure 41a), Gfap:Cre for astrocytes and ChAT:Cre for cholinergic neurons including motor neurons in spinal cord (Figure 42a). While Cox4i1 signals colocalized with GFP-OMM in all three crossings, other mitochondria were labeled in addition as previously seen in cerebellum (Figure 19). This further confirmed Cox4i1 as pan-mitochondrial protein.

Among mitochondrial markers enriched in neurons, I confirmed enrichment of Ociad2 and Protein NipSnap homolog 1 (Nipsnap1). In cerebellum, Ociad2 was enriched in Purkinje cells (Figure 25b and 26a) and was previously introduced as outer mitochondrial membrane protein. In mouse cortex, Ociad2 colocalized with a subset of neurons in the cortex and CA3 region of the hippocampus. Interestingly, Ociad2 signals overlapped well with the genetic label from Rbp4:Cre in layer 5/6 neurons. In spinal cord, Ociad2 signals appeared dim and mostly restricted to neuronal perikarya (Figure 41b). Astrocytic mitochondria were devoid of Ociad2 signal in both tissues (Figure 41c and 42c).

From our initial profiling of cerebellar mitochondria, we found Nipsnap1 (two-tailed, unpaired *t*-test with permutation-adjusted q-value: PC *vs* A: *0.79, 0.0027; GC *vs* A: *1.169, 0.0002; PC *vs* GC: -0.38, 0.1036) significantly enriched in granule cell mitochondria and I validated its neuronal enrichment in cerebellum as one of the selected candidates (Figure A1d). Immunofluorescence staining could not confirm a higher fold change in granule cell

Figure 41 | Cell type-specific mitochondrial markers distinguish neuronal and astrocytic mitochondria in cortex. (**a**) Cre-driver lines crossed to the MitoTag mouse line to tag mitochondria in excitatory neurons of layer 5/6 via Rbp4:Cre and astrocytes via Gfap:Cre. Brain overview shows general expression pattern for Rbp4:Cre and details show expression patterns for both lines in mouse cortex. Scale bars: 1 mm (brain); 25 µm cortex. (**b**-**c**) Immunofluorescence staining of candidates in cortex from (**b**) Rbp4:Cre$^+$/GFP-OMM and (**c**) Gfap:Cre$^+$/GFP-OMM mice. Cox4i1 is a ubiquitous mitochondrial protein. Proteins are enriched in: neurons, Nipsnap1 and Ociad2; and astrocytes, Gldc and Sfxn5. All proteins localize to mitochondria. Details show the merge channel and the single channels for GFP-OMM (green) and the candidate (magenta). Scale bars: 25 µm (detail 10 µm). Modified from Fecher et al. (2019), Supplementary Figure 12.

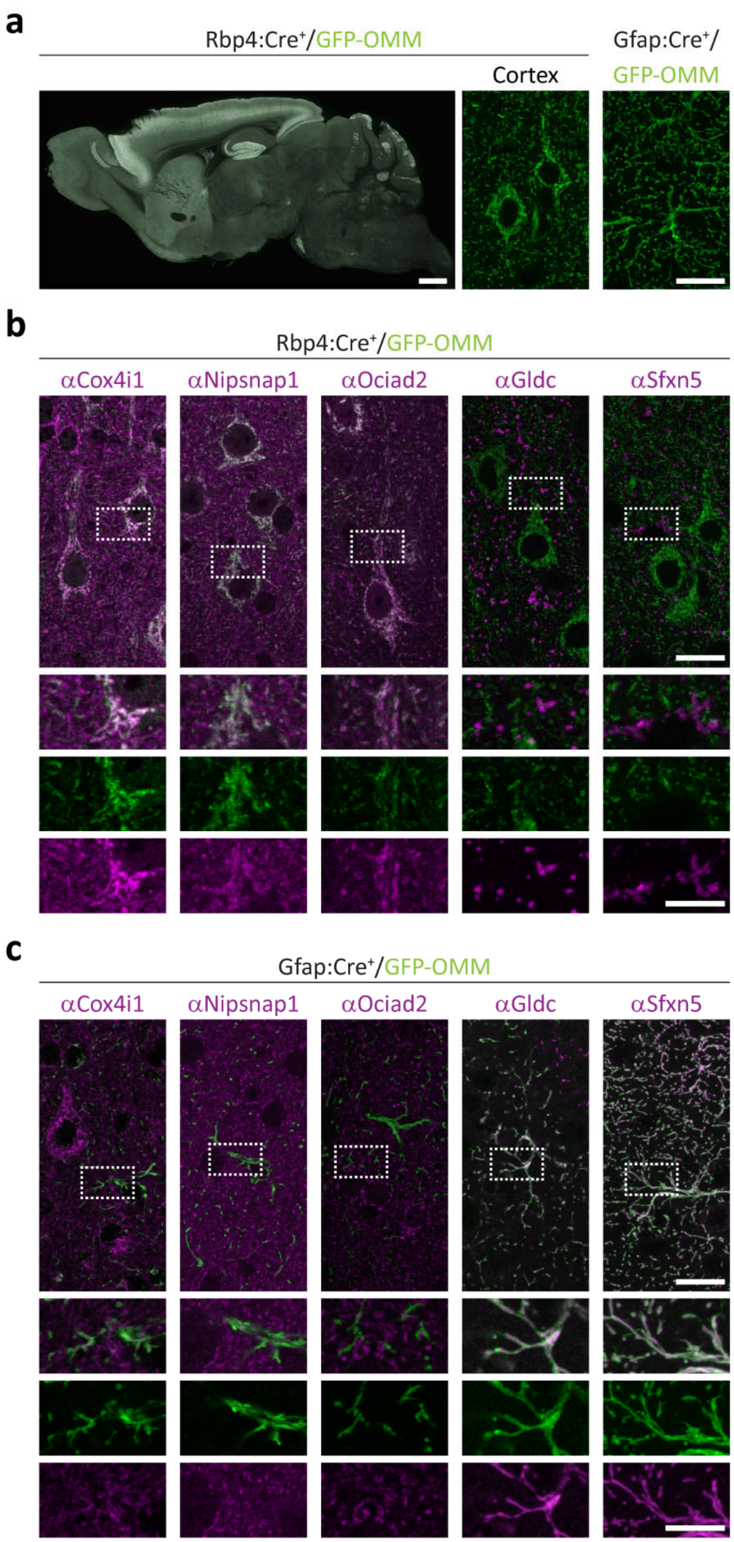
a
Rbp4:Cre+/GFP-OMM
Cortex
Gfap:Cre+/
GFP-OMM
b
Rbp4:Cre+/GFP-OMM
αCox4i1
αNipsnap1
αOciad2
αGldc
αSfxn5
c
Gfap:Cre+/GFP-OMM
αCox4i1
αNipsnap1
αOciad2
αGldc
αSfxn5

Figure 41| Cell type-specific mitochondrial markers distinguish neuronal and astrocytic mitochondria in cortex (see previous page for legend).

mitochondria compared to Purkinje cells and therefore, Nipsnap1 was classified as neuronal as previously reported by Nautiyal et al. (2010). This result was confirmed in mouse cortex and spinal cord, where Nipsnap1 signals colocalized with neuronal expressed GFP-OMM (Figure 41b and 42b), but not with astrocytic labeling (Figure 41c and 42c).

Among astrocytic candidates, I confirmed cell type-specific expression of Gldc and Sfxn5 in cortex and spinal cord (Figure 41c and 42c). Both proteins were absent in neuronal mitochondria (Figure 41b and 42b). While astrocytic mitochondria were evenly distributed in cortex – known as astrocyte tiling (Bushong et al., 2002), signals from astrocytic mitochondria were intense in spinal cord gray matter, but sparse in white matter (Figure 42a). This might reflect astrocyte density or heterogeneity (reviewed in Lundgaard et al., 2014).

Other cell type-enriched candidates from cerebellum were less useful to differentiate neural mitochondria in cortex and spinal cord. For example, Rmdn3 signals were present in neuronal mitochondria, but dimmer than in cerebellum and evenly distributed among neurons. In contrast, Got2 signals saturated at the tissue sections surface due to its high neuronal abundance. Mcu was highly enriched in CA3 neurons of the hippocampus as previously reported (Markus et al., 2016), but discriminated less well neuronal from astrocytic mitochondria than in cerebellum.

Still, the experiments in cortex and spinal cord provided use with a pan-neuronal (Nipsnap1), a neuronal subtype (Ociad2) and two astrocytic (Gldc, Sfxn5) markers that efficiently recognize cell type-specific mitochondria across tissues – in contrast to the pan-mitochondrial marker Cox4i1.

Secondly, we questioned whether mitochondrial diversity as observed in mouse cerebellum could be conserved across species and therefore tested mitochondrial markers in cerebellum of other mammals. Conservation across species would be a remarkable result given its application for biomedical research that often uses rodent animal models to explore human

Figure 42 | Cell type-specific mitochondrial markers distinguish neuronal and astrocytic mitochondria in spinal cord. (**a**) Cre-driver lines crossed to the MitoTag mouse line to tag mitochondria in cholinergic neurons including motor neurons via ChAT:Cre and astrocytes via Gfap:Cre. Spinal cord overviews show general expression pattern with details of ventral horn. Scale bars: 500 μm (detail 25 μm). (**b**-**c**) Immunofluorescence staining of candidates in spinal cord from (**b**) ChAT:Cre$^+$/GFP-OMM and (**c**) Gfap:Cre$^+$/GFP-OMM mice. Cox4i1 is a ubiquitous mitochondrial protein. Proteins are enriched in: neurons, Nipsnap1 and Ociad2; and astrocytes, Gldc and Sfxn5. All proteins localize to mitochondria. Details show the merge channel and the single channels for GFP-OMM (green) and the candidate (magenta). Scale bars: 25 μm (detail 10 μm). Modified from Fecher et al. (2019), Supplementary Figure 12.

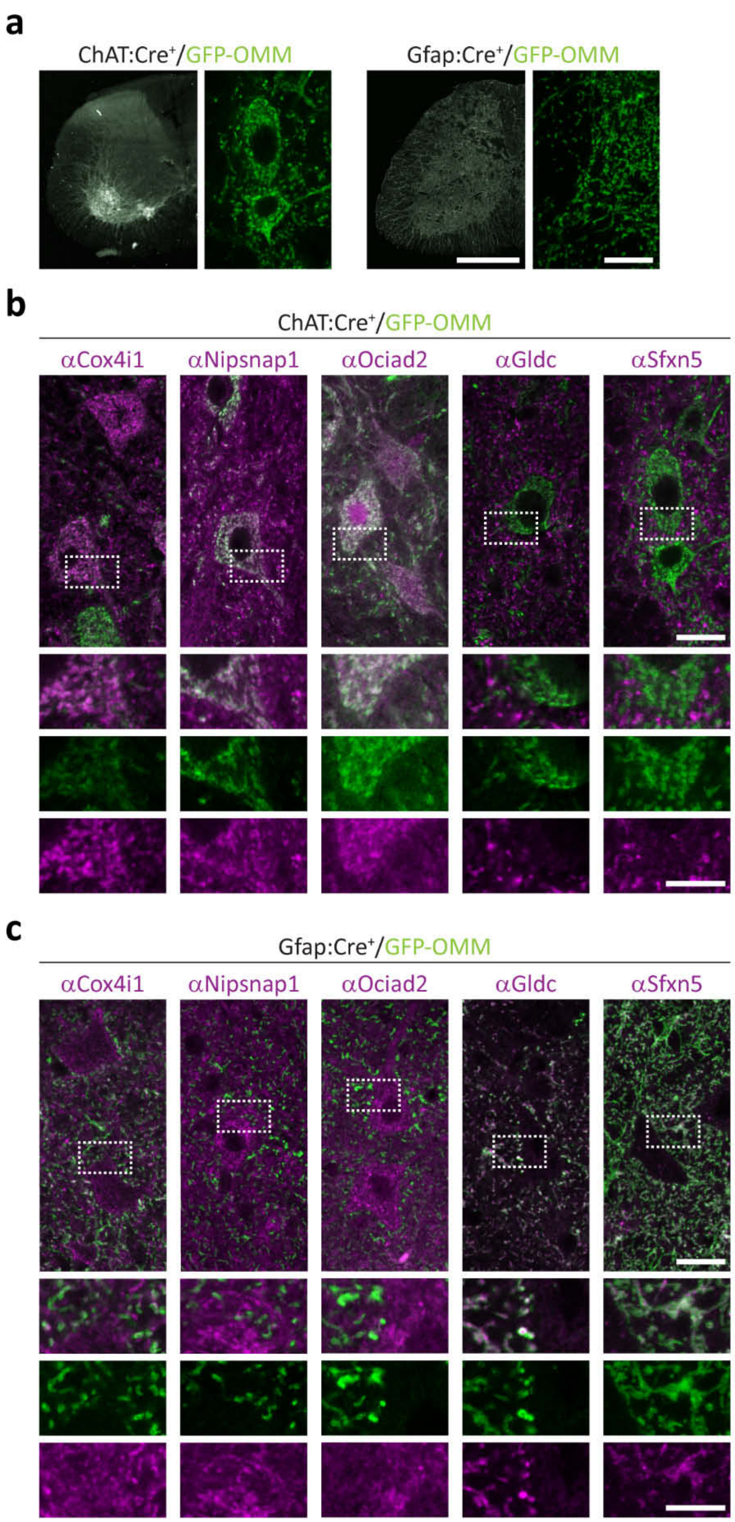
a
ChAT:Cre+/GFP-OMM
Gfap:Cre+/GFP-OMM
b
ChAT:Cre+/GFP-OMM
αCox4i1
αNipsnap1
αOciad2
αGldc
αSfxn5
c
Gfap:Cre+/GFP-OMM
αCox4i1
αNipsnap1
αOciad2
αGldc
αSfxn5

Figure 42| Cell type-specific mitochondrial markers distinguish neuronal and astrocytic mitochondria in spinal cord (see previous page for legend).

diseases with subsequent validation in human specimen. To answer this question, I chose four markers to illustrate mitochondrial heterogeneity across species: Nipsnap1, Got2, pan-neuronal; Rmdn3, Purkinje cell-enriched; and Gldc, Sfxn5, astrocyte-enriched.

The cerebellum of mouse, rat and human is similarly composed in structure with individual lobules and the organization into layers – despite their obvious difference in scale (Figure 43a). Human sample were provided by Doron Merkler and immunofluorescence staining performed by Ingrid Wagner (Department of Pathology and Immunology, University of Geneva, Switzerland). I performed acquisition of human samples and immunofluorescence staining in mouse and rat. In all three species, cell type-specific mitochondria were visualized with the selected markers (Figure 43b) – except for Nipsnap1 in human cerebellum, which was not tested and replaced by Got2 (pan-neuronal). Remarkably, I observed identical patterns and distributions of mitochondria in mouse and rat with the labeling of neuronal (Nipsnap1),

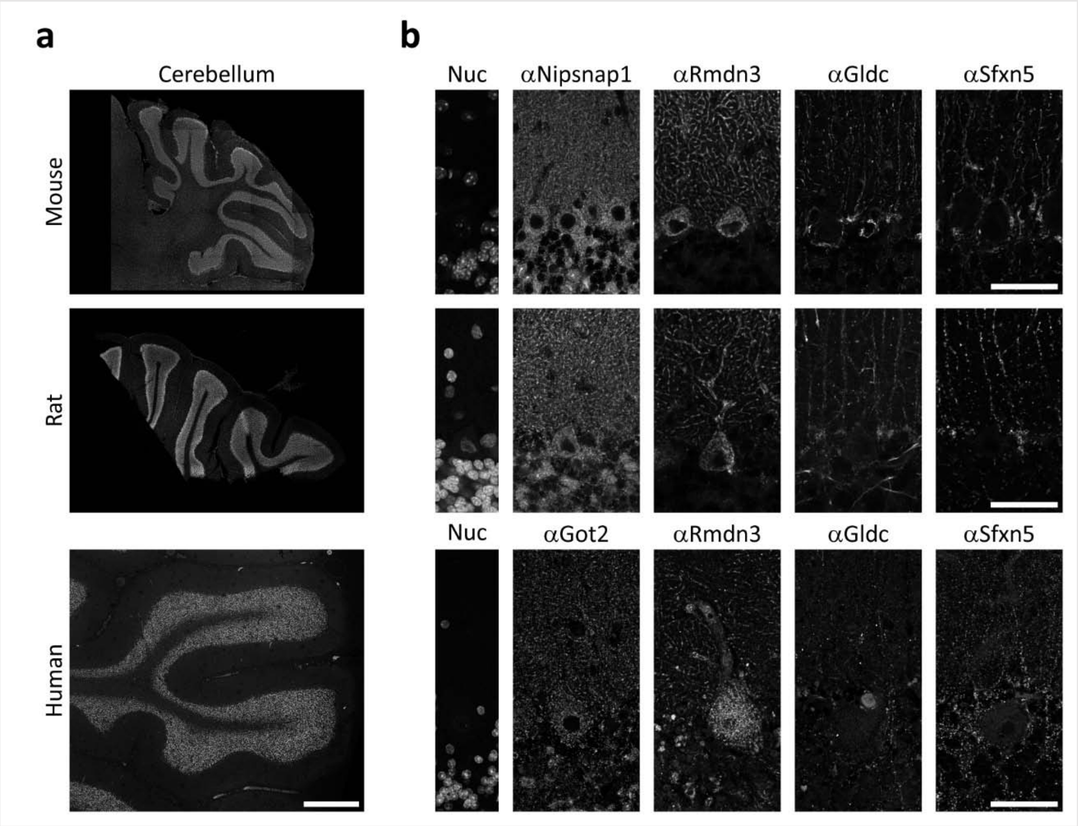

Figure 43│ Cell type-specific mitochondrial markers distinguish neuronal and astrocytic mitochondria in mouse, rat and human cerebellum. (**a**) Cerebellum overview from mouse (sagittal section, full), rat (coronal section, part) and human (coronal section, part) by visualizing nuclei with DAPI or Hoechst staining. Scale bar: 1 mm. (**b**) Immunofluorescence staining of candidates in cerebellum of different species. Cell type-specific mitochondria are stained against: Nipsnap1 and Got2 for neurons; Rmdn3 for Purkinje cells; and Gldc and Sfxn5 for astrocytes. Nuc, nuclear counter stain for tissue orientation. Scale bars: 50 µm.

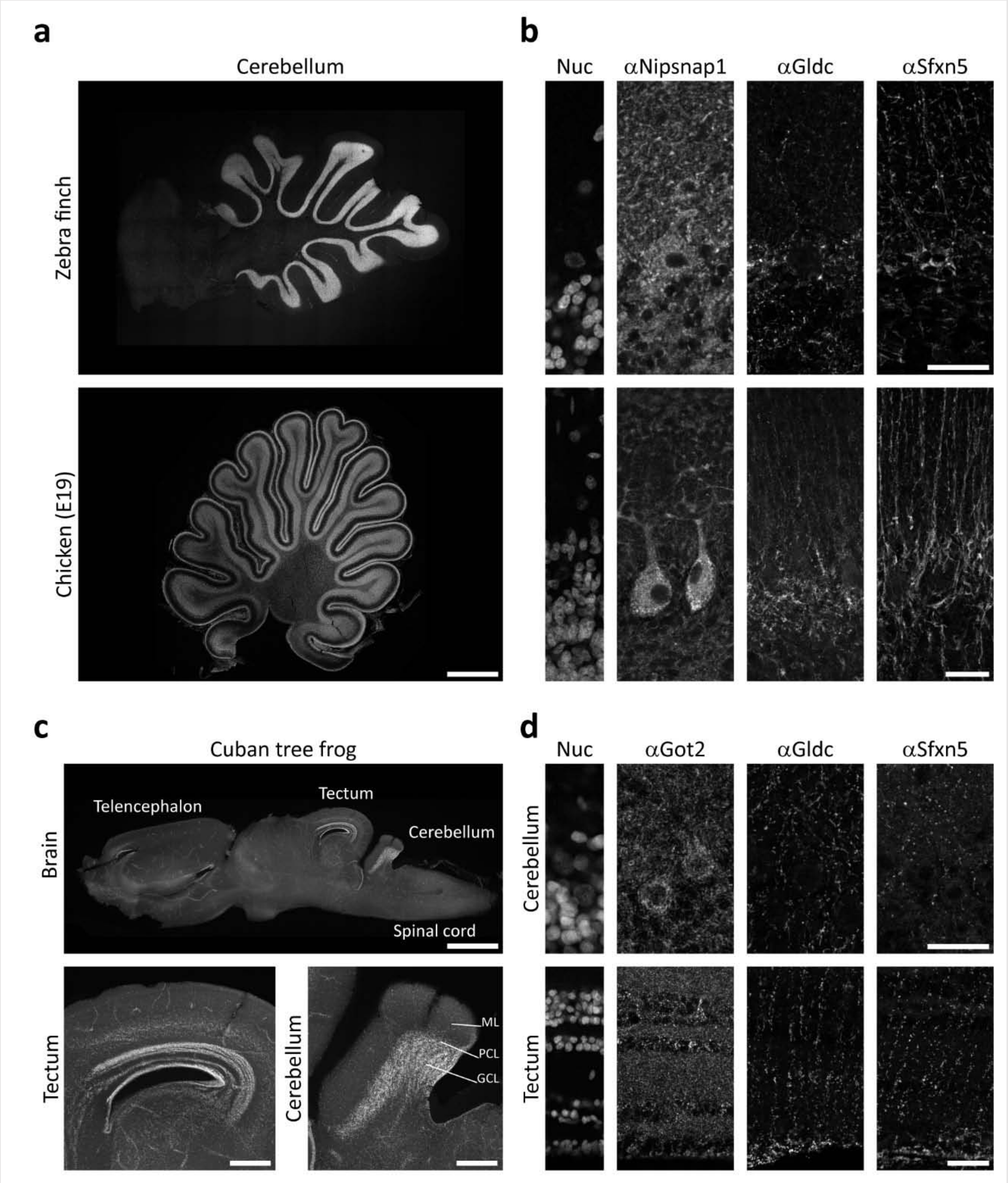
a
Cerebellum
Zebra finch
Chicken (E19)
b
Nuc
αNipsnap1
αGldc
αSfxn5
c
Cuban tree frog
Brain
Telencephalon
Tectum
Cerebellum
Spinal cord
Tectum
Cerebellum
ML
PCL
GCL
d
Nuc
αGot2
αGldc
αSfxn5
Cerebellum
Tectum

Figure 44│ Cell type-specific mitochondrial markers distinguish neuronal and astrocytic mitochondria in aves and amphibian. (**a**) Cerebellum overview (sagittal section) from embryonic day 19 chicken and zebra finch by visualizing nuclei with DAPI. Scale bar: 1 mm. (**b**) Immunofluorescence staining of candidates in avian cerebellum. Cell type-specific mitochondria are stained against: Nipsnap1 for neurons; Gldc and Sfxn5 for astrocytes. Note immature layering of chicken cerebellum due to developmental stage. Nuc, nuclear counter stain for tissue orientation. Scale bars: 25 µm. (**c**) Brain overview (sagittal section) and details of tectum and cerebellum from Cuban tree frog by visualizing nuclei with DAPI. GCL, granule cell layer; PCL, Purkinje cell layer; ML, molecular layer. Scale bars: 1 mm (detail 200 µm). (**d**) Immunofluorescence staining of candidates in cerebellum and tectum. Cell type-specific mitochondria are stained against: Got2 for neurons; Gldc and Sfxn5 for astrocytes. Nuc, nuclear counter stain for tissue orientation. Scale bars: 25 µm.

Purkinje cell (Rmdn3) and astrocytic (Gldc, Sfxn5) mitochondria. In human cerebellum, I noticed similar distributions and patterns as in rodents confirming the cell type-enrichment of our mitochondrial markers despite differences in signal contrast. These differences are likely due to altered fixation and staining method of human tissue (see Chapter 3.2.14.2).

After these exciting results in rodent and human tissue, I further questioned whether mitochondrial markers were also preserved in more distant species, like aves and amphibian (Figure 44). I performed these experiments during my fellowship at the Marine Biological Laboratory in Woods Hole, where I had access to these species through the generous donation from other Grass fellows. Among aves, I tested mitochondrial markers in adult zebra finch and embryonic day 19 (E19) chicken, which have a foliated cerebellum like mammals (Figure 44a). In all cases, the distribution of neural mitochondria was comparable to results in rodent and human tissue. Specifically, Gldc and Sfxn5 distinguished astrocytic mitochondria, while neuronal mitochondria were identified by Nipsnap1 in both species (Figure 44b); however, no Rmdn3 signals could be detected. Despite the advanced development of chicken cerebellum before hatching (Akar and Sur, 2010), I observed an immature Purkinje cell morphology and incomplete cell migration at E19 (Figure 44a, overview chicken).

Next, I performed immunofluorescence staining in tissue from Cuban tree frog, an amphibian, with a flat sheet cerebellum (Figure 44c). Despite the lack of foliation, the amphibian cerebellum is layered in GCL, PCL and ML. Again, I could not detect Rmdn3 signals. However, I observed Gldc and Sfxn5 signals that distinguished a subset of mitochondria in frog cerebellum – similar to mitochondria in Bergmann glia and astrocytes of mouse cerebellum (Figure 44d). Additionally, Nipsnap1 was abundantly present, labeled mitochondria-like structures and was likely specific to neurons. Similar results were obtained from another brain structure, the 8-layered optic tectum. While I observed a broad labeling with Nipsnap1, Gldc and Sfxn5 signals were sparsely distributed among layers indicating possibly astrocytic mitochondria and hinting to an overall neuronal *vs* astrocytic pattern.

In summary, these experiments demonstrated that cell type-specific mitochondrial candidates from cerebellum are conserved in their neuronal *vs* astrocytic distribution in mouse cortex and spinal cord. Hence, these proteins can be termed as cell type-specific 'markers' in the central nervous system. Furthermore, exploration of mitochondrial markers from cerebellum across species affirmed their presence in amphibian, aves, rodents and human.

4.6.2. Cell type-specific mitochondria in AD and ALS

After establishing our cell type-specific mitochondrial markers across tissues, we decided to demonstrate them as tool for biomedical research to characterize neural mitochondria in mouse models of neurodegeneration and related patient samples. Mitochondrial dysfunction is implicated in many neurodegenerative diseases, such as Parkinson's disease, Alzheimer's disease (AD) and amyotrophic lateral sclerosis (ALS; see Chapter 1.7). Here, morphological analysis of mitochondria – mostly via ultrastructure (Johnson and Blum, 1970; Baloyannis, 2006) – is exclusively focused on neurons and their cell soma given that this region can be identified in a cell type-specific manner via marker proteins (Grünewald et al., 2014; Lax et al., 2016). However, neuronal pathology often starts at neuronal processes with synaptic dysfunction and loss (reviewed in Gillingwater and Wishart, 2013); moreover, the contribution of glial mitochondria is yet unknown in most contexts of neurodegeneration.

For AD, we first decided to use a common mouse model created by overexpression of human APP_{Swe} and mutant presenilin 1 (APP23/PS45; Busche et al., 2008). In these mice, cortical amyloid-β plaques start appearing at 3-month of age. I performed immunofluorescence staining of Ociad2 (neuronal mitochondria) and Sfxn5 (astrocytic mitochondria) in cortex from 9-month-old APP23/PS45 and age-matched control animals. Uchida and Takahashi (2008) reported that nuclear acid dyes, such as DAPI and Hoechst, intercalate with amyloid-β plaques in transgenic APP mouse models; hence, I used Hoechst to visualize amyloid-β plaques. While transgenic APP mouse lines model the formation of amyloid-β plaque, the loss of neurons is less successful (reviewed in Wirths and Bayer, 2010) despite being a hallmark of human pathology. Hence, I observed normal distribution of neurons and astrocytes around amyloid-β plaques. Only the plaque core region was devoid of cell bodies. Mitochondria in surrounding neurons and astrocytes were unchanged in morphology between conditions – as observed by light microscopy (Figure 45a). Within the plaque area (Figure 45b), astrocytic mitochondria were present in all regions, while the core region was mostly free of neuronal mitochondria and their density decreased in the diffuse area. I found prominent astrogliosis in APP23/PS45 tissue by staining against glial fibrillary acidic protein (Gfap; Figure 45c). While mitochondria morphology was normal in reactive astrocytes, their mass seemed increased compared to control.

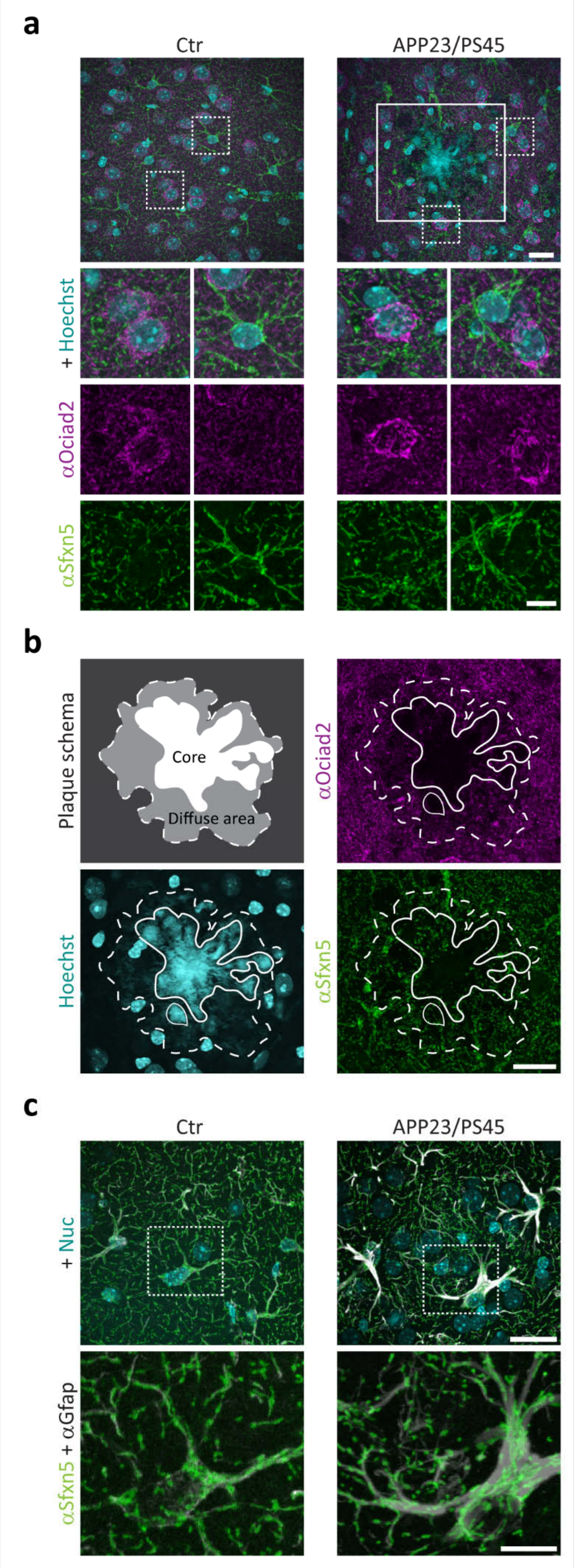
a
Ctr
APP23/PS45
+ Hoechst
αOciad2
αSfxn5
b
Plaque schema
Core
Diffuse area
αOciad2
Hoechst
αSfxn5
c
Ctr
APP23/PS45
+ Nuc
αSfxn5 + αGfap

Figure 45| Cell type-specific mitochondria in a mouse model of Alzheimer's disease. (**a**) Immunofluorescence staining against Ociad2 (magenta, neuronal mitochondria) and Sfxn5 (green, astrocytic mitochondria) in cortex from 9-month-old APP23/PS45 and wild type mice. Amyloid-β plaque and nuclei (cyan) are stained by Hoechst as previously reported for APP mouse models by Uchida and Takahashi (2008). Details show merged and single channels. Scale bars: 25 µm (detail 10 µm). (**b**) Detail of amyloid-β plaque region from **a**, APP23/PS45 showing plaque schema with dense core (line) and diffuse (dashed line) region, and single channels. Scale bar: 25 µm. (**c**) Astrogliosis in APP23/PS45 mouse cortex revealed by staining against Gfap (gray). Region is taken in 9-month-old mice and in distance from amyloid-β plaques. Astrocytic mitochondria are stained via Sfxn5 (green). Gamma was adjusted for Gfap staining to visualize mitochondrial staining in composites. Nuc, nuclear counter stain. Scale bars: 25 µm (detail 10 µm). Modified from Fecher et al. (2019), Figure 4 and Supplementary Figure 13.

Next, we performed immunofluorescence staining in postmortem human tissue from AD cases. Human tissue was provided by Doron Merkler (D.M.), staining performed by Ingrid Wagner (I.W.; Department of Pathology and Immunology, University of Geneva, Switzerland) and acquisition of samples performed by me. Overall, morphology and density of neuronal as well as astrocytic mitochondria was unchanged between samples (Figure 46). Neuronal mitochondria were equally present in all parts of the plaque contrary to my observation in the APP23/PS45 tissue. Astrogliosis did not morphologically alter astrocytic mitochondria, but increased their mass in cell bodies of reactive astrocytes – similar to the observations seen in APP23/PS45 tissue (Gfap; Figure 46b).

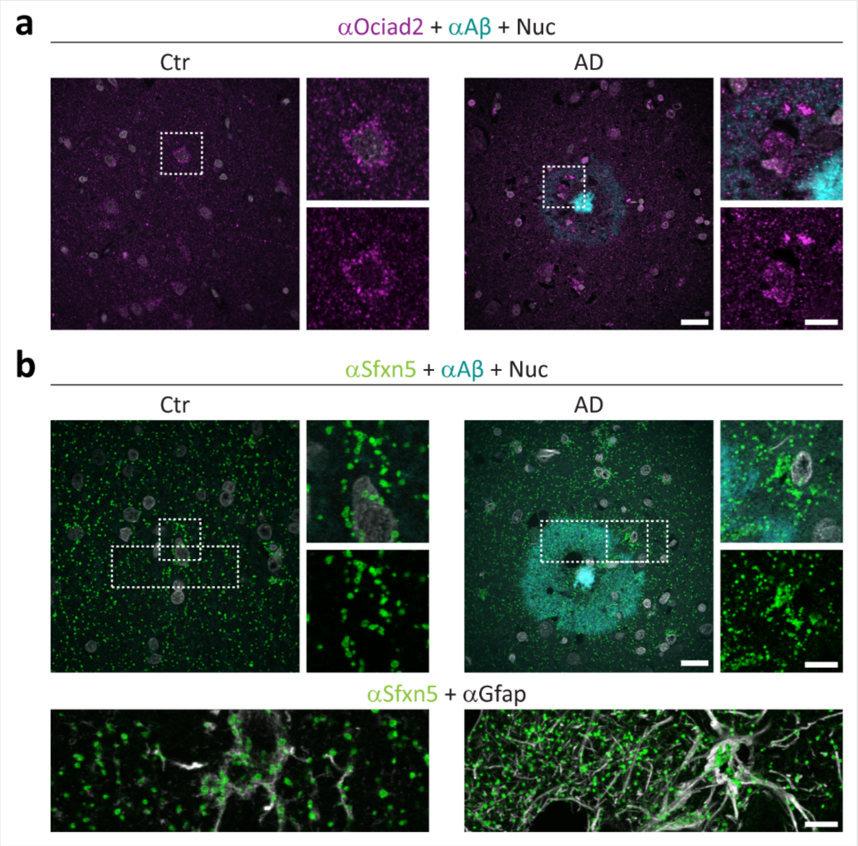

Figure 46 | Cell type-specific mitochondrial markers in human cortex from patients with Alzheimer's disease. (**a**-**b**) Immunofluorescence staining against amyloid-β (cyan), (**a**) Ociad2 (magenta, neuronal mitochondria) and (**b**) Sfxn5 (green, astrocytic mitochondria) in cortex from patients with Alzheimer's disease (AD) and control (Ctr). Overviews show general distribution in tissue and details show mitochondrial morphology around plaques. Rectangular details in **b** show staining against Gfap (gray) demonstrating astrogliosis in and around plaques in AD tissue. Nuc, nuclear counter stain. Scale bars: 25 μm (details 10 μm). Modified from Fecher et al. (2019), Supplementary Figure 13.

For ALS, we decided to use a mouse model created by overexpression of human Cu,Zn superoxide dismutase mutated at G93A (SOD1^{G93A}), which causes motor neuron degeneration followed by paralysis (Gurney et al., 1994). For experiments, I used non-symptomatic mice at the age of 5-month and performed immunofluorescence staining for Nipsnap1 (neuronal mitochondria), Sfxn5 (astrocytic mitochondria) and ChAT (motor neuron marker) in spinal cord. In controls, I observed a dense mitochondrial network stained by Nipsnap1 in motor neurons and a surrounding network of astrocytic mitochondria (Figure 47). In SOD1^{G93A} tissue, astrocytic mitochondria via Sfxn5 staining were present around motor

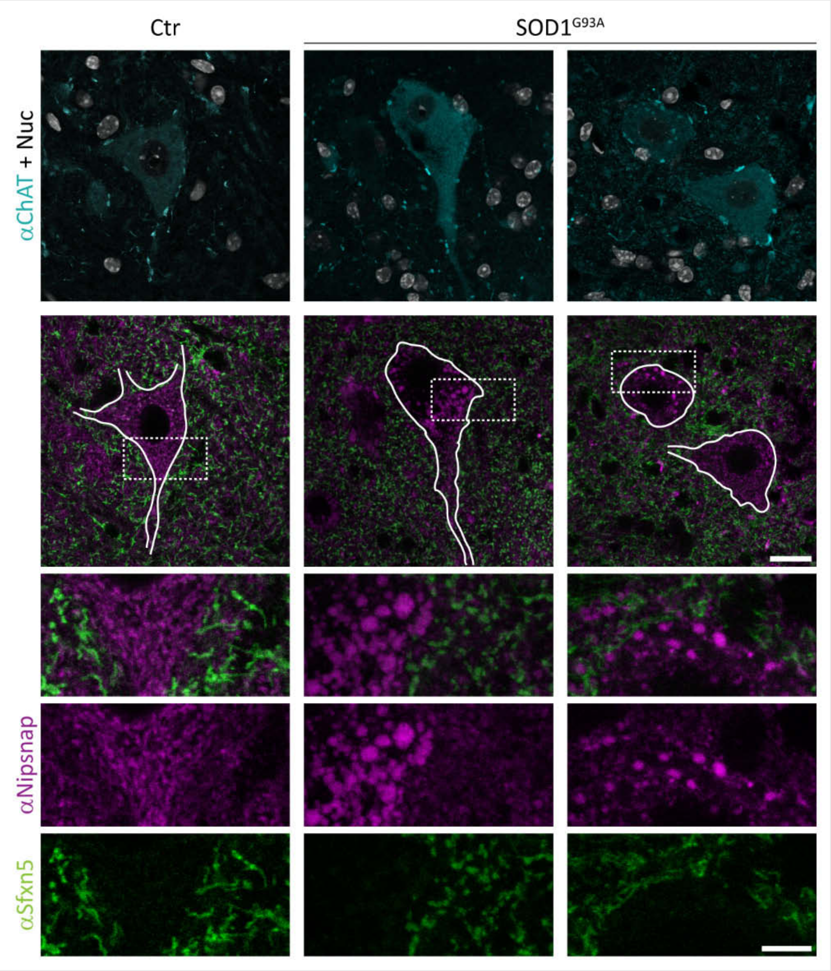

Figure 47| Cell type-specific mitochondria in a mouse model of amyotrophic lateral sclerosis. Immunofluorescence staining against Nipsnap1 (magenta, neuronal mitochondria) and Sfxn5 (green, astrocytic mitochondria) in spinal cord of 5-month-old SOD1^{G93A} and control (Ctr) mice. Motor neurons are stained via ChAT (cyan) and cell body outline (white line) created from this. Details show merged and single channels. Nuc, nuclear counter stain. Scale bars: 25 µm (details 10 µm).

neurons and unchanged in density and morphology. This was in contrast to neuronal mitochondria that had formed big aggregates in motor neurons.

We then performed similar immunofluorescence stainings in human spinal cord from ALS cases with the help of D.M. and I.W. (Department of Pathology and Immunology, University of Geneva, Switzerland). While I found a comparable network distribution of neuronal and astrocytic mitochondria in controls as previously seen in mouse spinal cord, neuronal

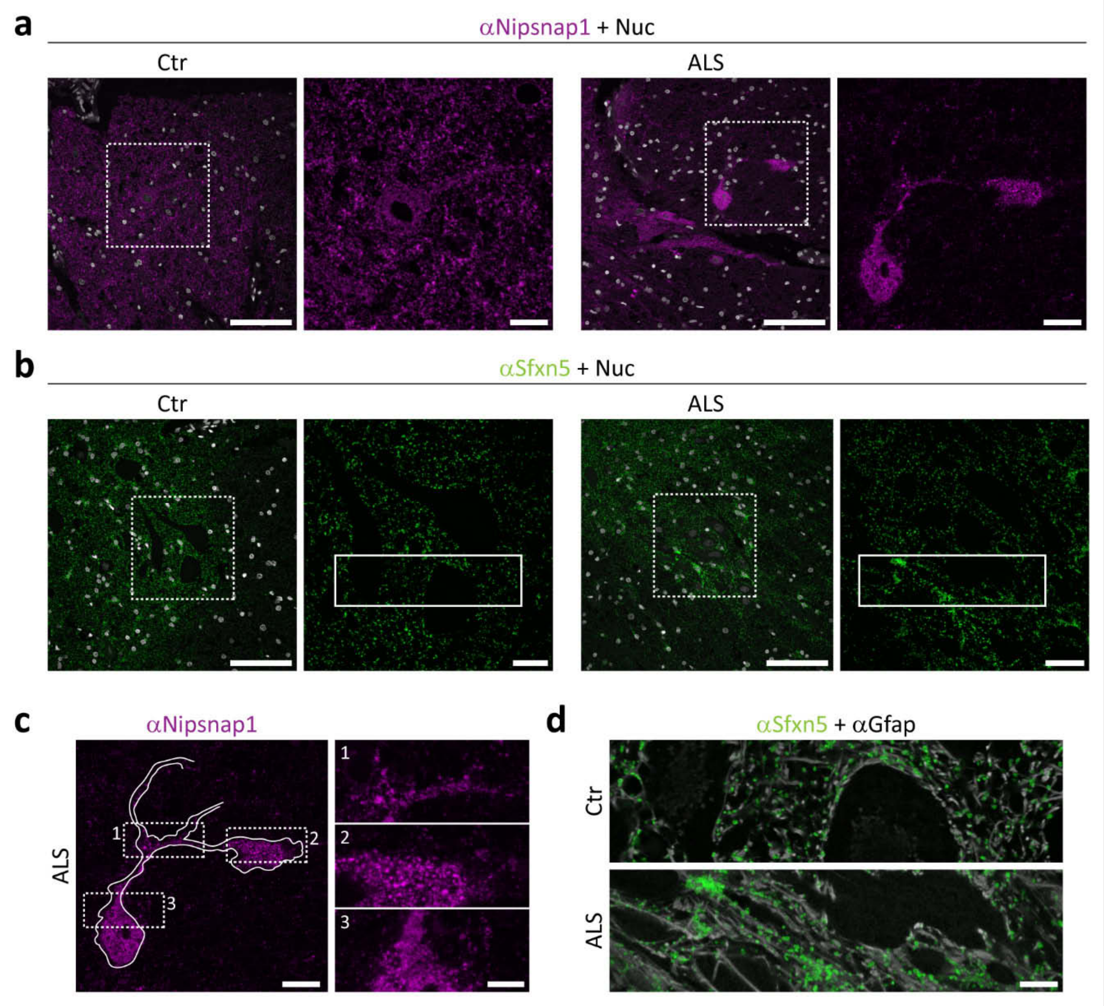

Figure 48│ Cell type-specific mitochondrial markers in human spinal cord from patients with amyotrophic lateral sclerosis. (**a**-**b**) Immunofluorescence staining against (**a**) Nipsnap1 (magenta, neuronal mitochondria) and (**b**) Sfxn5 (green, astrocytic mitochondria) in spinal cord from patients with amyotrophic lateral sclerosis (ALS) and control (Ctr). Overviews show general distribution in tissue and details show mitochondrial morphology. Note images are taken with different magnification. Nuc, nuclear counter stain. Scale bars: 100 µm (detail 25 µm). (**c**) Detail from **a**, ALS with cell outline from maximum projection and higher magnification details 1-3 showing mitochondrial morphology via Nipsnap1 staining. Scale bars: 25 µm (detail 10 µm). (**d**) Rectangular details from **b** showing astrogliosis in aged spinal cord. Sfxn5 staining (green) is merged with Gfap staining (gray). Scale bar: 10 µm. Modified from Fecher et al. (2019), Figure 4 and Supplementary Figure 14.

mitochondria were prominently altered in pathological cases (Figure 48). Overall Nipsnap1 intensity was drastically reduced with few neuronal cell bodies left (ALS; Figure 48a). Co-staining against ChAT was not performed and neuronal identity could not be determined. The mitochondrial network was similarly disrupted as seen in the presented mouse model and mitochondria rounded and clustered in remaining processes (Figure 48c, details). For astrocytic mitochondria, staining for Sfxn5 revealed an overall fragmented network with frequently rounded mitochondria in ALS and control tissue (Figure 48b). In some cases, I observed more intense and clustered Sfxn5 staining in pathological cases; however, this was independent from astrogliosis (Gfap; Figure 48d), which was ALS-independent.

In summary, we demonstrated the application of cell type-specific mitochondrial markers in the context of AD and ALS. Here, Nipsnap1 revealed neuronal mitochondria and Sfxn5 astrocytic mitochondria. While both markers could not demonstrate prominent mitochondrial alterations between pathological and control tissue in the AD mouse model and human cases, we found pathological changes in the context of ALS (Figure 47 and 48). In both the mouse model and human ALS cases, density and morphology of neuronal mitochondria were changed in soma and neurites. Additionally in the presented human case, clustering of astrocytic mitochondria was observed independent of astrogliosis (Figure 48).

DISCUSSION

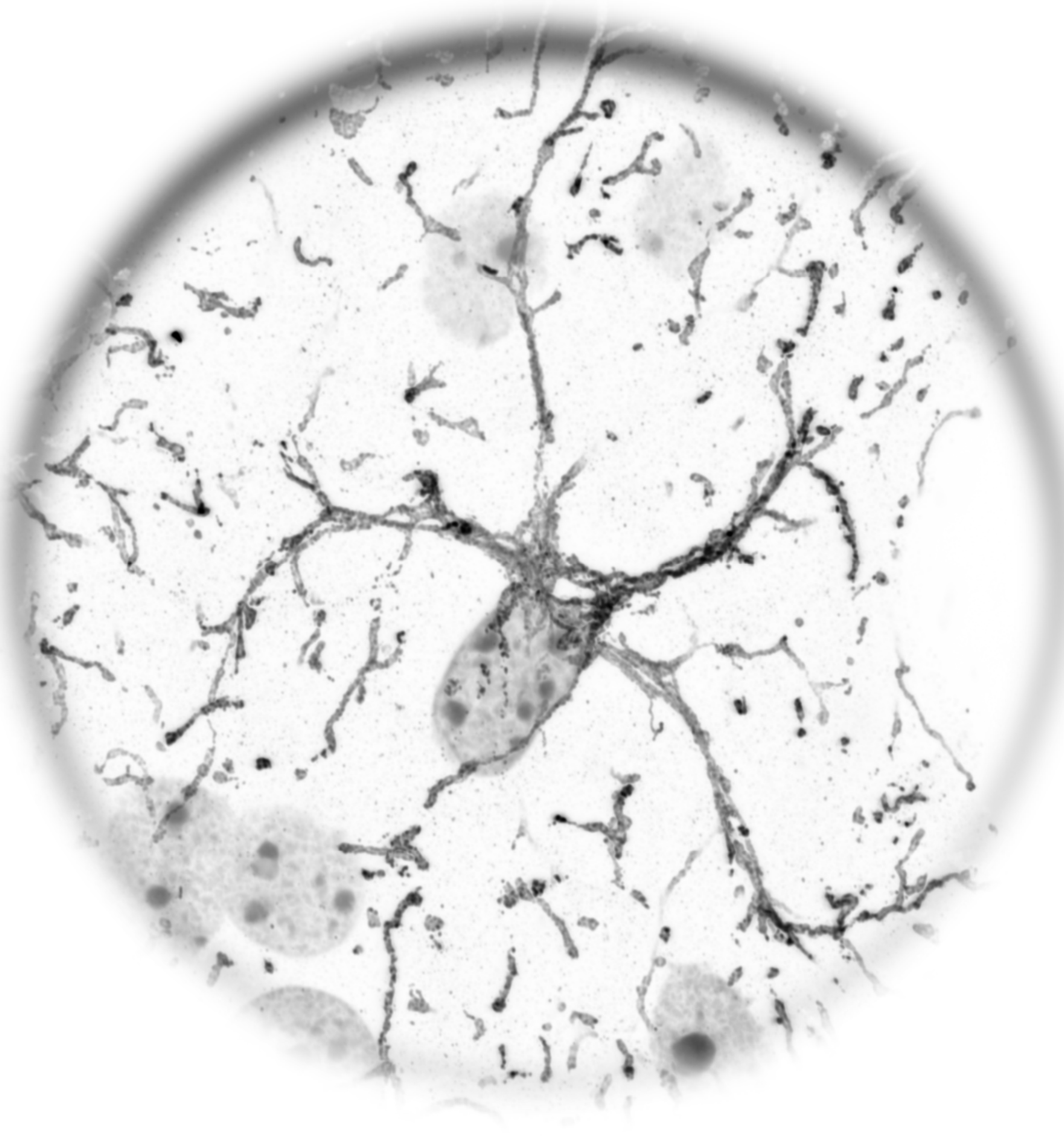

Chapter 5: Discussion

Mitochondria are involved in many cellular functions, such as catabolism, anabolism, apoptosis, Ca^{2+} homeostasis and iron-sulphur cluster assembly; in addition, they are a signaling and communication hub within cells. The fine-tuning of these functions, e.g. catabolism of fatty acids or anabolism of amino acids, is controlled by the cellular transcriptome and translatome given that >99% of mitochondrial proteins are nuclear encoded. Therefore, it is important to define mitochondrial phenotypes dependent on their cellular context, i.e. their cell type and its physiological state. This is especially true for the investigation of heterogeneous tissues, such as the nervous system, where the bulk analysis of brain mitochondria does not inform about the individual mitochondrial population of the estimated ~1,000 present cell types (Koch, 2019).

In this thesis, **I have introduced the MitoTag mouse model for the characterization of cell type-defined mitochondria**. Further, we have demonstrated its application in cerebellum from the profiling of cell type-specific mitochondrial proteomes to the validation of functional predictions from these profiles. Specifically, this work has identified that ~15% of mitochondrial annotated proteins (MitoCarta; Calvo et al., 2016) are cell type-enriched among Purkinje cells, granule cells and astrocytes. Of these proteins, I have validated 19 as cell type-enriched 'mitochondrial markers' in the central nervous system. Furthermore, we predicted cell type-enriched mitochondrial functions and corroborated these profiling predictions by independent assays probing for mitochondrial beta-oxidation, Ca^{2+} uptake and organelle contact sites. Hence, the present work elucidates the cell type-specific fine-tuning of mitochondrial biology in these major cerebellar cell types.

5.1. Technical advances and limitations of the MitoTag approach

Prior to this study, neural mitochondria from defined cell types could be isolated via three approaches: (i) the isolation of mitochondria from primary cells in culture, e.g. cortical neurons and astrocytes; (ii) the dissociation of neural cells from tissue and their fluorescence-activated cell sorting (FACSorting) with subsequent organelle isolation; and (iii) the dissociation of neural cells from tissue, their immunopurification via surface markers using antibody-coated magnetic beads and subsequent isolation of mitochondria. All three approaches have in common that mitochondria originate mostly from early postnatal tissue – even so FACSorting of adult neural cells is possible (Fischer et al., 2011) – and that a limited number of cell types can be adapted to them. In addition, cell culture media influence cellular metabolism (Cantor et al., 2017), and a substantial amount of time is needed for FACSorting and immunopurification via magnetic beads, while the recovered material is small. In contrast, these limitations are circumvented with the MitoTag mouse model. In brief, the MitoTag mouse model is based on a fluorescent GFP-tag localized to the outer mitochondrial membrane (GFP-OMM) and under the control of the loxP/Cre recombinase system for cell type specificity. Therefore, cell type-specific mitochondria are tagged in vivo and can be directly isolated from the tissue and the condition of interest, e.g. different ages, treatments or disease models. In addition, tagged mitochondria originate from all parts of the cell, e.g. from axon, dendrites, soma and synapses in neurons, while FACSorted and immunopurified cells mostly represent material from cell bodies. Of course, in cases where a compartment-specific subpopulation of mitochondria shall be characterized, anatomical features can be used, such as corticospinal projections, to separate somatodendritic from axonal mitochondria.

For the introduction of this model, **we evaluated several parameters to ensure faithful expression and localization, as well as intactness and functionality of immunocaptured organelles.** The faithful expression is directly linked to the Cre-driver line of interest and should be carefully evaluated because leakiness into other cell types, e.g. by a common cell lineage, will contaminate the purification effort. Due to this concern, Gella et al. (2019) recently reported the use of an adeno-associated viral vector to exclusively deliver Tomm20-3xHA to glutamatergic neurons of the vestibular nucleus (AAV1-DIO-mitoTag in Slc17a6:Cre mice). Our experiments support tag localization to the outer mitochondrial membrane in all tested cell types (Table A1); still, Costello et al. (2017) reported that endogenous OMP25 can be incorporated into peroxisomal membranes, and therefore other cell types should be evaluated prior to use. Based on our evaluation in motor neurons and cortical cells, we have demonstrated that mitochondrial function, e.g. axonal transport and oxygen consumption, is not influenced by tag expression or immunocapture.

Interestingly, Ahier et al. (2018b) introduced a similar invertebrate model using *Caenorhabditis elegans*. In brief, the authors generated Mos1-mediated single copy insertions of a transgene consisting of the outer mitochondrial membrane protein Tomm20 tagged with the fluorescent protein mKate2 and a HA-tag under the control of different cell type-specific promoters. Similar to our work, tag localization, faithful expression and functionality of tagged organelles was assessed – here in body wall muscle cells. The purification of tagged mitochondria was performed via magnetic beads against HA (Table 8). Additionally, the authors performed mixing experiments by adding mitochondria containing matrix localized GFP and mutant mtDNA to evaluate the performance of their affinity purification. I also determined our immunocapture protocol with similar mixing experiments and established that cell type-specific mitochondria from neural cell types can be enriched and purified from mouse brain. Here, the proximity of organelles influenced their separation during immunocapture. In fact, small amounts of mito-RFP, which represented material from untagged mitochondria, remained present in our isolations (Figure 16); however, this contamination was not influenced by the abundance of tagged mitochondria within the tissue (100-5% GFP-OMM$^+$, see Figure 17). I therefore concluded that this contamination is rather acquired during the isolation process by incorporation of abundant mitochondrial precursor proteins (like the transgene mito-RFP) than by the co-isolation of untagged, whole organelles. Due to advantages of their model system, Ahier et al. (2018b) could show the isolation of mitochondria from a single cell, namely the gustatory neuron ASEL, and from individual animals. While this is certainly useful in the case of mtDNA heteroplasmy, the amount of isolated mitochondria for functional assays is limited in the *Caenorhabditis elegans* model, e.g. 70,000 animals were required for one oxygen consumption experiment with only antimycin A/rotenone treatment. Interestingly, an introduced mutation in mtDNA – *uaDf5* deleting a 3.1 kb segment – differed in propagation among cell types with the least heteroplasmy in neurons and intestine, and the highest mutation load in germline. This mosaic pattern correlated with an overall increased mtDNA content and mitochondrial mass in germline cells, which are the only mitotically active cells in adult animal.

While the affinity protocol by Ahier et al. (2018b) and the presented immunocapture require approximately 2 – 2.5 hours for organelle isolation, Bayraktar et al. (2019) reported a rapid isolation protocol for metabolomics of cell type mitochondria of approximately 10 minutes (Table 8). Here, the authors generated a *Rosa26* knock-in mouse model harboring Cre-dependent 3xHA-GFP-OMM – similar to our MitoTag mouse model – and applied their mouse model to hepatocytes in liver under fasting/refeeding conditions. In contrast to proteins and DNA, metabolites are rapidly exchanged between cellular compartments and hence, a prolonged isolation process will gradually alter the mitochondrial metabolome. In mouse hepatocytes, Bayraktar et al. (2019) confirmed enrichment of mitochondrial metabolites and

Table 8. Comparison of isolation protocols for cell type-specific mitochondria from tissue.

Study	Fecher et al. (2019)	Ahier et al. (2018b)	Bayraktar et al. (2019)
Model organism	*Mus musculus*	*Caenorhabditis elegans*	*Mus musculus*
Cell type *Cell type driver*	Neural cells Emx1: Cre	Body wall muscle cells myo-3p	Hepatocytes Alb:Cre
Tag	GFP-OMM	Tom20-mKate2-HA	3xHA-GFP-OMM
Beads Cat. #	Miltenyi Biotec. 130-091-125	Thermo Fisher Scientific, 88837	Thermo Fisher Scientific, 88837
Beads (diameter)	paramagnetic (50 nm)	paramagnetic (1 μm)	paramagnetic (1 μm)
Beads amount	50 μl	100 μg	200 μl
Beads antibody	anti-GFP, mouse IgG_1	anti-HA, mouse IgG_1	anti-HA, mouse IgG_1
Tissue	Cortex	Whole animal	Liver
Tissue disruption	Nitrogen decompression	Mechanical disruption with 21 pestle strokes	Mechanical disruption with rotated pestle at 220 rpm
IP input	Post-nuclear lysate	Crude mitochondrial fraction	Post-nuclear supernatant
Amount	20 mg tissue	10,000 animals	~50 mg tissue
IP buffer	137 KCl, 2.5 MgCl, 3 KH_2PO_4, 1 EDTA, 10 HEPES, pH 7.4, 1% BSA, protease inhibitors	1× PBS, 2 mM EDTA, 1% BSA, protease inhibitors	136 mM KCl, 10 mM KH_2PO_4, pH 7.25, in Optima LC/MS water
Incubation time	60 minutes at 4C	60 minutes at 4C	3.5 minutes
Separation	Magnetic stand; 3x wash with 3ml; elution with 4ml; spin down 12,000g	Magnetic stand; 2x wash with 25 ml; elution with 25 μl	Magnetic stand; 3x wash; no elution
Total time, approx.	~2.5 hours	~2 hours	~10 minutes
Recovery	4.83 μg/mg tissue	1.01% total mitochondria (~30% with single animal)	n.d.

Also see Ahier et al. (2018a) and Chen et al. (2017) for protocol details.

511 proteins, of which 75.9% were mitochondrial annotated. No cytosolic or lysosomal metabolites were detected. Interestingly, when mice were fasted overnight and not refed, increased levels of acetyl-CoA from beta-oxidation, GMP, and glutamine from glutaminolysis as well as decreased methionine and increased alanine levels were exclusively identified on the cell level, but not on the total tissue level. While the nature of metabolites requires a timely isolation, it remains to be shown how the rapid isolation workflow performs with rare cell types, e.g. neuronal subpopulations in brain, and whether sufficient yield and purity can be achieved. For example, in the control IP from wild type tissue (MITO-Tag mice without Cre expression) a total of 1,204 proteins were identified, of which 511 proteins were >5 times enriched in the targeted HA-MITO IP (MITO-Tag mice with Alb:Cre expression). While the authors comment on the absence of lymphocyte-enriched proteins, like Bcl2, in their proteome, no detailed mixing experiments were performed – in fact, the tagged

mitochondrial population originated from ~70% of tissue cells (Ding et al., 2016), which contribute to the majority of biomass in liver.

In conclusion, the comparison of isolation protocols across studies demonstrates that researchers will have to adapt and validate their purification protocol for cell type-specific mitochondria not only dependent on tissue and cell type, but also dependent on assay and final readout. For example, the here presented immunocapture protocol for neural cells efficiently enriches mitochondria from the targeted cell types of interest – however, the isolation still represents a crude mitochondrial fraction with associated proteins, i.e. cytosolic and other organelle proteins that interact with the outer mitochondrial membrane. We deliberately chose this approach, as we were particularly interested in this group of proteins, such as organelle tethers, cytoskeletal motor proteins and adapters. In addition, the functional performance of isolated mitochondria was a central goal of our study and further purification steps are known to influence mitochondrial respiration (Wang et al., 2011b). Nevertheless, purity of cell type-specific mitochondria can be further improved after immunocapture, e.g. by a subsequent Percoll gradient step (Sims and Anderson, 2008) or the fractionation of submitochondrial compartments as performed by Morgenstern et al. (2017). Hence, **I am anticipating further modifications and breakthroughs in the efficient isolation of mitochondria from in vivo settings, which will adapt purity, yield and time dependent on cell types in the future.**

5.2. Cell type-enriched candidates reflect metabolic coupling of neural cells

The brain is energy demanding given that it consumes ~20% of total body energy. In recent years the field of 'neuroenergetics' emerged pioneered by the functional imaging of brain oxygen consumption and glucose utilization in humans via positron emission tomography and functional magnetic resonance imaging (reviewed in Raichle, 1998). Long before this, Roy and Sherrington (1890) provided one of the first evidences that local brain activity results in blood vessel modification to adjust supply to demand.

The demand in this case is oxygen and glucose (Sokoloff, 1981) with liver-derived ketone bodies as secondary energy source (reviewed in Fedorovich et al., 2018). Specifically, the computational units of the brain, neurons, rely on lactate, which is supplied by glial cells – mostly astrocytes (reviewed in Weber and Barros, 2015), but also oligodendrocytes (Fünfschilling et al., 2012). Thus, astrocytes and neurons form a metabolic unit in terms of energy supply, but also for neurotransmitter homeostasis. The catabolism of glucose – glycolysis – is localized to the cytosol; hence, our mitochondrial profiling cannot reveal cell type-specific differences in this pathway. However, mitochondrial candidates from our profiling clearly showed specialization of the TCA cycle and its associated catabolic pathways among neural mitochondria. These relate to the neural metabolic coupling, termed the astrocyte-neuron lactate shuttle hypothesis (ANLS; Pellerin and Magistretti, 1994), and are illustrated in Figure 49 and 50 together with cell type-enriched specializations of the TCA cycle, its fuel pathways and junctions, and other enriched processes.

For example, in the **ANLS**, neurons are provided with L-lactate, which is converted to pyruvate – the main substrate of the neuronal TCA cycle. In brief, astrocytes form connections with the vasculature via endfeet throughout the brain (63% coverage; Mathiisen et al., 2010) and receive glucose. Via glycolysis (Figure 49a), glucose is oxidized to pyruvate and further converted to L-lactate via L-lactate dehydrogenase (Ldha/b; Bittar et al., 1996) as part of aerobic glycolysis, termed the Warburg effect (Warburg, 1956). Interestingly, despite the presence of oxygen, pyruvate respiration is prevented in astrocytes in several ways. While the mitochondrial pyruvate carrier (MPC) was unchanged between neural cells in our data, astrocytic pyruvate kinase (Pkm2) interacts with Ldha via phosphorylation (Christofk et al., 2008) leading to direct conversion of formed pyruvate to L-lactate. Furthermore, Pellerin and Magistretti (1994) demonstrated that astrocytic glucose uptake and lactate release are stimulated by sodium-driven glutamate uptake during neurotransmission. This glutamate uptake acidifies the astrocytic cytosol and mitochondrial matrix leading to an altered mitochondrial membrane potential, and thereby decreases mitochondrial metabolism during activity-driven glycolysis (Azarias et al., 2011). Finally, pyruvate entry into the TCA cycle is blocked in astrocytes via phosphorylation of the pyruvate dehydrogenase complex (PDH) via pyruvate dehydrogenase kinase 4 (Pdk4, not identified in our proteomes; Halim et al., 2010). After generation, L-lactate is exported via monocarboxylate transporters (MCT1/4) and imported by neurons (MCT2; Pierre and Pellerin, 2005; Rafiki et al., 2003), where Ldhb converts it to pyruvate (Figure 49b). Sada et al. (2015) showed that disruption of astrocytic lactate supply significantly altered neuronal excitability and Machler et al. (2016) provided in vivo evidence for a lactate gradient from astrocytes to neurons.

The ANLS specifically states that during neuronal activity glycolysis is preferentially performed in astrocytes to produce L-lactate and supply neurons; however, this does not mean that

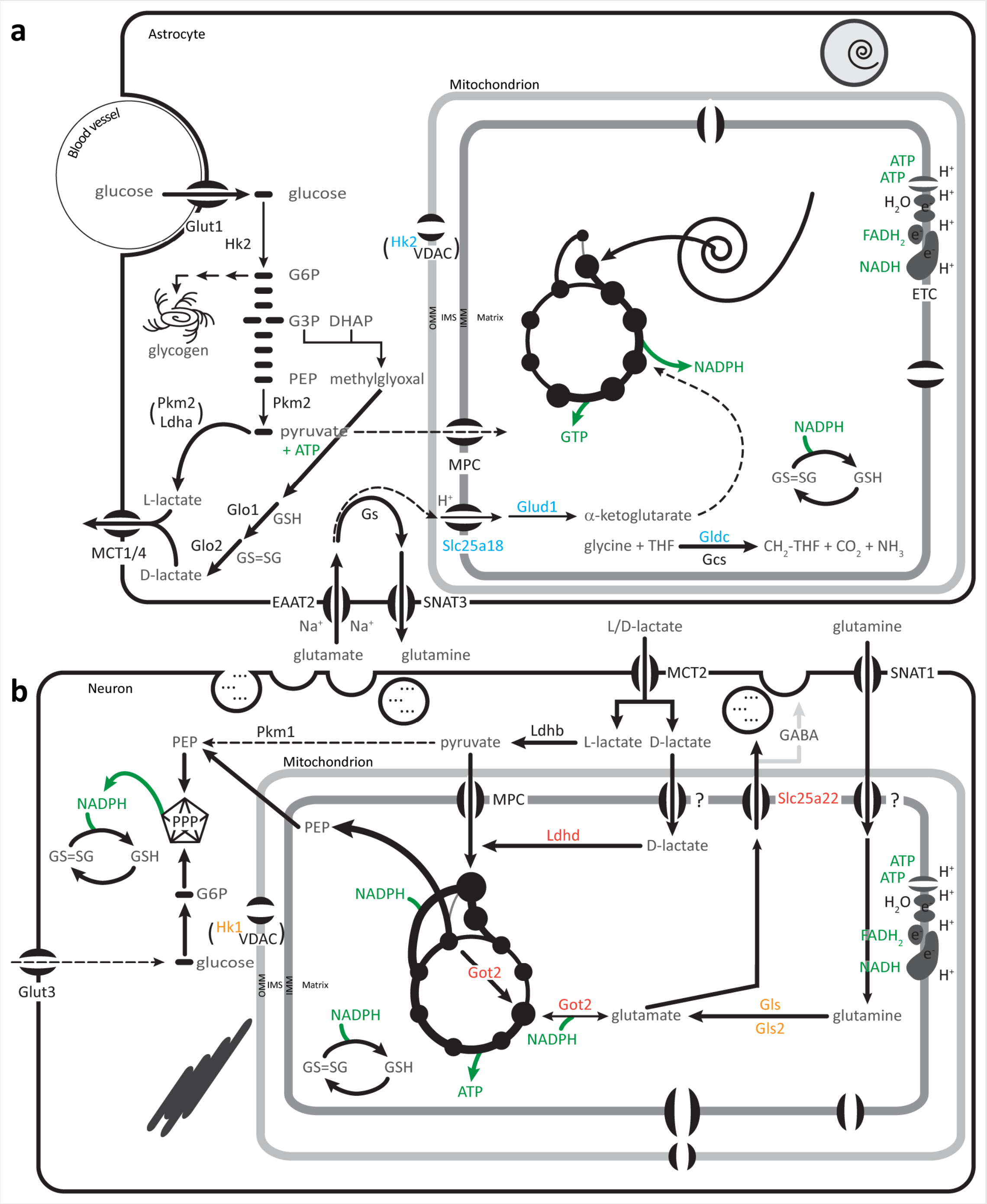
a
Astrocyte
Blood vessel
glucose
Glut1
glucose
Hk2
G6P
glycogen
G3P DHAP
PEP methylglyoxal
(Pkm2 Ldha)
Pkm2
pyruvate + ATP
L-lactate
Glo1
GSH
Glo2
GS=SG
MCT1/4
D-lactate
(Hk2 VDAC)
OMM IMS IMM Matrix
Mitochondrion
MPC
H^+
Slc25a18
Glud1
α-ketoglutarate
glycine + THF
Gldc
Gcs
CH_2-THF + CO_2 + NH_3
NADPH
GTP
NADPH
GS=SG GSH
ATP
ATP
H_2O
$FADH_2$
NADH
H^+
e^-
ETC
Gs
EAAT2
SNAT3
Na^+ Na^+
glutamate
glutamine
L/D-lactate
glutamine
b
Neuron
MCT2
SNAT1
L-lactate D-lactate
Ldhb
pyruvate
Pkm1
PEP
GABA
Mitochondrion
MPC
?
Slc25a22
?
PPP
NADPH
GS=SG GSH
G6P
(Hk1 VDAC)
glucose
Glut3
OMM IMS IMM Matrix
PEP
Ldhd
D-lactate
NADPH
Got2
Got2
glutamate
Gls
Gls2
glutamine
NADPH
NADPH
GS=SG GSH
ATP
ATP
ATP
H_2O
$FADH_2$
NADH
H^+
e^-

Figure 49| Metabolic coupling of astrocytes and neurons. Metabolic pathways in (**a**) astrocytes and (**b**) neurons linked to the astrocyte-neuron lactate shuttle hypothesis. Metabolites (gray and green), enzymes (black or color), protein interaction (brackets) and pathway importance (line width) are indicated. Cell type-enriched candidates from our mitochondrial profiling are shown in blue (astrocytes), red (neuronal) and orange (granule cell enriched). Neuronal or granule cell enrichment is based on the comparison PC *vs* GC (FC ≥ |0.5|, q-value <0.05) and not identical to Figure 24a. For simplicity, not all pathways and enzymes are shown. See also complementary schema in Figure 50 and abbreviation index (page 217) for details.

glycolysis is absent in neurons. Under steady-state conditions, glucose is taken up by neurons; yet, it is not converted to pyruvate, but primarily used for NADPH generation in the pentose phosphate pathway (PPP; Bolanos and Almeida, 2010). The NADPH pool is further used to regenerate glutathione (GSH), which protects neurons against oxidative stress (Vaughn and Deshmukh, 2008). Glucose-6-phosphate can enter the PPP after the first step of glycolysis, where hexokinase (Hk1/2) phosphorylates glucose. Hk1 is known to localize to the outer mitochondrial membrane via VDAC interaction (Felgner et al., 1979; Linden et al., 1982), while Hk2 can additionally translocate to the cytosol, where it is involved in glycogen synthesis (John et al., 2011). Hk1 and Hk2 were enriched in granule cell and astrocytic mitochondria, respectively. Interestingly, glycogen is primarily produced in astrocytes and its machinery is inactive in neurons (Dringen et al., 1993; Vilchez et al., 2007). Further, Duran et al. (2012) showed that neuronal overexpression of muscle glycogen synthase – the main isoform expressed in brain – causes neurodegeneration; however, its ectopic expression protects neurons during hypoxia (Saez et al., 2014).

While intermediates from the PPP could be redirected to glycolysis, this is not the case in experimental studies (Herrero-Mendez et al., 2009; Bolanos et al., 2010). Along with this, other reasons argue for a minor role of energy-producing glycolysis in neurons, namely: (i) the proteasomal degradation of 6-phosphofructo-2-kinase/fructose-2,6-bisphosphatase 3 (Pfkfb3); (ii) Pkm1 disability to modulate glycolysis; and (iii) reduced detoxification of methylglyoxal. First, glycolysis is controlled by the master regulator 6-phosphofructo-1-kinase (Pfk1), which is allosterically activated by fructose-2,6-bisphosphate, which in turn is generated from fructose-6-phosphate via the glycolytic enzyme Pfkfb3. In neurons, Pfkfb3 is actively degraded via the proteasome and upregulation of Pfkfb3 levels have been shown to cause oxidative stress and neuronal death (Herrero-Mendez et al., 2009). Secondly, Pkm metabolizes phosphoenolpyruvate (PEP) to pyruvate and ATP – the final step of glycolysis. The splice variants Pkm1 and Pkm2 are expressed in neurons and astrocytes, respectively (Zhang et al., 2014). However, only Pkm2 is regulated by posttranslational modifications (reviewed in Prakasam et al., 2018). For example, o-GluNAcylation at Thr^{405} and Ser^{406} leads to translocation of Pkm2 to the nucleus, where it stimulates the expression of glucose transporter type 1 (Glut1) and Ldha to increase glucose uptake and lactate production (Wang et al., 2017). Thus, glycolysis is activity-dependently regulated in astrocytes, while this feature is absent in neurons and the rate of glycolysis is fixed to a baseline (Almeida et al., 2001). Finally, methylglyoxal is a byproduct of glycolysis and forms neurotoxic advanced glycation endproducts (reviewed in Munch et al., 2012). It is produced via the stochastic fragmentation of glyceraldehyde-3-phosphate (G3P) and dihydroxyacetone phosphate (DHAP) and detoxified to D-lactate by the glyoxalase system, Glo1 and Glo2 (Allaman et al., 2015). This system is specifically enriched in astrocytes and repressed in neurons (Belanger et al., 2011). Interestingly, like L-lactate, D-lactate is transferred to neurons via MCT and here, it is converted to pyruvate via mitochondrial Ldhd, which I confirmed as neuronal candidate (Figure A1c). While debated for some time, Ldhd function was recently confirmed in humans (Monroe et al., 2019) and patients with D-lactic acidosis frequently present with broad neurological symptoms (reviewed in Uribarri et al., 1998), which however so far have been investigated in the context of an abnormal bacterial colon flora, but not as metabolic syndrome.

Hence, neurons uniquely depend on glial lactate supply, but can also use other substrates to fuel their TCA cycle. For example, the **neurotransmitter** glutamate is recycled by astrocytes and re-enters neurons as glutamine (Benjamin and Quastel, 1975). In this way, astrocytes contribute to the spatial and temporal resolution of neurotransmission via neurotransmitter uptake from the synaptic cleft. While glutamate-to-glutamine conversion is cytosolic in astrocytes (Gs; Figure 49a), the reverse process happens in neuronal mitochondria via the enzyme glutaminase (Gls, Gls2; Laake et al., 1999). Glutamate can then be used as neurotransmitter in glutamatergic neurons, be converted to GABA in GABAergic neurons or enter the TCA cycle as α-ketoglutarate via glutamate oxaloacetate transaminase (Got2; Figure 49b). This reaction also contributes to the NADPH pool. For example, in cerebellar slices, de Barry et al. (1983) quantified the recycling of free glutamate into 42% glutamine, 25% α-ketoglutarate and 1% GABA. We found Gls and Gls2 as enriched candidates in granule cell mitochondria according to the glutamatergic nature of these neurons. While glutaminase is less abundant in Purkinje cells, Got2 can generate glutamate starting from oxaloacetate – hence, providing glutamate for GABA generation independent from glutamine. Additionally, these Got2-mediated reactions are part of the ‘mini TCA cycle’ that operates in the absence of acetyl-CoA (Yudkoff et al., 1994).

Other neurotransmitter, like glycine and GABA, are also recycled in astrocytes (Gadea and Lopez-Colome, 2001a, b), e.g. via the glycine cleavage system (Gcs; Figure 49a). However, in contrast to glutamate, Chatton et al. (2003) could not detect a metabolic coupling between sodium-dependent GABA uptake and glycolysis. Thus, the coupling of neurotransmitter uptake and lactate generation is currently believed to be exclusive for glutamate. Still, without glial recycling, neurotransmitters would be lost into the blood stream resulting in a net loss of energy substrates and the demand to replace them for neurotransmission (discussed in Marcaggi and Attwell, 2004).

Additionally to glutamate-glutamine recycling in astrocytes, glutamate may be imported into astrocytic mitochondria via Slc25a18 and enter the TCA cycle as α-ketoglutarate via glutamate dehydrogenase 1 (Glud1; Figure 49a).

In addition to the ANLS, several other interesting specializations were revealed through our proteomic profiling between astrocytic and neuronal mitochondria (Figure 50).

First, as discussed before, pyruvate entry into the **astrocytic TCA cycle** is limited due to phosphorylation of PDH (Halim et al., 2010); however, we found that the major components of beta-oxidation are enriched in astrocytic mitochondria (see Chapter 4.3) and therefore acetyl-CoA can fuels the TCA cycle. Citrate synthase (CS) condensates acetyl-CoA and oxaloacetate to citrate, the first TCA cycle intermediate; hence, oxaloacetate levels are crucial in astrocytes. While this intermediate is provided in a ‘running’ TCA cycle, it can also be replenished via pyruvate carboxylase (PC), which is enriched in astrocytes (Yu et al., 1983; Shank et al., 1985).

Secondly, three reactions of the TCA cycle generate NADH, which is transferred to complex I. Interestingly, in astrocytes, one of these reactions is modified to generate NADPH via isocitrate dehydrogenase 2 (Idh2; Figure 50a). Idh2 can operate bidirectional and either generate isocitrate from α-ketoglutarate consuming NADPH, termed reductive carboxylation (Comte et al., 2002); or generate α-ketoglutarate and NADPH, which is used to recycle GSH by glutathione reductase (Vogel et al., 1999). As previously discussed, neuronal NADPH is generate via the PPP from glucose, but can also be formed via Got2 and malic enzymes (Me2) in mitochondria; hence, providing two local pools of GSH recycling. In addition to Idh2, nicotinamide nucleotide transhydrogenase (Nnt) was enriched in astrocytic mitochondria, which also generates NADPH via the proton motive force across the inner mitochondrial membrane (Earle et al., 1978; Leung et al., 2015). Thus, NADPH generation via Nnt is directly linked to the ETC activity unlike its generation via Got2, Me2 or Idh2. Sazanov and Jackson (1994) proposed that Nnt works synergistically with an Idh2-Idh3 cycle to control flux through the TCA cycle depending on demand. Here, Idh3 works in forward direction generation

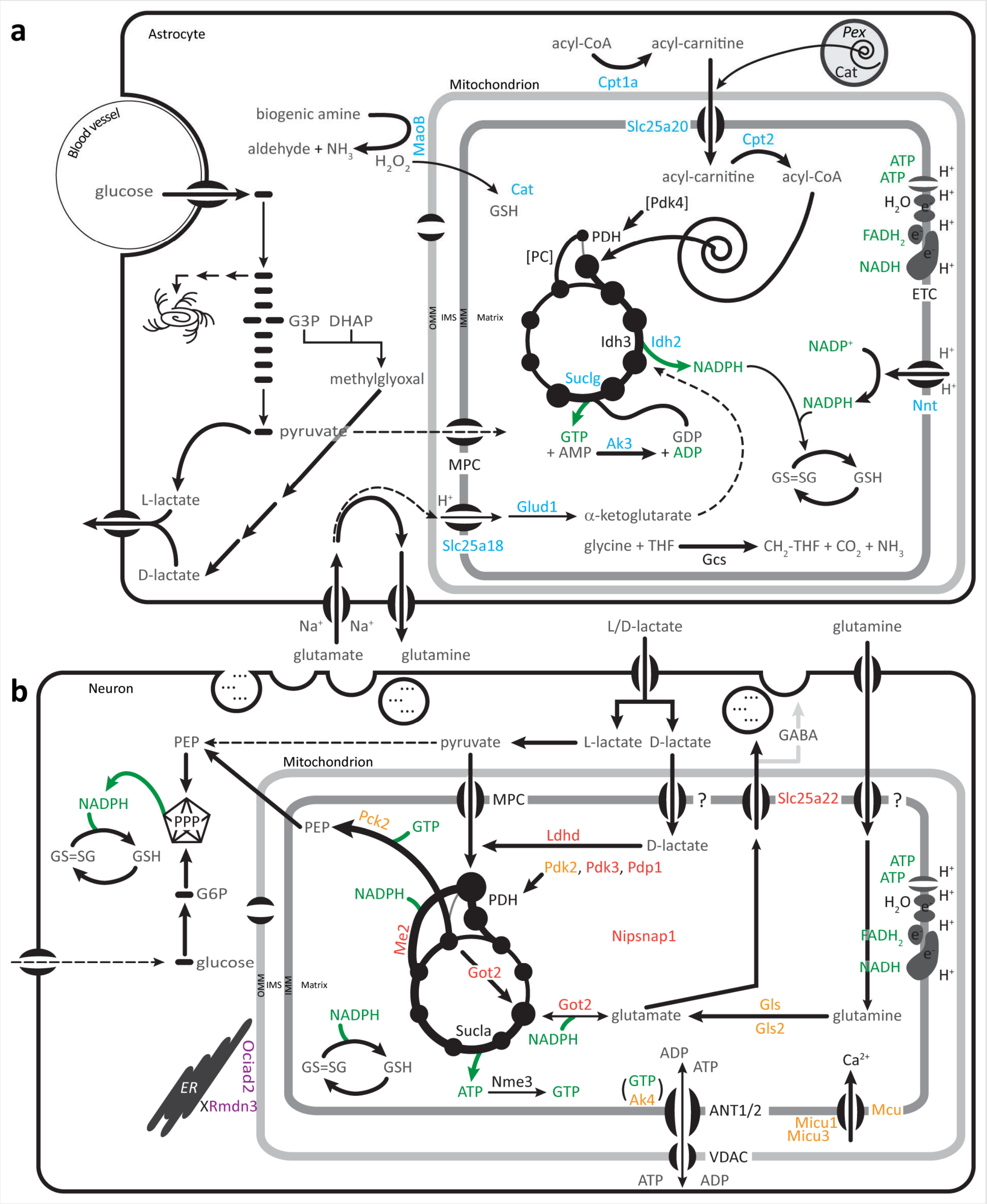
a
Astrocyte
acyl-CoA
acyl-carnitine
Cpt1a
Pex
Cat
Mitochondrion
biogenic amine
aldehyde + NH3
H2O2
MaoB
Blood vessel
glucose
Cat
GSH
Slc25a20
Cpt2
acyl-carnitine
acyl-CoA
[Pdk4]
PDH
[PC]
ATP
ATP
H2O
FADH2
NADH
H+
e-
ETC
G3P DHAP
methylglyoxal
OMM
IMS
IMM
Matrix
Idh3
Idh2
NADPH
NADP+
Suclg
NADPH
Nnt
pyruvate
MPC
GTP
+ AMP
Ak3
GDP
+ ADP
GS=SG
GSH
L-lactate
H+
Glud1
α-ketoglutarate
Slc25a18
glycine + THF
CH2-THF + CO2 + NH3
Gcs
D-lactate
Na+
Na+
glutamate
glutamine
L/D-lactate
glutamine
b
Neuron
PEP
pyruvate
L-lactate
D-lactate
GABA
Mitochondrion
NADPH
PPP
GS=SG
GSH
G6P
glucose
MPC
?
Slc25a22
?
PEP
Pck2
GTP
Ldhd
D-lactate
Pdk2, Pdk3, Pdp1
NADPH
PDH
Me2
Nipsnap1
ATP
ATP
H2O
FADH2
NADH
H+
e-
OMM
IMS
IMM
Matrix
Got2
Got2
glutamate
Gls
Gls2
glutamine
NADPH
NADPH
Sucla
GS=SG
GSH
ER
Ociad2
Rmdn3
ATP
Nme3
GTP
ADP
ATP
GTP
Ak4
ANT1/2
Ca2+
Micu1
Micu3
Mcu
VDAC
ATP
ADP

Figure 50| Neural specialization of TCA cycle, adjacent fuel and other pathways. Overview of enriched candidates in (**a**) astrocytes and (**b**) neurons linked to the TCA cycle, its fuel pathways and junctions. Metabolites (gray and green), enzymes (black or color), protein interaction (brackets) and pathway importance (line width) are indicated. Cell type-enriched candidates from our mitochondrial profiling are shown in blue (astrocytes), red (neuronal), orange (granule cell enriched) and magenta (Purkinje cell enriched). Neuronal, GC and PC enrichment is based on the comparison PC *vs* GC (FC ≥ |0.5|, q-value <0.05) and not identical to Figure 24a. [PC, Pdk4] were not identified in mass spectrometry, but their enrichment is supported via literature. For simplicity, not all pathways and enzymes are shown. See also complementary schema in Figure 49 and abbreviation index (page 217) for details.

α-ketoglutarate, while Idh2 works in reverse consuming NADPH provided by Nnt. Dependent on redox state and ETC activity, these reactions are adjusted. Under which conditions astrocytes depend on this regulatory mechanism is unknown; however, this cycle is disrupted in glioma due to Idh2 mutations causing a rewiring of the flux towards 2-hydroxyglutaric acid generation (Huang et al., 2019). NADPH generation in astrocytes strengthen their **antioxidant defense** in mitochondria, which for example is necessary for the breakdown of biogenic amines like dopamine via monoamine oxidase B (MaoB; Waldmeier, 1987) – a process generating H_2O_2. Recently, however, Graves et al. (2020) reported that dopamine clearance via MaoB does not necessarily increase local H_2O_2 levels. The authors discovered a transfer of free electrons to complex IV of the ETC, which fueled ATP production in neurons.

Thirdly and to our surprise, we found catalase (Cat) enriched in astrocytic mitochondria and I confirmed this observation independently (Figure 33b). This peroxisomal protein was previously reported in mitochondria (Radi et al., 1991), like several other proteins that are dually localized to these organelles (Costello et al., 2017). Furthermore, Petrova et al. (2004) showed that under stress conditions, Cat relocalizes to mitochondria by unknown import mechanisms. We also observed an enrichment of other peroxisomal proteins in astrocytic mitochondria (see Chapter 4.2.5), most of which are unlikely to relocate as proposed for Cat. Still, peroxisomes and mitochondria have an intimate relationship via interconnected functions and peroxisome de-novo biogenesis from mitochondrial vesicles (Sugiura et al., 2017). In particular, FA catabolism is shared between these organelles and FA are degraded dependent on chain length (Lazarow and De Duve, 1976). While mitochondria fully oxidize FA, peroxisomes cannot and shuttle acylcarnitine (C2, C3, C11) to mitochondria (Verhoeven et al., 1998).

Finally, while ATP is mostly generated on complex V within mitochondria, one reaction of the TCA cycle generates nucleoside triphosphates, known as **substrate level phosphorylation** (reviewed in Tretter et al., 2016). This reaction is mediate by succinyl-CoA ligase (Sucl; Johnson et al., 1998), which is a heterodimer of Suclg1 and either Sucla2 (ATP generating) or Suclg2 (GTP generating). In astrocytes, we found GTP generating Suclg2 enriched. Interestingly, GTP is not exported from mammalian mitochondria (Heldt and Schwalbach, 1967), while *Saccharomyces cerevisiae* lacks Suclg2 and expresses the GDP/GTP exchanger, Ggc1p (Vozza et al., 2004). GTP is essential for mtDNA maintenance (Kadrmas et al., 1991; Tokarska-Schlattner et al., 2008) and can be interconverted to other nucleotides via adenylate kinases

(Ak). In astrocytes, Ak3 is enriched, which scavenges GTP and uses this for mitochondrial AMP recycling to ADP (GTP + AMP --> GDP + ADP; Heldt and Schwalbach, 1967).

The **neuronal TCA cycle** (Figure 50b) is fueled via pyruvate, which originates from astrocytic lactate. In particular, Ldhd was found enriched in neuronal mitochondria and independently validated (Figure A1c). PDH is controlled via pyruvate dehydrogenase kinases (Pdk1-4) and pyruvate dehydrogenase phosphatases (Pdp1/2), which we found both enriched in neuronal mitochondria. Also, glutamate can fuel the neuronal TCA via Got2 activity. Defense against oxidative stress is essential for neurons (reviewed in Cenini et al., 2019) and thus, NADPH generation is present in cytosol via the PPP and in mitochondria via Got2 and Me2 – both enriched in our neuronal proteomes. Several studies link neuronal Got2 expression to ATP production and neuronal survival, for example during ischemia (Xu et al., 2019), traumatic brain injury (Arun et al., 2013) and experimental autoimmune encephalomyelitis (Honorat et al., 2017).

As described in Chapter 1.4.1, Nipsnap1 is a mitochondrial protein enriched in neurons (Nautiyal et al., 2010) and our experiments corroborate these previous reports. Despite this clear cell type annotation, Nipsnap1 function is unclear with reports documenting its interaction with amyloid precursor protein (APP; Tummala et al., 2010) or the branched-chain α-keto acid dehydrogenase enzyme complex (Nautiyal et al., 2010). Recently, Princely Abudu et al. (2019) showed that Nipsnap1 deletion causes neuronal death indicating its importance for certain neuronal populations. Still, these reports do not offer a clear molecular function of Nispnap1 in the context of neuronal physiology.

We also found **striking differences** between mitochondria from granule cells and Purkinje cells, for example, the enrichment of the mitochondrial calcium uniporter complex or the enrichment of contact sites between mitochondria and the endoplasmic reticulum (ER). Both findings contribute to the cellular Ca^{2+} homeostasis and are further discussed in Chapter 5.4.

Particularly enriched in **granule cell mitochondria** was phosphoenolpyruvate carboxykinase 2 (Pck2), which converts oxaloacetate to PEP using GTP (Stark et al., 2014). In contrast to astrocytes, GTP is not formed via Sucl in the TCA cycle, but can be generated via mitochondrial nucleoside diphosphate kinase (Nme3), which was not enriched in a cell type-specific manner (Figure 50b). PEP is then exported from mitochondria and can be used to fuel NADPH generation in the PPP. In fact, generation of PEP from oxaloacetate is energetically more efficient than PEP generation from lactate given that fewer enzymes and transporters are necessary (see discussion in Stark et al., 2014). Interestingly, granule cell mitochondria were enriched in Ak4, another GTP-dependent adenylate kinase. In contrast to astrocytic Ak3, neuronal Ak4 binds GTP but lacks phosphotransferase activity (Noma et al., 2001). Liu et al. (2009) reported that Ak4 acts as a stress sensor in cells by interacting with the ADP/ATP translocase (ANT1/2) and modulating ANT1/2 activity dependent on TCA cycle activity. Furthermore, this interaction was increased under oxidative stress and repressed cytochrome c release and apoptosis in neuronal SH-SY5Y cells.

Paradoxically, granule cells are more susceptible to oxidative stress than other neurons (Wang et al., 2009). In fact, **neuronal vulnerability to oxidative stress** correlates with increased levels of endogenous reactive oxygen species (ROS) and an increased defense against ROS at baseline (reviewed in Wang and Michaelis, 2010). It is therefore argued that the cellular ROS defense mechanisms cannot be further increased under a stress impact and hence, neuronal death is the consequence. Nevertheless, why do certain neuronal populations maintain this elevated ROS environment under steady-state conditions? Compelling evidence hints to a critical involvement of ROS as a signaling molecule (reviewed in Borquez et al., 2016). For example, Accardi et al. (2015) demonstrated in cerebellar granule cells that inhibitory synapses are strengthened in a mitochondrial ROS-dependent manner via the specific recruitment of α6-GABA$_A$ receptors to postsynaptic sites. This receptor recruitment happened independently from existing α1-GABA$_A$ receptors at distinct synapses and hence, complemented the already existing network. Similar results were obtained in inhibitory stellate cells with the recruitment of α3-GABA$_A$ receptors (Accardi et al., 2014). Therefore, Ak4 expression in granule cells may represent a significant mitochondrial fine-tuning under elevated ROS levels to preserve the physiology of these inhibitory neurons.

In summary, our cell type-specific profiling of mitochondria illustrates that a common cellular goal can be achieve via multiple pathways and hence is uniquely adapted to the sum of cellular processes. For example, mitochondria provide cells with ATP – however, ATP generation can be based on different fuels, like lactate, FA or glutamate, and furthermore can be provide by the blood stream and general body metabolism or the local supply via adjacent cell types. Similarly, the cellular redox defense via GSH can be maintained via the PPP, Got2 or Me2 activity in neurons, or via Nnt and Idh2 activity in astrocytes. While at a first glance these pathways seem parallel and possibly redundant, it is clear from the here presented overview in Figure 49 and 50 that certain preconditions argue against redundancy. For example, while astrocytes provide neurons with lactate and hence neuronal glucose uptake is not essential for ATP generation, glucose is an essential source for the generation of NADPH in the PPP. Furthermore, in granule cells, the supply of the PPP is further secured via conversion of oxaloacetate to PEP through Pck2. Hence, the active blockade of glycolysis in neurons is essential for their supply of NADPH and subsequent GSH recycling as demonstrated by increased oxidative stress under forced neuronal Pfkfb3 expression (Herrero-Mendez et al., 2009).

5.3. Fatty acid oxidation in the brain – local 'hotpots' in astrocytes

Fatty acids (FA) are the richest substrate available for energy production via oxidative phosphorylation. For example, one mole palmitic acid (C16:0) yields 106 mole ATP in contrast to 32 mole ATP per mole glucose (Schonfeld and Reiser, 2013). Palmitic acid oxidation also requires ~15% more oxygen and creates a $FADH_2$/NADH ratio of 0.48 in contrast to 0.2 with glucose. These differences – among several other arguments – contributed to a long debate regarding FA oxidation in the nervous system and in neurons (reviewed in Schonfeld and Reiser, 2013; Panov et al., 2014; Schonfeld and Reiser, 2017).

Initial arguments against FA oxidation in brain were: (i) the limited uptake of non-esterified FA over the blood-brain-barrier, which was experimentally refuted (Smith and Nagura, 2001; Ouellet et al., 2009); (ii) the low activation of FA via CoA conjugation and hence, toxic effect of free FA on mitochondrial membrane potential, ETC and permeability transition pore. While these hold true for long-chain FA, medium- and short-chain FA are rapidly activated (Ebert et al., 2003), and in particular, neurons are protected against free long-chain FA via the high expression of long-chain acyl-CoA thioesterase 7 (Acot7; Ellis et al., 2013); and (iii) the additional side effects such as hypoxic conditioning due to higher oxygen demand, enhanced ROS production and overall slow oxidation compared to neuronal demand. In fact, neural FA oxidation is slow compared to heart or kidney mitochondria (Bird et al., 1985; Yang et al., 1987), requires more oxygen due to a higher $FADH_2$/NADH ratio and hence, is not ideal to supply neurons with ATP under neurotransmission. However, glucose is neither an ideal substrate within this context and thus, neurons depend on glial lactate during neurotransmission and on ketone bodies during periods of fasting (reviewed in Morris, 2005). Further arguments for FA oxidation in neural cells come from transcriptome studies of cultured and FACSorted astrocytes, which quantified the machinery of mitochondrial beta-oxidation on the transcript level (Eraso-Pichot et al., 2018). Additionally, FA oxidation has been demonstrated in cultured astrocytes (Edmond et al., 1987; Sayre et al., 2017) and hypothalamic neurons (McFadden et al., 2014). Furthermore, Cpt2 deletion in *Drosophila melanogaster* let to the accumulation of triglycerides in neural cells (Schulz et al., 2015). Therefore, the presence of beta-oxidation in neural cells cannot be questioned anymore, while its distribution among neural cell types is unclear. For example, neural stem cells depend on FA oxidation during their quiescent state and modulate beta-oxidation for proliferation and differentiation (Knobloch et al., 2017; see Chapter 1.4.2).

Our proteomic profiling of immunocaptured mitochondria from the adult mouse cerebellum corroborate in vitro and transcriptome data by quantifying the majority of proteins involved in mitochondrial beta-oxidation and their enrichment in astrocytic mitochondria (Figure 34). We furthermore performed oxygen consumption assays on cell type-specific mitochondria from astrocytes and Purkinje cells. While these mitochondrial populations did not differ in their respiration on pyruvate/malate or succinate/rotenone, L-palmitoylcarnitine/malate oxidation was significantly reduced in neuronal mitochondria (Figure 36); hence, our experiments provide the so-far closest in vivo examination of long-chain FA oxidation in defined neural cell types. Still, the comparison across substrates confirmed the notion that even astrocytic beta-oxidation is slow and less efficient than respiration on pyruvate or succinate (reviewed in Schonfeld and Reiser, 2013). However, Panov et al. (2014) pointed out that in situ mitochondria are exposed to a mixture of substrates and that the in vitro analysis via one isolated substrate represents a rather artificial situation. In fact, when the authors combined long-chain FA with other substrates, an additive effect on mitochondrial respiration was observed with brain mitochondria.

In addition, astrocytic beta-oxidation in vivo might be further improved via the synergistic action of mitochondria and peroxisomes. While long-chain FA need to be imported via the carnitine shuttle system for mitochondrial beta-oxidation, these steps are absent in peroxisomes for the degradation of very long-chain FA. After initial breakdown, acylcarnitine is transferred from peroxisomes to mitochondria and here fully oxidized. We observed an enrichment of peroxisomal proteins in our proteome from astrocytic mitochondria (see Chapter 4.2.5). Further evaluation of peroxisome density in Purkinje cells and astrocytes did not confirm a differential abundance of this organelle (Figure A1d); thereby ruling out pure contamination as a possible explanation. Additionally, Pex11β and Eci2 have been described to tether mitochondria and peroxisomes (Shai et al., 2018; Fan et al., 2016) and Eci2 was significantly enriched in our proteome from astrocytic mitochondria (Table A2). Therefore, **I hypothesize that in astrocytes, mitochondria and peroxisomes form a metabolic unit for the efficient oxidation of FA under steady-state in vivo conditions** (Figure 51a). This unit not only improves the processing of FA, but also minimizes the exposure of mitochondria to free FA and reduces the generation of ROS via the synergistic clearance by peroxisomes and mitochondria.

Interestingly, Liu et al. (2017) showed that neuronal lipids are transferred to astrocytes in a ROS-dependent manner. This transfer was mediated via fatty acid transport proteins and apolipoproteins, and induced the formation of lipid droplets in astrocytes. FA transfer to astrocytes was neuroprotective and scavenged, peroxidized lipids, which are neurotoxic (Bailey et al., 2015). Presumably, under normal conditions, astrocytic lipid droplets are metabolized via beta-oxidation. Recently, Ioannou et al. (2019) further confirmed these results by demonstrating that also hyperactive neurons generate FA and expel them as apolipoprotein E-positive vesicles. These were taken up by astrocytes and either stored as lipid droplets or metabolized in mitochondria. The overall process was stimulated via neuronal activity and activated astrocytic programs to enhance beta-oxidation and antioxidant defense mechanisms. Furthermore, the authors confirmed lipid droplet formation in vivo in the

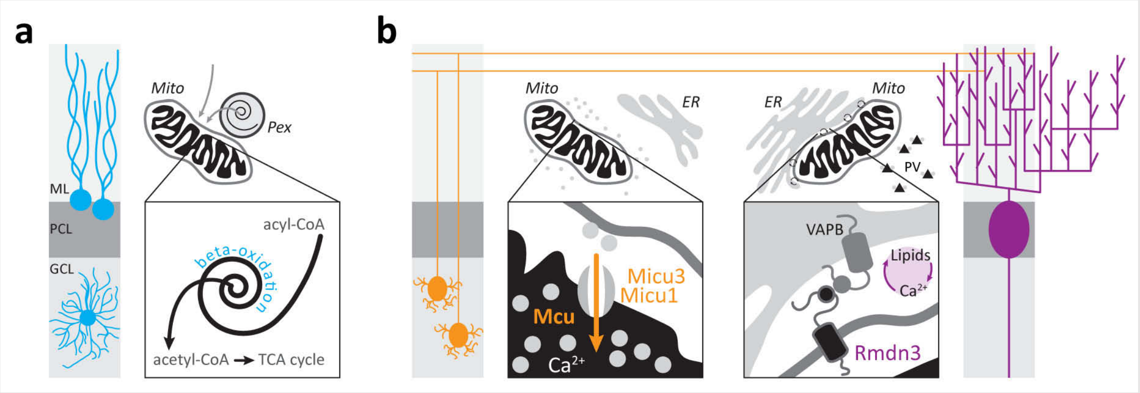

Figure 51│Functional specialization of cerebellar mitochondria. Proteomic profiling of cell type-specific mitochondria revealed fine-tuning of central mitochondrial functions among neural cells. (**a**) Astrocytic mitochondria (Mito) are specialized in beta-oxidation with possible cooperation of peroxisomes (Pex); while (**b**) neuronal mitochondria differentially regulate their Ca^{2+} homeostasis: in granule cells (orange) via enhanced Mcu expression and in Purkinje cells (magenta) via parvalbumin (PV) and increased contact sites to the endoplasmic reticulum (ER) mediated by Rmdn3 and its interactors (e.g. VAPB). ER-mitochondria contact sites are also known to mediate lipid exchange and signaling. ML, molecular layer; PCL, Purkinje cell layer; GCL, granule cell layer.

context of stroke. Hence, both reports provide evidence for a coupled FA metabolism between astrocytes and neurons.

In summary, while the evidence for FA oxidation in neurons is limited to certain neuronal subtypes, e.g. hypothalamic neurons, ample evidence exists that neural cells are able to oxidize long-chain FA. While this oxidation is not comparable to other tissues with high-energy demands and FA oxidation (e.g. heart and kidney), its neural form serves neuronal protection and cell survival. Hence, further deciphering of its regulation and cell type enrichment will advance our understanding of neurodegeneration.

5.4. Mitochondrial calcium signaling in cerebellar neurons – One signal, many goals

In cells, calcium (Ca^{2+}) is a ubiquitous signaling molecule. Dependent on speed, amplitude, spatial and temporal resolution, Ca^{2+} signals evoke a plethora of cellular functions aided by the action of channels, pumps, intracellular stores and buffer proteins (reviewed in Berridge et al., 2000). For example, in neurons, Ca^{2+} triggers exocytosis at the presynapse, activity-dependent synaptic plasticity at the postsynapse and gene expression in the nucleus (reviewed in Neher and Sakaba, 2008; Mateos-Aparicio and Rodríguez-Moreno, 2020; Tyssowski and Gray, 2019). While cytosolic free Ca^{2+} concentrations are kept low at rest (100 nM), the endoplasmic reticulum (ER) stores Ca^{2+} at a concentration ~100 μM. Mitochondria participate in the cellular Ca^{2+} homeostasis by acting as an additional buffer system in the cytosol and at privileged contact sites to the ER and plasma membrane (reviewed in Szymanski et al., 2017). These contact sites are established via tether and spacer proteins, which allow for the close apposition of membranes and the formation of Ca^{2+} microdomains with Ca^{2+} concentrations >10 μM during signaling events (Rizzuto et al., 1998; Csordas et al., 2010). Furthermore, mitochondrial Ca^{2+} activates the TCA cycle via modulation of PDH, Idh and α-Kgdh, the F_0F_1ATPase and controls apoptosis. In addition, mitochondria can store large amounts of bound Ca^{2+} as calcium-phosphate complexes, which is generated at free matrix Ca^{2+} concentrations of 0.2 – 2 μM (Chalmers and Nicholls, 2003).

Ca^{2+} enters mitochondria via the mitochondrial calcium uniporter (Mcu) complex in the inner mitochondrial membrane, which we found strikingly enriched in granule cell mitochondria (Figure 37a and b). Regulation of Mcu function has been described on the expression level of Mcu/McuB ratio, Mcu/Micu1 ratio and via posttranslational modifications (see Chapter 1.2.3). Given that mitochondrial Ca^{2+} handling is essential for proper neurotransmission

(Shutov et al., 2013; Marland et al., 2016), we were surprised to find Mcu differentially expressed between neuronal subtypes. In granule cells, I quantified a 3.2-fold enrichment of Mcu in comparison to Purkinje cells, which correlated with a drastic functional reduction of ex vivo Ca^{2+} uptake in Purkinje cell mitochondria (Figure 37c). Also in astrocytes, we observed a trend towards reduced Mcu levels and correlating diminished Ca^{2+} uptake compared to granule cell mitochondria. Boitier et al. (1999) showed that mitochondrial Ca^{2+} uptake reduces the propagation of astrocytic Ca^{2+} waves. Interestingly, Markus et al. (2016) previously showed differential Mcu expression between the hippocampal subregion, CA1 and CA2. Granule cell-specific ablation of Mcu completely abolished mitochondrial Ca^{2+} uptake in immunocaptured organelles from these cells (Figure 38), which is in contrast to a report by Hamilton et al. (2018) claiming that brain mitochondria uptake Ca^{2+} in a Mcu-independent way. Furthermore, Henzi and Schwaller (2015) reported that loss of parvalbumin increases Mcu, McuR1 and Micu1 expression levels as well as mitochondrial mass. Parvalbumin is a slow-onset, cytosolic Ca^{2+}-binding protein and highly expressed in Purkinje cells, where it prevents paired-pulse facilitation and contributes to short-term plasticity (Caillard et al., 2000). Mitochondrial mass was also increased in parvalbumin-deficient Purkinje cells, while calbindin deficiency did not alter mitochondrial abundance (Chen et al., 2006). Therefore, the authors hypothesized that parvalbumin deficiency is compensated via mitochondrial Ca^{2+} handling by restoring a similar spatiotemporal Ca^{2+} signaling. Hence, Mcu downregulation in Purkinje cells could be related to the abundant presence of parvalbumin. In contrast, granule cells do not contain parvalbumin but have calretinin as cytosolic buffer and Ca^{2+} sensor (Resibois and Rogers, 1992).

In Purkinje cells, we found the ER-mitochondrial tether regulator of microtubule dynamics protein 3 (Rmdn3) ≥3.5-fold enriched compared to mitochondria from granule cells and astrocytes (Figure 39a). De Vos et al. (2012) showed that Rmdn3 interacts with the ER-resident protein vesicle-associated membrane protein-associated protein B (VAPB). In vitro, the interaction of VAPB and Rmdn3 facilitates close contact sites between the ER and mitochondria and increases Ca^{2+} transfer between the organelles (Stoica et al., 2014). This interaction is increased with the ALS-associated mutant $VAPB^{P56S}$ (Nishimura et al., 2004) and disrupted by mutations in TDP-43 (Stoica et al., 2014), FUS (Stoica et al., 2016) and α-synuclein (Paillusson et al., 2017). In addition, Rmdn3 has been shown to be involved in mitochondrial phosphatidylserine synthesis via the interact with oxysterol-binding protein-related protein 5 and 8 (ORP5/8), which are also ER membrane proteins (Galmes et al., 2016). Correlating with the high abundance of Rmdn3 in Purkinje cell mitochondria, we observed increased ER-mitochondria contact sites (distance ≤30 nm) in these neurons in contrast to a low organelle contact frequency in granule cells and astrocytes (Figure 39c). Through the ablation of Rmdn3 (Figure 40), we further showed that approximately half of these contact sites are mediated via Rmdn3 in Purkinje cells. To our surprise, these animals do not develop behavioral alterations or Purkinje cell loss despite the observed structural phenotype, and further experiments will have to reveal the underlying compensatory mechanisms in Ca^{2+} homeostasis and/or lipid metabolism.

In summary, the inverse presence of Mcu complex and ER-mitochondria contact sites is a compelling difference between granule cell and Purkinje cell mitochondria. On the one hand, granule cell mitochondria have high Mcu, Micu1 and Micu3 levels, while they are rarely in contact with the ER. Recently, Patron et al. (2019) showed that Micu3 acts as Mcu activator in close contrast to the gatekeeping function of Micu2. Additionally, Ashrafi et al. (2020) demonstrated that neuronal mitochondria are able to uptake Ca^{2+} at a lower threshold and in the absence of ER contacts due to Micu3 properties. On the other hand, ~37% of mitochondrial surface is in close contact with the ER in Purkinje cells, while these organelles present with low levels of Mcu complex. A similar phenotype was observed upon Mfn2 deletion. Here, Filadi et al. (2015) observed – in contrast to an earlier report (de Brito and Scorrano, 2008) – an increase in ER-mitochondria contact sites and a reduction in Ca^{2+} uptake in Mfn2-deficient cells. Here, the authors argued that the loss of proper spacing between the organelles results in compensatory repression of Mcu expression to avoid mitochondrial Ca^{2+} overload. Hence, I speculate that non-compensatory close ER-mitochondrial contact sites, i.e. contacts under stead-state in vivo conditions as seen in Purkinje cells, might have a prominent role in signaling, lipid transfer and metabolic adaptation – rather than in enhanced Ca^{2+} transfer and buffering as commonly assumed. **I therefore hypothesizes that in granule cells, cytosolic Ca^{2+} buffering is achieved via mitochondria and their increased level of the Mcu complex** (Figure 51b, left side). Due to Micu3 properties, mitochondrial Ca^{2+} is taken up at lower cytosolic concentrations than with Micu2 and structural microdomains with the ER are not necessary. **In contrast, Ca^{2+} buffering in Purkinje cells is achieved via cytosolic parvalbumin and hence, mitochondria are fine-tuned for other functions associated with close ER juxtaposition, e.g. for lipid synthesis and signaling** (Figure 51b, right side). Still, even with low Mcu expression levels in vivo, mitochondrial Ca^{2+} signaling is probably accomplished via these enhanced organelle contact sites, even though ex vivo Ca^{2+} uptake cannot be recapitulated in isolated Purkinje cell organelles.

5.5. Future perspectives of cell type-specific mitochondria

Our profiling of cerebellar mitochondria has revealed the fine-tuning and cell type-specific enrichment of mitochondrial functions that so far could not be uncovered in this complexity due to the lack of a sufficient in vivo tool. The MitoTag mouse model provides us with such a tool to answer many questions covering mitochondrial biology across development, aging, under specific metabolic restrictions or disease models, and this in a cell type-resolved manner.

Interestingly, **mitochondrial diversity as observed in cerebellar neurons and astrocytes seems to be conserved during evolution**, given that I was able to differentiate mitochondrial populations from neurons and astrocytes in rodents, human, aves and amphibians (Figure 43 and 44). The conservation of mitochondrial diversity in the nervous system also allowed us to transfer our set of mitochondrial 'markers' from the cerebellum to other neuronal tissues. These cell type-resolved, mitochondrial 'markers' represent another important finding of this thesis, because they allow for the in situ probing of mitochondrial alterations in disease models and pathological tissue from human cases. This is possible without the need of additional transgene expression, e.g. mito-GFP, or the identification of neural cells by marker proteins. We here chose to demonstrate this possibility for Alzheimer's disease and amyotrophic lateral sclerosis, given that mitochondrial pathology has been reported in both diseases (see Chapter 1.7). While traditionally in neurodegeneration, the analysis of mitochondrial alterations is restricted to neuronal cell bodies due to the need of cell type markers (Grünewald et al., 2014; Lax et al., 2016), this limitation is eliminated with the introduced mitochondrial 'markers' and even axonal and synaptic organelles can now be included in the analysis.

Additionally, I anticipate that in the future, cell type-specific mitochondria will be examined with many more functional assays and omics-based screening, such as lipidomics, phosphoproteomics or metabolomics, than demonstrated in this thesis. These results will further elucidate mitochondria biology and intertwine it with the many possible cellular contexts that are present in vivo.

REFERENCES

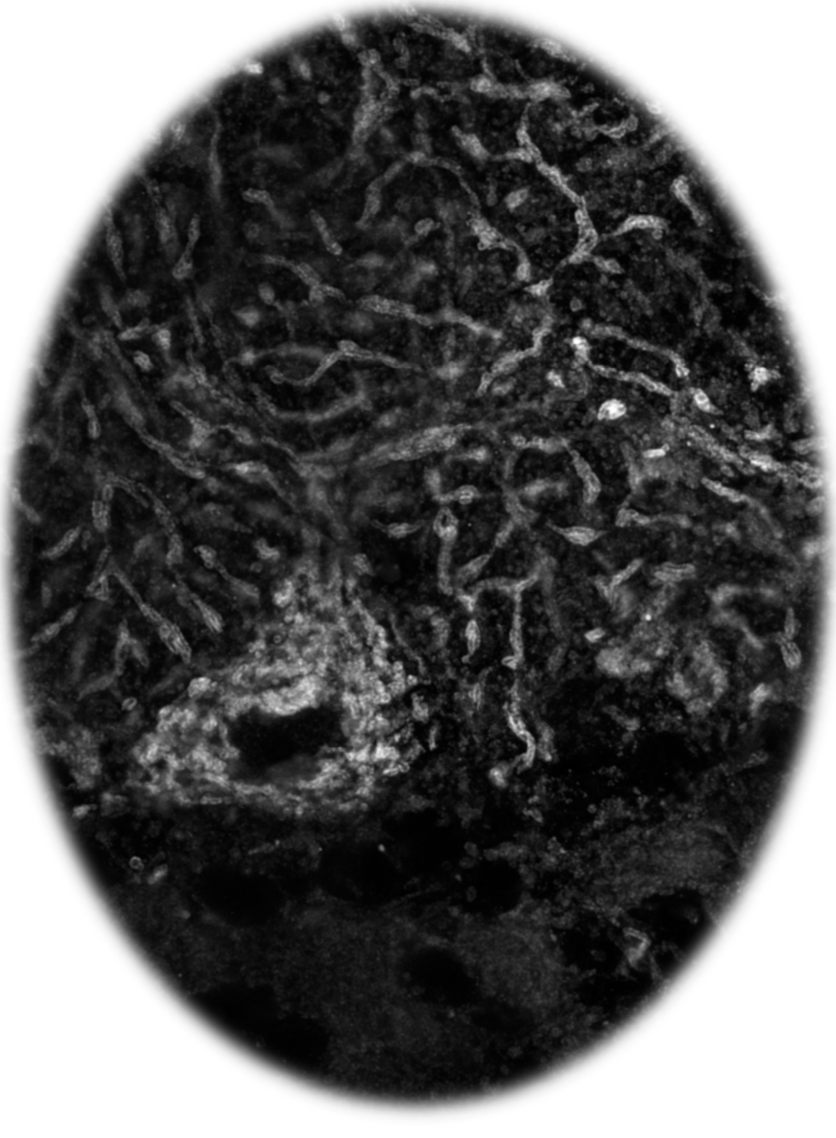

Chapter 6: References

Abe, Y., Shodai, T., Muto, T., Mihara, K., Torii, H., Nishikawa, S., Endo, T., and Kohda, D. (2000). Structural basis of presequence recognition by the mitochondrial protein import receptor Tom20. Cell *100*, 551-560.

Abu-Remaileh, M., Wyant, G.A., Kim, C., Laqtom, N.N., Abbasi, M., Chan, S.H., Freinkman, E., and Sabatini, D.M. (2017). Lysosomal metabolomics reveals V-ATPase- and mTOR-dependent regulation of amino acid efflux from lysosomes. Science *358*, 807-813.

Abudu, Y.P., Pankiv, S., Mathai, B.J., Lamark, T., Johansen, T., and Simonsen, A. (2019). NIPSNAP1 and NIPSNAP2 act as "eat me" signals to allow sustained recruitment of autophagy receptors during mitophagy. Autophagy *15*, 1845-1847.

Accardi, M.V., Brown, P.M., Miraucourt, L.S., Orser, B.A., and Bowie, D. (2015). alpha6-Containing GABAA Receptors Are the Principal Mediators of Inhibitory Synapse Strengthening by Insulin in Cerebellar Granule Cells. J Neurosci *35*, 9676-9688.

Accardi, M.V., Daniels, B.A., Brown, P.M., Fritschy, J.M., Tyagarajan, S.K., and Bowie, D. (2014). Mitochondrial reactive oxygen species regulate the strength of inhibitory GABA-mediated synaptic transmission. Nat Commun *5*, 3168.

Acosta, M.J., Vazquez Fonseca, L., Desbats, M.A., Cerqua, C., Zordan, R., Trevisson, E., and Salviati, L. (2016). Coenzyme Q biosynthesis in health and disease. Biochim Biophys Acta *1857*, 1079-1085.

Adachi, J., Kumar, C., Zhang, Y., and Mann, M. (2007). In-depth analysis of the adipocyte proteome by mass spectrometry and bioinformatics. Mol Cell Proteomics *6*, 1257-1273.

Adeva-Andany, M.M., Carneiro-Freire, N., Seco-Filgueira, M., Fernandez-Fernandez, C., and Mourino-Bayolo, D. (2019). Mitochondrial beta-oxidation of saturated fatty acids in humans. Mitochondrion *46*, 73-90.

Agarwal, A., Wu, P.H., Hughes, E.G., Fukaya, M., Tischfield, M.A., Langseth, A.J., Wirtz, D., and Bergles, D.E. (2017). Transient Opening of the Mitochondrial Permeability Transition Pore Induces Microdomain Calcium Transients in Astrocyte Processes. Neuron *93*, 587-605 e587.

Ahier, A., Ahier, A., and Zuryn, S. (2018a). Cell-specific mitochondrial affinity purification (CS-MAP) protocol. Protocol Exchange.

Ahier, A., Dai, C.Y., Tweedie, A., Bezawork-Geleta, A., Kirmes, I., and Zuryn, S. (2018b). Affinity purification of cell-specific mitochondria from whole animals resolves patterns of genetic mosaicism. Nat Cell Biol *20*, 352-360.

Ahtoniemi, T., Jaronen, M., Keksa-Goldsteine, V., Goldsteins, G., and Koistinaho, J. (2008). Mutant SOD1 from spinal cord of G93A rats is destabilized and binds to inner mitochondrial membrane. Neurobiol Dis *32*, 479-485.

Akar, S., and Sur, E. (2010). The development of chicken cerebellar cortex and the determination of AgNOR activity of the Purkinje cell nuclei. Belgian Journal of Zoology *140*.

Alcazar-Fabra, M., Trevisson, E., and Brea-Calvo, G. (2018). Clinical syndromes associated with Coenzyme Q10 deficiency. Essays Biochem *62*, 377-398.

Allaman, I., Belanger, M., and Magistretti, P.J. (2015). Methylglyoxal, the dark side of glycolysis. Front Neurosci *9*, 23.

Almeida, A., Almeida, J., Bolanos, J.P., and Moncada, S. (2001). Different responses of astrocytes and neurons to nitric oxide: the role of glycolytically generated ATP in astrocyte protection. Proc Natl Acad Sci U S A *98*, 15294-15299.

Alzheimer, A. (1907). Uber eine eigenartige erkrankung der hirnrinde allgem zeit psychiat. Psych-Gerich Med *64*, 146-148.

Anandatheerthavarada, H.K., Biswas, G., Robin, M.A., and Avadhani, N.G. (2003). Mitochondrial targeting and a novel transmembrane arrest of Alzheimer's amyloid precursor protein impairs mitochondrial function in neuronal cells. J Cell Biol *161*, 41-54.

Andrus, P.K., Fleck, T.J., Gurney, M.E., and Hall, E.D. (1998). Protein oxidative damage in a transgenic mouse model of familial amyotrophic lateral sclerosis. J Neurochem *71*, 2041-2048.

Angerer, H. (2015). Eukaryotic LYR Proteins Interact with Mitochondrial Protein Complexes. Biology (Basel) *4*, 133-150.

Antony, A.N., Paillard, M., Moffat, C., Juskeviciute, E., Correnti, J., Bolon, B., Rubin, E., Csordas, G., Seifert, E.L., Hoek, J.B.*, et al.* (2016). MICU1 regulation of mitochondrial Ca(2+) uptake dictates survival and tissue regeneration. Nat Commun *7*, 10955.

Aprison, M.H., and Daly, E.C. (1978). Biochemical Aspects of Transmission at Inhibitory Synapses: The Role of Glycine. In Advances in Neurochemistry, B.W. Agranoff, and M.H. Aprison, eds. (Boston, MA: Springer US), pp. 203-294.

Arun, P., Abu-Taleb, R., Oguntayo, S., Wang, Y., Valiyaveettil, M., Long, J.B., and Nambiar, M.P. (2013). Acute mitochondrial dysfunction after blast exposure: potential role of mitochondrial glutamate oxaloacetate transaminase. J Neurotrauma *30*, 1645-1651.

Aryaman, J., Johnston, I.G., and Jones, N.S. (2018). Mitochondrial Heterogeneity. Front Genet *9*, 718.

Ashburner, M., Ball, C.A., Blake, J.A., Botstein, D., Butler, H., Cherry, J.M., Davis, A.P., Dolinski, K., Dwight, S.S., Eppig, J.T.*, et al.* (2000). Gene ontology: tool for the unification of biology. The Gene Ontology Consortium. Nature genetics *25*, 25-29.

Ashraf, S., Gee, H.Y., Woerner, S., Xie, L.X., Vega-Warner, V., Lovric, S., Fang, H., Song, X., Cattran, D.C., Avila-Casado, C.*, et al.* (2013). ADCK4 mutations promote steroid-resistant nephrotic syndrome through CoQ10 biosynthesis disruption. J Clin Invest *123*, 5179-5189.

Ashrafi, G., de Juan-Sanz, J., Farrell, R.J., and Ryan, T.A. (2020). Molecular Tuning of the Axonal Mitochondrial Ca(2+) Uniporter Ensures Metabolic Flexibility of Neurotransmission. Neuron *105*, 678-687 e675.

Azarias, G., Perreten, H., Lengacher, S., Poburko, D., Demaurex, N., Magistretti, P.J., and Chatton, J.Y. (2011). Glutamate transport decreases mitochondrial pH and modulates oxidative metabolism in astrocytes. J Neurosci *31*, 3550-3559.

Azzi, A., Glerum, M., Koller, R., Mertens, W., and Spycher, S. (1993). The mitochondrial tricarboxylate carrier. J Bioenerg Biomembr *25*, 515-524.

Bailey, A.P., Koster, G., Guillermier, C., Hirst, E.M., MacRae, J.I., Lechene, C.P., Postle, A.D., and Gould, A.P. (2015). Antioxidant Role for Lipid Droplets in a Stem Cell Niche of Drosophila. Cell *163*, 340-353.

Baloyannis, S.J. (2006). Mitochondrial alterations in Alzheimer's disease. J Alzheimers Dis *9*, 119-126.

Banci, L., Bertini, I., Boca, M., Girotto, S., Martinelli, M., Valentine, J.S., and Vieru, M. (2008). SOD1 and amyotrophic lateral sclerosis: mutations and oligomerization. PloS one *3*, e1677.

Barber, S.C., and Shaw, P.J. (2010). Oxidative stress in ALS: key role in motor neuron injury and therapeutic target. Free Radic Biol Med *48*, 629-641.

Barski, J.J., Dethleffsen, K., and Meyer, M. (2000). Cre recombinase expression in cerebellar Purkinje cells. Genesis *28*, 93-98.

Baughman, J.M., Perocchi, F., Girgis, H.S., Plovanich, M., Belcher-Timme, C.A., Sancak, Y., Bao, X.R., Strittmatter, L., Goldberger, O., Bogorad, R.L*., et al.* (2011). Integrative genomics identifies MCU as an essential component of the mitochondrial calcium uniporter. Nature *476*, 341-345.

Bayraktar, E.C., Baudrier, L., Ozerdem, C., Lewis, C.A., Chan, S.H., Kunchok, T., Abu-Remaileh, M., Cangelosi, A.L., Sabatini, D.M., Birsoy, K.*, et al.* (2019). MITO-Tag Mice enable rapid isolation and multimodal profiling of mitochondria from specific cell types in vivo. Proc Natl Acad Sci U S A *116*, 303-312.

Beck, S.J., Guo, L., Phensy, A., Tian, J., Wang, L., Tandon, N., Gauba, E., Lu, L., Pascual, J.M., Kroener, S.*, et al.* (2016). Deregulation of mitochondrial F1FO-ATP synthase via OSCP in Alzheimer's disease. Nat Commun *7*, 11483.

Belanger, M., Yang, J., Petit, J.M., Laroche, T., Magistretti, P.J., and Allaman, I. (2011). Role of the glyoxalase system in astrocyte-mediated neuroprotection. J Neurosci *31*, 18338-18352.

Benard, G., Bellance, N., James, D., Parrone, P., Fernandez, H., Letellier, T., and Rossignol, R. (2007). Mitochondrial bioenergetics and structural network organization. J Cell Sci *120*, 838-848.

Benjamin, A.M., and Quastel, J.H. (1975). Metabolism of amino acids and ammonia in rat brain cortex slices in vitro: a possible role of ammonia in brain function. J Neurochem *25*, 197-206.

Benz, R. (1985). Porin from bacterial and mitochondrial outer membranes. CRC Crit Rev Biochem *19*, 145-190.

Berg, J.M., Tymoczko, J.L., and Stryer, L. (2002). Biochemistry, Fifth Edition (W.H. Freeman).

Berridge, M.J., Lipp, P., and Bootman, M.D. (2000). The versatility and universality of calcium signalling. Nature reviews Molecular cell biology *1*, 11-21.

Bharti, P., Schliebs, W., Schievelbusch, T., Neuhaus, A., David, C., Kock, K., Herrmann, C., Meyer, H.E., Wiese, S., Warscheid, B.*, et al.* (2011). PEX14 is required for microtubule-based peroxisome motility in human cells. J Cell Sci *124*, 1759-1768.

Bird, M.I., Munday, L.A., Saggerson, E.D., and Clark, J.B. (1985). Carnitine acyltransferase activities in rat brain mitochondria. Bimodal distribution, kinetic constants, regulation by malonyl-CoA and developmental pattern. Biochem J *226*, 323-330.

Bittar, P.G., Charnay, Y., Pellerin, L., Bouras, C., and Magistretti, P.J. (1996). Selective distribution of lactate dehydrogenase isoenzymes in neurons and astrocytes of human brain. J Cereb Blood Flow Metab *16*, 1079-1089.

Blaza, J.N., Serreli, R., Jones, A.J., Mohammed, K., and Hirst, J. (2014). Kinetic evidence against partitioning of the ubiquinone pool and the catalytic relevance of respiratory-chain supercomplexes. Proc Natl Acad Sci U S A *111*, 15735-15740.

Blazquez, C., Sanchez, C., Velasco, G., and Guzman, M. (1998). Role of carnitine palmitoyltransferase I in the control of ketogenesis in primary cultures of rat astrocytes. J Neurochem *71*, 1597-1606.

Bogenhagen, D.F., Rousseau, D., and Burke, S. (2008). The layered structure of human mitochondrial DNA nucleoids. J Biol Chem *283*, 3665-3675.

Boitier, E., Rea, R., and Duchen, M.R. (1999). Mitochondria exert a negative feedback on the propagation of intracellular Ca2+ waves in rat cortical astrocytes. J Cell Biol *145*, 795-808.

Bolanos, J.P., and Almeida, A. (2010). The pentose-phosphate pathway in neuronal survival against nitrosative stress. IUBMB Life *62*, 14-18.

Bolanos, J.P., Almeida, A., and Moncada, S. (2010). Glycolysis: a bioenergetic or a survival pathway? Trends Biochem Sci *35*, 145-149.

Bondarenko, A.I., Jean-Quartier, C., Malli, R., and Graier, W.F. (2013). Characterization of distinct single-channel properties of Ca(2)(+) inward currents in mitochondria. Pflugers Arch *465*, 997-1010.

Bonnefont, J.P., Djouadi, F., Prip-Buus, C., Gobin, S., Munnich, A., and Bastin, J. (2004). Carnitine palmitoyltransferases 1 and 2: biochemical, molecular and medical aspects. Mol Aspects Med *25*, 495-520.

Borquez, D.A., Urrutia, P.J., Wilson, C., van Zundert, B., Nunez, M.T., and Gonzalez-Billault, C. (2016). Dissecting the role of redox signaling in neuronal development. J Neurochem *137*, 506-517.

Borthwick, G.M., Johnson, M.A., Ince, P.G., Shaw, P.J., and Turnbull, D.M. (1999). Mitochondrial enzyme activity in amyotrophic lateral sclerosis: implications for the role of mitochondria in neuronal cell death. Ann Neurol *46*, 787-790.

Bradbury, M.W., Stump, D., Guarnieri, F., and Berk, P.D. (2011). Molecular modeling and functional confirmation of a predicted fatty acid binding site of mitochondrial aspartate aminotransferase. J Mol Biol *412*, 412-422.

Brandt, T., Cavellini, L., Kuhlbrandt, W., and Cohen, M.M. (2016). A mitofusin-dependent docking ring complex triggers mitochondrial fusion in vitro. Elife *5*, e14618.

Braverman, N.E., Raymond, G.V., Rizzo, W.B., Moser, A.B., Wilkinson, M.E., Stone, E.M., Steinberg, S.J., Wangler, M.F., Rush, E.T., Hacia, J.G.*, et al.* (2016). Peroxisome biogenesis disorders in the Zellweger spectrum: An overview of current diagnosis, clinical manifestations, and treatment guidelines. Mol Genet Metab *117*, 313-321.

Bravo-Alonso, I., Navarrete, R., Arribas-Carreira, L., Perona, A., Abia, D., Couce, M.L., Garcia-Cazorla, A., Morais, A., Domingo, R., Ramos, M.A.*, et al.* (2017). Nonketotic hyperglycinemia: Functional assessment of missense variants in GLDC to understand phenotypes of the disease. Hum Mutat *38*, 678-691.

Breckwoldt, M.O., Pfister, F.M., Bradley, P.M., Marinkovic, P., Williams, P.R., Brill, M.S., Plomer, B., Schmalz, A., St Clair, D.K., Naumann, R.*, et al.* (2014). Multiparametric optical analysis of mitochondrial redox signals during neuronal physiology and pathology in vivo. Nat Med *20*, 555-560.

Brill, M.S., Kleele, T., Ruschkies, L., Wang, M., Marahori, N.A., Reuter, M.S., Hausrat, T.J., Weigand, E., Fisher, M., Ahles, A.*, et al.* (2016). Branch-Specific Microtubule Destabilization Mediates Axon Branch Loss during Neuromuscular Synapse Elimination. Neuron *92*, 845-856.

Brody, S., Oh, C., Hoja, U., and Schweizer, E. (1997). Mitochondrial acyl carrier protein is involved in lipoic acid synthesis in Saccharomyces cerevisiae. FEBS Letters *408*, 217-220.

Bruin, W.J., Frantz, B.M., and Sallach, H.J. (1973). The occurrence of a glycine cleavage system in mammalian brain. J Neurochem *20*, 1649-1658.

Buckner, R.L. (2013). The cerebellum and cognitive function: 25 years of insight from anatomy and neuroimaging. Neuron *80*, 807-815.

Burre, J., Zimmermann, H., and Volknandt, W. (2007). Immunoisolation and subfractionation of synaptic vesicle proteins. Anal Biochem *362*, 172-181.

Busche, M.A., Eichhoff, G., Adelsberger, H., Abramowski, D., Wiederhold, K.H., Haass, C., Staufenbiel, M., Konnerth, A., and Garaschuk, O. (2008). Clusters of hyperactive neurons near amyloid plaques in a mouse model of Alzheimer's disease. Science *321*, 1686-1689.

Bushong, E.A., Martone, M.E., Jones, Y.Z., and Ellisman, M.H. (2002). Protoplasmic astrocytes in CA1 stratum radiatum occupy separate anatomical domains. J Neurosci *22*, 183-192.

Buttermore, E.D., Piochon, C., Wallace, M.L., Philpot, B.D., Hansel, C., and Bhat, M.A. (2012). Pinceau organization in the cerebellum requires distinct functions of neurofascin in Purkinje and basket neurons during postnatal development. J Neurosci *32*, 4724-4742.

Cabodevilla, A.G., Sanchez-Caballero, L., Nintou, E., Boiadjieva, V.G., Picatoste, F., Gubern, A., and Claro, E. (2013). Cell survival during complete nutrient deprivation depends on lipid droplet-fueled beta-oxidation of fatty acids. J Biol Chem *288*, 27777-27788.

Cabral-Costa, J.V., and Kowaltowski, A.J. (2020). Neurological disorders and mitochondria. Mol Aspects Med *71*, 100826.

Caillard, O., Moreno, H., Schwaller, B., Llano, I., Celio, M.R., and Marty, A. (2000). Role of the calcium-binding protein parvalbumin in short-term synaptic plasticity. Proc Natl Acad Sci U S A *97*, 13372-13377.

Calvo, S., Jain, M., Xie, X., Sheth, S.A., Chang, B., Goldberger, O.A., Spinazzola, A., Zeviani, M., Carr, S.A., and Mootha, V.K. (2006). Systematic identification of human mitochondrial disease genes through integrative genomics. Nature genetics *38*, 576-582.

Calvo, S.E., Clauser, K.R., and Mootha, V.K. (2016). MitoCarta2.0: an updated inventory of mammalian mitochondrial proteins. Nucleic Acids Res *44*, D1251-1257.

Calvo, S.E., Julien, O., Clauser, K.R., Shen, H., Kamer, K.J., Wells, J.A., and Mootha, V.K. (2017). Comparative Analysis of Mitochondrial N-Termini from Mouse, Human, and Yeast. Mol Cell Proteomics *16*, 512-523.

Calvo, S.E., and Mootha, V.K. (2010). The mitochondrial proteome and human disease. Annu Rev Genomics Hum Genet *11*, 25-44.

Campos-Sandoval, J.A., Martin-Rufian, M., Cardona, C., Lobo, C., Penalver, A., and Marquez, J. (2015). Glutaminases in brain: Multiple isoforms for many purposes. Neurochem Int *88*, 1-5.

Canevari, L., Clark, J.B., and Bates, T.E. (1999). beta-Amyloid fragment 25-35 selectively decreases complex IV activity in isolated mitochondria. FEBS Lett *457*, 131-134.

Cantor, J.R., Abu-Remaileh, M., Kanarek, N., Freinkman, E., Gao, X., Louissaint, A., Jr., Lewis, C.A., and Sabatini, D.M. (2017). Physiologic Medium Rewires Cellular Metabolism and Reveals Uric Acid as an Endogenous Inhibitor of UMP Synthase. Cell *169*, 258-272 e217.

Cardoso, S.M., Santos, S., Swerdlow, R.H., and Oliveira, C.R. (2001). Functional mitochondria are required for amyloid beta-mediated neurotoxicity. FASEB J *15*, 1439-1441.

Caroni, P. (1997). Overexpression of growth-associated proteins in the neurons of adult transgenic mice. J Neurosci Methods *71*, 3-9.

Carri, M.T., D'Ambrosi, N., and Cozzolino, M. (2017). Pathways to mitochondrial dysfunction in ALS pathogenesis. Biochem Biophys Res Commun *483*, 1187-1193.

Carta, I., Chen, C.H., Schott, A.L., Dorizan, S., and Khodakhah, K. (2019). Cerebellar modulation of the reward circuitry and social behavior. Science *363*, eaav0581.

Casley, C.S., Canevari, L., Land, J.M., Clark, J.B., and Sharpe, M.A. (2002). Beta-amyloid inhibits integrated mitochondrial respiration and key enzyme activities. J Neurochem *80*, 91-100.

Cenini, G., Lloret, A., and Cascella, R. (2019). Oxidative Stress in Neurodegenerative Diseases: From a Mitochondrial Point of View. Oxid Med Cell Longev *2019*, 2105607.

Cenini, G., and Voos, W. (2019). Mitochondria as Potential Targets in Alzheimer Disease Therapy: An Update. Frontiers in Pharmacology *10*, 902.

Chacinska, A., Koehler, C.M., Milenkovic, D., Lithgow, T., and Pfanner, N. (2009). Importing mitochondrial proteins: machineries and mechanisms. Cell *138*, 628-644.

Chalmers, S., and Nicholls, D.G. (2003). The Relationship between Free and Total Calcium Concentrations in the Matrix of Liver and Brain Mitochondria. Journal of Biological Chemistry *278*, 19062-19070.

Charcot, J.M. (1881). Lecture XIII on amyotrophic lateral sclerosis. symptomatology. Lectures on diseases of the nervous system London: New Sydenham Society, 192-204.

Chatton, J.Y., Pellerin, L., and Magistretti, P.J. (2003). GABA uptake into astrocytes is not associated with significant metabolic cost: implications for brain imaging of inhibitory transmission. Proc Natl Acad Sci U S A *100*, 12456-12461.

Chen, G., Racay, P., Bichet, S., Celio, M.R., Eggli, P., and Schwaller, B. (2006). Deficiency in parvalbumin, but not in calbindin D-28k upregulates mitochondrial volume and decreases smooth endoplasmic reticulum surface selectively in a peripheral, subplasmalemmal region in the soma of Purkinje cells. Neuroscience *142*, 97-105.

Chen, W.W., Freinkman, E., and Sabatini, D.M. (2017). Rapid immunopurification of mitochondria for metabolite profiling and absolute quantification of matrix metabolites. Nat Protoc *12*, 2215-2231.

Chen, W.W., Freinkman, E., Wang, T., Birsoy, K., and Sabatini, D.M. (2016). Absolute Quantification of Matrix Metabolites Reveals the Dynamics of Mitochondrial Metabolism. Cell *166*, 1324-1337 e1311.

Chio, A., Logroscino, G., Traynor, B.J., Collins, J., Simeone, J.C., Goldstein, L.A., and White, L.A. (2013). Global epidemiology of amyotrophic lateral sclerosis: a systematic review of the published literature. Neuroepidemiology *41*, 118-130.

Christofk, H.R., Vander Heiden, M.G., Wu, N., Asara, J.M., and Cantley, L.C. (2008). Pyruvate kinase M2 is a phosphotyrosine-binding protein. Nature *452*, 181-186.

Cogliati, S., Frezza, C., Soriano, M.E., Varanita, T., Quintana-Cabrera, R., Corrado, M., Cipolat, S., Costa, V., Casarin, A., Gomes, L.C.*, et al.* (2013). Mitochondrial cristae shape determines respiratory chain supercomplexes assembly and respiratory efficiency. Cell *155*, 160-171.

Cogswell, A.M., Stevens, R.J., and Hood, D.A. (1993). Properties of skeletal muscle mitochondria isolated from subsarcolemmal and intermyofibrillar regions. Am J Physiol *264*, C383-389.

Cohen, Y., Klug, Y.A., Dimitrov, L., Erez, Z., Chuartzman, S.G., Elinger, D., Yofe, I., Soliman, K., Gartner, J., Thoms, S.*, et al.* (2014). Peroxisomes are juxtaposed to strategic sites on mitochondria. Mol Biosyst *10*, 1742-1748.

Comte, B., Vincent, G., Bouchard, B., Benderdour, M., and Des Rosiers, C. (2002). Reverse flux through cardiac NADP(+)-isocitrate dehydrogenase under normoxia and ischemia. Am J Physiol Heart Circ Physiol *283*, H1505-1514.

Console, L., Giangregorio, N., Indiveri, C., and Tonazzi, A. (2014). Carnitine/acylcarnitine translocase and carnitine palmitoyltransferase 2 form a complex in the inner mitochondrial membrane. Mol Cell Biochem *394*, 307-314.

Costello, J.L., Castro, I.G., Camoes, F., Schrader, T.A., McNeall, D., Yang, J., Giannopoulou, E.A., Gomes, S., Pogenberg, V., Bonekamp, N.A.*, et al.* (2017). Predicting the targeting of tail-anchored proteins to subcellular compartments in mammalian cells. J Cell Sci *130*, 1675-1687.

Costello, J.L., Passmore, J.B., Islinger, M., and Schrader, M. (2018). Multi-localized Proteins: The Peroxisome-Mitochondria Connection. In Proteomics of Peroxisomes: Identifying Novel Functions and Regulatory Networks, L.A. del Río, and M. Schrader, eds. (Singapore: Springer Singapore), pp. 383-415.

Cotzias, G.C., and Dole, V.P. (1951). Metabolism of amines. II. Mitochondrial localization of monoamine oxidase. Proc Soc Exp Biol Med *78*, 157-160.

Cox, J., Hein, M.Y., Luber, C.A., Paron, I., Nagaraj, N., and Mann, M. (2014). Accurate proteome-wide label-free quantification by delayed normalization and maximal peptide ratio extraction, termed MaxLFQ. Mol Cell Proteomics *13*, 2513-2526.

Cox, J., and Mann, M. (2012). 1D and 2D annotation enrichment: a statistical method integrating quantitative proteomics with complementary high-throughput data. BMC Bioinformatics *13 Suppl 16*, S12.

Csordas, G., Golenar, T., Seifert, E.L., Kamer, K.J., Sancak, Y., Perocchi, F., Moffat, C., Weaver, D., de la Fuente Perez, S., Bogorad, R.*, et al.* (2013). MICU1 controls both the threshold and cooperative activation of the mitochondrial Ca(2)(+) uniporter. Cell Metab *17*, 976-987.

Csordas, G., Varnai, P., Golenar, T., Roy, S., Purkins, G., Schneider, T.G., Balla, T., and Hajnoczky, G. (2010). Imaging interorganelle contacts and local calcium dynamics at the ER-mitochondrial interface. Mol Cell *39*, 121-132.

Cummins, N., Tweedie, A., Zuryn, S., Bertran-Gonzalez, J., and Gotz, J. (2019). Disease-associated tau impairs mitophagy by inhibiting Parkin translocation to mitochondria. EMBO J *38*, e99360.

D'Erchia, A.M., Atlante, A., Gadaleta, G., Pavesi, G., Chiara, M., De Virgilio, C., Manzari, C., Mastropasqua, F., Prazzoli, G.M., Picardi, E.*, et al.* (2015). Tissue-specific mtDNA abundance from exome data and its correlation with mitochondrial transcription, mass and respiratory activity. Mitochondrion *20*, 13-21.

Daikhin, Y., and Yudkoff, M. (2000). Compartmentation of brain glutamate metabolism in neurons and glia. J Nutr *130*, 1026S-1031S.

Dalla Rosa, I., Durigon, R., Pearce, S.F., Rorbach, J., Hirst, E.M., Vidoni, S., Reyes, A., Brea-Calvo, G., Minczuk, M., Woellhaf, M.W.*, et al.* (2014). MPV17L2 is required for ribosome assembly in mitochondria. Nucleic Acids Res *42*, 8500-8515.

de Bari, L., Atlante, A., Guaragnella, N., Principato, G., and Passarella, S. (2002). D-Lactate transport and metabolism in rat liver mitochondria. Biochem J *365*, 391-403.

de Barry, J., Vincendon, G., and Gombos, G. (1983). Uptake and metabolism of L-[3H]glutamate and L-[3H]glutamine in adult rat cerebellar slices. Neurochem Res *8*, 1321-1335.

de Brito, O.M., and Scorrano, L. (2008). Mitofusin 2 tethers endoplasmic reticulum to mitochondria. Nature *456*, 605-610.

De Stefani, D., Raffaello, A., Teardo, E., Szabo, I., and Rizzuto, R. (2011). A forty-kilodalton protein of the inner membrane is the mitochondrial calcium uniporter. Nature *476*, 336-340.

De Stefani, D., Rizzuto, R., and Pozzan, T. (2016). Enjoy the Trip: Calcium in Mitochondria Back and Forth. Annu Rev Biochem *85*, 161-192.

De Vos, K.J., Morotz, G.M., Stoica, R., Tudor, E.L., Lau, K.F., Ackerley, S., Warley, A., Shaw, C.E., and Miller, C.C. (2012). VAPB interacts with the mitochondrial protein PTPIP51 to regulate calcium homeostasis. Hum Mol Genet *21*, 1299-1311.

Dehnes, Y., Chaudhry, F.A., Ullensvang, K., Lehre, K.P., Storm-Mathisen, J., and Danbolt, N.C. (1998). The glutamate transporter EAAT4 in rat cerebellar Purkinje cells: a glutamate-gated chloride channel concentrated near the synapse in parts of the dendritic membrane facing astroglia. J Neurosci *18*, 3606-3619.

Delgado, T., Petralia, R.S., Freeman, D.W., Sedlacek, M., Wang, Y.X., Brenowitz, S.D., Sheu, S.H., Gu, J.W., Kapogiannis, D., Mattson, M.P.*, et al.* (2019). Comparing 3D ultrastructure of presynaptic and postsynaptic mitochondria. Biol Open *8*, bio044834.

Deluca, H.F., and Engstrom, G.W. (1961). Calcium uptake by rat kidney mitochondria. Proc Natl Acad Sci U S A *47*, 1744-1750.

Demarquoy, J., and Le Borgne, F. (2015). Crosstalk between mitochondria and peroxisomes. World J Biol Chem *6*, 301-309.

Dennis, S.C., Lai, J.C., and Clark, J.B. (1977). Comparative studies on glutamate metabolism in synpatic and non-synaptic rat brain mitochondria. Biochem J *164*, 727-736.

Devine, M.J., and Kittler, J.T. (2018). Mitochondria at the neuronal presynapse in health and disease. Nat Rev Neurosci *19*, 63-80.

Ding, C., Li, Y., Guo, F., Jiang, Y., Ying, W., Li, D., Yang, D., Xia, X., Liu, W., Zhao, Y*., et al.* (2016). A Cell-type-resolved Liver Proteome. Mol Cell Proteomics *15*, 3190-3202.

Dixit, E., Boulant, S., Zhang, Y., Lee, A.S., Odendall, C., Shum, B., Hacohen, N., Chen, Z.J., Whelan, S.P., Fransen, M*., et al.* (2010). Peroxisomes are signaling platforms for antiviral innate immunity. Cell *141*, 668-681.

Doerflinger, N.H., Macklin, W.B., and Popko, B. (2003). Inducible site-specific recombination in myelinating cells. Genesis *35*, 63-72.

Doyle, J.P., Dougherty, J.D., Heiman, M., Schmidt, E.F., Stevens, T.R., Ma, G., Bupp, S., Shrestha, P., Shah, R.D., Doughty, M.L*., et al.* (2008). Application of a translational profiling approach for the comparative analysis of CNS cell types. Cell *135*, 749-762.

Drahota, Z., Rauchova, H., Mikova, M., Kaul, P., and Bass, A. (1983). Phosphoenolpyruvate shuttle--transport of energy from mitochondria to cytosol. FEBS Lett *157*, 347-349.

Dringen, R., Gebhardt, R., and Hamprecht, B. (1993). Glycogen in astrocytes: possible function as lactate supply for neighboring cells. Brain Research *623*, 208-214.

Du, H., Guo, L., Fang, F., Chen, D., Sosunov, A.A., McKhann, G.M., Yan, Y., Wang, C., Zhang, H., Molkentin, J.D*., et al.* (2008). Cyclophilin D deficiency attenuates mitochondrial and neuronal perturbation and ameliorates learning and memory in Alzheimer's disease. Nat Med *14*, 1097-1105.

Duran, J., Tevy, M.F., Garcia-Rocha, M., Calbo, J., Milan, M., and Guinovart, J.J. (2012). Deleterious effects of neuronal accumulation of glycogen in flies and mice. EMBO Mol Med *4*, 719-729.

Earle, S.R., Anderson, W.M., and Fisher, R.R. (1978). Evidence that reconstituted bovine heart mitochondrial transhydrogenase functions as a proton pump. FEBS Letters *91*, 21-24.

Eaton, S. (2002). Control of mitochondrial beta-oxidation flux. Prog Lipid Res *41*, 197-239.

Ebert, D., Haller, R.G., and Walton, M.E. (2003). Energy Contribution of Octanoate to Intact Rat Brain Metabolism Measured by13C Nuclear Magnetic Resonance Spectroscopy. The Journal of Neuroscience *23*, 5928-5935.

Edmond, J., Robbins, R.A., Bergstrom, J.D., Cole, R.A., and de Vellis, J. (1987). Capacity for substrate utilization in oxidative metabolism by neurons, astrocytes, and oligodendrocytes from developing brain in primary culture. J Neurosci Res *18*, 551-561.

Egner, A., Jakobs, S., and Hell, S.W. (2002). Fast 100-nm resolution three-dimensional microscope reveals structural plasticity of mitochondria in live yeast. Proc Natl Acad Sci U S A *99*, 3370-3375.

Eisenberg-Bord, M., Shai, N., Schuldiner, M., and Bohnert, M. (2016). A Tether Is a Tether Is a Tether: Tethering at Membrane Contact Sites. Developmental cell *39*, 395-409.

Eisner, V., Picard, M., and Hajnoczky, G. (2018). Mitochondrial dynamics in adaptive and maladaptive cellular stress responses. Nat Cell Biol *20*, 755-765.

Elgadi, K.M., Meguid, R.A., Qian, M., Souba, W.W., and Abcouwer, S.F. (1999). Cloning and analysis of unique human glutaminase isoforms generated by tissue-specific alternative splicing. Physiol Genomics *1*, 51-62.

Ellis, J.M., Wong, G.W., and Wolfgang, M.J. (2013). Acyl coenzyme A thioesterase 7 regulates neuronal fatty acid metabolism to prevent neurotoxicity. Mol Cell Biol *33*, 1869-1882.

Eraso-Pichot, A., Braso-Vives, M., Golbano, A., Menacho, C., Claro, E., Galea, E., and Masgrau, R. (2018). GSEA of mouse and human mitochondriomes reveals fatty acid oxidation in astrocytes. Glia *66*, 1724-1735.

Fan, J., Li, X., Issop, L., Culty, M., and Papadopoulos, V. (2016). ACBD2/ECI2-Mediated Peroxisome-Mitochondria Interactions in Leydig Cell Steroid Biosynthesis. Mol Endocrinol *30*, 763-782.

Fecher, C., Trovo, L., Muller, S.A., Snaidero, N., Wettmarshausen, J., Heink, S., Ortiz, O., Wagner, I., Kuhn, R., Hartmann, J.*, et al.* (2019). Cell-type-specific profiling of brain mitochondria reveals functional and molecular diversity. Nat Neurosci *22*, 1731-1742.

Fecher, C., Trovò, L., Müller, S.A., Snaidero, N., Wettmarshausen, J., Heink, S., Ortiz, O., Wagner, I., Kühn, R., Hartmann, J.*, et al.* (2018). Profound functional and molecular diversity of mitochondria revealed by cell type-specific profiling in vivo. bioRxiv, 403774.

Fedorovich, S.V., Voronina, P.P., and Waseem, T.V. (2018). Ketogenic diet versus ketoacidosis: what determines the influence of ketone bodies on neurons? Neural Regen Res *13*, 2060-2063.

Felgner, P.L., Messer, J.L., and Wilson, J.E. (1979). Purification of a hexokinase-binding protein from the outer mitochondrial membrane. J Biol Chem *254*, 4946-4949.

Ferdinandusse, S., Mulders, J., L, I.J., Denis, S., Dacremont, G., Waterham, H.R., and Wanders, R.J. (1999). Molecular cloning and expression of human carnitine octanoyltransferase: evidence for its role in the peroxisomal beta-oxidation of branched-chain fatty acids. Biochem Biophys Res Commun *263*, 213-218.

Fernandez-Busnadiego, R., Saheki, Y., and De Camilli, P. (2015). Three-dimensional architecture of extended synaptotagmin-mediated endoplasmic reticulum-plasma membrane contact sites. Proc Natl Acad Sci U S A *112*, E2004-2013.

Fieni, F., Lee, S.B., Jan, Y.N., and Kirichok, Y. (2012). Activity of the mitochondrial calcium uniporter varies greatly between tissues. Nat Commun *3*, 1317.

Filadi, R., Greotti, E., Turacchio, G., Luini, A., Pozzan, T., and Pizzo, P. (2015). Mitofusin 2 ablation increases endoplasmic reticulum-mitochondria coupling. Proc Natl Acad Sci U S A *112*, E2174-2181.

Finsterer, J., and Zarrouk-Mahjoub, S. (2018). Cerebellar atrophy is common among mitochondrial disorders. Metab Brain Dis *33*, 987-988.

Fischer, J., Beckervordersandforth, R., Tripathi, P., Steiner-Mezzadri, A., Ninkovic, J., and Gotz, M. (2011). Prospective isolation of adult neural stem cells from the mouse subependymal zone. Nat Protoc *6*, 1981-1989.

Fleming, M.D., Campagna, D.R., Haslett, J.N., Trenor, C.C., and Andrews, N.C. (2001). A mutation in a mitochondrial transmembrane protein is responsible for the pleiotropic hematological and skeletal phenotype of flexed-tail (f/f) mice. Genes & Development *15*, 652-657.

Flick, M.J., and Konieczny, S.F. (2002). Identification of putative mammalian D-lactate dehydrogenase enzymes. Biochem Biophys Res Commun *295*, 910-916.

Floyd, B.J., Wilkerson, E.M., Veling, M.T., Minogue, C.E., Xia, C., Beebe, E.T., Wrobel, R.L., Cho, H., Kremer, L.S., Alston, C.L.*, et al.* (2016). Mitochondrial Protein Interaction Mapping Identifies Regulators of Respiratory Chain Function. Mol Cell *63*, 621-632.

Forner, F., Foster, L.J., Campanaro, S., Valle, G., and Mann, M. (2006). Quantitative proteomic comparison of rat mitochondria from muscle, heart, and liver. Mol Cell Proteomics *5*, 608-619.

Foster, L.J., de Hoog, C.L., Zhang, Y., Zhang, Y., Xie, X., Mootha, V.K., and Mann, M. (2006). A mammalian organelle map by protein correlation profiling. Cell *125*, 187-199.

Fowler, J.S., Logan, J., Volkow, N.D., Wang, G.J., MacGregor, R.R., and Ding, Y.S. (2002). Monoamine oxidase: radiotracer development and human studies. Methods *27*, 263-277.

Franko, A., Baris, O.R., Bergschneider, E., von Toerne, C., Hauck, S.M., Aichler, M., Walch, A.K., Wurst, W., Wiesner, R.J., Johnston, I.C.*, et al.* (2013). Efficient isolation of pure and functional mitochondria from mouse tissues using automated tissue disruption and enrichment with anti-TOM22 magnetic beads. PloS one *8*, e82392.

Fransen, M., Terlecky, S.R., and Subramani, S. (1998). Identification of a human PTS1 receptor docking protein directly required for peroxisomal protein import. Proc Natl Acad Sci U S A *95*, 8087-8092.

Friedman, J.R., Lackner, L.L., West, M., DiBenedetto, J.R., Nunnari, J., and Voeltz, G.K. (2011). ER tubules mark sites of mitochondrial division. Science *334*, 358-362.

Friedman, J.R., and Nunnari, J. (2014). Mitochondrial form and function. Nature *505*, 335-343.

Fünfschilling, U., and Reichardt, L.F. (2002). Cre-mediated recombination in rhombic lip derivatives. Genesis *33*, 160-169.

Fünfschilling, U., Supplie, L.M., Mahad, D., Boretius, S., Saab, A.S., Edgar, J., Brinkmann, B.G., Kassmann, C.M., Tzvetanova, I.D., Mobius, W*., et al.* (2012). Glycolytic oligodendrocytes maintain myelin and long-term axonal integrity. Nature *485*, 517-521.

Gabaldon, T., and Huynen, M.A. (2007). From endosymbiont to host-controlled organelle: the hijacking of mitochondrial protein synthesis and metabolism. PLoS Comput Biol *3*, e219.

Gabuzda, D., Busciglio, J., Chen, L.B., Matsudaira, P., and Yankner, B.A. (1994). Inhibition of energy metabolism alters the processing of amyloid precursor protein and induces a potentially amyloidogenic derivative. J Biol Chem *269*, 13623-13628.

Gadea, A., and Lopez-Colome, A.M. (2001a). Glial transporters for glutamate, glycine, and GABA III. Glycine transporters. J Neurosci Res *64*, 218-222.

Gadea, A., and Lopez-Colome, A.M. (2001b). Glial transporters for glutamate, glycine, and GABA: II. GABA transporters. J Neurosci Res *63*, 461-468.

Galmes, R., Houcine, A., van Vliet, A.R., Agostinis, P., Jackson, C.L., and Giordano, F. (2016). ORP5/ORP8 localize to endoplasmic reticulum-mitochondria contacts and are involved in mitochondrial function. EMBO Rep *17*, 800-810.

Ganat, Y.M., Silbereis, J., Cave, C., Ngu, H., Anderson, G.M., Ohkubo, Y., Ment, L.R., and Vaccarino, F.M. (2006). Early postnatal astroglial cells produce multilineage precursors and neural stem cells in vivo. J Neurosci *26*, 8609-8621.

Gandre-Babbe, S., and van der Bliek, A.M. (2008). The novel tail-anchored membrane protein Mff controls mitochondrial and peroxisomal fission in mammalian cells. Mol Biol Cell *19*, 2402-2412.

Gaston, D., Tsaousis, A.D., and Roger, A.J. (2009). Chapter 2 Predicting Proteomes of Mitochondria and Related Organelles from Genomic and Expressed Sequence Tag Data. In Mitochondrial Function, Part B: Mitochondrial Protein Kinases, Protein Phosphatases and Mitochondrial Diseases (Academic Press), pp. 21-47.

Gella, A., Prada-Dacasa, P., Carrascal, M., González-Torres, M., Abian, J., Sanz, E., and Quintana, A. (2019). Mitochondrial Proteome of Affected Neurons in a Mouse Model of Leigh Syndrome. bioRxiv, 2019.2012.2029.890541.

Genin, E.C., Plutino, M., Bannwarth, S., Villa, E., Cisneros-Barroso, E., Roy, M., Ortega-Vila, B., Fragaki, K., Lespinasse, F., Pinero-Martos, E*., et al.* (2016). CHCHD10 mutations promote loss of mitochondrial cristae junctions with impaired mitochondrial genome maintenance and inhibition of apoptosis. EMBO Mol Med *8*, 58-72.

Gerfen, C.R., Paletzki, R., and Heintz, N. (2013). GENSAT BAC cre-recombinase driver lines to study the functional organization of cerebral cortical and basal ganglia circuits. Neuron *80*, 1368-1383.

Ghazalpour, A., Bennett, B., Petyuk, V.A., Orozco, L., Hagopian, R., Mungrue, I.N., Farber, C.R., Sinsheimer, J., Kang, H.M., Furlotte, N*., et al.* (2011). Comparative analysis of proteome and transcriptome variation in mouse. PLoS Genet *7*, e1001393.

Gherardi, G., Nogara, L., Ciciliot, S., Fadini, G.P., Blaauw, B., Braghetta, P., Bonaldo, P., De Stefani, D., Rizzuto, R., and Mammucari, C. (2019). Loss of mitochondrial calcium uniporter rewires skeletal muscle metabolism and substrate preference. Cell Death Differ *26*, 362-381.

Gibson, G.E., Starkov, A., Blass, J.P., Ratan, R.R., and Beal, M.F. (2010). Cause and consequence: mitochondrial dysfunction initiates and propagates neuronal dysfunction, neuronal death and behavioral abnormalities in age-associated neurodegenerative diseases. Biochim Biophys Acta *1802*, 122-134.

Giles, R.E., Blanc, H., Cann, H.M., and Wallace, D.C. (1980). Maternal inheritance of human mitochondrial DNA. Proc Natl Acad Sci U S A *77*, 6715-6719.

Gill, J.S., and Sillitoe, R.V. (2019). Functional Outcomes of Cerebellar Malformations. Front Cell Neurosci *13*, 441.

Gillingwater, T.H., and Wishart, T.M. (2013). Mechanisms underlying synaptic vulnerability and degeneration in neurodegenerative disease. Neuropathol Appl Neurobiol *39*, 320-334.

Godin, N., and Eichler, J. (2017). The Mitochondrial Protein Atlas: A Database of Experimentally Verified Information on the Human Mitochondrial Proteome. J Comput Biol *24*, 906-916.

Goldberg, T., Hecht, M., Hamp, T., Karl, T., Yachdav, G., Ahmed, N., Altermann, U., Angerer, P., Ansorge, S., Balasz, K.*, et al.* (2014). LocTree3 prediction of localization. Nucleic Acids Res *42*, W350-355.

Gong, S., Doughty, M., Harbaugh, C.R., Cummins, A., Hatten, M.E., Heintz, N., and Gerfen, C.R. (2007). Targeting Cre recombinase to specific neuron populations with bacterial artificial chromosome constructs. J Neurosci *27*, 9817-9823.

Gong, S., Zheng, C., Doughty, M.L., Losos, K., Didkovsky, N., Schambra, U.B., Nowak, N.J., Joyner, A., Leblanc, G., Hatten, M.E.*, et al.* (2003). A gene expression atlas of the central nervous system based on bacterial artificial chromosomes. Nature *425*, 917-925.

Gorski, J.A., Talley, T., Qiu, M., Puelles, L., Rubenstein, J.L., and Jones, K.R. (2002). Cortical excitatory neurons and glia, but not GABAergic neurons, are produced in the Emx1-expressing lineage. J Neurosci *22*, 6309-6314.

Graham, L.C., Eaton, S.L., Brunton, P.J., Atrih, A., Smith, C., Lamont, D.J., Gillingwater, T.H., Pennetta, G., Skehel, P., and Wishart, T.M. (2017). Proteomic profiling of neuronal mitochondria reveals modulators of synaptic architecture. Mol Neurodegener *12*, 77.

Graves, S.M., Xie, Z., Stout, K.A., Zampese, E., Burbulla, L.F., Shih, J.C., Kondapalli, J., Patriarchi, T., Tian, L., Brichta, L.*, et al.* (2020). Dopamine metabolism by a monoamine oxidase mitochondrial shuttle activates the electron transport chain. Nat Neurosci *23*, 15-20.

Gregorian, C., Nakashima, J., Le Belle, J., Ohab, J., Kim, R., Liu, A., Smith, K.B., Groszer, M., Garcia, A.D., Sofroniew, M.V.*, et al.* (2009). Pten deletion in adult neural stem/progenitor cells enhances constitutive neurogenesis. J Neurosci *29*, 1874-1886.

Gronowicz, G., Swift, H., and Steck, T.L. (1984). Maturation of the reticulocyte in vitro. J Cell Sci *71*, 177-197.

Grünewald, A., Lax, N.Z., Rocha, M.C., Reeve, A.K., Hepplewhite, P.D., Rygiel, K.A., Taylor, R.W., and Turnbull, D.M. (2014). Quantitative quadruple-label immunofluorescence of mitochondrial and cytoplasmic proteins in single neurons from human midbrain tissue. J Neurosci Methods *232*, 143-149.

Guidetti, P., Amori, L., Sapko, M.T., Okuno, E., and Schwarcz, R. (2007). Mitochondrial aspartate aminotransferase: a third kynurenate-producing enzyme in the mammalian brain. J Neurochem *102*, 103-111.

Guo, X., Niemi, N.M., Hutchins, P.D., Condon, S.G.F., Jochem, A., Ulbrich, A., Higbee, A.J., Russell, J.D., Senes, A., Coon, J.J.*, et al.* (2017). Ptc7p Dephosphorylates Select Mitochondrial Proteins to Enhance Metabolic Function. Cell Rep *18*, 307-313.

Gurney, M.E., Pu, H., Chiu, A.Y., Dal Canto, M.C., Polchow, C.Y., Alexander, D.D., Caliendo, J., Hentati, A., Kwon, Y.W., Deng, H.X.*, et al.* (1994). Motor neuron degeneration in mice that express a human Cu,Zn superoxide dismutase mutation. Science *264*, 1772-1775.

Hakonen, A.H., Goffart, S., Marjavaara, S., Paetau, A., Cooper, H., Mattila, K., Lampinen, M., Sajantila, A., Lonnqvist, T., Spelbrink, J.N.*, et al.* (2008). Infantile-onset spinocerebellar ataxia and mitochondrial recessive ataxia syndrome are associated with neuronal complex I defect and mtDNA depletion. Hum Mol Genet *17*, 3822-3835.

Halim, N.D., McFate, T., Mohyeldin, A., Okagaki, P., Korotchkina, L.G., Patel, M.S., Jeoung, N.H., Harris, R.A., Schell, M.J., and Verma, A. (2010). Phosphorylation status of pyruvate dehydrogenase distinguishes metabolic phenotypes of cultured rat brain astrocytes and neurons. Glia *58*, 1168-1176.

Hamilton, J., Brustovetsky, T., Rysted, J.E., Lin, Z., Usachev, Y.M., and Brustovetsky, N. (2018). Deletion of mitochondrial calcium uniporter incompletely inhibits calcium uptake and induction of the permeability transition pore in brain mitochondria. J Biol Chem *293*, 15652-15663.

Han, J., Jung, S., Jang, J., Kam, T.I., Choi, H., Kim, B.J., Nah, J., Jo, D.G., Nakagawa, T., Nishimura, M.*, et al.* (2014). OCIAD2 activates gamma-secretase to enhance amyloid beta production by interacting with nicastrin. Cell Mol Life Sci *71*, 2561-2576.

Han, Q., Robinson, H., Cai, T., Tagle, D.A., and Li, J. (2011). Biochemical and structural characterization of mouse mitochondrial aspartate aminotransferase, a newly identified kynurenine aminotransferase-IV. Biosci Rep *31*, 323-332.

Hansson Petersen, C.A., Alikhani, N., Behbahani, H., Wiehager, B., Pavlov, P.F., Alafuzoff, I., Leinonen, V., Ito, A., Winblad, B., Glaser, E.*, et al.* (2008). The amyloid beta-peptide is imported into mitochondria via the TOM import machinery and localized to mitochondrial cristae. Proc Natl Acad Sci U S A *105*, 13145-13150.

Hardy, J., and Allsop, D. (1991). Amyloid deposition as the central event in the aetiology of Alzheimer's disease. Trends in Pharmacological Sciences *12*, 383-388.

Hardy, J.A., and Higgins, G.A. (1992). Alzheimer's disease: the amyloid cascade hypothesis. Science *256*, 184-185.

Harrington, J.L., and Murphy, E. (2015). The mitochondrial calcium uniporter: mice can live and die without it. Journal of molecular and cellular cardiology *78*, 46-53.

Harrower, T., Stewart, J.D., Hudson, G., Houlden, H., Warner, G., O'Donovan, D.G., Findlay, L.J., Taylor, R.W., De Silva, R., and Chinnery, P.F. (2008). POLG1 mutations manifesting as autosomal recessive axonal Charcot-Marie-Tooth disease. Arch Neurol *65*, 133-136.

Hartong, D.T., Dange, M., McGee, T.L., Berson, E.L., Dryja, T.P., and Colman, R.F. (2008). Insights from retinitis pigmentosa into the roles of isocitrate dehydrogenases in the Krebs cycle. Nature genetics *40*, 1230-1234.

Hassel, B. (2000). Carboxylation and anaplerosis in neurons and glia. Mol Neurobiol *22*, 21-40.

Hawkes, R., and Leclerc, N. (1987). Antigenic map of the rat cerebellar cortex: the distribution of parasagittal bands as revealed by monoclonal anti-Purkinje cell antibody mabQ113. J Comp Neurol *256*, 29-41.

Hayashi, S., and McMahon, A.P. (2002). Efficient recombination in diverse tissues by a tamoxifen-inducible form of Cre: a tool for temporally regulated gene activation/inactivation in the mouse. Dev Biol *244*, 305-318.

He, M., Pei, Z., Mohsen, A.W., Watkins, P., Murdoch, G., Van Veldhoven, P.P., Ensenauer, R., and Vockley, J. (2011). Identification and characterization of new long chain acyl-CoA dehydrogenases. Mol Genet Metab *102*, 418-429.

Heiman, M., Schaefer, A., Gong, S., Peterson, J.D., Day, M., Ramsey, K.E., Suarez-Farinas, M., Schwarz, C., Stephan, D.A., Surmeier, D.J.*, et al.* (2008). A translational profiling approach for the molecular characterization of CNS cell types. Cell *135*, 738-748.

Heldt, H.W., and Schwalbach, K. (1967). The Participation of GTP-AMP-P Transferase in Substrate Level Phosphate Transfer of Rat Liver Mitochondria1. European Journal of Biochemistry *1*, 199-206.

Henzi, T., and Schwaller, B. (2015). Antagonistic Regulation of Parvalbumin Expression and Mitochondrial Calcium Handling Capacity in Renal Epithelial Cells. PloS one *10*, e0142005.

Herculano-Houzel, S., Mota, B., and Lent, R. (2006). Cellular scaling rules for rodent brains. Proc Natl Acad Sci U S A *103*, 12138-12143.

Hernansanz-Agustin, P., Ramos, E., Navarro, E., Parada, E., Sanchez-Lopez, N., Pelaez-Aguado, L., Cabrera-Garcia, J.D., Tello, D., Buendia, I., Marina, A.*, et al.* (2017). Mitochondrial complex I deactivation is related to superoxide production in acute hypoxia. Redox Biol *12*, 1040-1051.

Herrero-Mendez, A., Almeida, A., Fernandez, E., Maestre, C., Moncada, S., and Bolanos, J.P. (2009). The bioenergetic and antioxidant status of neurons is controlled by continuous degradation of a key glycolytic enzyme by APC/C-Cdh1. Nat Cell Biol *11*, 747-752.

Herzig, M.C., Winkler, D.T., Burgermeister, P., Pfeifer, M., Kohler, E., Schmidt, S.D., Danner, S., Abramowski, D., Sturchler-Pierrat, C., Burki, K.*, et al.* (2004). Abeta is targeted to the vasculature in a mouse model of hereditary cerebral hemorrhage with amyloidosis. Nat Neurosci *7*, 954-960.

Hirai, K., Aliev, G., Nunomura, A., Fujioka, H., Russell, R.L., Atwood, C.S., Johnson, A.B., Kress, Y., Vinters, H.V., Tabaton, M.*, et al.* (2001). Mitochondrial abnormalities in Alzheimer's disease. J Neurosci *21*, 3017-3023.

Hitz, C., Steuber-Buchberger, P., Delic, S., Wurst, W., and Kuhn, R. (2009). Generation of shRNA transgenic mice. Methods Mol Biol *530*, 101-129.

Hitz, C., Wurst, W., and Kuhn, R. (2007). Conditional brain-specific knockdown of MAPK using Cre/loxP regulated RNA interference. Nucleic Acids Res *35*, e90.

Hodge, R.D., Bakken, T.E., Miller, J.A., Smith, K.A., Barkan, E.R., Graybuck, L.T., Close, J.L., Long, B., Johansen, N., Penn, O.*, et al.* (2019). Conserved cell types with divergent features in human versus mouse cortex. Nature *573*, 61-68.

Hoitzing, H., Johnston, I.G., and Jones, N.S. (2015). What is the function of mitochondrial networks? A theoretical assessment of hypotheses and proposal for future research. Bioessays *37*, 687-700.

Hojeberg, B., and Rydstrom, J. (1977). Purification and molecular properties of reconstitutively active nicotinamide nucleotide transhydrogenase from beef heart mitochondria. Biochem Biophys Res Commun *78*, 1183-1190.

Hollander, J.M., Thapa, D., and Shepherd, D.L. (2014). Physiological and structural differences in spatially distinct subpopulations of cardiac mitochondria: influence of cardiac pathologies. Am J Physiol Heart Circ Physiol *307*, H1-14.

Honorat, J.A., Nakatsuji, Y., Shimizu, M., Kinoshita, M., Sumi-Akamaru, H., Sasaki, T., Takata, K., Koda, T., Namba, A., Yamashita, K*., et al.* (2017). Febuxostat ameliorates secondary progressive experimental autoimmune encephalomyelitis by restoring mitochondrial energy production in a GOT2-dependent manner. PloS one *12*, e0187215.

Horie, C., Suzuki, H., Sakaguchi, M., and Mihara, K. (2002). Characterization of signal that directs C-tail-anchored proteins to mammalian mitochondrial outer membrane. Mol Biol Cell *13*, 1615-1625.

Hornig-Do, H.T., Gunther, G., Bust, M., Lehnartz, P., Bosio, A., and Wiesner, R.J. (2009). Isolation of functional pure mitochondria by superparamagnetic microbeads. Anal Biochem *389*, 1-5.

Houten, S.M., and Wanders, R.J. (2010). A general introduction to the biochemistry of mitochondrial fatty acid beta-oxidation. J Inherit Metab Dis *33*, 469-477.

Hovelmeyer, N., Hao, Z., Kranidioti, K., Kassiotis, G., Buch, T., Frommer, F., von Hoch, L., Kramer, D., Minichiello, L., Kollias, G*., et al.* (2005). Apoptosis of oligodendrocytes via Fas and TNF-R1 is a key event in the induction of experimental autoimmune encephalomyelitis. J Immunol *175*, 5875-5884.

Hsieh, P.C., Wang, C.C., Tsai, C.L., Yeh, Y.M., Lee, Y.S., and Wu, Y.R. (2019). POLG R964C and GBA L444P mutations in familial Parkinson's disease: Case report and literature review. Brain Behav *9*, e01281.

Huang, J., Yu, J., Tu, L., Huang, N., Li, H., and Luo, Y. (2019). Isocitrate Dehydrogenase Mutations in Glioma: From Basic Discovery to Therapeutics Development. Front Oncol *9*, 506.

Hung, V., Lam, S.S., Udeshi, N.D., Svinkina, T., Guzman, G., Mootha, V.K., Carr, S.A., and Ting, A.Y. (2017). Proteomic mapping of cytosol-facing outer mitochondrial and ER membranes in living human cells by proximity biotinylation. Elife *6*, e24463.

Hung, V., Zou, P., Rhee, H.W., Udeshi, N.D., Cracan, V., Svinkina, T., Carr, S.A., Mootha, V.K., and Ting, A.Y. (2014). Proteomic mapping of the human mitochondrial intermembrane space in live cells via ratiometric APEX tagging. Mol Cell *55*, 332-341.

Iacobazzi, V., Invernizzi, F., Baratta, S., Pons, R., Chung, W., Garavaglia, B., Dionisi-Vici, C., Ribes, A., Parini, R., Huertas, M.D*., et al.* (2004). Molecular and functional analysis of SLC25A20 mutations causing carnitine-acylcarnitine translocase deficiency. Hum Mutat *24*, 312-320.

Ikeda, Y., Dabrowski, C., and Tanaka, K. (1983). Separation and properties of five distinct acyl-CoA dehydrogenases from rat liver mitochondria. Identification of a new 2-methyl branched chain acyl-CoA dehydrogenase. J Biol Chem *258*, 1066-1076.

Inbar-Feigenberg, M., Blaser, S., Hawkins, C., Shannon, P., Hewson, S., and Chitayat, D. (2018). Mitochondrial POLG related disorder presenting prenatally with fetal cerebellar growth arrest. Metab Brain Dis *33*, 1369-1373.

Ioannou, M.S., Jackson, J., Sheu, S.H., Chang, C.L., Weigel, A.V., Liu, H., Pasolli, H.A., Xu, C.S., Pang, S., Matthies, D*., et al.* (2019). Neuron-Astrocyte Metabolic Coupling Protects against Activity-Induced Fatty Acid Toxicity. Cell *177*, 1522-1535 e1514.

Israelson, A., Arbel, N., Da Cruz, S., Ilieva, H., Yamanaka, K., Shoshan-Barmatz, V., and Cleveland, D.W. (2010). Misfolded mutant SOD1 directly inhibits VDAC1 conductance in a mouse model of inherited ALS. Neuron *67*, 575-587.

Ito, M., and Itō, M. (1984). The cerebellum and neural control (Raven press).

Itoh, Y., Esaki, T., Shimoji, K., Cook, M., Law, M.J., Kaufman, E., and Sokoloff, L. (2003). Dichloroacetate effects on glucose and lactate oxidation by neurons and astroglia in vitro and on glucose utilization by brain in vivo. Proc Natl Acad Sci U S A *100*, 4879-4884.

Itzhak, D.N., Tyanova, S., Cox, J., and Borner, G.H. (2016). Global, quantitative and dynamic mapping of protein subcellular localization. Elife *5*, e16950.

Jadiya, P., Kolmetzky, D.W., Tomar, D., Di Meco, A., Lombardi, A.A., Lambert, J.P., Luongo, T.S., Ludtmann, M.H., Pratico, D., and Elrod, J.W. (2019). Impaired mitochondrial calcium efflux contributes to disease progression in models of Alzheimer's disease. Nat Commun *10*, 3885.

James, D.I., Parone, P.A., Mattenberger, Y., and Martinou, J.C. (2003). hFis1, a novel component of the mammalian mitochondrial fission machinery. J Biol Chem *278*, 36373-36379.

Jernberg, J.N., Bowman, C.E., Wolfgang, M.J., and Scafidi, S. (2017). Developmental regulation and localization of carnitine palmitoyltransferases (CPTs) in rat brain. J Neurochem *142*, 407-419.

Jethva, R., Bennett, M.J., and Vockley, J. (2008). Short-chain acyl-coenzyme A dehydrogenase deficiency. Mol Genet Metab *95*, 195-200.

John, S., Weiss, J.N., and Ribalet, B. (2011). Subcellular localization of hexokinases I and II directs the metabolic fate of glucose. PloS one *6*, e17674.

Johnson, A.B., and Blum, N.R. (1970). Nucleoside phosphatase activities associated with the tangles and plaques of alzheimer's disease: a histochemical study of natural and experimental neurofibrillary tangles. J Neuropathol Exp Neurol *29*, 463-478.

Johnson, D.T., Harris, R.A., French, S., Blair, P.V., You, J., Bemis, K.G., Wang, M., and Balaban, R.S. (2007). Tissue heterogeneity of the mammalian mitochondrial proteome. Am J Physiol Cell Physiol *292*, C689-697.

Johnson, J.D., Mehus, J.G., Tews, K., Milavetz, B.I., and Lambeth, D.O. (1998). Genetic evidence for the expression of ATP- and GTP-specific succinyl-CoA synthetases in multicellular eucaryotes. J Biol Chem *273*, 27580-27586.

Johnson, J.W., and Ascher, P. (1987). Glycine potentiates the NMDA response in cultured mouse brain neurons. Nature *325*, 529-531.

Kacso, G., Ravasz, D., Doczi, J., Nemeth, B., Madgar, O., Saada, A., Ilin, P., Miller, C., Ostergaard, E., Iordanov, I., *et al.* (2016). Two transgenic mouse models for beta-subunit components of succinate-CoA ligase yielding pleiotropic metabolic alterations. Biochem J *473*, 3463-3485.

Kadenbach, B. (2003). Intrinsic and extrinsic uncoupling of oxidative phosphorylation. Biochim Biophys Acta *1604*, 77-94.

Kadrmas, E.F., Ray, P.D., and Lambeth, D.O. (1991). Apparent ATP-linked succinate thiokinase activity and its relation to nucleoside diphosphate kinase in mitochondrial matrix preparations from rabbit. Biochim Biophys Acta *1074*, 339-346.

Kang, J.S., Tian, J.H., Pan, P.Y., Zald, P., Li, C., Deng, C., and Sheng, Z.H. (2008). Docking of axonal mitochondria by syntaphilin controls their mobility and affects short-term facilitation. Cell *132*, 137-148.

Katunuma, N., Matsuzawa, T., and Huzino, A. (1962). Differences between the transaminases in mitochondria and soluble fraction. II. Glutamic-oxaloacetic transaminase. J Vitaminol (Kyoto) *8*, 74-79.

Kennedy, S.R., Salk, J.J., Schmitt, M.W., and Loeb, L.A. (2013). Ultra-sensitive sequencing reveals an age-related increase in somatic mitochondrial mutations that are inconsistent with oxidative damage. PLoS Genet *9*, e1003794.

Kerschensteiner, M., Reuter, M.S., Lichtman, J.W., and Misgeld, T. (2008). Ex vivo imaging of motor axon dynamics in murine triangularis sterni explants. Nat Protoc *3*, 1645-1653.

Kim, Y.S., Shin, J.H., Hall, F.S., and Linden, D.J. (2009). Dopamine signaling is required for depolarization-induced slow current in cerebellar Purkinje cells. J Neurosci *29*, 8530-8538.

Kinoshita, A., Noda, M., and Kinoshita, M. (2000). Differential localization of septins in the mouse brain. J Comp Neurol *428*, 223-239.

Kislinger, T., Cox, B., Kannan, A., Chung, C., Hu, P., Ignatchenko, A., Scott, M.S., Gramolini, A.O., Morris, Q., Hallett, M.T., *et al.* (2006). Global survey of organ and organelle protein expression in mouse: combined proteomic and transcriptomic profiling. Cell *125*, 173-186.

Klecker, T., Scholz, D., Fortsch, J., and Westermann, B. (2013). The yeast cell cortical protein Num1 integrates mitochondrial dynamics into cellular architecture. J Cell Sci *126*, 2924-2930.

Knobloch, M., Braun, S.M., Zurkirchen, L., von Schoultz, C., Zamboni, N., Arauzo-Bravo, M.J., Kovacs, W.J., Karalay, O., Suter, U., Machado, R.A.*, et al.* (2013). Metabolic control of adult neural stem cell activity by Fasn-dependent lipogenesis. Nature *493*, 226-230.

Knobloch, M., Pilz, G.A., Ghesquiere, B., Kovacs, W.J., Wegleiter, T., Moore, D.L., Hruzova, M., Zamboni, N., Carmeliet, P., and Jessberger, S. (2017). A Fatty Acid Oxidation-Dependent Metabolic Shift Regulates Adult Neural Stem Cell Activity. Cell Rep *20*, 2144-2155.

Koch, C. (2019). The Diversity of Cell Types in the Human Brain. Brains, Minds and Machines Summer Course 2019, MBL Woods Hole, online lecture; https://cbmm.mit.edu/video/diversity-cell-types-human-brain.

Koch, J., and Brocard, C. (2012). PEX11 proteins attract Mff and human Fis1 to coordinate peroxisomal fission. J Cell Sci *125*, 3813-3826.

Koch, P., Viard, M., Stenzinger, A., Brobeil, A., Tag, C., Steger, K., and Wimmer, M. (2009). Expression profile of PTPIP51 in mouse brain. J Comp Neurol *517*, 892-905.

Kong, M.J., Han, S.J., Kim, J.I., Park, J.W., and Park, K.M. (2018). Mitochondrial NADP(+)-dependent isocitrate dehydrogenase deficiency increases cisplatin-induced oxidative damage in the kidney tubule cells. Cell Death Dis *9*, 488.

Kory, N., Wyant, G.A., Prakash, G., Uit de Bos, J., Bottanelli, F., Pacold, M.E., Chan, S.H., Lewis, C.A., Wang, T., Keys, H.R.*, et al.* (2018). SFXN1 is a mitochondrial serine transporter required for one-carbon metabolism. Science *362*, eaat9528.

Kovacs-Bogdan, E., Sancak, Y., Kamer, K.J., Plovanich, M., Jambhekar, A., Huber, R.J., Myre, M.A., Blower, M.D., and Mootha, V.K. (2014). Reconstitution of the mitochondrial calcium uniporter in yeast. Proc Natl Acad Sci U S A *111*, 8985-8990.

Krebs, H.A. (1935). Metabolism of amino-acids: The synthesis of glutamine from glutamic acid and ammonia, and the enzymic hydrolysis of glutamine in animal tissues. Biochem J *29*, 1951-1969.

Krebs, H.A. (1970). The history of the tricarboxylic acid cycle. Perspect Biol Med *14*, 154-170.

Kulkarni, V., Khadilkar, R.J., Magadi, S.S., and Inamdar, M.S. (2011). Asrij maintains the stem cell niche and controls differentiation during Drosophila lymph gland hematopoiesis. PloS one *6*, e27667.

Kure, S., Kato, K., Dinopoulos, A., Gail, C., DeGrauw, T.J., Christodoulou, J., Bzduch, V., Kalmanchey, R., Fekete, G., Trojovsky, A.*, et al.* (2006). Comprehensive mutation analysis of GLDC, AMT, and GCSH in nonketotic hyperglycinemia. Hum Mutat *27*, 343-352.

Kurland, C.G., and Andersson, S.G. (2000). Origin and evolution of the mitochondrial proteome. Microbiol Mol Biol Rev *64*, 786-820.

Kustatscher, G., Grabowski, P., Schrader, T.A., Passmore, J.B., Schrader, M., and Rappsilber, J. (2019). Co-regulation map of the human proteome enables identification of protein functions. Nat Biotechnol *37*, 1361-1371.

Kvamme, E., Tveit, B., and Svenneby, G. (1970). Glutaminase from pig renal cortex. I. Purification and general properties. J Biol Chem *245*, 1871-1877.

Laake, J.H., Takumi, Y., Eidet, J., Torgner, I.A., Roberg, B., Kvamme, E., and Ottersen, O.P. (1999). Postembedding immunogold labelling reveals subcellular localization and pathway-specific enrichment of phosphate activated glutaminase in rat cerebellum. Neuroscience *88*, 1137-1151.

Lagier-Tourenne, C., Tazir, M., Lopez, L.C., Quinzii, C.M., Assoum, M., Drouot, N., Busso, C., Makri, S., Ali-Pacha, L., Benhassine, T.*, et al.* (2008). ADCK3, an ancestral kinase, is mutated in a form of recessive ataxia associated with coenzyme Q10 deficiency. Am J Hum Genet *82*, 661-672.

Lai, J.C., Walsh, J.M., Dennis, S.C., and Clark, J.B. (1977). Synaptic and non-synaptic mitochondria from rat brain: isolation and characterization. J Neurochem *28*, 625-631.

Laine, J., and Axelrad, H. (1994). The candelabrum cell: a new interneuron in the cerebellar cortex. J Comp Neurol *339*, 159-173.

Lambert, J.P., Luongo, T.S., Tomar, D., Jadiya, P., Gao, E., Zhang, X., Lucchese, A.M., Kolmetzky, D.W., Shah, N.S., and Elrod, J.W. (2019). MCUB Regulates the Molecular Composition of the Mitochondrial Calcium Uniporter Channel to Limit Mitochondrial Calcium Overload During Stress. Circulation *140*, 1720-1733.

Lamers, Y., Williamson, J., Theriaque, D.W., Shuster, J.J., Gilbert, L.R., Keeling, C., Stacpoole, P.W., and Gregory, J.F., 3rd (2009). Production of 1-carbon units from glycine is extensive in healthy men and women. J Nutr *139*, 666-671.

Lao, G., Scheuss, V., Gerwin, C.M., Su, Q., Mochida, S., Rettig, J., and Sheng, Z.-H. (2000). Syntaphilin: A Syntaxin-1 Clamp that Controls SNARE Assembly. Neuron *25*, 191-201.

Lawson, E.L., Clifton, J.G., Huang, F., Li, X., Hixson, D.C., and Josic, D. (2006). Use of magnetic beads with immobilized monoclonal antibodies for isolation of highly pure plasma membranes. Electrophoresis *27*, 2747-2758.

Lax, N.Z., Campbell, G.R., Reeve, A.K., Ohno, N., Zambonin, J., Blakely, E.L., Taylor, R.W., Bonilla, E., Tanji, K., DiMauro, S.*, et al.* (2012a). Loss of myelin-associated glycoprotein in kearns-sayre syndrome. Arch Neurol *69*, 490-499.

Lax, N.Z., Gorman, G.S., and Turnbull, D.M. (2017). Review: Central nervous system involvement in mitochondrial disease. Neuropathol Appl Neurobiol *43*, 102-118.

Lax, N.Z., Grady, J., Laude, A., Chan, F., Hepplewhite, P.D., Gorman, G., Whittaker, R.G., Ng, Y., Cunningham, M.O., and Turnbull, D.M. (2016). Extensive respiratory chain defects in inhibitory interneurones in patients with mitochondrial disease. Neuropathol Appl Neurobiol *42*, 180-193.

Lax, N.Z., Hepplewhite, P.D., Reeve, A.K., Nesbitt, V., McFarland, R., Jaros, E., Taylor, R.W., and Turnbull, D.M. (2012b). Cerebellar ataxia in patients with mitochondrial DNA disease: a molecular clinicopathological study. J Neuropathol Exp Neurol *71*, 148-161.

Lazarow, P.B., and De Duve, C. (1976). A fatty acyl-CoA oxidizing system in rat liver peroxisomes; enhancement by clofibrate, a hypolipidemic drug. Proc Natl Acad Sci U S A *73*, 2043-2046.

Lehninger, A.L. (1974). Role of phosphate and other proton-donating anions in respiration-coupled transport of Ca2+ by mitochondria. Proc Natl Acad Sci U S A *71*, 1520-1524.

Leung, J.H., Schurig-Briccio, L.A., Yamaguchi, M., Moeller, A., Speir, J.A., Gennis, R.B., and Stout, C.D. (2015). Structural biology. Division of labor in transhydrogenase by alternating proton translocation and hydride transfer. Science *347*, 178-181.

Lewandoski, M., Meyers, E.N., and Martin, G.R. (1997). Analysis of Fgf8 gene function in vertebrate development. Cold Spring Harb Symp Quant Biol *62*, 159-168.

Lewis, T.L., Jr., Kwon, S.K., Lee, A., Shaw, R., and Polleux, F. (2018). MFF-dependent mitochondrial fission regulates presynaptic release and axon branching by limiting axonal mitochondria size. Nat Commun *9*, 5008.

Liao, Y., Wang, J., Jaehnig, E.J., Shi, Z., and Zhang, B. (2019). WebGestalt 2019: gene set analysis toolkit with revamped UIs and APIs. Nucleic Acids Res *47*, W199-W205.

Lill, R., Hoffmann, B., Molik, S., Pierik, A.J., Rietzschel, N., Stehling, O., Uzarska, M.A., Webert, H., Wilbrecht, C., and Muhlenhoff, U. (2012). The role of mitochondria in cellular iron-sulfur protein biogenesis and iron metabolism. Biochim Biophys Acta *1823*, 1491-1508.

Lin, M.Y., and Sheng, Z.H. (2015). Regulation of mitochondrial transport in neurons. Exp Cell Res *334*, 35-44.

Linden, M., Gellerfors, P., and Nelson, B.D. (1982). Pore protein and the hexokinase-binding protein from the outer membrane of rat liver mitochondria are identical. FEBS Lett *141*, 189-192.

Lismont, C., Nordgren, M., Van Veldhoven, P.P., and Fransen, M. (2015). Redox interplay between mitochondria and peroxisomes. Front Cell Dev Biol *3*, 35.

Liu, J.C., Liu, J., Holmstrom, K.M., Menazza, S., Parks, R.J., Fergusson, M.M., Yu, Z.X., Springer, D.A., Halsey, C., Liu, C.*, et al.* (2016). MICU1 Serves as a Molecular Gatekeeper to Prevent In Vivo Mitochondrial Calcium Overload. Cell Rep *16*, 1561-1573.

Liu, L., MacKenzie, K.R., Putluri, N., Maletic-Savatic, M., and Bellen, H.J. (2017). The Glia-Neuron Lactate Shuttle and Elevated ROS Promote Lipid Synthesis in Neurons and Lipid Droplet Accumulation in Glia via APOE/D. Cell Metab *26*, 719-737 e716.

Liu, R., and Chan, D.C. (2015). The mitochondrial fission receptor Mff selectively recruits oligomerized Drp1. Mol Biol Cell *26*, 4466-4477.

Liu, R., Strom, A.L., Zhai, J., Gal, J., Bao, S., Gong, W., and Zhu, H. (2009). Enzymatically inactive adenylate kinase 4 interacts with mitochondrial ADP/ATP translocase. Int J Biochem Cell Biol *41*, 1371-1380.

Lopez-Fabuel, I., Le Douce, J., Logan, A., James, A.M., Bonvento, G., Murphy, M.P., Almeida, A., and Bolanos, J.P. (2016). Complex I assembly into supercomplexes determines differential mitochondrial ROS production in neurons and astrocytes. Proc Natl Acad Sci U S A *113*, 13063-13068.

Loson, O.C., Song, Z., Chen, H., and Chan, D.C. (2013). Fis1, Mff, MiD49, and MiD51 mediate Drp1 recruitment in mitochondrial fission. Mol Biol Cell *24*, 659-667.

Lotz, C., Lin, A.J., Black, C.M., Zhang, J., Lau, E., Deng, N., Wang, Y., Zong, N.C., Choi, J.H., Xu, T.*, et al.* (2014). Characterization, design, and function of the mitochondrial proteome: from organs to organisms. J Proteome Res *13*, 433-446.

Luers, G.H., Hartig, R., Mohr, H., Hausmann, M., Fahimi, H.D., Cremer, C., and Volkl, A. (1998). Immuno-isolation of highly purified peroxisomes using magnetic beads and continuous immunomagnetic sorting. Electrophoresis *19*, 1205-1210.

Lundgaard, I., Osorio, M.J., Kress, B.T., Sanggaard, S., and Nedergaard, M. (2014). White matter astrocytes in health and disease. Neuroscience *276*, 161-173.

Luongo, T.S., Lambert, J.P., Yuan, A., Zhang, X., Gross, P., Song, J., Shanmughapriya, S., Gao, E., Jain, M., Houser, S.R.*, et al.* (2015). The Mitochondrial Calcium Uniporter Matches Energetic Supply with Cardiac Workload during Stress and Modulates Permeability Transition. Cell Rep *12*, 23-34.

Luque, J.M., Kwan, S.W., Abell, C.W., Da Prada, M., and Richards, J.G. (1995). Cellular expression of mRNAs encoding monoamine oxidases A and B in the rat central nervous system. J Comp Neurol *363*, 665-680.

Luquet, E., Biesemann, C., Munier, A., and Herzog, E. (2017). Purification of Synaptosome Populations Using Fluorescence-Activated Synaptosome Sorting. In Synapse Development: Methods and Protocols, A. Poulopoulos, ed. (New York, NY: Springer New York), pp. 121-134.

Lustbader, J.W., Cirilli, M., Lin, C., Xu, H.W., Takuma, K., Wang, N., Caspersen, C., Chen, X., Pollak, S., Chaney, M.*, et al.* (2004). ABAD directly links Abeta to mitochondrial toxicity in Alzheimer's disease. Science *304*, 448-452.

Lv, B.F., Yu, C.F., Chen, Y.Y., Lu, Y., Guo, J.H., Song, Q.S., Ma, D.L., Shi, T.P., and Wang, L. (2006). Protein tyrosine phosphatase interacting protein 51 (PTPIP51) is a novel mitochondria protein with an N-terminal mitochondrial targeting sequence and induces apoptosis. Apoptosis *11*, 1489-1501.

MacDonald, J.A., Bothun, A.M., Annis, S.N., Sheehan, H., Ray, S., Gao, Y., Ivanov, A.R., Khrapko, K., Tilly, J.L., and Woods, D.C. (2019). A nanoscale, multi-parametric flow cytometry-based platform to study mitochondrial heterogeneity and mitochondrial DNA dynamics. Commun Biol *2*, 258.

Machler, P., Wyss, M.T., Elsayed, M., Stobart, J., Gutierrez, R., von Faber-Castell, A., Kaelin, V., Zuend, M., San Martin, A., Romero-Gomez, I.*, et al.* (2016). In Vivo Evidence for a Lactate Gradient from Astrocytes to Neurons. Cell Metab *23*, 94-102.

Madisen, L., Zwingman, T.A., Sunkin, S.M., Oh, S.W., Zariwala, H.A., Gu, H., Ng, L.L., Palmiter, R.D., Hawrylycz, M.J., Jones, A.R.*, et al.* (2010). A robust and high-throughput Cre reporting and characterization system for the whole mouse brain. Nat Neurosci *13*, 133-140.

Madreiter-Sokolowski, C.T., Klec, C., Parichatikanond, W., Stryeck, S., Gottschalk, B., Pulido, S., Rost, R., Eroglu, E., Hofmann, N.A., Bondarenko, A.I.*, et al.* (2016). PRMT1-mediated methylation of MICU1 determines the UCP2/3 dependency of mitochondrial Ca(2+) uptake in immortalized cells. Nat Commun *7*, 12897.

Magrane, J., Cortez, C., Gan, W.B., and Manfredi, G. (2014). Abnormal mitochondrial transport and morphology are common pathological denominators in SOD1 and TDP43 ALS mouse models. Hum Mol Genet *23*, 1413-1424.

Mallilankaraman, K., Cardenas, C., Doonan, P.J., Chandramoorthy, H.C., Irrinki, K.M., Golenar, T., Csordas, G., Madireddi, P., Yang, J., Muller, M.*, et al.* (2012a). MCUR1 is an essential component of mitochondrial Ca2+ uptake that regulates cellular metabolism. Nat Cell Biol *14*, 1336-1343.

Mallilankaraman, K., Doonan, P., Cardenas, C., Chandramoorthy, H.C., Muller, M., Miller, R., Hoffman, N.E., Gandhirajan, R.K., Molgo, J., Birnbaum, M.J.*, et al.* (2012b). MICU1 is an essential gatekeeper for MCU-mediated mitochondrial Ca(2+) uptake that regulates cell survival. Cell *151*, 630-644.

Mandelkow, E.M., Stamer, K., Vogel, R., Thies, E., and Mandelkow, E. (2003). Clogging of axons by tau, inhibition of axonal traffic and starvation of synapses. Neurobiol Aging *24*, 1079-1085.

Maranzana, E., Barbero, G., Falasca, A.I., Lenaz, G., and Genova, M.L. (2013). Mitochondrial respiratory supercomplex association limits production of reactive oxygen species from complex I. Antioxid Redox Signal *19*, 1469-1480.

Marcaggi, P., and Attwell, D. (2004). Role of glial amino acid transporters in synaptic transmission and brain energetics. Glia *47*, 217-225.

Marchi, S., Corricelli, M., Branchini, A., Vitto, V.A.M., Missiroli, S., Morciano, G., Perrone, M., Ferrarese, M., Giorgi, C., Pinotti, M.*, et al.* (2019). Akt-mediated phosphorylation of MICU1 regulates mitochondrial Ca(2+) levels and tumor growth. EMBO J *38*, e99435.

Marinkovic, P., Reuter, M.S., Brill, M.S., Godinho, L., Kerschensteiner, M., and Misgeld, T. (2012). Axonal transport deficits and degeneration can evolve independently in mouse models of amyotrophic lateral sclerosis. Proc Natl Acad Sci U S A *109*, 4296-4301.

Markus, N.M., Hasel, P., Qiu, J., Bell, K.F., Heron, S., Kind, P.C., Dando, O., Simpson, T.I., and Hardingham, G.E. (2016). Expression of mRNA Encoding Mcu and Other Mitochondrial Calcium Regulatory Genes Depends on Cell Type, Neuronal Subtype, and Ca2+ Signaling. PloS one *11*, e0148164.

Marland, J.R., Hasel, P., Bonnycastle, K., and Cousin, M.A. (2016). Mitochondrial Calcium Uptake Modulates Synaptic Vesicle Endocytosis in Central Nerve Terminals. J Biol Chem *291*, 2080-2086.

Marquez, J., de la Oliva, A.R., Mates, J.M., Segura, J.A., and Alonso, F.J. (2006). Glutaminase: a multifaceted protein not only involved in generating glutamate. Neurochem Int *48*, 465-471.

Marquez, J., Tosina, M., de la Rosa, V., Segura, J.A., Alonso, F.J., Mates, J.M., and Campos-Sandoval, J.A. (2009). New insights into brain glutaminases: beyond their role on glutamatergic transmission. Neurochem Int *55*, 64-70.

Martijn, J., Vosseberg, J., Guy, L., Offre, P., and Ettema, T.J.G. (2018). Deep mitochondrial origin outside the sampled alphaproteobacteria. Nature *557*, 101-105.

Martin-Rufian, M., Tosina, M., Campos-Sandoval, J.A., Manzanares, E., Lobo, C., Segura, J.A., Alonso, F.J., Mates, J.M., and Marquez, J. (2012). Mammalian glutaminase Gls2 gene encodes two functional alternative transcripts by a surrogate promoter usage mechanism. PloS one *7*, e38380.

Masson, J., Darmon, M., Conjard, A., Chuhma, N., Ropert, N., Thoby-Brisson, M., Foutz, A.S., Parrot, S., Miller, G.M., Jorisch, R.*, et al.* (2006). Mice lacking brain/kidney phosphate-activated glutaminase have impaired glutamatergic synaptic transmission, altered breathing, disorganized goal-directed behavior and die shortly after birth. J Neurosci *26*, 4660-4671.

Mateos-Aparicio, P., and Rodríguez-Moreno, A. (2020). Calcium Dynamics and Synaptic Plasticity. In Calcium Signaling, M.S. Islam, ed. (Cham: Springer International Publishing), pp. 965-984.

Mateos, J.M., Osorio, A., Azkue, J.J., Benítez, R., Elezgarai, I., Bilbao, A., Díez, J., Puente, N., Kuhn, R., and Knopfel, T. (2001). Parasagittal compartmentalization of the metabotropic glutamate receptor mGluR1b in the cerebellar cortex. European Journal of Anatomy *5*, 15-21.

Mathiisen, T.M., Lehre, K.P., Danbolt, N.C., and Ottersen, O.P. (2010). The perivascular astroglial sheath provides a complete covering of the brain microvessels: an electron microscopic 3D reconstruction. Glia *58*, 1094-1103.

Matsuda, W., Furuta, T., Nakamura, K.C., Hioki, H., Fujiyama, F., Arai, R., and Kaneko, T. (2009). Single nigrostriatal dopaminergic neurons form widely spread and highly dense axonal arborizations in the neostriatum. J Neurosci *29*, 444-453.

McFadden, J.W., Aja, S., Li, Q., Bandaru, V.V., Kim, E.K., Haughey, N.J., Kuhajda, F.P., and Ronnett, G.V. (2014). Increasing fatty acid oxidation remodels the hypothalamic neurometabolome to mitigate stress and inflammation. PloS one *9*, e115642.

McKenna, M.C., Stevenson, J.H., Huang, X., and Hopkins, I.B. (2000). Differential distribution of the enzymes glutamate dehydrogenase and aspartate aminotransferase in cortical synaptic mitochondria contributes to metabolic compartmentation in cortical synaptic terminals. Neurochem Int *37*, 229-241.

McMillin-Wood, J., Wolkowicz, P.E., Chu, A., Tate, C.A., Goldstein, M.A., and Entman, M.L. (1980). Calcium uptake by two preparations of mitochondria from heart. Biochim Biophys Acta *591*, 251-265.

Meeusen, S., McCaffery, J.M., and Nunnari, J. (2004). Mitochondrial fusion intermediates revealed in vitro. Science *305*, 1747-1752.

Meyer, A.H., Katona, I., Blatow, M., Rozov, A., and Monyer, H. (2002). In vivo labeling of parvalbumin-positive interneurons and analysis of electrical coupling in identified neurons. J Neurosci *22*, 7055-7064.

Misgeld, T., Kerschensteiner, M., Bareyre, F.M., Burgess, R.W., and Lichtman, J.W. (2007). Imaging axonal transport of mitochondria in vivo. Nat Methods *4*, 559-561.

Misgeld, T., and Schwarz, T.L. (2017). Mitostasis in Neurons: Maintaining Mitochondria in an Extended Cellular Architecture. Neuron *96*, 651-666.

Mitchell, P. (1961). Coupling of phosphorylation to electron and hydrogen transfer by a chemi-osmotic type of mechanism. Nature *191*, 144-148.

Miyake, S., Yamashita, T., Taniguchi, M., Tamatani, M., Sato, K., and Tohyama, M. (2002). Identification and characterization of a novel mitochondrial tricarboxylate carrier. Biochem Biophys Res Commun *295*, 463-468.

Miyoshi, K., Akazawa, Y., Horiguchi, T., and Noma, T. (2009). Localization of adenylate kinase 4 in mouse tissues. Acta Histochem Cytochem *42*, 55-64.

Moffett, J.R., Ross, B., Arun, P., Madhavarao, C.N., and Namboodiri, A.M. (2007). N-Acetylaspartate in the CNS: from neurodiagnostics to neurobiology. Prog Neurobiol *81*, 89-131.

Moggio, M., Colombo, I., Peverelli, L., Villa, L., Xhani, R., Testolin, S., Di Mauro, S., and Sciacco, M. (2014). Mitochondrial disease heterogeneity: a prognostic challenge. Acta Myol *33*, 86-93.

Monroe, G.R., van Eerde, A.M., Tessadori, F., Duran, K.J., Savelberg, S.M.C., van Alfen, J.C., Terhal, P.A., van der Crabben, S.N., Lichtenbelt, K.D., Fuchs, S.A.*, et al.* (2019). Identification of human D lactate dehydrogenase deficiency. Nat Commun *10*, 1477.

Mookerjee, S.A., Gerencser, A.A., Nicholls, D.G., and Brand, M.D. (2017). Quantifying intracellular rates of glycolytic and oxidative ATP production and consumption using extracellular flux measurements. Journal of Biological Chemistry *292*, 7189-7207.

Mootha, V.K., Bunkenborg, J., Olsen, J.V., Hjerrild, M., Wisniewski, J.R., Stahl, E., Bolouri, M.S., Ray, H.N., Sihag, S., Kamal, M.*, et al.* (2003). Integrated analysis of protein composition, tissue diversity, and gene regulation in mouse mitochondria. Cell *115*, 629-640.

Morciano, M., Burre, J., Corvey, C., Karas, M., Zimmermann, H., and Volknandt, W. (2005). Immunoisolation of two synaptic vesicle pools from synaptosomes: a proteomics analysis. J Neurochem *95*, 1732-1745.

Morgenstern, M., Stiller, S.B., Lubbert, P., Peikert, C.D., Dannenmaier, S., Drepper, F., Weill, U., Hoss, P., Feuerstein, R., Gebert, M.*, et al.* (2017). Definition of a High-Confidence Mitochondrial Proteome at Quantitative Scale. Cell Rep *19*, 2836-2852.

Morris, A.A. (2005). Cerebral ketone body metabolism. J Inherit Metab Dis *28*, 109-121.

Morris, J., Na, Y.J., Zhu, H., Lee, J.H., Giang, H., Ulyanova, A.V., Baltuch, G.H., Brem, S., Chen, H.I., Kung, D.K.*, et al.* (2017). Pervasive within-Mitochondrion Single-Nucleotide Variant Heteroplasmy as Revealed by Single-Mitochondrion Sequencing. Cell Rep *21*, 2706-2713.

Motokawa, Y., and Kikuchi, G. (1971). Glycine metabolism in rat liver mitochondria. V. Intramitochondrial localization of the reversible glycine cleavage system and serine hydroxymethyltransferase. Arch Biochem Biophys *146*, 461-464.

Munch, G., Westcott, B., Menini, T., and Gugliucci, A. (2012). Advanced glycation endproducts and their pathogenic roles in neurological disorders. Amino Acids *42*, 1221-1236.

Murgia, M., Nagaraj, N., Deshmukh, A.S., Zeiler, M., Cancellara, P., Moretti, I., Reggiani, C., Schiaffino, S., and Mann, M. (2015). Single muscle fiber proteomics reveals unexpected mitochondrial specialization. EMBO Rep *16*, 387-395.

Murphy, E., Pan, X., Nguyen, T., Liu, J., Holmstrom, K.M., and Finkel, T. (2014). Unresolved questions from the analysis of mice lacking MCU expression. Biochem Biophys Res Commun *449*, 384-385.

Nagase, T., Shimozawa, N., Takemoto, Y., Suzuki, Y., Komori, M., and Kondo, N. (2004). Peroxisomal localization in the developing mouse cerebellum: implications for neuronal abnormalities related to deficiencies in peroxisomes. Biochim Biophys Acta *1671*, 26-33.

Nakazawa, A., Yamada, M., Tanaka, H., Shahjahan, M., and Tanabe, T. (1990). Gene structures of three vertebrate adenylate kinase isozymes. Prog Clin Biol Res *344*, 495-514.

Nass, M.M., and Nass, S. (1963). Intramitochondrial Fibers with DNA Characteristics. I. Fixation and Electron Staining Reactions. J Cell Biol *19*, 593-611.

Nautiyal, M., Sweatt, A.J., MacKenzie, J.A., Mark Payne, R., Szucs, S., Matalon, R., Wallin, R., and Hutson, S.M. (2010). Neuronal localization of the mitochondrial protein NIPSNAP1 in rat nervous system. Eur J Neurosci *32*, 560-569.

Nedergaard, J., Cannon, B., and Lindberg, O. (1977). Microcalorimetry of isolated mammalian cells. Nature *267*, 518-520.

Neher, E., and Sakaba, T. (2008). Multiple roles of calcium ions in the regulation of neurotransmitter release. Neuron *59*, 861-872.

Nemoto, Y., and De Camilli, P. (1999). Recruitment of an alternatively spliced form of synaptojanin 2 to mitochondria by the interaction with the PDZ domain of a mitochondrial outer membrane protein. EMBO J *18*, 2991-3006.

Nichols, M., Pavlov, E.V., and Robertson, G.S. (2018). Tamoxifen-induced knockdown of the mitochondrial calcium uniporter in Thy1-expressing neurons protects mice from hypoxic/ischemic brain injury. Cell Death Dis *9*, 606.

Niemi, N.M., Wilson, G.M., Overmyer, K.A., Vogtle, F.N., Myketin, L., Lohman, D.C., Schueler, K.L., Attie, A.D., Meisinger, C., Coon, J.J., *et al.* (2019). Pptc7 is an essential phosphatase for promoting mammalian mitochondrial metabolism and biogenesis. Nat Commun *10*, 3197.

Nishimura, A.L., Mitne-Neto, M., Silva, H.C., Richieri-Costa, A., Middleton, S., Cascio, D., Kok, F., Oliveira, J.R., Gillingwater, T., Webb, J., *et al.* (2004). A mutation in the vesicle-trafficking protein VAPB causes late-onset spinal muscular atrophy and amyotrophic lateral sclerosis. Am J Hum Genet *75*, 822-831.

Noma, T., Fujisawa, K., Yamashiro, Y., Shinohara, M., Nakazawa, A., Gondo, T., Ishihara, T., and Yoshinobu, K. (2001). Structure and expression of human mitochondrial adenylate kinase targeted to the mitochondrial matrix. Biochem J *358*, 225-232.

Nowinski, S.M., Van Vranken, J.G., Dove, K.K., and Rutter, J. (2018). Impact of Mitochondrial Fatty Acid Synthesis on Mitochondrial Biogenesis. Curr Biol *28*, R1212-R1219.

Nylandsted, J., Becker, A.C., Bunkenborg, J., Andersen, J.S., Dengjel, J., and Jaattela, M. (2011). ErbB2-associated changes in the lysosomal proteome. Proteomics *11*, 2830-2838.

Okamoto, K., Hirai, S., Shoji, M., Senoh, Y., and Yamazaki, T. (1990). Axonal swellings in the corticospinal tracts in amyotrophic lateral sclerosis. Acta Neuropathol *80*, 222-226.

Olalla, L., Gutierrez, A., Campos, J.A., Khan, Z.U., Alonso, F.J., Segura, J.A., Marquez, J., and Aledo, J.C. (2002). Nuclear localization of L-type glutaminase in mammalian brain. J Biol Chem *277*, 38939-38944.

Ortiz, O., Wurst, W., and Kuhn, R. (2013). Reversible and tissue-specific activation of MAP kinase signaling by tamoxifen in Braf(V637)ER(T2) mice. Genesis *51*, 448-455.

Ostergaard, E. (2008). Disorders caused by deficiency of succinate-CoA ligase. J Inherit Metab Dis *31*, 226-229.

Ouellet, M., Emond, V., Chen, C.T., Julien, C., Bourasset, F., Oddo, S., LaFerla, F., Bazinet, R.P., and Calon, F. (2009). Diffusion of docosahexaenoic and eicosapentaenoic acids through the blood-brain barrier: An in situ cerebral perfusion study. Neurochem Int *55*, 476-482.

Owen, O.E., Kalhan, S.C., and Hanson, R.W. (2002). The key role of anaplerosis and cataplerosis for citric acid cycle function. J Biol Chem *277*, 30409-30412.

Pagani, L., and Eckert, A. (2011). Amyloid-Beta interaction with mitochondria. Int J Alzheimers Dis *2011*, 925050.

Pagliarini, D.J., Calvo, S.E., Chang, B., Sheth, S.A., Vafai, S.B., Ong, S.E., Walford, G.A., Sugiana, C., Boneh, A., Chen, W.K*., et al.* (2008). A mitochondrial protein compendium elucidates complex I disease biology. Cell *134*, 112-123.

Pagliarini, D.J., and Rutter, J. (2013). Hallmarks of a new era in mitochondrial biochemistry. Genes Dev *27*, 2615-2627.

Paillard, M., Csordas, G., Szanda, G., Golenar, T., Debattisti, V., Bartok, A., Wang, N., Moffat, C., Seifert, E.L., Spat, A*., et al.* (2017). Tissue-Specific Mitochondrial Decoding of Cytoplasmic Ca(2+) Signals Is Controlled by the Stoichiometry of MICU1/2 and MCU. Cell Rep *18*, 2291-2300.

Paillusson, S., Gomez-Suaga, P., Stoica, R., Little, D., Gissen, P., Devine, M.J., Noble, W., Hanger, D.P., and Miller, C.C.J. (2017). alpha-Synuclein binds to the ER-mitochondria tethering protein VAPB to disrupt Ca(2+) homeostasis and mitochondrial ATP production. Acta Neuropathol *134*, 129-149.

Palmer, J.W., Tandler, B., and Hoppel, C.L. (1977). Biochemical properties of subsarcolemmal and interfibrillar mitochondria isolated from rat cardiac muscle. J Biol Chem *252*, 8731-8739.

Pan, X., Liu, J., Nguyen, T., Liu, C., Sun, J., Teng, Y., Fergusson, M.M., Rovira, II, Allen, M., Springer, D.A*., et al.* (2013). The physiological role of mitochondrial calcium revealed by mice lacking the mitochondrial calcium uniporter. Nat Cell Biol *15*, 1464-1472.

Panov, A., Orynbayeva, Z., Vavilin, V., and Lyakhovich, V. (2014). Fatty acids in energy metabolism of the central nervous system. Biomed Res Int *2014*, 472459.

Pare, B., Lehmann, M., Beaudin, M., Nordstrom, U., Saikali, S., Julien, J.P., Gilthorpe, J.D., Marklund, S.L., Cashman, N.R., Andersen, P.M*., et al.* (2018). Misfolded SOD1 pathology in sporadic Amyotrophic Lateral Sclerosis. Sci Rep *8*, 14223.

Parker, W.D., Jr., Filley, C.M., and Parks, J.K. (1990). Cytochrome oxidase deficiency in Alzheimer's disease. Neurology *40*, 1302-1303.

Pasinelli, P., Belford, M.E., Lennon, N., Bacskai, B.J., Hyman, B.T., Trotti, D., and Brown, R.H., Jr. (2004). Amyotrophic lateral sclerosis-associated SOD1 mutant proteins bind and aggregate with Bcl-2 in spinal cord mitochondria. Neuron *43*, 19-30.

Patel, M.S., and Korotchkina, L.G. (2001). Regulation of mammalian pyruvate dehydrogenase complex by phosphorylation: complexity of multiple phosphorylation sites and kinases. Exp Mol Med *33*, 191-197.

Patron, M., Checchetto, V., Raffaello, A., Teardo, E., Vecellio Reane, D., Mantoan, M., Granatiero, V., Szabo, I., De Stefani, D., and Rizzuto, R. (2014). MICU1 and MICU2 finely tune the mitochondrial Ca2+ uniporter by exerting opposite effects on MCU activity. Mol Cell *53*, 726-737.

Patron, M., Granatiero, V., Espino, J., Rizzuto, R., and De Stefani, D. (2019). MICU3 is a tissue-specific enhancer of mitochondrial calcium uptake. Cell Death Differ *26*, 179-195.

Paul, B.T., Tesfay, L., Winkler, C.R., Torti, F.M., and Torti, S.V. (2019). Sideroflexin 4 affects Fe-S cluster biogenesis, iron metabolism, mitochondrial respiration and heme biosynthetic enzymes. Sci Rep *9*, 19634.

Paupe, V., Prudent, J., Dassa, E.P., Rendon, O.Z., and Shoubridge, E.A. (2015). CCDC90A (MCUR1) is a cytochrome c oxidase assembly factor and not a regulator of the mitochondrial calcium uniporter. Cell Metab *21*, 109-116.

Pedrini, S., Sau, D., Guareschi, S., Bogush, M., Brown, R.H., Jr., Naniche, N., Kia, A., Trotti, D., and Pasinelli, P. (2010). ALS-linked mutant SOD1 damages mitochondria by promoting conformational changes in Bcl-2. Hum Mol Genet *19*, 2974-2986.

Pei, Z., Oey, N.A., Zuidervaart, M.M., Jia, Z., Li, Y., Steinberg, S.J., Smith, K.D., and Watkins, P.A. (2003). The Acyl-CoA Synthetase “Bubblegum” (Lipidosin): FURTHER CHARACTERIZATION AND ROLE IN NEURONAL FATTY ACID β-OXIDATION. Journal of Biological Chemistry *278*, 47070-47078.

Pellerin, L., and Magistretti, P.J. (1994). Glutamate uptake into astrocytes stimulates aerobic glycolysis: a mechanism coupling neuronal activity to glucose utilization. Proc Natl Acad Sci U S A *91*, 10625-10629.

Peng, J., Sheng, A.L., Xiao, Q., Shen, L., Ju, X.C., Zhang, M., He, S.T., Wu, C., and Luo, Z.G. (2019). Single-cell transcriptomes reveal molecular specializations of neuronal cell types in the developing cerebellum. J Mol Cell Biol *11*, 636-648.

Perham, R.N. (2000). Swinging arms and swinging domains in multifunctional enzymes: catalytic machines for multistep reactions. Annu Rev Biochem *69*, 961-1004.

Perocchi, F., Gohil, V.M., Girgis, H.S., Bao, X.R., McCombs, J.E., Palmer, A.E., and Mootha, V.K. (2010). MICU1 encodes a mitochondrial EF hand protein required for Ca(2+) uptake. Nature *467*, 291-296.

Petrova, V.Y., Drescher, D., Kujumdzieva, A.V., and Schmitt, M.J. (2004). Dual targeting of yeast catalase A to peroxisomes and mitochondria. Biochem J *380*, 393-400.

Pflugradt, R., Schmidt, U., Landenberger, B., Sanger, T., and Lutz-Bonengel, S. (2011). A novel and effective separation method for single mitochondria analysis. Mitochondrion *11*, 308-314.

Pierre, K., and Pellerin, L. (2005). Monocarboxylate transporters in the central nervous system: distribution, regulation and function. J Neurochem *94*, 1-14.

Ping, H.A., Kraft, L.M., Chen, W., Nilles, A.E., and Lackner, L.L. (2016). Num1 anchors mitochondria to the plasma membrane via two domains with different lipid binding specificities. J Cell Biol *213*, 513-524.

Plovanich, M., Bogorad, R.L., Sancak, Y., Kamer, K.J., Strittmatter, L., Li, A.A., Girgis, H.S., Kuchimanchi, S., De Groot, J., Speciner, L.*, et al.* (2013). MICU2, a paralog of MICU1, resides within the mitochondrial uniporter complex to regulate calcium handling. PloS one *8*, e55785.

Polanco, J.C., Li, C., Bodea, L.G., Martinez-Marmol, R., Meunier, F.A., and Gotz, J. (2018). Amyloid-beta and tau complexity - towards improved biomarkers and targeted therapies. Nat Rev Neurol *14*, 22-39.

Prakasam, G., Iqbal, M.A., Bamezai, R.N.K., and Mazurek, S. (2018). Posttranslational Modifications of Pyruvate Kinase M2: Tweaks that Benefit Cancer. Frontiers in Oncology *8*, 22.

Princely Abudu, Y., Pankiv, S., Mathai, B.J., Hakon Lystad, A., Bindesboll, C., Brenne, H.B., Yoke Wui Ng, M., Thiede, B., Yamamoto, A., Mutugi Nthiga, T.*, et al.* (2019). NIPSNAP1 and NIPSNAP2 Act as "Eat Me" Signals for Mitophagy. Developmental cell *49*, 509-525 e512.

Qu, Q., Zeng, F., Liu, X., Wang, Q.J., and Deng, F. (2016). Fatty acid oxidation and carnitine palmitoyltransferase I: emerging therapeutic targets in cancer. Cell Death Dis *7*, e2226.

Rabilloud, T., Kieffer, S., Procaccio, V., Louwagie, M., Courchesne, P.L., Patterson, S.D., Martinez, P., Garin, J., and Lunardi, J. (1998). Two-dimensional electrophoresis of human placental mitochondria and protein identification by mass spectrometry: toward a human mitochondrial proteome. Electrophoresis *19*, 1006-1014.

Radi, R., Turrens, J.F., Chang, L.Y., Bush, K.M., Crapo, J.D., and Freeman, B.A. (1991). Detection of catalase in rat heart mitochondria. J Biol Chem *266*, 22028-22034.

Raffaello, A., De Stefani, D., Sabbadin, D., Teardo, E., Merli, G., Picard, A., Checchetto, V., Moro, S., Szabo, I., and Rizzuto, R. (2013). The mitochondrial calcium uniporter is a multimer that can include a dominant-negative pore-forming subunit. EMBO J *32*, 2362-2376.

Raffaello, A., Mammucari, C., Gherardi, G., and Rizzuto, R. (2016). Calcium at the Center of Cell Signaling: Interplay between Endoplasmic Reticulum, Mitochondria, and Lysosomes. Trends Biochem Sci *41*, 1035-1049.

Rafiki, A., Boulland, J.L., Halestrap, A.P., Ottersen, O.P., and Bergersen, L. (2003). Highly differential expression of the monocarboxylate transporters MCT2 and MCT4 in the developing rat brain. Neuroscience *122*, 677-688.

Raiborg, C., Wenzel, E.M., Pedersen, N.M., Olsvik, H., Schink, K.O., Schultz, S.W., Vietri, M., Nisi, V., Bucci, C., Brech, A.*, et al.* (2015). Repeated ER-endosome contacts promote endosome translocation and neurite outgrowth. Nature *520*, 234-238.

Raichle, M.E. (1998). Behind the scenes of functional brain imaging: a historical and physiological perspective. Proc Natl Acad Sci U S A *95*, 765-772.

Ramos, C.W., Guldener, U., Klein, S., Hegemann, J.H., Gonzalez, S., and Rodriguez-Medina, J.R. (2000). Molecular analysis of the Saccharomyces cerevisiae YHR076w gene. IUBMB Life *50*, 371-377.

Rappsilber, J., Ishihama, Y., and Mann, M. (2003). Stop and go extraction tips for matrix-assisted laser desorption/ionization, nanoelectrospray, and LC/MS sample pretreatment in proteomics. Anal Chem *75*, 663-670.

Resibois, A., and Rogers, J.H. (1992). Calretinin in rat brain: an immunohistochemical study. Neuroscience *46*, 101-134.

Rhee, H.W., Zou, P., Udeshi, N.D., Martell, J.D., Mootha, V.K., Carr, S.A., and Ting, A.Y. (2013). Proteomic mapping of mitochondria in living cells via spatially restricted enzymatic tagging. Science *339*, 1328-1331.

Rivell, A., Petralia, R.S., Wang, Y.X., Mattson, M.P., and Yao, P.J. (2019). Sideroflexin 3 is a Mitochondrial Protein Enriched in Neurons. Neuromolecular Med *21*, 314-321.

Rizzuto, R., Pinton, P., Carrington, W., Fay, F.S., Fogarty, K.E., Lifshitz, L.M., Tuft, R.A., and Pozzan, T. (1998). Close contacts with the endoplasmic reticulum as determinants of mitochondrial Ca2+ responses. Science *280*, 1763-1766.

Rodriguez, C.I., Buchholz, F., Galloway, J., Sequerra, R., Kasper, J., Ayala, R., Stewart, A.F., and Dymecki, S.M. (2000). High-efficiency deleter mice show that FLPe is an alternative to Cre-loxP. Nature genetics *25*, 139-140.

Roger, A.J., Munoz-Gomez, S.A., and Kamikawa, R. (2017). The Origin and Diversification of Mitochondria. Curr Biol *27*, R1177-R1192.

Roh, H.C., Tsai, L.T., Lyubetskaya, A., Tenen, D., Kumari, M., and Rosen, E.D. (2017). Simultaneous Transcriptional and Epigenomic Profiling from Specific Cell Types within Heterogeneous Tissues In Vivo. Cell Rep *18*, 1048-1061.

Rossi, C.S., and Lehninger, A.L. (1964). Stoichiometry of Respiratory Stimulation, Accumulation of Ca++ and Phosphate, and Oxidative Phosphorylation in Rat Liver Mitochondria. J Biol Chem *239*, 3971-3980.

Rossi, J., Balthasar, N., Olson, D., Scott, M., Berglund, E., Lee, C.E., Choi, M.J., Lauzon, D., Lowell, B.B., and Elmquist, J.K. (2011). Melanocortin-4 receptors expressed by cholinergic neurons regulate energy balance and glucose homeostasis. Cell Metab *13*, 195-204.

Rossignol, R., Faustin, B., Rocher, C., Malgat, M., Mazat, J.P., and Letellier, T. (2003). Mitochondrial threshold effects. Biochem J *370*, 751-762.

Roy, C.S., and Sherrington, C.S. (1890). On the Regulation of the Blood-supply of the Brain. J Physiol *11*, 85-158 117.

Runswick, M.J., Fearnley, I.M., Skehel, J.M., and Walker, J.E. (1991). Presence of an acyl carrier protein in NADH:ubiquinone oxidoreductase from bovine heart mitochondria. FEBS Lett *286*, 121-124.

Sacksteder, K.A., Jones, J.M., South, S.T., Li, X., Liu, Y., and Gould, S.J. (2000). PEX19 binds multiple peroxisomal membrane proteins, is predominantly cytoplasmic, and is required for peroxisome membrane synthesis. J Cell Biol *148*, 931-944.

Sada, N., Lee, S., Katsu, T., Otsuki, T., and Inoue, T. (2015). Epilepsy treatment. Targeting LDH enzymes with a stiripentol analog to treat epilepsy. Science *347*, 1362-1367.

Saez, I., Duran, J., Sinadinos, C., Beltran, A., Yanes, O., Tevy, M.F., Martinez-Pons, C., Milan, M., and Guinovart, J.J. (2014). Neurons have an active glycogen metabolism that contributes to tolerance to hypoxia. J Cereb Blood Flow Metab *34*, 945-955.

Sagan, L. (1967). On the origin of mitosing cells. J Theor Biol *14*, 255-274.

Sancak, Y., Markhard, A.L., Kitami, T., Kovacs-Bogdan, E., Kamer, K.J., Udeshi, N.D., Carr, S.A., Chaudhuri, D., Clapham, D.E., Li, A.A.*, et al.* (2013). EMRE is an essential component of the mitochondrial calcium uniporter complex. Science *342*, 1379-1382.

Saneto, R.P., and Naviaux, R.K. (2010). Polymerase gamma disease through the ages. Dev Disabil Res Rev *16*, 163-174.

Santos, H.J., Makiuchi, T., and Nozaki, T. (2018). Reinventing an Organelle: The Reduced Mitochondrion in Parasitic Protists. Trends Parasitol *34*, 1038-1055.

Sanz, E., Yang, L., Su, T., Morris, D.R., McKnight, G.S., and Amieux, P.S. (2009). Cell-type-specific isolation of ribosome-associated mRNA from complex tissues. Proc Natl Acad Sci U S A *106*, 13939-13944.

Sarna, J.R., Marzban, H., Watanabe, M., and Hawkes, R. (2006). Complementary stripes of phospholipase Cbeta3 and Cbeta4 expression by Purkinje cell subsets in the mouse cerebellum. J Comp Neurol *496*, 303-313.

Sasaki, S., and Iwata, M. (2007). Mitochondrial alterations in the spinal cord of patients with sporadic amyotrophic lateral sclerosis. J Neuropathol Exp Neurol *66*, 10-16.

Sathyanesan, A., Zhou, J., Scafidi, J., Heck, D.H., Sillitoe, R.V., and Gallo, V. (2019). Emerging connections between cerebellar development, behaviour and complex brain disorders. Nat Rev Neurosci *20*, 298-313.

Sato, K., Yoshida, S., Fujiwara, K., Tada, K., and Tohyama, M. (1991). Glycine cleavage system in astrocytes. Brain Res *567*, 64-70.

Satori, C.P., Kostal, V., and Arriaga, E.A. (2012). Review on recent advances in the analysis of isolated organelles. Anal Chim Acta *753*, 8-18.

Sayre, N.L., Sifuentes, M., Holstein, D., Cheng, S.Y., Zhu, X., and Lechleiter, J.D. (2017). Stimulation of astrocyte fatty acid oxidation by thyroid hormone is protective against ischemic stroke-induced damage. J Cereb Blood Flow Metab *37*, 514-527.

Sazanov, L.A., and Jackson, J.B. (1994). Proton-translocating transhydrogenase and NAD- and NADP-linked isocitrate dehydrogenases operate in a substrate cycle which contributes to fine regulation of the tricarboxylic acid cycle activity in mitochondria. FEBS Letters *344*, 109-116.

Scaglia, F., Wong, L.-J.C., Vladutiu, G.D., and Hunter, J.V. (2005). Predominant Cerebellar Volume Loss as a Neuroradiologic Feature of Pediatric Respiratory Chain Defects. American Journal of Neuroradiology *26*, 1675.

Scheffler, K., Krohn, M., Dunkelmann, T., Stenzel, J., Miroux, B., Ibrahim, S., von Bohlen Und Halbach, O., Heinze, H.J., Walker, L.C., Gsponer, J.A*., et al.* (2012). Mitochondrial DNA polymorphisms specifically modify cerebral beta-amyloid proteostasis. Acta Neuropathol *124*, 199-208.

Schermelleh, L., Heintzmann, R., and Leonhardt, H. (2010). A guide to super-resolution fluorescence microscopy. J Cell Biol *190*, 165-175.

Schiaffino, S., Reggiani, C., Kostrominova, T.Y., Mann, M., and Murgia, M. (2015). Mitochondrial specialization revealed by single muscle fiber proteomics: focus on the Krebs cycle. Scand J Med Sci Sports *25 Suppl 4*, 41-48.

Schindelin, J., Arganda-Carreras, I., Frise, E., Kaynig, V., Longair, M., Pietzsch, T., Preibisch, S., Rueden, C., Saalfeld, S., Schmid, B*., et al.* (2012). Fiji: an open-source platform for biological-image analysis. Nat Methods *9*, 676-682.

Schmidt, O., Pfanner, N., and Meisinger, C. (2010). Mitochondrial protein import: from proteomics to functional mechanisms. Nature reviews Molecular cell biology *11*, 655-667.

Schnaitman, C., Erwin, V.G., and Greenawalt, J.W. (1967). The submitochondrial localization of monoamine oxidase. An enzymatic marker for the outer membrane of rat liver mitochondria. J Cell Biol *32*, 719-735.

Schonfeld, P., and Reiser, G. (2013). Why does brain metabolism not favor burning of fatty acids to provide energy? Reflections on disadvantages of the use of free fatty acids as fuel for brain. J Cereb Blood Flow Metab *33*, 1493-1499.

Schonfeld, P., and Reiser, G. (2017). Brain energy metabolism spurns fatty acids as fuel due to their inherent mitotoxicity and potential capacity to unleash neurodegeneration. Neurochem Int *109*, 68-77.

Schulz, J.G., Laranjeira, A., Van Huffel, L., Gartner, A., Vilain, S., Bastianen, J., Van Veldhoven, P.P., and Dotti, C.G. (2015). Glial beta-oxidation regulates Drosophila energy metabolism. Sci Rep *5*, 7805.

Scorrano, L., De Matteis, M.A., Emr, S., Giordano, F., Hajnoczky, G., Kornmann, B., Lackner, L.L., Levine, T.P., Pellegrini, L., Reinisch, K*., et al.* (2019). Coming together to define membrane contact sites. Nat Commun *10*, 1287.

Shai, N., Yifrach, E., van Roermund, C.W.T., Cohen, N., Bibi, C., L, I.J., Cavellini, L., Meurisse, J., Schuster, R., Zada, L*., et al.* (2018). Systematic mapping of contact sites reveals tethers and a function for the peroxisome-mitochondria contact. Nat Commun *9*, 1761.

Shank, R.P., Bennett, G.S., Freytag, S.O., and Campbell, G.L. (1985). Pyruvate carboxylase: an astrocyte-specific enzyme implicated in the replenishment of amino acid neurotransmitter pools. Brain Res *329*, 364-367.

Sharma, K., Schmitt, S., Bergner, C.G., Tyanova, S., Kannaiyan, N., Manrique-Hoyos, N., Kongi, K., Cantuti, L., Hanisch, U.K., Philips, M.A*., et al.* (2015). Cell type- and brain region-resolved mouse brain proteome. Nat Neurosci *18*, 1819-1831.

Shepherd, G.M. (2015). Foundations of the neuron doctrine (Oxford University Press).

Shetty, D.K., Kalamkar, K.P., and Inamdar, M.S. (2018). OCIAD1 Controls Electron Transport Chain Complex I Activity to Regulate Energy Metabolism in Human Pluripotent Stem Cells. Stem Cell Reports *11*, 128-141.

Shimada, T., Horita, K., Murakami, M., and Ogura, R. (1984). Morphological studies of different mitochondrial populations in monkey myocardial cells. Cell Tissue Res *238*, 577-582.

Shin, J.B., Krey, J.F., Hassan, A., Metlagel, Z., Tauscher, A.N., Pagana, J.M., Sherman, N.E., Jeffery, E.D., Spinelli, K.J., Zhao, H*., et al.* (2013). Molecular architecture of the chick vestibular hair bundle. Nat Neurosci *16*, 365-374.

Shutov, L.P., Kim, M.S., Houlihan, P.R., Medvedeva, Y.V., and Usachev, Y.M. (2013). Mitochondria and plasma membrane Ca2+-ATPase control presynaptic Ca2+ clearance in capsaicin-sensitive rat sensory neurons. J Physiol *591*, 2443-2462.

Sims, N.R., and Anderson, M.F. (2008). Isolation of mitochondria from rat brain using Percoll density gradient centrifugation. Nat Protoc *3*, 1228-1239.

Sinha, S., Bheemsetty, V.A., and Inamdar, M.S. (2018). A double helical motif in OCIAD2 is essential for its localization, interactions and STAT3 activation. Sci Rep *8*, 7362.

Skarnes, W.C., Rosen, B., West, A.P., Koutsourakis, M., Bushell, W., Iyer, V., Mujica, A.O., Thomas, M., Harrow, J., Cox, T*., et al.* (2011). A conditional knockout resource for the genome-wide study of mouse gene function. Nature *474*, 337-342.

Smith, A.C., and Robinson, A.J. (2016). MitoMiner v3.1, an update on the mitochondrial proteomics database. Nucleic Acids Res *44*, D1258-1261.

Smith, A.G., Raven, E.L., and Chernova, T. (2011). The regulatory role of heme in neurons. Metallomics *3*, 955-962.

Smith, Q.R., and Nagura, H. (2001). Fatty acid uptake and incorporation in brain: studies with the perfusion model. J Mol Neurosci *16*, 167-172; discussion 215-121.

Sokoloff, L. (1981). Localization of functional activity in the central nervous system by measurement of glucose utilization with radioactive deoxyglucose. J Cereb Blood Flow Metab *1*, 7-36.

Somjen, G.G. (1988). Nervenkitt: notes on the history of the concept of neuroglia. Glia *1*, 2-9.

Stark, R., Guebre-Egziabher, F., Zhao, X., Feriod, C., Dong, J., Alves, T.C., Ioja, S., Pongratz, R.L., Bhanot, S., Roden, M*., et al.* (2014). A role for mitochondrial phosphoenolpyruvate carboxykinase (PEPCK-M) in the regulation of hepatic gluconeogenesis. J Biol Chem *289*, 7257-7263.

Stauch, K.L., Purnell, P.R., and Fox, H.S. (2014). Quantitative proteomics of synaptic and nonsynaptic mitochondria: insights for synaptic mitochondrial vulnerability. J Proteome Res *13*, 2620-2636.

Stauch, K.L., Villeneuve, L.M., Totusek, S., Lamberty, B., Ciborowski, P., and Fox, H.S. (2019). Quantitative Proteomics of Presynaptic Mitochondria Reveal an Overexpression and Biological Relevance of Neuronal MitoNEET in Postnatal Brain Development. Dev Neurobiol *79*, 370-386.

Stefely, J.A., Kwiecien, N.W., Freiberger, E.C., Richards, A.L., Jochem, A., Rush, M.J.P., Ulbrich, A., Robinson, K.P., Hutchins, P.D., Veling, M.T*., et al.* (2016a). Mitochondrial protein functions elucidated by multi-omic mass spectrometry profiling. Nat Biotechnol *34*, 1191-1197.

Stefely, J.A., Licitra, F., Laredj, L., Reidenbach, A.G., Kemmerer, Z.A., Grangeray, A., Jaeg-Ehret, T., Minogue, C.E., Ulbrich, A., Hutchins, P.D*., et al.* (2016b). Cerebellar Ataxia and Coenzyme Q Deficiency through Loss of Unorthodox Kinase Activity. Mol Cell *63*, 608-620.

Stefely, J.A., and Pagliarini, D.J. (2017). Biochemistry of Mitochondrial Coenzyme Q Biosynthesis. Trends Biochem Sci *42*, 824-843.

Stefely, J.A., Reidenbach, A.G., Ulbrich, A., Oruganty, K., Floyd, B.J., Jochem, A., Saunders, J.M., Johnson, I.E., Minogue, C.E., Wrobel, R.L*., et al.* (2015). Mitochondrial ADCK3 employs an atypical protein kinase-like fold to enable coenzyme Q biosynthesis. Mol Cell *57*, 83-94.

Stoica, R., De Vos, K.J., Paillusson, S., Mueller, S., Sancho, R.M., Lau, K.F., Vizcay-Barrena, G., Lin, W.L., Xu, Y.F., Lewis, J.*, et al.* (2014). ER-mitochondria associations are regulated by the VAPB-PTPIP51 interaction and are disrupted by ALS/FTD-associated TDP-43. Nat Commun *5*, 3996.

Stoica, R., Paillusson, S., Gomez-Suaga, P., Mitchell, J.C., Lau, D.H., Gray, E.H., Sancho, R.M., Vizcay-Barrena, G., De Vos, K.J., Shaw, C.E.*, et al.* (2016). ALS/FTD-associated FUS activates GSK-3beta to disrupt the VAPB-PTPIP51 interaction and ER-mitochondria associations. EMBO Rep *17*, 1326-1342.

Straub, I.R., Janer, A., Weraarpachai, W., Zinman, L., Robertson, J., Rogaeva, E., and Shoubridge, E.A. (2018). Loss of CHCHD10-CHCHD2 complexes required for respiration underlies the pathogenicity of a CHCHD10 mutation in ALS. Hum Mol Genet *27*, 178-189.

Stump, D.D., Zhou, S.L., and Berk, P.D. (1993). Comparison of plasma membrane FABP and mitochondrial isoform of aspartate aminotransferase from rat liver. Am J Physiol *265*, G894-902.

Sturchler-Pierrat, C., Abramowski, D., Duke, M., Wiederhold, K.H., Mistl, C., Rothacher, S., Ledermann, B., Burki, K., Frey, P., Paganetti, P.A.*, et al.* (1997). Two amyloid precursor protein transgenic mouse models with Alzheimer disease-like pathology. Proc Natl Acad Sci U S A *94*, 13287-13292.

Sugiura, A., Mattie, S., Prudent, J., and McBride, H.M. (2017). Newly born peroxisomes are a hybrid of mitochondrial and ER-derived pre-peroxisomes. Nature *542*, 251-254.

Susin, S.A., Lorenzo, H.K., Zamzami, N., Marzo, I., Snow, B.E., Brothers, G.M., Mangion, J., Jacotot, E., Costantini, P., Loeffler, M.*, et al.* (1999). Molecular characterization of mitochondrial apoptosis-inducing factor. Nature *397*, 441-446.

Swerdlow, R.H. (2018). Mitochondria and Mitochondrial Cascades in Alzheimer's Disease. J Alzheimers Dis *62*, 1403-1416.

Swerdlow, R.H., and Khan, S.M. (2004). A "mitochondrial cascade hypothesis" for sporadic Alzheimer's disease. Med Hypotheses *63*, 8-20.

Szklarczyk, R., and Huynen, M.A. (2010). Mosaic origin of the mitochondrial proteome. Proteomics *10*, 4012-4024.

Szymanski, J., Janikiewicz, J., Michalska, B., Patalas-Krawczyk, P., Perrone, M., Ziolkowski, W., Duszynski, J., Pinton, P., Dobrzyn, A., and Wieckowski, M.R. (2017). Interaction of Mitochondria with the Endoplasmic Reticulum and Plasma Membrane in Calcium Homeostasis, Lipid Trafficking and Mitochondrial Structure. Int J Mol Sci *18*.

Taniguchi, H., He, M., Wu, P., Kim, S., Paik, R., Sugino, K., Kvitsiani, D., Fu, Y., Lu, J., Lin, Y.*, et al.* (2011). A resource of Cre driver lines for genetic targeting of GABAergic neurons in cerebral cortex. Neuron *71*, 995-1013.

Tasic, B., Menon, V., Nguyen, T.N., Kim, T.K., Jarsky, T., Yao, Z., Levi, B., Gray, L.T., Sorensen, S.A., Dolbeare, T.*, et al.* (2016). Adult mouse cortical cell taxonomy revealed by single cell transcriptomics. Nat Neurosci *19*, 335-346.

Taylor, S.W., Fahy, E., Zhang, B., Glenn, G.M., Warnock, D.E., Wiley, S., Murphy, A.N., Gaucher, S.P., Capaldi, R.A., Gibson, B.W.*, et al.* (2003). Characterization of the human heart mitochondrial proteome. Nat Biotechnol *21*, 281-286.

The Gene Ontology, C. (2019). The Gene Ontology Resource: 20 years and still GOing strong. Nucleic Acids Res *47*, D330-D338.

Thorsness, P.E., and Fox, T.D. (1990). Escape of DNA from mitochondria to the nucleus in Saccharomyces cerevisiae. Nature *346*, 376-379.

Tibbetts, A.S., and Appling, D.R. (2010). Compartmentalization of Mammalian folate-mediated one-carbon metabolism. Annu Rev Nutr *30*, 57-81.

Tien, A.C., Tsai, H.H., Molofsky, A.V., McMahon, M., Foo, L.C., Kaul, A., Dougherty, J.D., Heintz, N., Gutmann, D.H., Barres, B.A.*, et al.* (2012). Regulated temporal-spatial astrocyte precursor cell proliferation involves BRAF signalling in mammalian spinal cord. Development *139*, 2477-2487.

Tillberg, P.W., Chen, F., Piatkevich, K.D., Zhao, Y., Yu, C.C., English, B.P., Gao, L., Martorell, A., Suk, H.J., Yoshida, F.*, et al.* (2016). Protein-retention expansion microscopy of cells and tissues labeled using standard fluorescent proteins and antibodies. Nat Biotechnol *34*, 987-992.

Tilokani, L., Nagashima, S., Paupe, V., and Prudent, J. (2018). Mitochondrial dynamics: overview of molecular mechanisms. Essays Biochem *62*, 341-360.

Tokarska-Schlattner, M., Boissan, M., Munier, A., Borot, C., Mailleau, C., Speer, O., Schlattner, U., and Lacombe, M.L. (2008). The nucleoside diphosphate kinase D (NM23-H4) binds the inner mitochondrial membrane with high affinity to cardiolipin and couples nucleotide transfer with respiration. J Biol Chem *283*, 26198-26207.

Tomar, D., Jana, F., Dong, Z., Quinn, W.J., 3rd, Jadiya, P., Breves, S.L., Daw, C.C., Srikantan, S., Shanmughapriya, S., Nemani, N*., et al.* (2019a). Blockade of MCU-Mediated Ca(2+) Uptake Perturbs Lipid Metabolism via PP4-Dependent AMPK Dephosphorylation. Cell Rep *26*, 3709-3725 e3707.

Tomar, D., Thomas, M., Garbincius, J.F., Kolmetzky, D.W., Salik, O., Jadiya, P., Carpenter, A.C., and Elrod, J.W. (2019b). MICU1 regulates mitochondrial cristae structure and function independent of the mitochondrial calcium uniporter channel. bioRxiv, 803213.

Tretter, L., Patocs, A., and Chinopoulos, C. (2016). Succinate, an intermediate in metabolism, signal transduction, ROS, hypoxia, and tumorigenesis. Biochim Biophys Acta *1857*, 1086-1101.

Truernit, E., and Hibberd, J.M. (2007). Immunogenic tagging of chloroplasts allows their isolation from defined cell types. Plant J *50*, 926-932.

Tufi, R., Gleeson, T.P., von Stockum, S., Hewitt, V.L., Lee, J.J., Terriente-Felix, A., Sanchez-Martinez, A., Ziviani, E., and Whitworth, A.J. (2019). Comprehensive Genetic Characterization of Mitochondrial Ca(2+) Uniporter Components Reveals Their Different Physiological Requirements In Vivo. Cell Rep *27*, 1541-1550 e1545.

Tummala, H., Li, X., and Homayouni, R. (2010). Interaction of a novel mitochondrial protein, 4-nitrophenylphosphatase domain and non-neuronal SNAP25-like protein homolog 1 (NIPSNAP1), with the amyloid precursor protein family. Eur J Neurosci *31*, 1926-1934.

Tyanova, S., Temu, T., Sinitcyn, P., Carlson, A., Hein, M.Y., Geiger, T., Mann, M., and Cox, J. (2016). The Perseus computational platform for comprehensive analysis of (prote)omics data. Nat Methods *13*, 731-740.

Tyssowski, K.M., and Gray, J.M. (2019). The neuronal stimulation-transcription coupling map. Curr Opin Neurobiol *59*, 87-94.

Tzoulis, C., Neckelmann, G., Mork, S.J., Engelsen, B.E., Viscomi, C., Moen, G., Ersland, L., Zeviani, M., and Bindoff, L.A. (2010). Localized cerebral energy failure in DNA polymerase gamma-associated encephalopathy syndromes. Brain *133*, 1428-1437.

Uchida, Y., Izai, K., Orii, T., and Hashimoto, T. (1992). Novel fatty acid beta-oxidation enzymes in rat liver mitochondria. II. Purification and properties of enoyl-coenzyme A (CoA) hydratase/3-hydroxyacyl-CoA dehydrogenase/3-ketoacyl-CoA thiolase trifunctional protein. J Biol Chem *267*, 1034-1041.

Uchida, Y., and Takahashi, H. (2008). Rapid detection of Abeta deposits in APP transgenic mice by Hoechst 33342. Neuroscience letters *448*, 279-281.

Uhlen, M., Fagerberg, L., Hallstrom, B.M., Lindskog, C., Oksvold, P., Mardinoglu, A., Sivertsson, A., Kampf, C., Sjostedt, E., Asplund, A*., et al.* (2015). Proteomics. Tissue-based map of the human proteome. Science *347*, 1260419.

UniProt, C. (2019). UniProt: a worldwide hub of protein knowledge. Nucleic Acids Res *47*, D506-D515.

Uribarri, J., Oh, M.S., and Carroll, H.J. (1998). D-lactic acidosis. A review of clinical presentation, biochemical features, and pathophysiologic mechanisms. Medicine (Baltimore) *77*, 73-82.

Utter, M.F., and Keech, D.B. (1960). Formation of Oxaloacetate from Pyruvate and CO2. Journal of Biological Chemistry *235*, PC17-PC18.

Vafai, S.B., and Mootha, V.K. (2012). Mitochondrial disorders as windows into an ancient organelle. Nature *491*, 374-383.

Valm, A.M., Cohen, S., Legant, W.R., Melunis, J., Hershberg, U., Wait, E., Cohen, A.R., Davidson, M.W., Betzig, E., and Lippincott-Schwartz, J. (2017). Applying systems-level spectral imaging and analysis to reveal the organelle interactome. Nature *546*, 162-167.

van der Leij, F.R., Kram, A.M., Bartelds, B., Roelofsen, H., Smid, G.B., Takens, J., Zammit, V.A., and Kuipers, J.R. (1999). Cytological evidence that the C-terminus of carnitine palmitoyltransferase I is on the cytosolic face of the mitochondrial outer membrane. Biochem J *341 (Pt 3)*, 777-784.

van der Windt, G.J., and Pearce, E.L. (2012). Metabolic switching and fuel choice during T-cell differentiation and memory development. Immunol Rev *249*, 27-42.

Van Vranken, J.G., Jeong, M.Y., Wei, P., Chen, Y.C., Gygi, S.P., Winge, D.R., and Rutter, J. (2016). The mitochondrial acyl carrier protein (ACP) coordinates mitochondrial fatty acid synthesis with iron sulfur cluster biogenesis. Elife *5*, e17828.

Van Vranken, J.G., Nowinski, S.M., Clowers, K.J., Jeong, M.Y., Ouyang, Y., Berg, J.A., Gygi, J.P., Gygi, S.P., Winge, D.R., and Rutter, J. (2018). ACP Acylation Is an Acetyl-CoA-Dependent Modification Required for Electron Transport Chain Assembly. Mol Cell *71*, 567-580 e564.

van Wilpe, S., Ryan, M.T., Hill, K., Maarse, A.C., Meisinger, C., Brix, J., Dekker, P.J., Moczko, M., Wagner, R., Meijer, M.*, et al.* (1999). Tom22 is a multifunctional organizer of the mitochondrial preprotein translocase. Nature *401*, 485-489.

Vance, J.E. (1990). Phospholipid synthesis in a membrane fraction associated with mitochondria. J Biol Chem *265*, 7248-7256.

Vaughn, A.E., and Deshmukh, M. (2008). Glucose metabolism inhibits apoptosis in neurons and cancer cells by redox inactivation of cytochrome c. Nat Cell Biol *10*, 1477-1483.

Verhoeven, N.M., Roe, D.S., Kok, R.M., Wanders, R.J., Jakobs, C., and Roe, C.R. (1998). Phytanic acid and pristanic acid are oxidized by sequential peroxisomal and mitochondrial reactions in cultured fibroblasts. J Lipid Res *39*, 66-74.

Verleysdonk, S., Martin, H., Willker, W., Leibfritz, D., and Hamprecht, B. (1999). Rapid uptake and degradation of glycine by astroglial cells in culture: synthesis and release of serine and lactate. Glia *27*, 239-248.

Vidal, M., Morris, R., Grosveld, F., and Spanopoulou, E. (1990). Tissue-specific control elements of the Thy-1 gene. EMBO J *9*, 833-840.

Vielhaber, S., Kunz, D., Winkler, K., Wiedemann, F.R., Kirches, E., Feistner, H., Heinze, H.J., Elger, C.E., Schubert, W., and Kunz, W.S. (2000). Mitochondrial DNA abnormalities in skeletal muscle of patients with sporadic amyotrophic lateral sclerosis. Brain *123 (Pt 7)*, 1339-1348.

Vilchez, D., Ros, S., Cifuentes, D., Pujadas, L., Valles, J., Garcia-Fojeda, B., Criado-Garcia, O., Fernandez-Sanchez, E., Medrano-Fernandez, I., Dominguez, J.*, et al.* (2007). Mechanism suppressing glycogen synthesis in neurons and its demise in progressive myoclonus epilepsy. Nat Neurosci *10*, 1407-1413.

Vincent, E.E., Sergushichev, A., Griss, T., Gingras, M.C., Samborska, B., Ntimbane, T., Coelho, P.P., Blagih, J., Raissi, T.C., Choiniere, L.*, et al.* (2015). Mitochondrial Phosphoenolpyruvate Carboxykinase Regulates Metabolic Adaptation and Enables Glucose-Independent Tumor Growth. Mol Cell *60*, 195-207.

Visser, W., van Spronsen, E.A., Nanninga, N., Pronk, J.T., Gijs Kuenen, J., and van Dijken, J.P. (1995). Effects of growth conditions on mitochondrial morphology in Saccharomyces cerevisiae. Antonie Van Leeuwenhoek *67*, 243-253.

Vizcaino, J.A., Csordas, A., del-Toro, N., Dianes, J.A., Griss, J., Lavidas, I., Mayer, G., Perez-Riverol, Y., Reisinger, F., Ternent, T.*, et al.* (2016). 2016 update of the PRIDE database and its related tools. Nucleic Acids Res *44*, D447-456.

Vogel, R., Wiesinger, H., Hamprecht, B., and Dringen, R. (1999). The regeneration of reduced glutathione in rat forebrain mitochondria identifies metabolic pathways providing the NADPH required. Neuroscience letters *275*, 97-100.

Vogtle, F.N., Wortelkamp, S., Zahedi, R.P., Becker, D., Leidhold, C., Gevaert, K., Kellermann, J., Voos, W., Sickmann, A., Pfanner, N.*, et al.* (2009). Global analysis of the mitochondrial N-proteome identifies a processing peptidase critical for protein stability. Cell *139*, 428-439.

von Heijne, G. (1986). Why mitochondria need a genome. FEBS Lett *198*, 1-4.

Vozza, A., Blanco, E., Palmieri, L., and Palmieri, F. (2004). Identification of the mitochondrial GTP/GDP transporter in Saccharomyces cerevisiae. J Biol Chem *279*, 20850-20857.

Waagepetersen, H.S., Qu, H., Schousboe, A., and Sonnewald, U. (2001). Elucidation of the quantitative significance of pyruvate carboxylation in cultured cerebellar neurons and astrocytes. J Neurosci Res *66*, 763-770.

Wai, T., and Langer, T. (2016). Mitochondrial Dynamics and Metabolic Regulation. Trends Endocrinol Metab *27*, 105-117.

Waldmeier, P.C. (1987). Amine oxidases and their endogenous substrates (with special reference to monoamine oxidase and the brain). In Monoamine Oxidase Enzymes: Review and Overview, L. Oreland, and B.A. Callingham, eds. (Vienna: Springer Vienna), pp. 55-72.

Walker, J.E. (1998). ATP Synthesis by Rotary Catalysis (Nobel lecture). Angew Chem Int Ed Engl *37*, 2308-2319.

Wan, B., LaNoue, K.F., Cheung, J.Y., and Scaduto, R.C., Jr. (1989). Regulation of citric acid cycle by calcium. J Biol Chem *264*, 13430-13439.

Wanders, R.J.A., Waterham, H.R., and Ferdinandusse, S. (2016). Metabolic Interplay between Peroxisomes and Other Subcellular Organelles Including Mitochondria and the Endoplasmic Reticulum. Frontiers in Cell and Developmental Biology *3*, 83.

Wang, H., Sreenivasan, U., Hu, H., Saladino, A., Polster, B.M., Lund, L.M., Gong, D.W., Stanley, W.C., and Sztalryd, C. (2011a). Perilipin 5, a lipid droplet-associated protein, provides physical and metabolic linkage to mitochondria. J Lipid Res *52*, 2159-2168.

Wang, X., Leverin, A.L., Han, W., Zhu, C., Johansson, B.R., Jacotot, E., Ten, V.S., Sims, N.R., and Hagberg, H. (2011b). Isolation of brain mitochondria from neonatal mice. J Neurochem *119*, 1253-1261.

Wang, X., and Michaelis, E.K. (2010). Selective neuronal vulnerability to oxidative stress in the brain. Front Aging Neurosci *2*, 12.

Wang, X., Su, B., Siedlak, S.L., Moreira, P.I., Fujioka, H., Wang, Y., Casadesus, G., and Zhu, X. (2008). Amyloid-beta overproduction causes abnormal mitochondrial dynamics via differential modulation of mitochondrial fission/fusion proteins. Proc Natl Acad Sci U S A *105*, 19318-19323.

Wang, X., Zaidi, A., Pal, R., Garrett, A.S., Braceras, R., Chen, X.W., Michaelis, M.L., and Michaelis, E.K. (2009). Genomic and biochemical approaches in the discovery of mechanisms for selective neuronal vulnerability to oxidative stress. BMC Neurosci *10*, 12.

Wang, Y., Liu, J., Jin, X., Zhang, D., Li, D., Hao, F., Feng, Y., Gu, S., Meng, F., Tian, M.*, et al.* (2017). O-GlcNAcylation destabilizes the active tetrameric PKM2 to promote the Warburg effect. Proc Natl Acad Sci U S A *114*, 13732-13737.

Wang, Y.Z., and Savas, J.N. (2018). Uncovering Discrete Synaptic Proteomes to Understand Neurological Disorders. Proteomes *6*.

Warburg, O. (1956). On the origin of cancer cells. Science *123*, 309-314.

Watkins, P.A. (2008). Very-long-chain acyl-CoA synthetases. J Biol Chem *283*, 1773-1777.

Watkins, P.A., Ferrell, E.V., Jr., Pedersen, J.I., and Hoefler, G. (1991). Peroxisomal fatty acid beta-oxidation in HepG2 cells. Arch Biochem Biophys *289*, 329-336.

Watkins, P.A., Maiguel, D., Jia, Z., and Pevsner, J. (2007). Evidence for 26 distinct acyl-coenzyme A synthetase genes in the human genome. J Lipid Res *48*, 2736-2750.

Watt, I.N., Montgomery, M.G., Runswick, M.J., Leslie, A.G., and Walker, J.E. (2010). Bioenergetic cost of making an adenosine triphosphate molecule in animal mitochondria. Proc Natl Acad Sci U S A *107*, 16823-16827.

Weber, B., and Barros, L.F. (2015). The Astrocyte: Powerhouse and Recycling Center. Cold Spring Harb Perspect Biol *7*.

Webster, M.T., Pearce, B.R., Bowen, D.M., and Francis, P.T. (1998). The effects of perturbed energy metabolism on the processing of amyloid precursor protein in PC12 cells. J Neural Transm (Vienna) *105*, 839-853.

Wettmarshausen, J., and Perocchi, F. (2017). Isolation of Functional Mitochondria from Cultured Cells and Mouse Tissues. Methods Mol Biol *1567*, 15-32.

White, K., Kim, M.J., Han, C., Park, H.J., Ding, D., Boyd, K., Walker, L., Linser, P., Meneses, Z., Slade, C.*, et al.* (2018). Loss of IDH2 Accelerates Age-related Hearing Loss in Male Mice. Sci Rep *8*, 5039.

Wiedemann, F.R., Manfredi, G., Mawrin, C., Beal, M.F., and Schon, E.A. (2002). Mitochondrial DNA and respiratory chain function in spinal cords of ALS patients. J Neurochem *80*, 616-625.

Wiedemann, F.R., Winkler, K., Kuznetsov, A.V., Bartels, C., Vielhaber, S., Feistner, H., and Kunz, W.S. (1998). Impairment of mitochondrial function in skeletal muscle of patients with amyotrophic lateral sclerosis. J Neurol Sci *156*, 65-72.

Williamson, J.R., Browning, E.T., Scholz, R., Kreisberg, R.A., and Fritz, I.B. (1968). Inhibition of fatty acid stimulation of gluconeogenesis by (+)-decanoylcarnitine in perfused rat liver. Diabetes *17*, 194-208.

Wirths, O., and Bayer, T.A. (2010). Neuron loss in transgenic mouse models of Alzheimer's disease. Int J Alzheimers Dis *2010*, 723782.

Wisniewski, J.R., Zougman, A., Nagaraj, N., and Mann, M. (2009). Universal sample preparation method for proteome analysis. Nat Methods *6*, 359-362.

Wong, P.C., Pardo, C.A., Borchelt, D.R., Lee, M.K., Copeland, N.G., Jenkins, N.A., Sisodia, S.S., Cleveland, D.W., and Price, D.L. (1995). An adverse property of a familial ALS-linked SOD1 mutation causes motor neuron disease characterized by vacuolar degeneration of mitochondria. Neuron *14*, 1105-1116.

Wong, Y.C., Ysselstein, D., and Krainc, D. (2018). Mitochondria-lysosome contacts regulate mitochondrial fission via RAB7 GTP hydrolysis. Nature *554*, 382-386.

Wu, H., Williams, J., and Nathans, J. (2014). Complete morphologies of basal forebrain cholinergic neurons in the mouse. Elife *3*, e02444.

Xie, Z., Jones, A., Deeney, J.T., Hur, S.K., and Bankaitis, V.A. (2016). Inborn Errors of Long-Chain Fatty Acid beta-Oxidation Link Neural Stem Cell Self-Renewal to Autism. Cell Rep *14*, 991-999.

Xing, Y., Wang, M., Wang, J., Nie, Z., Wu, G., Yang, X., and Shen, Y. (2019). Dimerization of MICU Proteins Controls Ca(2+) Influx through the Mitochondrial Ca(2+) Uniporter. Cell Rep *26*, 1203-1212 e1204.

Xu, J., Khoury, N., Jackson, C.W., Escobar, I., Stegelmann, S.D., Dave, K.R., and Perez-Pinzon, M.A. (2019). Ischemic Neuroprotectant PKCepsilon Restores Mitochondrial Glutamate Oxaloacetate Transaminase in the Neuronal NADH Shuttle after Ischemic Injury. Transl Stroke Res.

Xu, Y.F., Gendron, T.F., Zhang, Y.J., Lin, W.L., D'Alton, S., Sheng, H., Casey, M.C., Tong, J., Knight, J., Yu, X*., et al.* (2010). Wild-type human TDP-43 expression causes TDP-43 phosphorylation, mitochondrial aggregation, motor deficits, and early mortality in transgenic mice. J Neurosci *30*, 10851-10859.

Yamamoto, H., Esaki, M., Kanamori, T., Tamura, Y., Nishikawa, S.-i., and Endo, T. (2002). Tim50 Is a Subunit of the TIM23 Complex that Links Protein Translocation across the Outer and Inner Mitochondrial Membranes. Cell *111*, 519-528.

Yang, S.Y., He, X.Y., and Schulz, H. (1987). Fatty acid oxidation in rat brain is limited by the low activity of 3-ketoacyl-coenzyme A thiolase. Journal of Biological Chemistry *262*, 13027-13032.

Yates, D.W., and Garland, P.B. (1970). Carnitine palmitoyltransferase activities (EC 2.3.1.-) of rat liver mitochondria. Biochem J *119*, 547-552.

Yim, A., Koti, P., Bonnard, A., Marchiano, F., Durrbaum, M., Garcia-Perez, C., Villaveces, J., Gamal, S., Cardone, G., Perocchi, F*., et al.* (2020). mitoXplorer, a visual data mining platform to systematically analyze and visualize mitochondrial expression dynamics and mutations. Nucleic Acids Res *48*, 605-632.

Yona, S., Kim, K.W., Wolf, Y., Mildner, A., Varol, D., Breker, M., Strauss-Ayali, D., Viukov, S., Guilliams, M., Misharin, A*., et al.* (2013). Fate mapping reveals origins and dynamics of monocytes and tissue macrophages under homeostasis. Immunity *38*, 79-91.

Yoneda, T., Sato, M., Maeda, M., and Takagi, H. (1998). Identification of a novel adenylate kinase system in the brain: cloning of the fourth adenylate kinase. Brain Res Mol Brain Res *62*, 187-195.

Yoon, W., Hwang, S.H., Lee, S.H., and Chung, J. (2019). Drosophila ADCK1 is critical for maintaining mitochondrial structures and functions in the muscle. PLoS Genet *15*, e1008184.

Yoon, Y., Krueger, E.W., Oswald, B.J., and McNiven, M.A. (2003). The mitochondrial protein hFis1 regulates mitochondrial fission in mammalian cells through an interaction with the dynamin-like protein DLP1. Mol Cell Biol *23*, 5409-5420.

Yoshii, S.R., Kishi, C., Ishihara, N., and Mizushima, N. (2011). Parkin mediates proteasome-dependent protein degradation and rupture of the outer mitochondrial membrane. J Biol Chem *286*, 19630-19640.

Yu, A.C., Drejer, J., Hertz, L., and Schousboe, A. (1983). Pyruvate carboxylase activity in primary cultures of astrocytes and neurons. J Neurochem *41*, 1484-1487.

Yudkoff, M., Nelson, D., Daikhin, Y., and Erecinska, M. (1994). Tricarboxylic acid cycle in rat brain synaptosomes. Fluxes and interactions with aspartate aminotransferase and malate/aspartate shuttle. J Biol Chem *269*, 27414-27420.

Zamponi, N., Zamponi, E., Cannas, S.A., Billoni, O.V., Helguera, P.R., and Chialvo, D.R. (2018). Mitochondrial network complexity emerges from fission/fusion dynamics. Sci Rep *8*, 363.

Zamzami, N., Susin, S.A., Marchetti, P., Hirsch, T., Gomez-Monterrey, I., Castedo, M., and Kroemer, G. (1996). Mitochondrial control of nuclear apoptosis. J Exp Med *183*, 1533-1544.

Zeng, H., and Sanes, J.R. (2017). Neuronal cell-type classification: challenges, opportunities and the path forward. Nat Rev Neurosci *18*, 530-546.

Zhang, Y., Chen, K., Sloan, S.A., Bennett, M.L., Scholze, A.R., O'Keeffe, S., Phatnani, H.P., Guarnieri, P., Caneda, C., Ruderisch, N.*, et al.* (2014). An RNA-sequencing transcriptome and splicing database of glia, neurons, and vascular cells of the cerebral cortex. J Neurosci *34*, 11929-11947.

Zick, M., Rabl, R., and Reichert, A.S. (2009). Cristae formation-linking ultrastructure and function of mitochondria. Biochim Biophys Acta *1793*, 5-19.

Chapter 7: Appendix

7.1. MitoTag expression in different Cre-driver lines

Table A1. MitoTag expression in tested Cre-driver lines.

Cre-driver line	*Reported cell type/ lineage*
Emx1:Cre (Gorski et al., 2002)	B6.129S2-Emx1$^{tm1(cre)Krj}$/J (JAX#005628) MGI:2684610 ~88% of neurons in neocortex and hippocampus, and in glial cells of the pallium
	Expression with MitoTag: reported expression
Actin:Cre (Lewandoski et al., 1997)	B6N.FVB-Tmem163$^{Tg(ACTB\text{-}cre)2Mrt}$/CjDswJ (JAX#019099) MGI:2176050 Cre recombinase activity is widespread in the embryo by the blastocyst stage of development.
	Expression with MitoTag: reported expression
Gfap:Cre (Gregorian et al., 2009)	B6.Gc-Tg(Gfap-cre)77.6Mvs/2J (JAX#024098) MGI:3838840 most astrocytes in brain and spinal cord tissues, and all astrocytes following CNS injury; no Cre recombinase activity in postnatal or adult neural stem cells (or their progeny) from the hippocampus or other brain regions
	Expression with MitoTag: reported expression
L7:Cre (Barski et al., 2000)	B6.129-Tg(Pcp2-cre)2Mpin/J (JAX#004146) MGI:2174502 most Purkinje cells (>P6) and some retinal bipolar neurons
	Expression with MitoTag: reported expression
Gabra6:Cre (Fünfschilling and Reichardt, 2002)	Tg(mα6-cre)B1LFR MGI:4358481 postnatally in granule cells of the cerebellum and dorsal cochlear nucleus, as well as in a subset of precerebellar nuclei in the brainstem
	Expression with MitoTag: reported expression
Mog:iCre (Hovelmeyer et al., 2005)	Mog$^{tm1(cre)}$Gkl MGI:3689957 mature oligodendrocytes in the central nervous system without expression in neurons, astrocytes or oligodendrocyte precursor cells
	Expression with MitoTag: reported expression
Plp:CreERT (Doerflinger et al., 2003)	B6.Cg-Tg(Plp1-cre/ERT)3Pop/J (JAX#005975) MGI:3695909 after tamoxifen administration in oligodendrocytes and Schwann cells
	Expression with MitoTag: reported expression, but inefficient recombination in CNS
Cx3Cr1:CreERT (Yona et al., 2013)	B6.129P2(C)-Cx3cr1$^{tm2.1(cre/ERT2)Jung}$/J (JAX#020940) MGI:5568569 after tamoxifen administration in monocytes, macrophages and microglia
	Expression with MitoTag: reported expression, but inefficient recombination
Pvalb:Cre (Madisen et al., 2010)	B6.Cg-Pvalb$^{tm1.1(cre)Aibs}$/J (JAX#012358) MGI:4440464 in scattered interneuron populations in the cortex and hippocampus, as well as neuronal populations in other brain regions; additional layer 5 neurons
	Expression with MitoTag: reported expression

Cre-driver line	*Reported cell type/ lineage*
Sst:Cre (Taniguchi et al., 2011)	B6J.Cg-Sst$^{\mathrm{tm2.1(cre)Zjh}}$/MwarJ (JAX#028864) MGI:4838416 in somatostatin positive neurons including Martinotti cells and Oriens-Lacunosum-Moleculare cells
	Expression with MitoTag: reported expression
Vip:Cre (Taniguchi et al., 2011)	STOCK Vip$^{\mathrm{tm1(cre)Zjh}}$/J (JAX#010908) MGI:4437225 in GABAergic neurons in neocortex, hippocampus, olfactory bulb, suprachiasmatic nuclei, and other discrete midbrain and brainstem regions
	Expression with MitoTag: reported expression
CAG:CreERT (Hayashi and McMahon, 2002)	B6.Tg(CAG-cre/Esr1*)5Amc/J (JAX#004682) MGI:2680708 after tamoxifen administration in widespread cells or tissues
	Expression with MitoTag: reported expression with efficient recombination
Aldh:Cre (Tien et al., 2012)	B6;FVB-Tg(Aldh1l1-cre)JD1884Htz/J (JAX#023748) MGI:5514359 glial cells of the spinal cord; 75% of labeled cells also express GFAP, 15% co-express OLIG2 and 10% express NeuN.
	Expression with MitoTag: reported expression in astrocytes and subset of neurons
hGfap:CreERT (Ganat et al., 2006)	B6.Cg-Tg(GFAP-cre/ERT2)505Fmv/J (JAX#012849) MGI:4458023 after tamoxifen administration in subventricular zone, dentate gyrus, celebellum, mesencephalon, diencephalon, and cerebral cortex
	Expression with MitoTag: reported expression, but inefficient recombination in CNS
Sept4:Cre (Gong et al., 2003; Kinoshita et al., 2000)	Tg(Sept4-cre)OX54Gsat/Mmucd MGI:5519914 intense expression in Bergmann glia, moderate expression in other brain regions – presumably astrocytes
	Expression with MitoTag: expression in all astrocytes throughout the brain and spinal cord
Rbp4:Cre (Gerfen et al., 2013)	STOCK Tg(Rbp4-cre)KL100Gsat (#031125-UCD) MGI:4367068 restricted to most layer 5 neurons throughout neocortical and periallocortical areas with expression in pyramidal tract and intertelencephalic corticostriatal neurons; hippocampal granule cells
	Expression with MitoTag: reported expression
ChAT:Cre (Rossi et al., 2011)	B6;129S6-Chat$^{\mathrm{tm2(cre)Lowl}}$/J (JAX#006410) MGI:3699161 in all cholinergic neurons
	Expression with MitoTag: reported expression

7.2. Cell type-enriched candidates in Purkinje cells, granule cells and astrocytes

Table A2. Candidates predicted to be enriched in cerebellar cell type.
Taken from Fecher et al. (2019), Supplementary Data.

Gene name	*Candidate*	*PC vs A*			*GC vs A*			*PC vs GC*			*MitoCarta*	*Localization, predicted*
		*****	**FC**	**$-log_{10}(P)$**	*****	**FC**	**$-log_{10}(P)$**	*****	**FC**	**$-log_{10}(P)$**		
Aass	A	*	-3.270	6.600	*	-3.124	4.728		-0.147	0.105	+	mito
Abat	A	*	-0.932	4.626	*	-1.335	7.068		0.404	1.782	+	mito
Abcd3	A	*	-1.645	7.596	*	-2.054	7.839		0.409	2.142	+	peroxi MEM
Acaa1a	A	*	-2.007	7.839	*	-1.535	6.669	*	-0.472	2.939	+	peroxi
Acaa2	A	*	-2.228	7.923	*	-2.306	9.980		0.078	0.214	+	mito
Acad10	A	*	-2.357	7.403	*	-2.630	8.089		0.273	0.693	+	mito
Acad11	A	*	-3.097	4.842	*	-3.673	5.160		0.576	1.001	+	
Acadm	A	*	-2.588	8.720	*	-2.283	8.227		-0.305	1.045	+	mito
Acadl	A	*	-2.378	10.341	*	-2.081	8.166		-0.297	1.756	+	
Acads	A	*	-2.814	7.788	*	-2.639	9.550		-0.175	0.384	+	mito
Acadsb	A	*	-0.889	4.288	*	-1.294	5.004		0.405	1.658	+	mito
Acadvl	A	*	-1.439	6.551	*	-1.295	6.866		-0.144	0.504	+	mito
Acbd5	A	*	-1.845	5.677	*	-2.141	6.874		0.296	0.754		peroxi MEM
Acot2	A	*	-2.753	5.772	*	-2.143	7.333		-0.610	1.141	+	mito
Acot8	A	*	-1.575	6.156	*	-1.459	5.174		-0.116	0.289		peroxi
Acox1	A	*	-2.322	8.297	*	-2.422	7.275		0.101	0.532	+	peroxi
Acox3	A	*	-0.980	4.541	*	-1.348	5.092		0.369	1.263	+	peroxi
Acsf2	A	*	-2.726	12.126	*	-2.792	10.402		0.067	0.352	+	mito
Acsm5	A		0.000	0.000	*	-1.535	3.278		0.000	0.000	+	mito
Acss1	A	*	-2.796	10.005	*	-2.698	7.303		-0.099	0.291	+	mito
Acss3	A	*	-2.197	5.613		nd	nd		nd	nd	+	cytoplasm
Adck1	A	*	-1.138	4.261	*	-0.941	3.516		-0.197	0.373	+	chloro
Adhfe1	A	*	-2.046	5.614	*	-2.147	5.476		0.101	0.132	+	mito
Agpat5	A	*	-1.555	5.651	*	-1.238	4.051		-0.317	0.721	+	ER MEM
Agps	A	*	-1.397	2.708		-1.037	1.907		-0.360	0.808		peroxi
Ak3	A	*	-2.100	7.645	*	-1.335	6.507	*	-0.766	3.213	+	mito
Aldh2	A	*	-1.984	7.425	*	-2.074	6.633		0.090	0.291	+	mito
Aldh4a1	A	*	-2.169	8.724	*	-2.075	7.979		-0.094	0.286	+	mito
Aldh6a1	A	*	-2.471	10.001	*	-1.941	7.349	*	-0.529	2.992	+	mito
Aldh7a1	A	*	-1.669	9.680	*	-1.760	8.467		0.091	0.669	+	cytoplasm
Aldh9a1	A	*	-1.153	5.141	*	-0.847	3.746		-0.306	1.561	+	cytoplasm
Amt	A	*	-2.084	6.833	*	-1.894	5.515		-0.190	0.515	+	mito
Bcat2	A	*	-0.501	2.073	*	-1.029	4.755		0.528	1.639	+	mito
Cat	A	*	-2.255	8.368	*	-2.237	7.580		-0.019	0.046	+	peroxi
Cbr4	A	*	-0.482	2.552	*	-1.387	5.674	*	0.905	3.855	+	mito
Ccbl2	A	*	-0.563	2.212	*	-1.507	6.532	*	0.944	3.023	+	cytoplasm

Gene name	*Candidate*	*PC vs A*			*GC vs A*			*PC vs GC*			*MitoCarta*	*Localization, predicted*
		*****	**FC**	$-\log_{10}(P)$	*****	**FC**	$-\log_{10}(P)$	*****	**FC**	$-\log_{10}(P)$		
Ccdc90b	A	*	-2.008	4.883	*	-1.902	4.513		-0.106	0.167	+	mito MEM
Chdh	A	*	-1.942	6.478		nd	nd		nd	nd	+	secreted
Cpt1a	A	*	-2.225	8.630	*	-2.351	8.351		0.126	0.380	+	mito MEM
Cpt2	A	*	-1.401	5.872	*	-0.864	5.571		-0.536	2.333	+	mito MEM
Crot	A		nd	nd	*	-3.917	3.680		nd	nd	+	mito MEM
Dao	A	*	-2.968	9.938	*	-2.916	11.119		-0.052	0.175		peroxi
Dbt	A	*	-0.995	4.087	*	-1.298	5.411		0.303	0.840	+	mito
Ddo	A		nd	nd	*	-3.530	6.506		nd	nd		peroxi
Decr1	A	*	-2.178	7.054	*	-1.711	6.148		-0.467	2.416	+	mito
Dhrs4	A	*	-2.247	6.948	*	-1.620	5.502		-0.627	2.407	+	peroxi
Ech1	A	*	-2.204	8.149	*	-2.305	7.874		0.101	0.311	+	mito
Echdc2	A	*	-2.131	4.321	*	-1.432	4.098		-0.699	0.952	+	mito
Echdc3	A	*	-2.046	5.710		nd	nd		nd	nd	+	mito
Echs1	A	*	-1.003	5.340	*	-0.959	3.833		-0.044	0.097	+	mito
Eci1	A	*	-1.728	7.366	*	-1.319	5.188		-0.409	1.677	+	mito
Eci2	A	*	-1.501	8.179	*	-1.544	8.391		0.043	0.205	+	peroxi MEM
Ephx2	A	*	-1.455	3.620	*	-1.263	5.275		-0.192	0.406	+	mito
Etfa	A	*	-0.849	3.693	*	-1.084	4.080		0.235	0.585	+	mito
Fam213a	A	*	-1.467	8.952	*	-1.382	5.639		-0.085	0.259	+	cytoplasm
Gatm	A	*	-1.418	6.900	*	-0.968	4.308		-0.450	1.589	+	cytoplasm
Gcdh	A	*	-1.466	7.571	*	-1.412	6.335		-0.054	0.144	+	mito
Gldc	A	*	-4.443	5.890	*	-2.625	7.940		-1.818	2.289	+	mito
Glud1	A	*	-1.743	8.194	*	-1.615	7.632		-0.128	0.525	+	mito
Gnpat	A	*	-1.296	2.497	*	-1.625	2.395		0.329	0.457		mito MEM
Gpam	A		nd	nd	*	-1.012	2.967		nd	nd	+	mito MEM
Gpt2	A	*	-2.185	8.529	*	-2.259	7.814		0.074	0.182	+	cytoplasm
Gstk1	A	*	-2.614	9.721	*	-2.316	8.777		-0.298	1.370	+	mito
Hsd17b8	A		-0.426	1.723	*	-1.067	4.908		0.641	2.357	+	mito
Hacl1	A	*	-2.620	7.825	*	-2.589	7.043		-0.031	0.087		peroxi
Hadh	A	*	-2.258	7.347	*	-2.359	8.861		0.101	0.297	+	mito
Hadha	A	*	-1.846	7.858	*	-1.718	8.392		-0.128	0.458	+	mito
Hadhb	A	*	-1.938	7.654	*	-1.981	8.065		0.043	0.104	+	peroxi
Hk2	A		nd	nd	*	-1.827	3.474		nd	nd	+	chloro MEM
Hsd17b10	A	*	-1.133	3.715	*	-0.427	2.197		-0.706	1.760	+	mito
Hsd17b4	A	*	-1.908	8.329	*	-2.012	7.607		0.104	0.978	+	peroxi
Idh2	A	*	-2.208	8.973	*	-1.440	6.640	*	-0.768	3.961	+	mito
Isoc2a	A	*	-1.428	3.893	*	-1.055	2.377		-0.373	0.669	+	cytoplasm
Isoc2b	A		-0.856	2.040	*	-1.004	2.137		0.148	0.248		cytoplasm
Ivd	A	*	-1.642	6.715	*	-1.594	7.015		-0.048	0.139	+	mito
Lonp2	A	*	-2.785	2.770	*	-2.885	3.166		0.100	0.118	+	peroxi
MaoB	A	*	-2.750	11.720	*	-2.698	7.235		-0.052	0.117	+	cytoplasm

Gene name	*Candidate*	*PC vs A*			*GC vs A*			*PC vs GC*			*MitoCarta*	*Localization, predicted*
		*****	**FC**	$-log_{10}(P)$	*****	**FC**	$-log_{10}(P)$	*****	**FC**	$-log_{10}(P)$		
Marc2	A	*	-1.877	7.190	*	-1.966	6.053		0.088	0.178	+	mito MEM
March5	A	*	-0.321	2.682	*	0.531	3.857	*	-0.853	4.520	+	golgi MEM
Mavs	A	*	-2.769	5.844	*	-2.337	7.397		-0.431	0.731	+	plasma MEM
Mccc1	A	*	-1.011	4.940	*	-1.278	6.815		0.267	1.045	+	mito
Mcee	A	*	-1.543	4.128		-0.449	1.155		-1.095	2.310	+	mito
Mcur1	A	*	-2.260	7.736	*	-2.305	8.823		0.045	0.112	+	mito MEM
Mgst1	A	*	-1.067	2.179	*	-1.299	4.619		0.232	0.271	+	ER MEM
Mpv17	A	*	-2.110	3.279	*	-0.996	2.606		-1.114	1.345	+	mito MEM
Mpv17l2	A	*	-0.745	2.095	*	-1.699	6.122		0.954	2.202	+	mito MEM
Mut	A	*	-0.894	3.745	*	-1.305	6.421		0.411	1.231	+	mito
Nadk2	A	*	-2.107	9.397	*	-1.233	6.661	*	-0.873	4.848	+	mito
Nnt	A	*	-1.062	4.283	*	-1.151	5.132		0.089	0.187	+	plasma MEM
Nudt7	A	*	-2.240	2.217		nd	nd		nd	nd		peroxi
Oat	A	*	-2.419	7.821	*	-1.921	6.968		-0.498	1.562	+	mito
Pex14	A	*	-1.359	3.820		-0.874	1.955		-0.485	1.110		peroxi MEM
Phyh	A	*	-3.032	5.900	*	-2.912	4.343		-0.120	0.237	+	peroxi
Prodh	A	*	-2.602	9.468	*	-2.541	7.070		-0.061	0.137	+	mito
Pxmp2	A	*	-1.918	2.895	*	-3.033	5.646		1.115	1.584	+	peroxi MEM
Rexo2	A	*	-1.108	5.169	*	-0.538	3.176	*	-0.571	2.911	+	mito
Sardh	A	*	-2.868	12.386	*	-2.691	9.581		-0.177	0.985	+	mito
Scp2	A	*	-2.154	9.152	*	-1.942	8.238		-0.212	1.186	+	peroxi
Serhl	A	*	-1.967	5.999		nd	nd		nd	nd		mito
Sfxn5	A	*	-1.910	7.230	*	-2.054	5.915		0.144	0.350	+	mito MEM
Slc25a1	A	*	-1.016	3.634	*	-0.562	3.212		-0.453	1.265	+	mito MEM
Slc25a18	A	*	-2.541	8.082	*	-2.603	6.636		0.063	0.185	+	mito MEM
Slc25a20	A	*	-0.993	4.536	*	-1.297	6.565		0.304	1.099	+	mito MEM
Slc25a21	A	*	-2.258	4.883		nd	nd		nd	nd	+	mito MEM
Slc25a33	A	*	-1.351	3.018		nd	nd		nd	nd	+	mito MEM
Slc27a1	A	*	-1.102	6.314	*	-0.946	4.715		-0.156	0.603		ER MEM
Sqrdl	A	*	-2.160	7.262	*	-1.566	6.560		-0.594	2.436	+	mito
Suclg2	A	*	-2.665	8.527	*	-2.707	8.221		0.042	0.089	+	mito
Sugct	A	*	-2.377	4.520	*	-2.460	8.144		0.082	0.086	+	mito
Suox	A	*	-2.033	8.091	*	-1.746	7.901		-0.287	1.118	+	mito
Them4	A	*	-1.838	6.298	*	-1.809	6.000		-0.029	0.051	+	mito
Tspo	A		-0.145	0.165	*	-1.134	2.134		0.989	1.969	+	mito MEM
Tst	A	*	-2.595	9.305	*	-2.589	7.741		-0.006	0.014	+	mito
Ucp3	A	*	-2.442	4.618		nd	nd		nd	nd	+	mito MEM
Zadh2	A	*	-1.578	5.877	*	-0.685	3.038	*	-0.893	4.109	+	peroxi
Aars2	GC	*	0.688	4.127	*	1.049	5.798		-0.361	1.989	+	mito
Abcb10	GC		-0.883	1.901	*	0.722	2.863	*	-1.605	2.998	+	mito MEM
Abhd10	GC		0.185	0.420	*	1.337	4.844	*	-1.151	3.284	+	mito

Gene name	*Candidate*	*PC vs A*			*GC vs A*			*PC vs GC*			*MitoCarta*	*Localization, predicted*
		*****	**FC**	***$-log_{10}(P)$***	*****	**FC**	***$-log_{10}(P)$***	*****	**FC**	***$-log_{10}(P)$***		
Acot9	GC	*	0.753	4.696	*	1.559	6.075	*	-0.805	3.400	+	cytoplasm
Ak4	GC	*	-1.127	4.566	*	1.214	4.412	*	-2.341	5.807	+	mito
Angel2	GC		0.287	0.978	*	1.056	4.055	*	-0.769	3.680	+	secreted
Auh	GC	*	0.759	3.819	*	1.198	4.647		-0.438	1.471	+	
Cend1	GC	*	0.711	2.191	*	1.112	3.397		-0.401	1.385		nucleus
Ckmt1	GC	*	0.744	3.869	*	1.471	6.920	*	-0.727	3.240	+	cytoplasm
Cpox	GC	*	0.812	3.258	*	1.279	4.433		-0.466	2.028	+	mito
Ethe1	GC		-0.306	0.769	*	1.074	3.188	*	-1.379	4.681	+	mito
Exog	GC		0.212	1.731	*	1.304	5.340	*	-1.092	4.833	+	secreted
Fastkd2	GC		1.013	2.044	*	1.506	2.473		-0.493	1.018	+	nucleus
Gdap1	GC	*	0.731	4.686	*	1.246	6.078	*	-0.516	3.377	+	cytoplasm
Gdap1l1	GC		0.172	1.012	*	1.366	5.175	*	-1.194	4.201		mito MEM
Gls	GC		0.328	1.777	*	1.823	7.319	*	-1.496	6.020	+	mito
Gls2	GC		0.385	1.039	*	2.191	5.587	*	-1.806	5.058	+	mito
Synj2bp	GC		-0.090	0.206	*	0.503	1.453	*	-0.593	2.051	+	cytoplasm
Gtpbp8	GC		nd	nd		nd	nd	*	-1.006	4.442		chloro
Guf1	GC		0.425	1.283	*	1.246	4.414		-0.822	2.393	+	plastid
Hist2h2aa1	GC		-0.730	1.089		0.850	1.196	*	-1.580	2.786		nucleus
Hist2h2ac	GC		-0.730	1.089		0.850	1.196	*	-1.580	2.786		nucleus
Hk1	GC	*	-0.412	2.879	*	1.163	8.033	*	-1.575	7.065	+	chloro MEM
Hmgcl	GC		-0.337	1.491	*	0.691	3.035	*	-1.028	3.804	+	mito
Isca1	GC	*	0.614	2.302	*	1.005	3.027		-0.391	0.930	+	mito
Macrod1	GC	*	-0.926	3.892		0.261	0.500	*	-1.187	3.542	+	nucleus
Mcu	GC	*	-0.602	2.260	*	1.404	5.791	*	-2.006	5.472	+	mito MEM
Mfn2	GC	*	0.408	3.154	*	1.074	6.352	*	-0.666	3.816	+	mito MEM
Mgst3	GC	*	0.868	5.058	*	1.239	5.505		-0.371	2.450	+	ER MEM
Micu1	GC		-0.137	0.578	*	1.387	5.490	*	-1.524	5.483	+	mito MEM
Micu3	GC		-0.216	1.106	*	1.406	5.780	*	-1.622	7.067		mito
Mtch2	GC		-0.001	0.002	*	1.067	5.702	*	-1.068	5.409	+	mito MEM
Mthfd1l	GC		0.130	1.047	*	1.547	8.227	*	-1.417	9.765	+	mito
Nipsnap1	GC	*	0.790	3.620	*	1.168	5.249		-0.378	1.936	+	cytoplasm
Pck2	GC	*	-0.443	2.408	*	1.189	6.242	*	-1.632	6.394	+	
Pdk2	GC	*	-0.501	2.667	*	0.576	3.077	*	-1.077	4.591	+	mito
Pdk3	GC	*	0.973	5.305	*	1.219	5.491		-0.246	1.301	+	mito
Pdp1	GC	*	0.712	3.522	*	1.110	5.023		-0.398	1.807	+	mito
Pdpr	GC	*	0.442	3.035	*	1.057	5.814	*	-0.615	2.957	+	mito
Pgam5	GC		0.108	0.431	*	1.562	5.866	*	-1.454	7.142	+	mito MEM
Pgs1	GC		0.315	1.664	*	1.174	6.136	*	-0.859	4.518	+	mito
Polg2	GC		-0.802	1.628		0.423	1.637	*	-1.225	2.705	+	mito
Pycr2	GC		0.196	0.536	*	1.153	3.405	*	-0.957	4.010	+	cytoplasm
Rcc1	GC		0.257	0.471	*	1.249	2.183		-0.993	1.947		nucleus

Gene name	*Candidate*	*PC vs A*			*GC vs A*			*PC vs GC*			*MitoCarta*	*Localization, predicted*
		*****	**FC**	***-log$_{10}$(P)***	*****	**FC**	***-log$_{10}$(P)***	*****	**FC**	***-log$_{10}$(P)***		
Sdr39u1	GC	*	0.627	4.853	*	1.223	4.755		-0.596	2.410	+	mito
Sfxn3	GC	*	0.614	2.940	*	1.086	4.949		-0.472	2.016	+	mito MEM
Slc25a12	GC	*	0.634	3.492	*	1.191	4.978	*	-0.558	2.542	+	mito MEM
Tmem65	GC	*	0.666	2.324	*	1.170	4.522		-0.504	1.336	+	mito MEM
Tomm70a	GC	*	0.452	2.389	*	1.258	5.623	*	-0.806	4.174	+	mito MEM
Trabd	GC		-0.171	0.416	*	0.940	3.461	*	-1.110	3.494		plasma MEM
Trmu	GC		-0.589	1.712	*	0.543	2.697	*	-1.132	3.160	+	mito
Yars2	GC	*	0.593	3.151	*	1.087	4.590	*	-0.494	2.688	+	mito
Adck3	PC	*	1.002	3.522	*	0.681	2.340		0.320	0.634	+	mito
Bcat1	PC	*	1.144	3.938	*	0.670	3.300		0.474	1.608	+	cytoplasm
Coq3	PC	*	1.401	4.432	*	0.953	3.359		0.448	1.162	+	mito
Coq6	PC	*	1.103	4.868	*	0.919	4.728		0.184	0.490	+	mito
Cyp27a1	PC	*	1.285	5.482		-0.308	0.713	*	1.593	4.222	+	mito
Dhx30	PC	*	1.031	2.612		0.682	1.542		0.349	1.024	+	nucleus
Elmod1	PC	*	1.545	5.425	*	0.697	4.615	*	0.848	2.876		mito
Lyrm9	PC	*	1.312	3.219	*	0.962	2.168		0.350	1.171		mito
Me2	PC	*	1.167	6.415	*	0.995	4.524		0.172	0.693	+	mito
Mrs2	PC	*	1.245	6.098	*	0.692	2.368		0.554	1.849	+	plasma MEM
Nt5m	PC	*	1.246	5.165	*	0.428	2.731	*	0.817	2.871	+	mito
Ociad2	PC	*	2.413	6.615		0.588	1.746	*	1.825	4.527		secreted
Pam16	PC	*	1.199	3.151	*	0.590	2.697		0.608	1.428	+	mito
Pptc7	PC	*	1.571	5.560	*	0.984	2.923		0.587	1.671	+	mito
Ptpn4	PC	*	1.098	5.023		0.135	0.498	*	0.963	4.215	+	cytoplasm
Pvalb	PC	*	1.104	2.806		0.401	0.992		0.703	1.421		cytoplasm
Rmdn3	PC	*	2.042	5.868		0.238	0.817	*	1.803	4.172	+	cytoplasm
Tmem70	PC	*	0.946	5.193		-0.062	0.258	*	1.008	5.011	+	mito MEM
Gpd2	GC-A	*	-1.533	7.574		-0.058	0.261	*	-1.475	6.142	+	mito
Maoa	GC-A	*	-2.093	8.254	*	-0.931	4.039	*	-1.162	4.377	+	chloro
Mfn1	GC-A	*	-2.216	8.083	*	-0.967	3.939	*	-1.249	4.798	+	mito MEM
Nlrx1	GC-A	*	-1.429	5.429		-0.306	1.382	*	-1.124	4.479	+	nucleus
Acad8	PC-A		-0.574	2.009	*	-1.740	9.211	*	1.166	3.583	+	
Cryzl1	PC-A		0.357	0.294	*	-1.856	4.766	*	2.213	2.766		mito
Lama1	PC-A		-0.140	0.213	*	-1.764	2.692	*	1.624	3.101		secreted
Tpp1	PC-A		0.041	0.110	*	-1.165	2.582	*	1.207	2.658		secreted
Aldh18a1	Neuro	*	1.098	4.676	*	1.287	5.161		-0.189	0.547	+	cytoplasm
Got2	Neuro	*	1.093	5.321	*	1.109	5.606		-0.017	0.043	+	mito
Ldhd	Neuro	*	2.571	4.208	*	1.633	3.446		0.938	1.431	+	mito
Nt5dc3	Neuro	*	1.483	6.237	*	1.160	4.235		0.323	0.820	+	cytoplasm
Slc25a22	Neuro	*	1.126	4.841	*	1.304	5.725		-0.177	0.796	+	mito MEM

7.3. Immunofluorescence staining of mitochondrial candidates in cerebellum

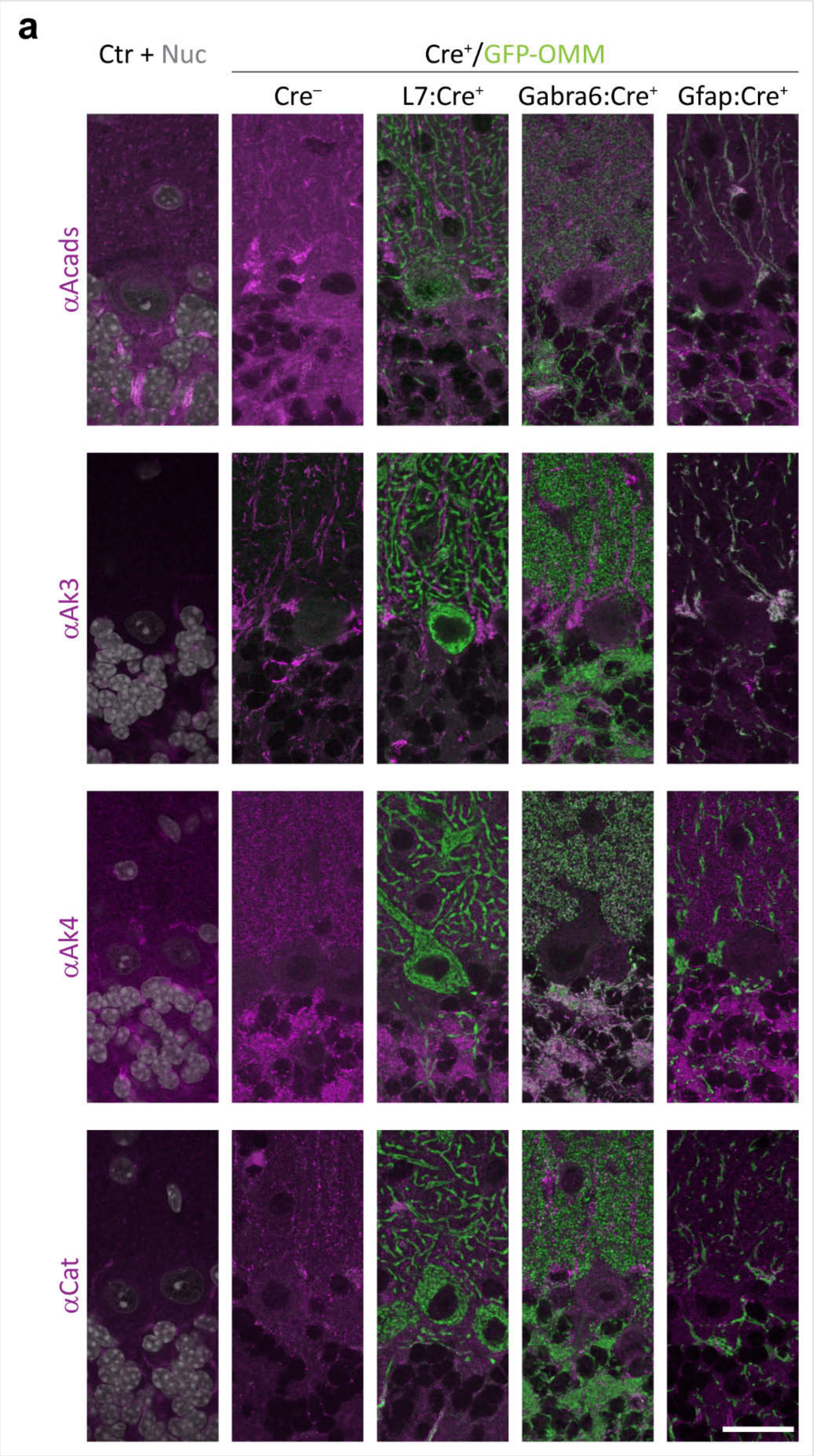
a
Ctr + Nuc
Cre⁺/GFP-OMM
Cre⁻
L7:Cre⁺
Gabra6:Cre⁺
Gfap:Cre⁺
αAcads
αAk3
αAk4
αCat

Figure A1│ Immunofluorescence staining of candidates in mouse cerebellum. Staining in cerebellum from wild type (Cre⁻), L7:Cre⁺/GFP-OMM, Gabra6:Cre⁺/GFP-OMM and Gfap:Cre⁺/GFP-OMM mice. Ctr, control for secondary antibody by omission of primary antibody; Nuc, nuclear counter stain. (**a**) Acads, Ak3 and Ak4, Cat. Scale bar: 25 µm. Modified from Fecher et al. (2019), Supplementary Figure 9.

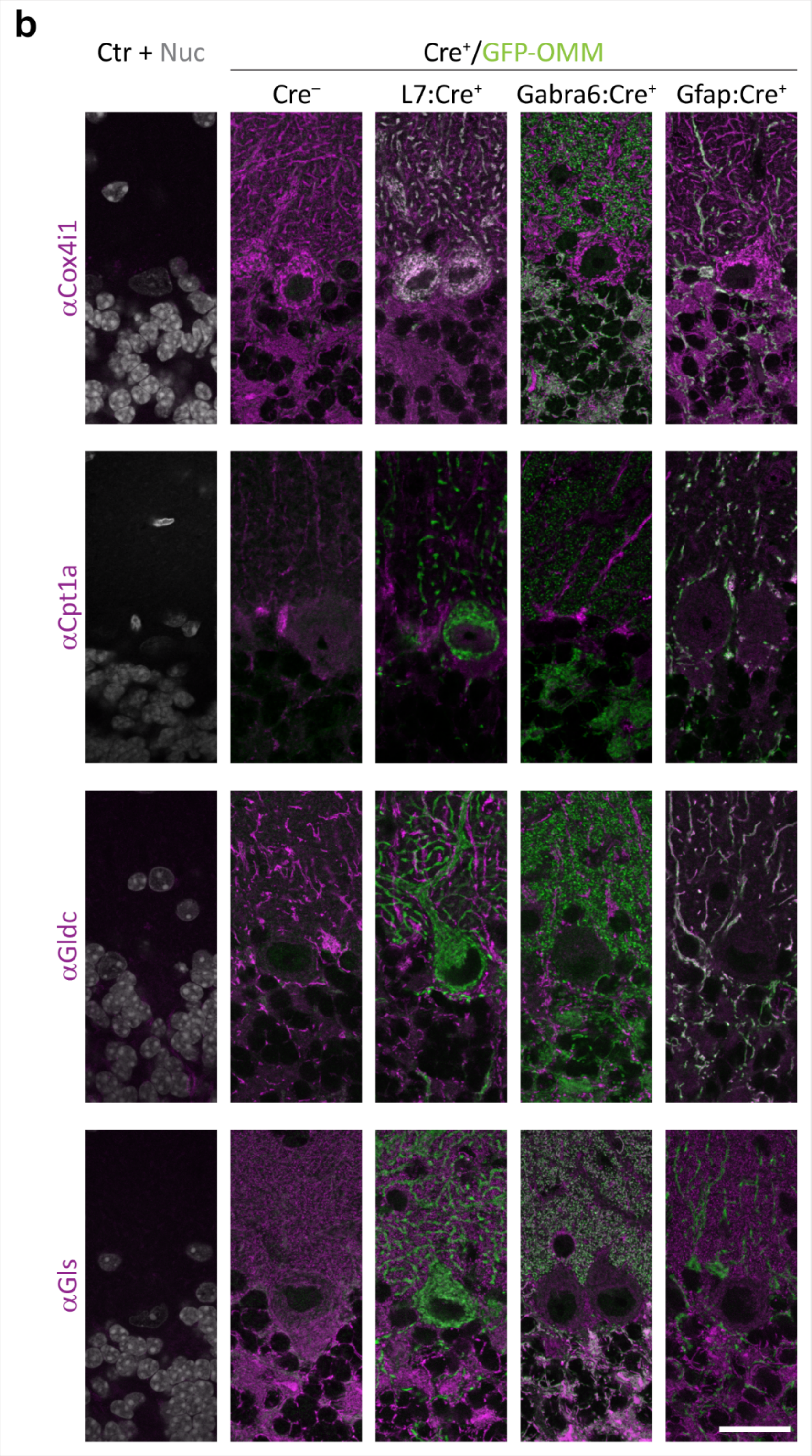
b
Ctr + Nuc
Cre⁺/GFP-OMM
Cre⁻
L7:Cre⁺
Gabra6:Cre⁺
Gfap:Cre⁺
αCox4i1
αCpt1a
αGldc
αGls

Figure A1│ Immunofluorescence staining of candidates in mouse cerebellum (continued). Staining in cerebellum from wild type (Cre⁻), L7:Cre⁺/GFP-OMM, Gabra6:Cre⁺/GFP-OMM and Gfap:Cre⁺/GFP-OMM mice. Ctr, control for secondary antibody by omission of primary antibody; Nuc, nuclear counter stain. (**b**) Cox4i1, Cpt1a, Gldc and Gls. Scale bar: 25 µm. Modified from Fecher et al. (2019), Supplementary Figure 9.

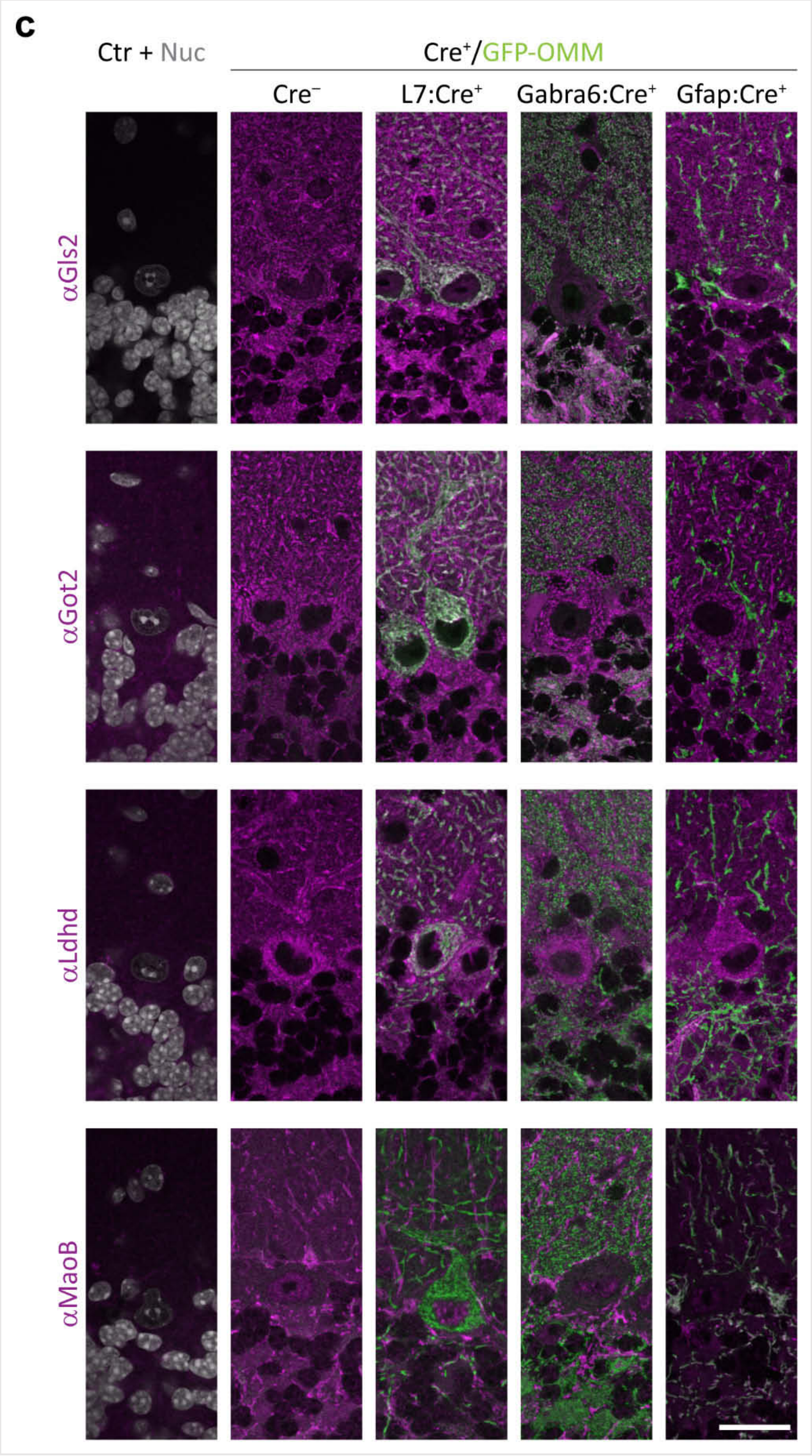
c
Ctr + Nuc
Cre+/GFP-OMM
Cre−
L7:Cre+
Gabra6:Cre+
Gfap:Cre+
αGls2
αGot2
αLdhd
αMaoB

Figure A1│ Immunofluorescence staining of candidates in mouse cerebellum (continued). Staining in cerebellum from wild type (Cre⁻), L7:Cre⁺/GFP-OMM, Gabra6:Cre⁺/GFP-OMM and Gfap:Cre⁺/GFP-OMM mice. Ctr, control for secondary antibody by omission of primary antibody; Nuc, nuclear counter stain. (**c**) Gls2, Got2, Ldhd and MaoB. Scale bar: 25 μm. Modified from Fecher et al. (2019), Supplementary Figure 9.

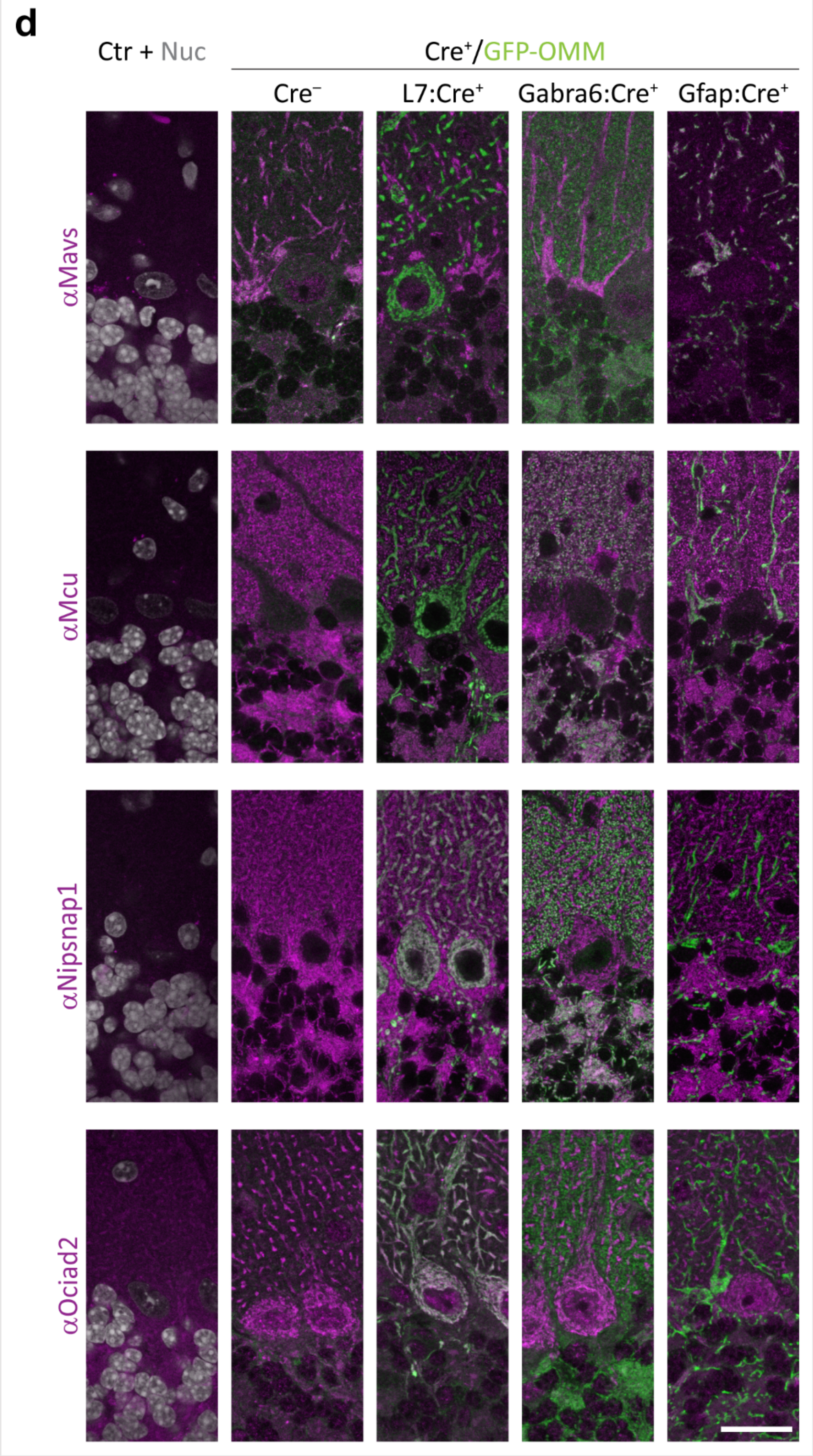
d
Ctr + Nuc
Cre+/GFP-OMM
Cre−
L7:Cre+
Gabra6:Cre+
Gfap:Cre+
αMavs
αMcu
αNipsnap1
αOciad2

Figure A1│ Immunofluorescence staining of candidates in mouse cerebellum (continued). Staining in cerebellum from wild type (Cre⁻), L7:Cre⁺/GFP-OMM, Gabra6:Cre⁺/GFP-OMM and Gfap:Cre⁺/GFP-OMM mice. Ctr, control for secondary antibody by omission of primary antibody; Nuc, nuclear counter stain. (**d**) Mavs, Mcu, Nispnap1 and Ociad2. Scale bar: 25 µm. Modified from Fecher et al. (2019), Supplementary Figure 9.

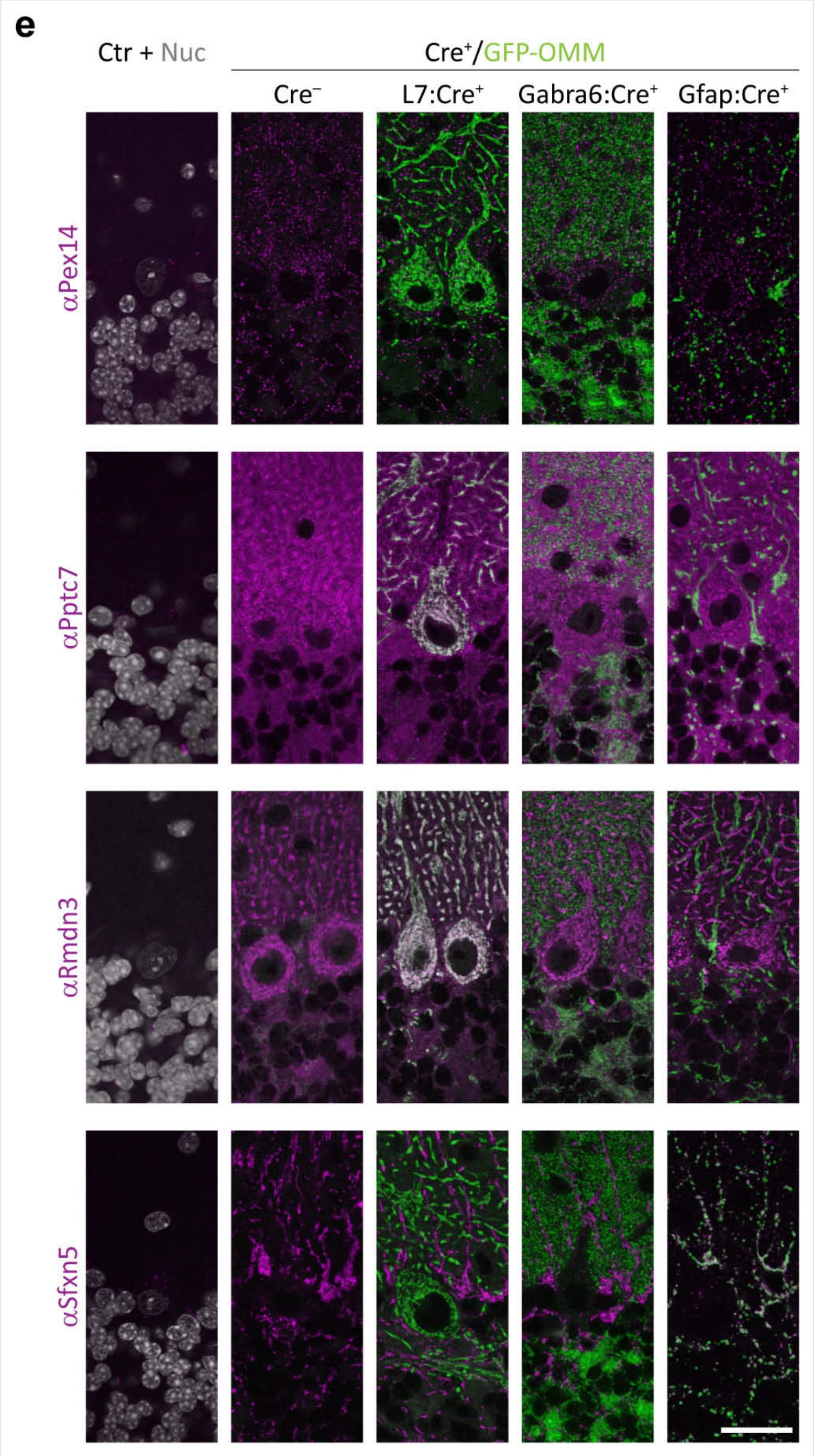
e
Ctr + Nuc
Cre⁺/GFP-OMM
Cre⁻
L7:Cre⁺
Gabra6:Cre⁺
Gfap:Cre⁺
αPex14
αPptc7
αRmdn3
αSfxn5

Figure A1│ Immunofluorescence staining of candidates in mouse cerebellum (continued). Staining in cerebellum from wild type (Cre⁻), L7:Cre⁺/GFP-OMM, Gabra6:Cre⁺/GFP-OMM and Gfap:Cre⁺/GFP-OMM mice. Ctr, control for secondary antibody by omission of primary antibody; Nuc, nuclear counter stain. (**e**) Pex14, Pptc7, Rmdn3 and Sfxn5. Scale bar: 25 µm. Modified from Fecher et al. (2019), Supplementary Figure 9.

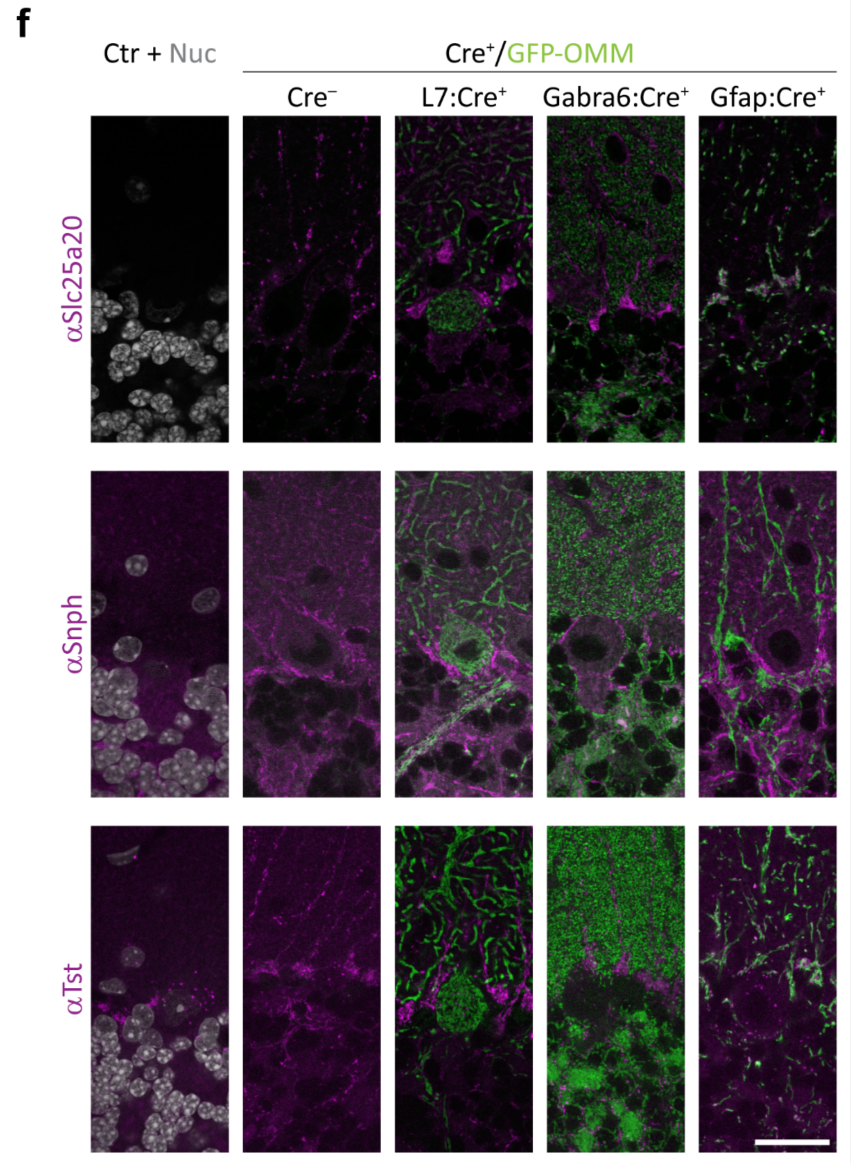
f
Ctr + Nuc
Cre⁺/GFP-OMM
Cre⁻
L7:Cre⁺
Gabra6:Cre⁺
Gfap:Cre⁺
αSlc25a20
αSnph
αTst

Figure A1│ Immunofluorescence staining of candidates in mouse cerebellum (continued). Staining in cerebellum from wild type (Cre$^-$), L7:Cre$^+$/GFP-OMM, Gabra6:Cre$^+$/GFP-OMM and Gfap:Cre$^+$/GFP-OMM mice. Ctr, control for secondary antibody by omission of primary antibody; Nuc, nuclear counter stain. (**f**) Slc25a20, Snph and Tst. Scale bar: 25 µm. Modified from Fecher et al. (2019), Supplementary Figure 9.

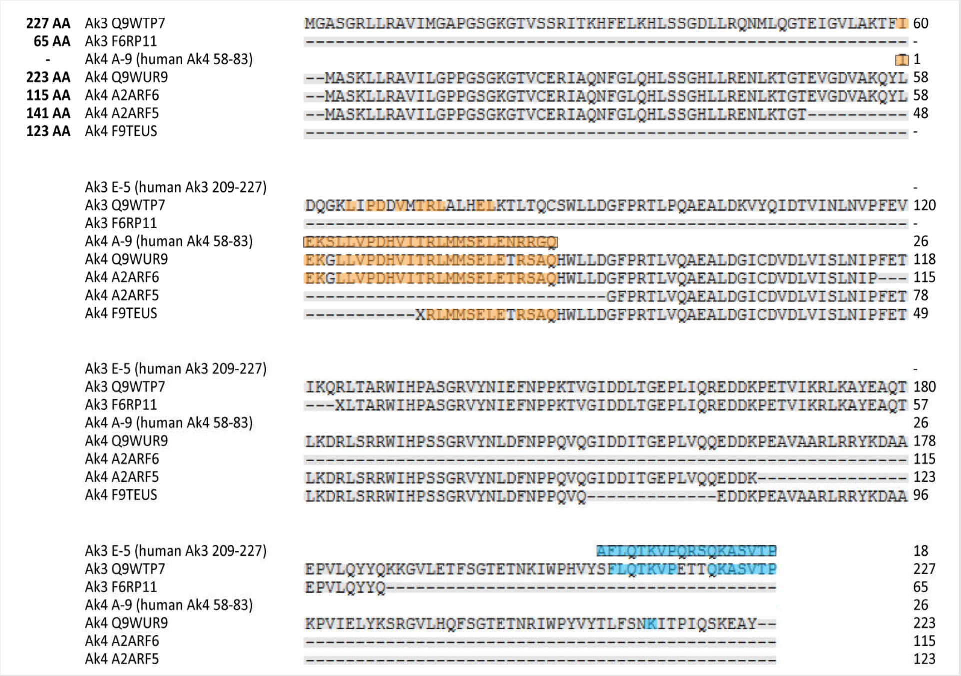

```
227 AA  Ak3 Q9WTP7                   MGASGRLLRAVIMGAPGSGKGTVSSRITKHFELKHLSSGDLLRQNMLQGTEIGVLAKTFI 60
 65 AA  Ak3 F6RP11                   ------------------------------------------------------------ -
   -    Ak4 A-9 (human Ak4 58-83)                                                               I 1
223 AA  Ak4 Q9WUR9                   --MASKLLRAVILGPPGSGKGTVCERIAQNFGLQHLSSGHLLRENLKTGTEVGDVAKQYL 58
115 AA  Ak4 A2ARF6                   --MASKLLRAVILGPPGSGKGTVCERIAQNFGLQHLSSGHLLRENLKTGTEVGDVAKQYL 58
141 AA  Ak4 A2ARF5                   --MASKLLRAVILGPPGSGKGTVCERIAQNFGLQHLSSGHLLRENLKTGT---------- 48
123 AA  Ak4 F9TEUS                   ------------------------------------------------------------ -


        Ak3 E-5 (human Ak3 209-227)                                                               -
        Ak3 Q9WTP7                   DQGKLIPDDVMTRLALHELKTLTQCSWLLDGFPRTLPQAEALDKVYQIDTVINLNVPFEV 120
        Ak3 F6RP11                   ------------------------------------------------------------ -
        Ak4 A-9 (human Ak4 58-83)    EKSLLVPDHVITRLMMSELENRRGQ                                    26
        Ak4 Q9WUR9                   EKGLLVPDHVITRLMMSELETRSAQHWLLDGFPRTLVQAEALDGICDVDLVISLNIPFET 118
        Ak4 A2ARF6                   EKGLLVPDHVITRLMMSELETRSAQHWLLDGFPRTLVQAEALDGICDVDLVISLNIP--- 115
        Ak4 A2ARF5                   ------------------------------GFPRTLVQAEALDGICDVDLVISLNIPFET 78
        Ak4 F9TEUS                   -----------XRLMMSELETRSAQHWLLDGFPRTLVQAEALDGICDVDLVISLNIPFET 49


        Ak3 E-5 (human Ak3 209-227)                                                               -
        Ak3 Q9WTP7                   IKQRLTARWIHPASGRVYNIEFNPPKTVGIDDLTGEPLIQREDDKPETVIKRLKAYEAQT 180
        Ak3 F6RP11                   ---XLTARWIHPASGRVYNIEFNPPKTVGIDDLTGEPLIQREDDKPETVIKRLKAYEAQT 57
        Ak4 A-9 (human Ak4 58-83)                                                                 26
        Ak4 Q9WUR9                   LKDRLSRRWIHPSSGRVYNLDFNPPQVQGIDDITGEPLVQQEDDKPEAVAARLRRYKDAA 178
        Ak4 A2ARF6                   ------------------------------------------------------------ 115
        Ak4 A2ARF5                   LKDRLSRRWIHPSSGRVYNLDFNPPQVQGIDDITGEPLVQQEDDK--------------- 123
        Ak4 F9TEUS                   LKDRLSRRWIHPSSGRVYNLDFNPPQVQ-------------EDDKPEAVAARLRRYKDAA 96


        Ak3 E-5 (human Ak3 209-227)                                AFLQTKVPQRSQKASVTP              18
        Ak3 Q9WTP7                   EPVLQYYQKKGVLETFSGTETNKIWPHVYSFLQTKVPETTQKASVTP              227
        Ak3 F6RP11                   EPVLQYYQ---------------------------------------              65
        Ak4 A-9 (human Ak4 58-83)                                                                 26
        Ak4 Q9WUR9                   KPVIELYKSRGVLHQFSGTETNRIWPYVYTLFSNKITPIQSKEAY--              223
        Ak4 A2ARF6                   -----------------------------------------------              115
        Ak4 A2ARF5                   -----------------------------------------------              123
```

Figure A2| Ak3 and Ak4 antibodies are paralog specific. Alignment of mouse Ak3 and Ak4 isoforms with the human epitopes for αAk3 (AA 209-227, orange) and αAk4 (AA 58-83, blue) antibodies. Conserved amino acids between epitopes and isoforms are color-coded. AA, amino acid.

Due to antibody performance, Elmod1, MaoA, Mfn1, Mfn2, Micu1, Micu3, and Pgam5 could not be validated by immunofluorescence staining.

Table A3. Candidates without validation due to antibody performance.

Candidate	*Epitope*	*#*	*Species*	*Tested conditions*
Elmod1	human ELMOD1, full length	12761-1-AP	Rabbit	Triton X100, methanol, acetone, HIER 1-7
	human ELMOD1, AA 105-135	ab173691	Rabbit	
MaoA	human MaoA, AA 458-527	sc-271123	Mouse IgG_1	
Mfn1	human Mfn1, AA 683-732	ab57602	Rabbit	
Mfn2	human Mfn2, AA 461-528	sc-515647	Mouse IgG_1	
	human Mfn2, AA 38-55	M6319	Rabbit	
Micu1	-	StJ-97447	Mouse IgG_1	
	human Micu1, AA 287-371	HPA037480	Rabbit	
Micu3	human Micu3, AA 238-309	HPA024771	Rabbit	
	human Micu3, AA 410-479	HPA024048	Rabbit	
Pgam5	human PGAM5, AA 61-146	ab126534	Rabbit	

7.4. Overrepresentation analysis of candidate-enriched pathways

ORA was performed with WebGestalt (Liao et al., 2019) and Figure 31b displays the top10 significant GOTerm and KEGG pathways with the highest enrichment ratio.

Table A4. ORA analysis of neuronal candidates.

Gene set	*Name*	*Size*	*Candidates*	*Enrichment*	*FDR*
mmu00130	Ubiquinone and other terpenoid-quinone biosynthesis	11	2	48.9394	0.0385
mmu00220	Arginine biosynthesis	19	3	42.5000	0.0046
mmu00250	Alanine, aspartate and glutamate metabolism	37	3	21.8243	0.0212
mmu00330	Arginine and proline metabolism	50	4	21.5333	0.0046
GO:0043648	Dicarboxylic acid metabolic process	99	8	17.5556	0.0000
mmu01230	Biosynthesis of amino acids	78	4	13.8034	0.0146
GO:0006090	Pyruvate metabolic process	102	6	12.7794	0.0010
GO:0070585	Protein localization to mitochondrion	89	5	12.2051	0.0049
GO:0006839	Mitochondrial transport	165	9	11.8500	0.0000
GO:0006520	Cellular amino acid metabolic process	260	12	10.0269	0.0000
GO:0016053	Organic acid biosynthetic process	349	11	6.8474	0.0001
GO:0051186	Cofactor metabolic process	488	15	6.6778	0.0000
GO:0044282	Small molecule catabolic process	328	9	5.9611	0.0018
GO:0044262	Cellular carbohydrate metabolic process	285	7	5.3360	0.0239
GO:0072521	Purine-containing compound metabolic process	481	11	4.9683	0.0012
GO:0019693	Ribose phosphate metabolic process	443	9	4.4137	0.0147
GO:0007005	Mitochondrion organization	433	8	4.0139	0.0498
GO:0044270	Cellular nitrogen compound catabolic process	434	8	4.0046	0.0498
GO:0046700	Heterocycle catabolic process	438	8	3.9680	0.0498
mmu01100	Metabolic pathways	1351	18	3.5862	0.0000

Table A5. ORA analysis of astrocytic candidates.

Gene set	*Name*	*Size*	*Candidates*	*Enrichment*	*FDR*
mmu00071	Fatty acid degradation	50	20	38.9157	0.0000
mmu00280	Valine, leucine and isoleucine degradation	56	21	36.4834	0.0000
mmu00640	Propanoate metabolism	31	11	34.5220	0.0000
mmu04146	Peroxisome	84	26	30.1133	0.0000
GO:0007031	Peroxisome organization	33	7	29.7912	0.0000
mmu01212	Fatty acid metabolism	52	14	26.1932	0.0000
mmu00410	β-Alanine metabolism	32	8	24.3223	0.0000
mmu00650	Butanoate metabolism	27	6	21.6198	0.0000
mmu00920	Sulfur metabolism	9	2	21.6198	0.0426

Gene set	*Name*	*Size*	*Candidates*	*Enrichment*	*FDR*
GO:0042398	Cellular modified amino acid biosynthetic process	39	6	21.6068	0.0000
mmu00062	Fatty acid elongation	32	7	21.2820	0.0000
GO:0018904	Ether metabolic process	20	3	21.0667	0.0148
GO:0044282	Small molecule catabolic process	328	47	20.1247	0.0000
GO:0033865	Nucleoside bisphosphate metabolic process	106	15	19.8742	0.0000
mmu00260	Glycine, serine and threonine metabolism	40	8	19.4578	0.0000
mmu00380	Tryptophan metabolism	46	9	19.0348	0.0000
mmu00630	Glyoxylate and dicarboxylate metabolism	31	6	18.8302	0.0000
mmu01040	Biosynthesis of unsaturated fatty acids	32	6	18.2417	0.0000
mmu00120	Primary bile acid biosynthesis	16	3	18.2417	0.0081
GO:0030258	Lipid modification	224	29	18.1825	0.0000
mmu00330	Arginine and proline metabolism	50	9	17.5120	0.0000
GO:0006631	Fatty acid metabolic process	372	43	16.2342	0.0000
mmu00340	Histidine metabolism	24	4	16.2149	0.0016
GO:0043648	Dicarboxylic acid metabolic process	99	11	15.6049	0.0000
mmu01210	2-Oxocarboxylic acid metabolism	19	3	15.3614	0.0121
GO:0016042	Lipid catabolic process	293	30	14.3800	0.0000
mmu00310	Lysine degradation	59	8	13.1918	0.0000
mmu00250	Alanine, aspartate and glutamate metabolism	37	5	13.1472	0.0006
mmu01200	Carbon metabolism	120	16	12.9719	0.0000
mmu00592	α-Linolenic acid metabolism	25	3	11.6747	0.0263
mmu00053	Ascorbate and aldarate metabolism	27	3	10.8099	0.0316
GO:0006520	Cellular amino acid metabolic process	260	20	10.8034	0.0000
mmu00620	Pyruvate metabolism	38	4	10.2410	0.0083
GO:0006575	Cellular modified amino acid metabolic process	161	11	9.5956	0.0000
GO:0097164	Ammonium ion metabolic process	167	11	9.2508	0.0000
GO:0006790	Sulfur compound metabolic process	275	18	9.1927	0.0000
mmu03320	PPAR signaling pathway	85	8	9.1566	0.0000
GO:0072527	Pyrimidine-containing compound metabolic process	68	4	8.2614	0.0389
GO:0014823	Response to activity	70	4	8.0254	0.0419
mmu00561	Glycerolipid metabolism	61	5	7.9745	0.0062
GO:0006839	Mitochondrial transport	165	9	7.6606	0.0001
GO:0051186	Cofactor metabolic process	488	26	7.4827	0.0000
mmu00010	Glycolysis / Gluconeogenesis	67	5	7.2604	0.0083
GO:0051262	Protein tetramerization	149	7	6.5981	0.0039
GO:0098754	Detoxification	108	5	6.5021	0.0311
GO:0019693	Ribose phosphate metabolic process	443	19	6.0236	0.0000
GO:0016999	Antibiotic metabolic process	140	6	6.0190	0.0180
GO:0006638	Neutral lipid metabolic process	121	5	5.8035	0.0435
GO:0042737	Drug catabolic process	151	6	5.5806	0.0246
GO:0072521	Purine-containing compound metabolic process	481	19	5.5477	0.0000
GO:0016053	Organic acid biosynthetic process	349	13	5.2315	0.0001
GO:0042180	Cellular ketone metabolic process	182	6	4.6300	0.0467

Gene set	*Name*	*Size*	*Candidates*	*Enrichment*	*FDR*
GO:0006091	Generation of precursor metabolites and energy	389	12	4.3325	0.0009
mmu01100	Metabolic pathways	1351	57	4.1047	0.0000
GO:0008202	Steroid metabolic process	276	8	4.0709	0.0255
GO:0015849	Organic acid transport	310	8	3.6244	0.0432
GO:0051260	Protein homooligomerization	358	9	3.5307	0.0311
GO:0001505	Regulation of neurotransmitter levels	361	9	3.5014	0.0312
GO:1901615	Organic hydroxy compound metabolic process	457	11	3.3805	0.0154
GO:0090407	Organophosphate biosynthetic process	484	11	3.1919	0.0228

7.5. Patient information related to human specimens

Human tissue samples were selected by Doron Merkler (University of Geneva and Geneva University Hospital, Switzerland) and immunofluorescence staining performed by Ingrid Wagner (University of Geneva, Switzerland) with assistance from me regarding mitochondrial markers (Chapter 3.2.14.2).

Table A6. Information on human tissue samples used in this study. Modified from Fecher et al. (2019), Supplementary Table 3.

Case #	*Age (years)*	*Sex*	*Histological specimen*	*Tissue*
1	56	m	Spinal cord without lesion	Spinal cord
2	52	m	Spinal cord without lesion	Spinal cord
4	77	f	Spinal cord with ALS pathology	Spinal cord
6	66	m	Spinal cord with ALS pathology	Spinal cord
9	52	m	Normal temporal lobe (hippocampus)	Cortex
10	67	m	Normal temporal lobe (hippocampus)	Cortex
11	58	m	Normal temporal lobe (hippocampus)	Cortex
14	88	f	Temporal lobe with AD type degenerative encephalopathy	Cortex
15	91	f	Temporal lobe with AD type degenerative encephalopathy	Cortex
16	82	f	Temporal lobe with AD type degenerative encephalopathy	Cortex

Table A7. Information on handling of human tissue samples according to BRISQ. Modified from Fecher et al. (2019), Supplementary Table 3.

Criterion	*AD*	*ALS*
Biospecimen type	Solid tissue	
Anatomical site	Brain	Spinal cord
Disease status of patients	Non-neurological diseased tissue; Alzheimer's disease	Non-neurological disease (control); amyotrophic lateral sclerosis
Clinical characteristics	Dementia	Tetraparesis
State of patient	Postmortem	
Clinical diagnosis	Non-neurological diseased tissue; Alzheimer's disease	Normal tissue; amyotrophic lateral sclerosis type degeneration of motor neurons
Pathology	AD type degenerative encephalopathy	ALS type degeneration of motor neurons
Collection mechanism	Autopsy	
Type of stabilization	4°C	
Type of preservation	10% neutral-buffered formalin fixative	
Storage	20-25°C; duration unknown	
Shipping temperature	20-25°C	
Composition assessment and selection	Control: no microscopic alterations; AD: pathological neurotic plaques and neurofibrillary degeneration	Control: no microscopic alterations; ALS: motor neuron loss with TDP43 inclusions

7.6. Uncropped western blots used in figures of this study

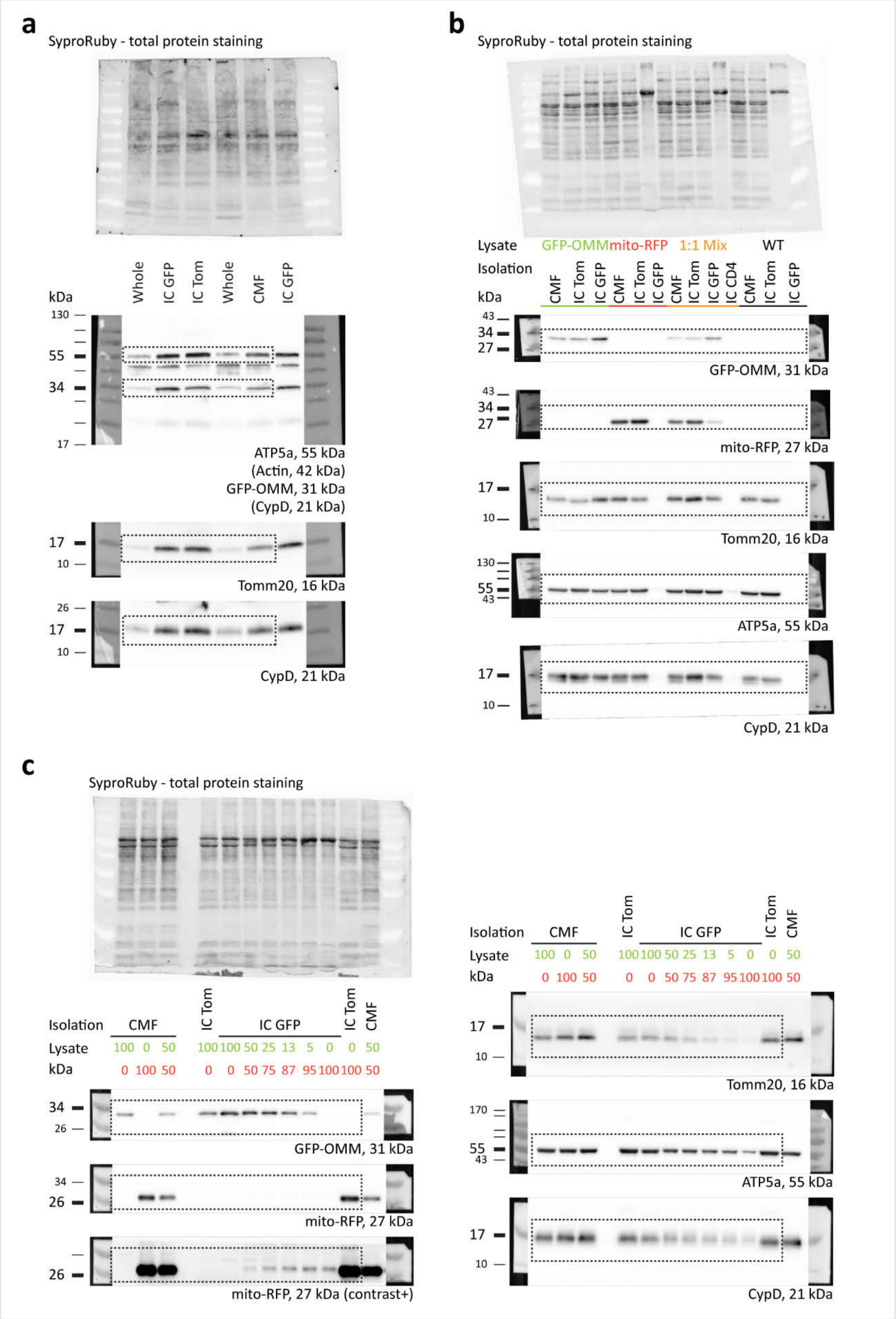
a
SyproRuby - total protein staining
kDa
Whole
IC GFP
IC Tom
Whole
CMF
IC GFP
130
55
34
17
ATP5a, 55 kDa
(Actin, 42 kDa)
GFP-OMM, 31 kDa
(CypD, 21 kDa)
17
10
Tomm20, 16 kDa
26
17
10
CypD, 21 kDa
b
SyproRuby - total protein staining
Lysate
GFP-OMM
mito-RFP
1:1 Mix
WT
Isolation
CMF
IC Tom
IC GFP
CMF
IC Tom
IC GFP
CMF
IC Tom
IC GFP
IC CD4
CMF
IC Tom
IC GFP
kDa
43
34
27
GFP-OMM, 31 kDa
43
34
27
mito-RFP, 27 kDa
17
10
Tomm20, 16 kDa
130
55
43
ATP5a, 55 kDa
17
10
CypD, 21 kDa
c
SyproRuby - total protein staining
Isolation
CMF
IC Tom
IC GFP
IC Tom
CMF
Lysate
100 0 50
100 100 50 25 13 5 0
0 50
kDa
0 100 50
0 0 50 75 87 95 100
100 50
34
26
GFP-OMM, 31 kDa
34
26
mito-RFP, 27 kDa
26
mito-RFP, 27 kDa (contrast+)
Isolation
CMF
IC Tom
IC GFP
IC Tom
CMF
Lysate
100 0 50
100 100 50 25 13 5 0
0 50
kDa
0 100 50
0 0 50 75 87 95 100
100 50
17
10
Tomm20, 16 kDa
170
55
43
ATP5a, 55 kDa
17
10
CypD, 21 kDa

Figure A3| Uncropped western blots related to (**a**) Figure 14c, (**b**) Figure 16c and (**c**) Figure 17b. Modified from Fecher et al. (2019), Supplementary Figure 18.

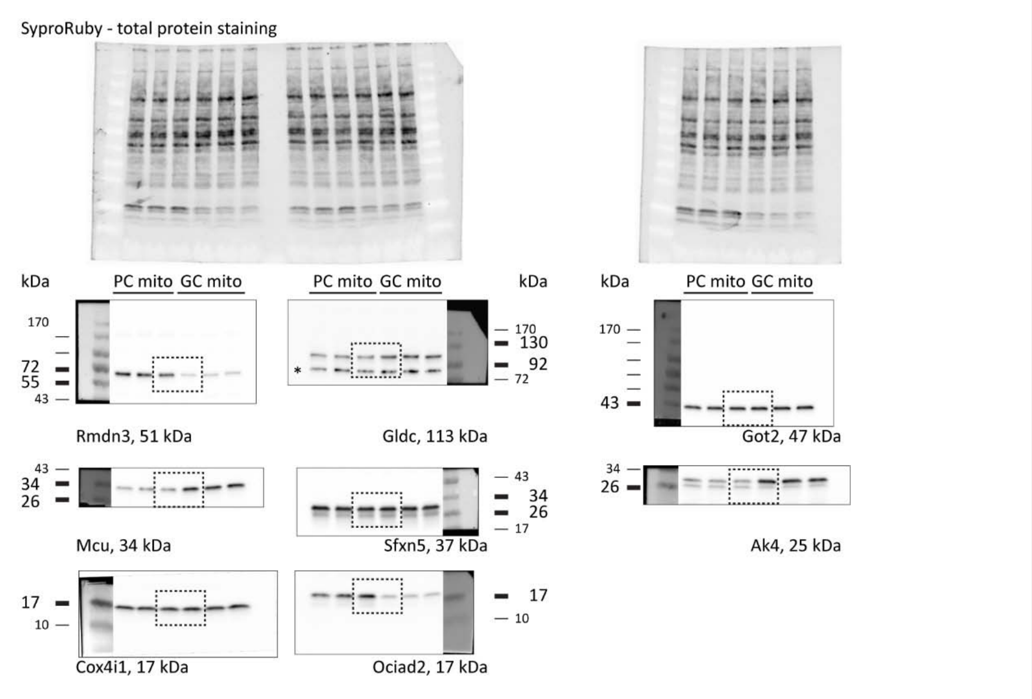
SyproRuby - total protein staining
kDa
PC mito GC mito
170
72
55
43
Rmdn3, 51 kDa
PC mito GC mito
kDa
*
170
130
92
72
Gldc, 113 kDa
kDa
PC mito GC mito
170
43
Got2, 47 kDa
43
34
26
Mcu, 34 kDa
43
34
26
17
Sfxn5, 37 kDa
34
26
Ak4, 25 kDa
17
10
Cox4i1, 17 kDa
17
10
Ociad2, 17 kDa

Figure A4│ Uncropped western blots related to Figure 28a. Modified from Fecher et al. (2019), Supplementary Figure 10.

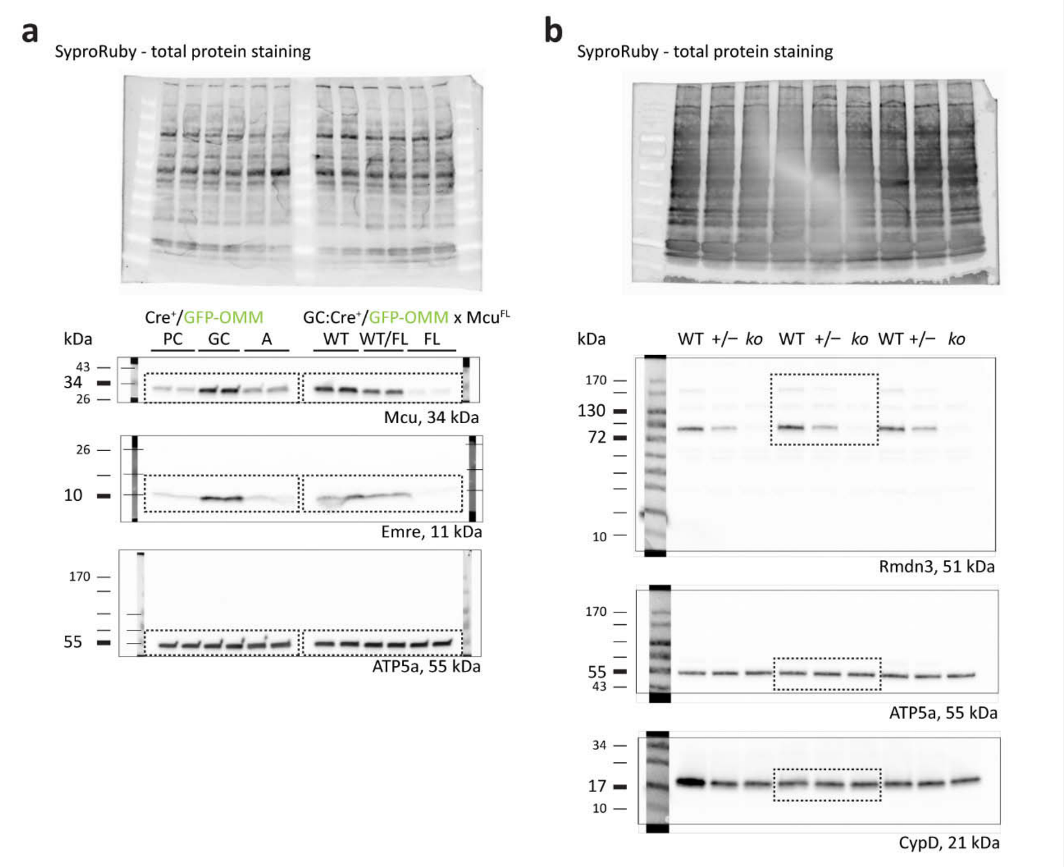
a
SyproRuby - total protein staining
Cre⁺/GFP-OMM
GC:Cre⁺/GFP-OMM x Mcu^FL
kDa
PC GC A
WT WT/FL FL
43
34
26
Mcu, 34 kDa
26
10
Emre, 11 kDa
170
55
ATP5a, 55 kDa
b
SyproRuby - total protein staining
kDa
WT +/– ko WT +/– ko WT +/– ko
170
130
72
10
Rmdn3, 51 kDa
170
55
43
ATP5a, 55 kDa
34
17
10
CypD, 21 kDa

Figure A5│ Uncropped western blots related to (**a**) Figure 37b and 38b, and (**b**) Figure 40b. Modified from Fecher et al. (2019), Figure 6 and Figure 7.

7.7. Comprehensive statistical information on experiments of this study

Table A8. Statistical information. Modified from Fecher et al. (2019), Supplementary Table 4.

Figure	*Exp. #*	*Conditions*	*Testing*
1a	2	Electron microscopy	-
1b	-	Schema	-
2	-	Schemata	-
3a	-	Pagliarini et al. (2008)	Figure 1
3b	-	Pagliarini et al. (2008)	Figure 4c
3c	-	Pagliarini et al. (2008)	Figure 4d
4	-	Schemata	-
5a	-	Schema	-
5b	-	Plasmid map	-
5c	3	Expression in cells	-
5d	-	Plasmid map	-
6	-	Schemata	-
7	-	Schemata	-
8	-	See Chapter 3.2.12	-
9	-	Schemata	-
10a	1	Tissue sections after treatment	-
10b	2	Immunofluorescence staining	-
11b	≥5	Expression pattern	-
11c	≥5	Expression pattern	-
11d	≥3	Immunofluorescence staining	-
11e	2	Expansion microcopy	-
12a	10	Mitochondrial transport: Anterograde: Cre^{-} (29) *vs* Cre^{+} (30); Retrograde: Cre^{-} (29) *vs* Cre^{+} (30)	Two-tailed, unpaired Welch's test: t(54.14)=0.2044, *P*=0.8388; t(53.03)=1.288, *P*=0.2034
12b	10	Mitochondrial shape: Length: Cre^{-} (171) *vs* Cre^{+} (222); Width: Cre^{-} (170) *vs* Cre^{+} (222)	Two-tailed, unpaired Welch's test: t(353.9)=0.5751, *P*=0.5658; t(353.9)=0.5751, *P*=0.5658
12c	≥3	Immunofluorescence staining	-
12d	8	NMJ size: Cre^{-} (88) *vs* Cre^{+} (83); AChR density: Cre^{-} (56) *vs* Cre^{+} (54);	Two-tailed, unpaired Welch's test: t(168.9)=0.9931, *P*=0.3221; t(98.37)=0.845, *P*=0.4002

Figure	*Exp. #*	*Conditions*		*Testing*
13a	-	Schema		-
13b	3	Complex I		Two-tailed, unpaired Welch's test:
			CE	t(7.449)=0.3236, *P*=0.7551;
			RCR	t(6.403)=0.1959, *P*=0.8507;
			SRC	t(6.348)=0.5323, *P*=0.6126
13c	3	Complex II	CE	t(4.336)=0.5852, *P*=0.5875;
			RCR	t(6.431)=0.4233, *P*=0.6859;
			SRC	t(5.644)=0.03813, *P*=0.9709

14a	-	Schema	-
14b	2	Electron microscopy	-
14c	1	Western blot	-

15a	-	Schema		-
15b	≥3	Complex I		One-way ANOVA, Tukey's post hoc:
			CE	F(2, 12)=0.0836, *P*=0.9203;
			RCR	F(2, 12)=0.5447, *P*=0.5937;
			SRC	F(2,15)=0.62, *P*=0.5512
		Complex II	CE	F(2, 13)=0.4186, *P*=0.6665;
			RCR	F(2, 13)=0.9171, *P*=0.4241;
			SRC	F(2, 15)=0.3878, *P*=0.6851

16a	-	Schema	-
16b	≥5	Confocal images	-
	5	Flow cytometry data	-
16c	1	Representative western blot	-
16d	5	Western blot quantification:	One-tailed, ratio-paired *t*-test:
		GFP-OMM: IC Tom (5) *vs* IC GFP (5);	t(4)=11.03, *P*=0.0002;
		mito-RFP: IC Tom (5) *vs* IC GFP (5)	t(4)=2.411, *P*=0.0368

17a	-	Schema	-
17b	4	Representative western blot	-
17c	4	Western blot quantification:	One-way Friedman test, Dunn's post hoc:
		GFP-OMM: IC GFP 100-50-25-13-5;	F(4)=8.2, *P*=0.0720;
		IC GFP 100 *vs* 50	*P*>0.9999;
		IC GFP 100 *vs* 25	*P*>0.9999;
		IC GFP 100 *vs* 13	*P*>0.9999;
		IC GFP 100 *vs* 5	*P*>0.1014;
		mito-RFP: IC GFP 100-50-25-13-5;	F(4)=7.158, *P*=0.1211;
		IC GFP 100 *vs* 50	*P*=0.2946;
		IC GFP 100 *vs* 25	*P*=0.2946;
		IC GFP 100 *vs* 13	*P*=0.2946;
		IC GFP 100 *vs* 5	*P*=0.0556

Figure	*Exp. #*	*Conditions*	*Testing*
18a	≥5	Confocal images	-
	≥4	Flow cytometry data	-
18b	5	Western blot quantification:	One-tailed, ratio-paired *t*-test:
		GFP-OMM: IC Tom (5) *vs* IC GFP (5);	t(4)=10.33, *P*=0.0002;
		mito-RFP: IC Tom (5) *vs* IC GFP (5)	t(4)=1.867, *P*=0.0677
19a-c	≥5	Expression pattern;	-
	≥3	Immunofluorescence staining	-
20-24	-	See Chapter 3.2.12.4	
25a	-	See Chapter 3.2.12.4	
25b	≥3	Immunofluorescence staining	-
26a	2	Immunofluorescence staining	-
26b	-	Protein sequence alignment	
27a	-	See Chapter 3.2.12.4	
27b	≥3	Immunofluorescence staining	-
28a	3	Representative western blot	-
28b	3	Western blot quantification	-
28c	-	See Chapter 3.2.12.4	
29a	≥3	Immunofluorescence staining	-
29b	2	Expression pattern	-
29c	2	Immunofluorescence staining	-
29d	2	Immunofluorescence staining	-
30a	-	See Chapter 3.2.12.4	
30b	≥3	Immunofluorescence staining	-
31	-	See Chapter 3.2.12.4	
32	-	See Chapter 3.2.12.4	
33a	≥3	Immunofluorescence staining	-
33b	≥3	Immunofluorescence staining	-
34	-	See Chapter 3.2.12.4	
35a	≥3	Immunofluorescence staining	-
35b	1	Immunofluorescence staining	-

Figure	*Exp. #*	*Conditions*		*Testing*
36a	-	Schema		-
36b	12	Beta-oxidation		One-tailed, unpaired Welch's test:
			CE	t(11.48)=2.092, *P*=0.0297;
			RCR	t(16.83)=5.028, *P*<0.0001;
			SRC	t(15.86)=5.228, *P*<0.0001
36c	9	Complex I		One-tailed, unpaired Welch's test:
			CE	t(6.352)=0.8558, *P*=0.2116;
			RCR	t(8.527)=0.8953, *P*=0.1976;
			SRC	t(10.87)=1.382, *P*=0.0973
36d	9	Complex II		One-tailed, unpaired Welch's test:
			CE	t(11.21)=0.1861, *P*=0.4279;
			RCR	t(7.615)=0.6322, *P*=0.2729;
			SRC	t(9.102)=1.072, *P*=0.1556

37a	≥3	Immunofluorescence staining	-
37b	4	Representative western blot;	-
		Western blot quantification:	One-way Friedman test, Dunn's post hoc:
		PC *vs* GC *vs* A;	F(3)=10.0, *P*=0.0008;
		PC mito (5) *vs* GC mito (5)	*P*=0.0047;
		PC mito (5) *vs* A mito (5)	*P*=0.3415;
		GC mito (5) *vs* A mito (5)	*P*=0.3415
37c	8	Representative experiment	-
37d	8	Quantification:	One-way ANOVA, Tukey's post hoc:
		PC *vs* GC *vs* A;	F(2, 16)=8.881, *P*=0.0025;
		PC mito (7) *vs* GC mito (5)	t(16)=5.944, *P*=0.0018;
		PC mito (7) *vs* A mito (7)	t(16)=3.108, *P*=0.1020;
		GC mito (5) *vs* A mito (7)	t(16)=3.106, *P*=0.1023

38a	≥3	Immunofluorescence staining	-
38b	6	Representative western blot;	-
		Western blot quantification:	One-way REML with Geisser-Greenhouse correction, Holm-Sidak's post hoc:
		WT *vs* WT/FL *vs* FL;	F(1.023, 6.14)=382.7, *P*<0.0001;
		WT (4) *vs* WT/FL (6)	t(5)=11.4, *P*<0.0001;
		WT (4) *vs* FL (8)	t(5)=115.0, *P*<0.0001;
		WT/FL (6) *vs* FL (8)	t(7)=13.74, *P*<0.0001
38c	6	Representative experiment	-
38d	6	Quantification:	One-way ANOVA, Tukey's post hoc:
		WT *vs* WT/FL *vs* FL;	F(2, 15)=33.99, *P*<0.0001;
		WT (5) *vs* WT/FL (6)	t(15)=2.073, *P*=0.3344;
		WT (5) *vs* FL (7)	t(15)=10.64, *P*<0.0001;
		WT/FL (6) *vs* FL (7)	t(15)=8.947, *P*<0.0001

Figure	*Exp. #*	*Conditions*	*Testing*
39a	≥3	Immunofluorescence staining	-
39b	2	Electron microscopy	-
39c	1	Quantification (mitochondria): PC (160) *vs* GC (134) *vs* A (120); PC (160) *vs* GC (134) PC (160) *vs* A (120) GC (134) *vs* A (120)	One-way Kruskal-Wallis, Dunn's post hoc: F(3, 414)=243.8, *P*<0.0001; *P*<0.0001; *P*<0.0001; *P*<0.0001
		PC (10) vs GC (74) vs A (16); cells	-
40a	2	Immunofluorescence staining	-

40b	3	Representative western blot;
		Western blot quantification:
		WT (4) *vs* +/− (4) *vs* ko (4)
		WT (4) *vs* +/− (4)
		WT (4) *vs* ko (4)
		+/− (4) *vs* ko (4)
			-
			RM one-way ANOVA, Tukey's post hoc:
			F(2,6)=460.7, *P*<0.0001
			t(6)=25.72, *P*<0.0001;
			t(6)=42.63, *P*<0.0001;
			t(6)=16.91, *P*<0.0001

40c	2	Quantification (PC cells):
		WT (12) *vs* +/− (8) *vs* ko (14);
		WT (12) *vs* +/− (8)
		WT (12) *vs* ko (14)
		+/− (8) *vs* ko (14)
			One-way ANOVA, Tukey's post hoc:
			F(2, 31)=37.45, *P*<0.0001;
			t(31)=5.254, *P*=0.0022;
			t(31)=12.23, *P*<0.0001;
			t(31)=5.444, *P*=0.0016

		WT (207) *vs* +/− (189) *vs* ko (306); PC mitochondria	-
		Quantification (A cells): WT (12) *vs* +/− (10) *vs* ko (11);	One-way ANOVA, Tukey's post hoc: F(2, 30)=2.567, *P*=0.0935;
		WT (135) *vs* +/− (105) *vs* ko (119); A mitochondria	-
41a	≥5	Expression pattern	-
41b	2	Immunofluorescence staining	-
41c	2	Immunofluorescence staining	-
42a	≥5	Expression pattern	-
42b	2	Immunofluorescence staining	-
42c	2	Immunofluorescence staining	-
43a-b	- ≥3 3 1	Immunofluorescence staining: mouse rat human	-
44a	≥3	Immunofluorescence staining	-
44b	3	Immunofluorescence staining	-
44c	≥3	Immunofluorescence staining	-
44d	3	Immunofluorescence staining	-

Figure	*Exp. #*	*Conditions*	*Testing*
45a	2	Immunofluorescence staining	-
45b	2	Immunofluorescence staining	-
45c	2	Immunofluorescence staining	-
46a	1	Immunofluorescence staining	-
46b	1	Immunofluorescence staining	-
47	≥3	Immunofluorescence staining	-
48a	1	Immunofluorescence staining	-
48b	1	Immunofluorescence staining	-
48c	1	Immunofluorescence staining	-
48d	1	Immunofluorescence staining	-
49-51	-	Schemata	-

Index of Figures & Tables

Figure 1 Structural organization of the mitochondrion. ____________ 4

Figure 2 Tricarboxylic acid cycle and electron transport chain. ____________ 6

Figure 3 MitoCarta catalog of 1,098 mitochondrial genes. ____________ 16

Figure 4 Organization of mouse cerebellum. ____________ 25

Figure 5 GFP-OMM fusion protein, its vectors for expression and transfection in cells. ____________ 43

Figure 6 Knockout-first allele of the murine Mcu locus. ____________ 46

Figure 7 Knockout-first allele of the murine Rmdn3 locus. ____________ 46

Figure 8 Flow chart depicting secondary analysis of mass spectrometry data comparing mitochondrial proteomes from Purkinje cells, granule cells and astrocytes. ____________ 56

Figure 9 Gating strategy to quantify cell type-specific mitochondria in Cre^{+}/GFP-OMM mouse lines. ____________ 59

Figure 10 Detection of candidates via heat-induced antigen retrieval. Sagittal cerebellum. ____________ 61

Figure 11 MitoTag mice enable the cell type-specific expression of outer mitochondrial membrane targeted GFP. ____________ 70

Figure 12 Axonal transport, mitochondrial shape and NMJ area are normal in ChAT:Cre^{+}/GFP-OMM mice. ____________ 73

Figure 13 Mitochondrial respiration is normal in GFP-OMM tagged mitochondria from cortex. ____________ 74

Figure 14 Immunocapture enriches mitochondria. ____________ 77

Figure 15 Mitochondrial respiration is unaltered between GFP-OMM tagged and untagged organelles after immunocapture. ____________ 79

Figure 16 Immunocapture enriches GFP-OMM tagged mitochondria and separates them from other mitochondria. ____________ 81

Figure 17 Immunocapture performance persists even for small populations of GFP-OMM tagged mitochondria. ____________ 83

Figure 18 Immunocapture separates directly adjacent mitochondrial populations from one tissue. ____________ 84

Figure 19 Cre-driver lines crossed to MitoTag line to tag mitochondria in Purkinje cells, granule cells and astrocytes. ____________ 85

Figure 20 Proteomic comparison among IC Tom, mitochondria in Pagliarini et al. (2008) and whole tissue in Sharma et al. (2015) to MitoCarta (Calvo et al., 2016). ____________ 87

Figure 21 Proteomic composition of the electron transport chain in cell type-specific mitochondria. ____________ 88

Figure 22 Proteomic composition of core mitochondrial processes in cell type-specific mitochondria. ___________ 89

Figure 23 Comparison of cell type-specific mitochondrial proteomes among Purkinje cells, granule cells and astrocytes. ___________ 90

Figure 24 Cell type-enriched candidates and their predicted localization in cells. ___________ 91

Figure 25 Candidates enriched in Purkinje cells mitochondria. ___________ 93

Figure 26 Ociad2 isoforms are localized to mitochondria in Purkinje cells and granule cells. ___________ 95

Figure 27 Candidates enriched in granule cell mitochondria. ___________ 97

Figure 28 Western blot analysis of mitochondrial proteins found in cell type-specific mitochondria from Purkinje cells and granule cells by mass spectrometry. ___________ 99

Figure 29 Syntaphilin is enriched in cerebellar basket cells and their axons forming the pinceau organization. ___________ 101

Figure 30 Candidates enriched in astrocytic mitochondria. ___________ 103

Figure 31 Pathway analysis of enriched candidates in mitochondria from astrocytes and cerebellar neurons. ___________ 105

Figure 32 Peroxisomal proteins among mitochondrial proteomes from cell type-specific mitochondria. ___________ 106

Figure 33 Peroxisomal Pex14 and catalase mainly localize to peroxisomes. ___________ 107

Figure 34 Proteins involved in beta-oxidation are enriched in astrocytic mitochondria. ___________ 108

Figure 35 Import machinery for long-chain fatty acids is enriched in astrocytic mitochondria. ___________ 109

Figure 36 Astrocytic mitochondria respire better on long-chain fatty acids than neuronal mitochondria. ___________ 111

Figure 37 Mcu is enriched in granule cell mitochondria and enables their Ca^{2+}-uptake capacity. ___________ 114

Figure 38 Ablation of Mcu in granule cells disrupts Ca^{2+}-uptake capacity. ___________ 116

Figure 39 Rmdn3 and ER-mitochondria contact sites are enriched in Purkinje cells. ___________ 118

Figure 40 Rmdn3 mediates ER-mitochondria contact sites in Purkinje cells in vivo. ___________ 120

Figure 41 Cell type-specific mitochondrial markers distinguish neuronal and astrocytic mitochondria in cortex. ___________ 123

Figure 42 Cell type-specific mitochondrial markers distinguish neuronal and astrocytic mitochondria in spinal cord. ___________ 125

Figure 43 Cell type-specific mitochondrial markers distinguish neuronal and astrocytic mitochondria in mouse, rat and human cerebellum. ___________ 126

Figure 44 Cell type-specific mitochondrial markers distinguish neuronal and astrocytic mitochondria in aves and amphibian. ____ 127
Figure 45 Cell type-specific mitochondria in a mouse model of Alzheimer's disease. ____ 130
Figure 46 Cell type-specific mitochondrial markers in human cortex from patients with Alzheimer's disease. ____ 131
Figure 47 Cell type-specific mitochondria in a mouse model of amyotrophic lateral sclerosis. ____ 132
Figure 48 Cell type-specific mitochondrial markers in human spinal cord from patients with amyotrophic lateral sclerosis. ____ 133
Figure 49 Metabolic coupling of astrocytes and neurons. ____ 142
Figure 50 Neural specialization of TCA cycle, adjacent fuel and other pathways. ____ 146
Figure 51 Functional specialization of cerebellar mitochondria. ____ 152
Figure A1 Immunofluorescence staining of candidates in mouse cerebellum. ____ 195
Figure A2 Ak3 and Ak4 antibodies are paralog specific. ____ 201
Figure A3 Uncropped western blots related to (a) Figure 14c, (b) Figure 16c and (c) Figure 17b. ____ 206
Figure A4 Uncropped western blots related to Figure 28a. ____ 207
Figure A5 Uncropped western blots related to (a) Figure 37b and 38b, and (b) Figure 40b. ____ 207

Table 1 Experimental studies defining the mitochondrial proteome. ____ 14
Table 2 Amounts of mitochondria per substrate and tissue origin. ____ 50
Table 3 Substrates and inhibitors used for testing mitochondrial respiration. ____ 50
Table 4 Criteria for cell type enrichment. ____ 57
Table 5 Annotation list for core mitochondrial functions. ____ 58
Table 6 Details for immunofluorescence staining of mitochondrial markers in mouse tissue. ____ 61
Table 7 Details for immunofluorescence staining of mitochondrial markers in human tissue. ____ 63
Table 8 Comparison of isolation protocols for cell type-specific mitochondria from tissue. ____ 139
Table A1 MitoTag expression in tested Cre-driver lines. ____ 188
Table A2 Candidates predicted to be enriched in cerebellar cell type. ____ 190
Table A3 Candidates without validation due to antibody performance. ____ 201
Table A4 ORA analysis of neuronal candidates. ____ 202

Table A5 ORA analysis of astrocytic candidates. 202
Table A6 Information on human tissue samples used in this study. 205
Table A7 Information on handling of human tissue samples according to BRISQ. 205
Table A8 Statistical information. 208

Index of Abbreviations

1C metabolism	one-carbon metabolism
A	Astrocyte
AA	Amino acid
AChR	Acetylcholine receptor
ACP	Acyl carrier protein
Acs	Acyl-CoA synthetase
AD	Alzheimer’s disease
ADP	Adenosine diphosphate
ALS	Amyotrophic lateral sclerosis
ANLS	Astrocyte-neuron lactate shuttle
ANS	Ataxia neuropathy spectrum
APP	Amyloid precursor protein
ASEL	One member of Amphid neurons, single ciliated endings
ATP	Adenosine triphosphate
AUC	Area under the curve
Aβ	Amyloid-beta peptide
Bs	Basket cell
CA1/2	Cornu Ammonis 1/2 of the hippocampus
Ca^{2+}	Calcium ions
CAG	Cytomegalovirus early enhancer element, chicken β-actin promoter, rabbit β-globin splice acceptor
CCCP	Carbonyl cyanide m-chlorophenyl hydrazone
CE	Coupling efficiency
CMF	Crude mitochondrial fraction
CoA	Coenzyme A
CoQ	Coenzyme Q
Cre	Cre recombinase
Ctr	Control
Cyto	Cytosol
DAPI	4’,6-diamidino-2-phenylindole
DHAP	Dihydroxyacetone phosphate
DNA	Deoxyribonucleic acid
E19	Embryonic day 19
ER	Endoplasmic reticulum
ETC	Electron transport chain
FA	Fatty acids
FACSorting	Fluorescence activated cell sorting
FAD^+	Flavin adenine dinucleotide
FASP	Filter-aided sample preparation
FDR	False discovery rate
G3P	Glyceraldehyde-3-phosphate
GABA	γ-aminobutyric acid
GC	Granule cell
GCL	Granule cell layer
GCS	Glycine cleavage system
GFP	Green fluorescent protein
GFP-OMM	GFP localized to the outer mitochondrial membrane
GOTerm	Gene ontology term
GSH	Glutathione
HA	Hemagglutinin
HIER	Heat-induced antigen retrieval

IB	Isolation buffer
iBAQ	Intensity-based absolute quantification
IC	Immunocapture
IC GFP	Immunocapture against GFP-OMM
IC Tom	Immunocapture against Tom22
ICB	Immunocapture buffer
IMM	Inner mitochondrial membrane
IMS	Intermembrane space
kDa	Kilo dalton
KEGG	Kyoto encyclopedia of genes and genomes
LFQ	Label-free quantification
LS-MS/MS	Liquid chromatography–mass spectrometry/mass spectrometry
LYR protein	Protein with leucine-tyrosine-arginine motif
MCHS	Childhood myocerebrohepatopathy spectrum disorders
MEMSA	Myoclonic epilepsy myopathy sensory ataxia
MIA	Mitochondrial intermembrane space assembly
ML	Molecular layer
mRNA	Messenger RNA
mtDNA	Mitochondrial DNA
mtFAS	Mitochondrial fatty acid synthesis
NAD^+	Nicotinamide adenine dinucleotide
NADPH	Nicotinamide adenine dinucleotide phosphate
NMJ	Neuromuscular junction
Nuc	Nuclear counter stain
OCR	Oxygen consumption rate
OMM	Outer mitochondria membrane
ORA	Over-representation analysis
OXA	Insertase/export machinery of the inner membrane
PAM	Presequence translocase-associated motor
PC	Pyruvate carboxylase
PC	Purkinje cell
PCL	Purkinje cell layer
PDH	Pyruvate dehydrogenase
PEO	Progressive external ophthalmoplegia
PEP	Phosphoenolpyruvate
Pex	Peroxisome
PM	Plasma membrane
PPP	Pentose phosphate pathway
RB	Respiration buffer
RCR	Respiratory control ratio
RFP	Red fluorescence protein
RNA	Ribonucleic acid
ROS	Reactive oxygen species
SAM	Sorting and assembly machinery
SANDO	Sensory ataxic neuropathy, dysarthria and ophthalmoparesis
Sdh	Succinate dehydrogenase complex
SNARE	Soluble N-ethylmaleimide-sensitive fusion protein attachment protein receptors
SRC	Spare respiration capacity
Sucl	Succinyl-CoA ligase
TCA	Tricarboxylic acid
TIM22	Carrier translocase of the inner membrane
TIM23	Translocase of the inner membrane
TOM	Translocase of the outer membrane
TSA	Tyramide signal amplification

uaDf5	uaDf5 allele containing a 3.1 kb mtDNA deletion affecting 4 protein-coding and 11 tRNA-coding genes
$\Delta\Psi_m$	Mitochondrial membrane potential

α-Kgdh	α-ketoglutarate dehydrogenase complex

Protein names

Aars2	Mitochondrial alanine-tRNA ligase
Abcb6	Mitochondrial ATP-binding cassette sub-family B member 6
Acadm	Medium-chain specific acyl-CoA dehydrogenase
Acads	Short-chain specific acyl-CoA dehydrogenase
Aco2	Mitochondrial aconitase
Acot7	Acyl-CoA thioesterase 7
Acox1	Peroxisomal acyl-coenzyme A oxidase 1
Acsbg	Acyl-CoA synthetase bubblegum family member 2
Acsl	Long-chain fatty acid-CoA ligase
Acsm5	Acyl-CoA synthetase medium-chain family member 5
Acss1/3	Acyl-CoA synthetase short-chain family member 1/3
Adck1	AarF domain-containing protein kinase 1
Ak3/4	Adenylate kinase 3/4
ANT1/2	Adenine nucleotide translocator 1/2
Asns	Asparagine synthetase
Ass	Argininosuccinate synthase
ATP5a	Mitochondrial ATP synthase subunit alpha
Atp5po	Mitochondrial ATP synthase subunit O
Bcl2	Apoptosis regulator Bcl-2
Calb	Calbindin
Cat	Catalase

ChAT	Choline O-acetyltransferase
CHCHD2	Coiled-coil-helix-coiled-coil-helix domain-containing protein 2
Coq8a/b	Mitochondrial atypical kinase COQ8A/B
Cox4i1	Cytochrome c oxidase subunit 4 isoform 1
Cpt1a/2	Carnitine O-palmitoyltransferase 1/2
CS	Mitochondrial citrate synthase
CypD	Cyclophilin D/F
Dao	D-amino-acid oxidase
Drp1	Dynamin-1-like protein
EAAT2/4	Excitatory amino acid transporter 2/4
Echs1	Mitochondrial enoyl-CoA hydratase
Eci2	Mitochondrial enoyl-CoA delta isomerase 2
Eci2	Mitochondrial enoyl-CoA delta isomerase 2
Emre	Mitochondrial essential MCU regulator
Emx1	Empty spiracles homeobox protein 1
F_0F_1ATPase	Complex V or mitochondrial ATP synthase
Fh	Fumarase
Fis1	Mitochondrial fission 1 protein
FUS	RNA-binding protein FUS/TLS (Fused in Sarcoma/Translocated in Sarcoma)

Gfap	Glial fibrillary acidic protein
Ggc1p	Mitochondrial GTP/GDP carrier
Gldc	Glycine dehydrogenase
Glo1/2	Glyoxalase 1/2
Gls/2	Glutaminase, kidney/liver isoform
Glut1/3	Glucose transporter type 1/3
Got2	Glutamate oxaloacetate transaminase 2
Gpt2	Alanine aminotransferase 2
Gs	Glutamine synthetase
Hk1/2	Hexokinase 1/2
Hsd17b10	3-hydroxyacyl-CoA dehydrogenase type-2
Idh2/3	Mitochondrial isocitrate dehydrogenase
Ldha/b	L-lactate dehydrogenase A/B chain
Ldhd	Mitochondrial D-lactate dehydrogenase
MaoB	Monoamine oxidase type B
MAP2	Microtubule-associated protein 2
Mavs	Mitochondrial antiviral-signaling protein
MCT1-4	Monocarboxylate transporter 1-4
Mcu	Mitochondrial calcium uniporter
McuB	Mitochondrial calcium uniporter regulatory subunit MCUb
McuR1	Mitochondrial calcium uniporter regulator 1
Mdh	Malate dehydrogenase
Me2/3	Malic enzyme 2/3
Mff	Mitochondrial fission factor
Mfn1/2	Mitofusin-1/2
mGluR1β	Metabotropic glutamate receptor 1
MIC60	MICOS complex subunit MIC60
Micu1-3	Mitochondrial calcium uptake protein 1-3
Mim1	Mitochondrial import protein 1
Mos1	*Drosophila mauritiana* transposon Mos1
MPC1/2	Mitochondrial pyruvate carrier 1/2
Mpv17l2	Mitochondrial inner membrane protein like 2
Mut	Mitochondrial methylmalonyl-CoA mutase
NCLX	Mitochondrial sodium/calcium exchanger protein
Ndufs1	Mitochondrial NADH-ubiquinone oxidoreductase 75 kDa subunit
Nipsnap1	4-nitrophenylphosphatase domain and non-neuronal SNAP25-like protein homolog 1
Nme3	Nucleoside diphosphate kinase 3
Nnt	NAD(P) transhydrogenase
Num1	Nuclear migration protein NUM1
Oat	Mitochondrial ornithine aminotransferase
Ociad1/2	Ovarian carcinoma immunoreactive antigen domain–containing protein 1/2
OMP25	Mitochondrial outer membrane protein 25
Opa1	Optic atrophy protein 1 homolog
ORP5/8	Oxysterol-binding protein-related protein 5/8
PCC	Propionyl-CoA carboxylase
Pck1/2	Phosphoenolpyruvate carboxykinase 1/2
Pdk1-4	Mitochondrial [pyruvate dehydrogenase (acetyl-transferring)] kinase isozyme 1-4

Pdp1/2	Mitochondrial [pyruvate dehydrogenase [acetyl-transferring]]-phosphatase 1
Pex11β	Peroxisomal membrane protein 11B
Pex11β	Peroxisomal membrane protein 11B
Pex14	Peroxisomal membrane protein PEX14
Pex34	Peroxisomal membrane protein PEX34
Pfk1	6-phosphofructo-1-kinase
Pfkfb3	6-phosphofructo-2-kinase/fructose-2,6-bisphosphatase 3
PLCβ3/4	1-phosphatidylinositol 4,5-bisphosphate phosphodiesterase beta-3/4
Plin5	Perilipin 5
POLG	DNA polymerase subunit gamma-1
Pptc7	Protein phosphatase PTC7 homolog
PS45	Presenilin 1 G384A mutant
Pvalb, PV	Parvalbumin
Pycr	Mitochondrial pyrroline-5-carboxylate reductase
Rab7	Ras-related protein Rab 7
RanGAP1	Ran GTPase-activating protein 1
Rmdn3	Regulator of microtubule dynamics protein 3;
Rpl10a	60S ribosomal protein L10a
Rpl22	60S ribosomal protein L22
Sfxn3-5	Sideroflexin 3-5
Slc25a18	Glutamate/H(+) symporter 2
Slc25a20	Mitochondrial carnitine/acylcarnitine carrier protein
Slc25a22	Mitochondrial glutamate carrier 1
Slc25a38	Mitochondrial glycine transporter
Slc6a9	Sodium-/chloride-dependent glycine transporter 1
SNAP25	Synaptosomal-associated protein 25
Snph	Syntaphilin
SOD1	Superoxide dismutase [Cu-Zn]
Sucla2	Mitochondrial succinate-CoA ligase [ADP-forming] subunit beta
Suclg1	Mitochondrial succinate--CoA ligase [ADP/GDP-forming] subunit alpha
Suclg2	Mitochondrial succinate-CoA ligase [GDP-forming] subunit beta
TDP-43	TAR DNA-binding protein 43
TFAM	Mitochondrial transcription factor A
Tom22	Mitochondrial import receptor subunit TOM22 homolog
Tomm20	Mitochondrial import receptor subunit TOM20 homolog
VAPB	Vesicle-associated membrane protein-associated protein B/C
VDAC	Voltage-dependent anion-selective channel
Yme1L1	ATP-dependent zinc metalloprotease YME1L1

Publications

Baumann, T., Dunkel, A., Schmid, C., Schmitt, S., Hiltensperger, S.M., Lohr, K., Laketa, V., Donakonda, S., Ahting, U., Lorenz-Depiereux, B. , Heil, J.E., Schredelseker, J., Simeoni, L., **Fecher, C.**, Körber, N., Bauer, T., Hüser, N., Hartmann, D., Lschinger, M., Eyerich, K., Eyerich, S., Anton, M., Streeter, M., Wang, T., Schraven, B., Spiegel, D., Assaad, F., Misgeld, T., Zischka, H., Murray, P.J., Heine, A., Heikenwälder, M., Korn, T., Dawid, C., Hofmann, T., Knolle, P.A., Höchst, B. (2020) Regulatory myeloid cells paralyze T cells through cell-cell transfer of the metabolite methylglyoxal. Nature Immunology 21(5): 555-566.

Fecher, C.#, Trovò, L.#, Müller, A.S., Snaidero, N., Wettmarshausen, J., Heink, S., Ortiz, O., Wagner, I., Kühn, R., Hartmann, J., Karl, R.M., Konnerth, A., Korn, T., Wurst, W., Merkler, D., Lichtenthaler, S.L., Perocchi, F., Misgeld, T. (2019) Cell type-specific profiling of brain mitochondria reveals functional and molecular diversity. Nature Neuroscience 22(10): 1731-1742. (# equal contribution)

Samtleben, S., Jaepel, J., **Fecher, C.**, Andreska, T., Rehberg, M., and Blum, R. (2013). Direct imaging of ER calcium with targeted-esterase induced dye loading (TED). Journal of visualized experiments: JoVE, e50317.

Weber, C., Meiler, S., Döring, Y., Koch, M., Drechsler, M., Megens, R.T., Rowinska, Z., Bidzhekov, K., **Fecher, C.**, Ribechini, E., van Zandvoort, M.A., Binder, C.J., Jelinek, I., Hirstov, M., Boon, L., Jung, S., Korn, T., Lutz, M.B., Förster, I., Zenke, M., Hieronymus, T., Junt, T., Zernecke, A. (2011) CCL17-expressing dendritic cells drive atherosclerosis by restraining regulatory T cell homeostasis in mice. Journal of Clinical Investigation Jul 1;121(7):2898-910.

(NON-PEER-REVIEWED)

Fecher, C.#, Trovò, L.#, Müller, A.S., Snaidero, N., Wettmarshausen, J., Heink, S., Ortiz, O., Wagner, I., Kühn, R., Hartmann, J., Karl, R.M., Konnerth, A., Korn, T., Wurst, W., Merkler, D., Lichtenthaler, S.L., Perocchi, F., Misgeld, T. Profound functional and molecular diversity of mitochondria revealed by cell type-specific profiling in vivo. bioRxiv. doi.org/10.1101/403774 (Preprint posted August 28, 2018).

Engerer, P., **Fecher, C.**, and Misgeld, T. (2016). Super-resolution microscopy writ large. Nature Biotechnology 34, 928-930.

Copyright Information

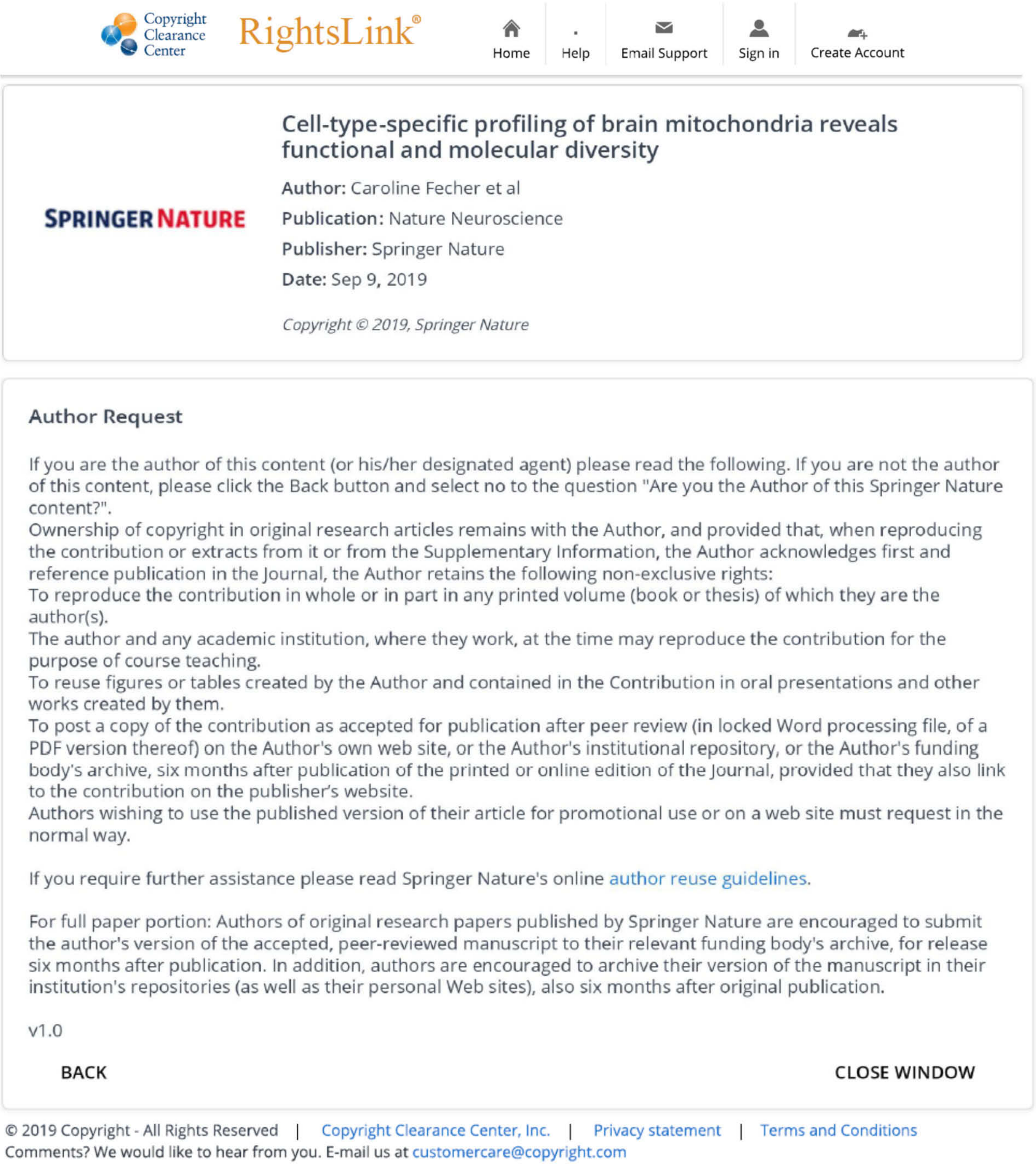

Cell-type-specific profiling of brain mitochondria reveals functional and molecular diversity

Author: Caroline Fecher et al

Publication: Nature Neuroscience

Publisher: Springer Nature

Date: Sep 9, 2019

Copyright © 2019, Springer Nature

Author Request

If you are the author of this content (or his/her designated agent) please read the following. If you are not the author of this content, please click the Back button and select no to the question "Are you the Author of this Springer Nature content?".
Ownership of copyright in original research articles remains with the Author, and provided that, when reproducing the contribution or extracts from it or from the Supplementary Information, the Author acknowledges first and reference publication in the Journal, the Author retains the following non-exclusive rights:
To reproduce the contribution in whole or in part in any printed volume (book or thesis) of which they are the author(s).
The author and any academic institution, where they work, at the time may reproduce the contribution for the purpose of course teaching.
To reuse figures or tables created by the Author and contained in the Contribution in oral presentations and other works created by them.
To post a copy of the contribution as accepted for publication after peer review (in locked Word processing file, of a PDF version thereof) on the Author's own web site, or the Author's institutional repository, or the Author's funding body's archive, six months after publication of the printed or online edition of the Journal, provided that they also link to the contribution on the publisher's website.
Authors wishing to use the published version of their article for promotional use or on a web site must request in the normal way.

If you require further assistance please read Springer Nature's online author reuse guidelines.

For full paper portion: Authors of original research papers published by Springer Nature are encouraged to submit the author's version of the accepted, peer-reviewed manuscript to their relevant funding body's archive, for release six months after publication. In addition, authors are encouraged to archive their version of the manuscript in their institution's repositories (as well as their personal Web sites), also six months after original publication.

v1.0

© 2019 Copyright - All Rights Reserved | Copyright Clearance Center, Inc. | Privacy statement | Terms and Conditions
Comments? We would like to hear from you. E-mail us at customercare@copyright.com

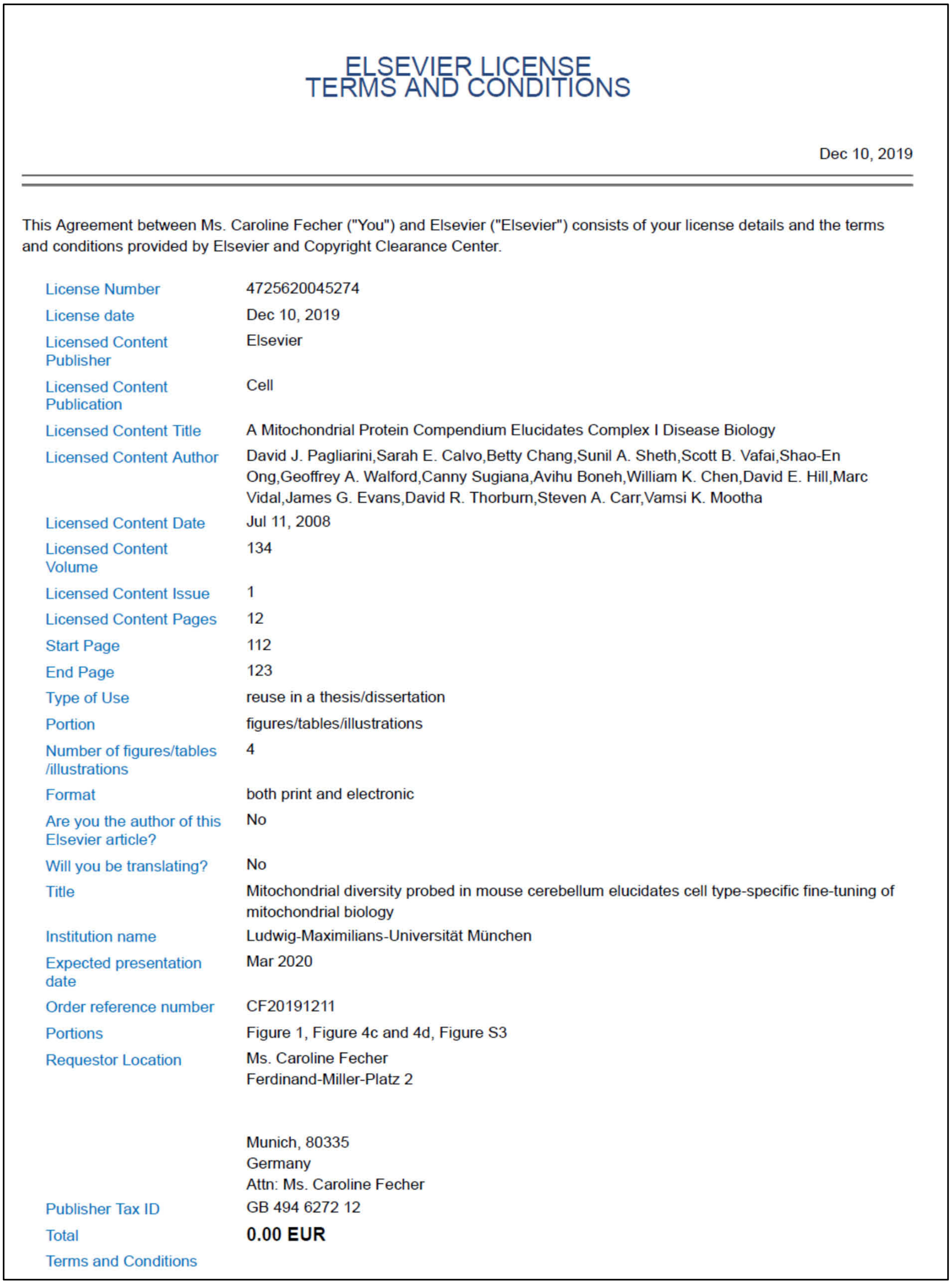

ELSEVIER LICENSE
TERMS AND CONDITIONS

Dec 10, 2019

This Agreement between Ms. Caroline Fecher ("You") and Elsevier ("Elsevier") consists of your license details and the terms and conditions provided by Elsevier and Copyright Clearance Center.

License Number	4725620045274
License date	Dec 10, 2019
Licensed Content Publisher	Elsevier
Licensed Content Publication	Cell
Licensed Content Title	A Mitochondrial Protein Compendium Elucidates Complex I Disease Biology
Licensed Content Author	David J. Pagliarini,Sarah E. Calvo,Betty Chang,Sunil A. Sheth,Scott B. Vafai,Shao-En Ong,Geoffrey A. Walford,Canny Sugiana,Avihu Boneh,William K. Chen,David E. Hill,Marc Vidal,James G. Evans,David R. Thorburn,Steven A. Carr,Vamsi K. Mootha
Licensed Content Date	Jul 11, 2008
Licensed Content Volume	134
Licensed Content Issue	1
Licensed Content Pages	12
Start Page	112
End Page	123
Type of Use	reuse in a thesis/dissertation
Portion	figures/tables/illustrations
Number of figures/tables /illustrations	4
Format	both print and electronic
Are you the author of this Elsevier article?	No
Will you be translating?	No
Title	Mitochondrial diversity probed in mouse cerebellum elucidates cell type-specific fine-tuning of mitochondrial biology
Institution name	Ludwig-Maximilians-Universität München
Expected presentation date	Mar 2020
Order reference number	CF20191211
Portions	Figure 1, Figure 4c and 4d, Figure S3
Requestor Location	Ms. Caroline Fecher Ferdinand-Miller-Platz 2 Munich, 80335 Germany Attn: Ms. Caroline Fecher
Publisher Tax ID	GB 494 6272 12
Total	**0.00 EUR**
Terms and Conditions	

Declaration of author contributions

Caroline Fecher*, Laura Trovò*, Stephan A. Müller, Nicolas Snaidero, Jennifer Wettmarshausen, Sylvia Heink, Oskar Ortiz, Ingrid Wagner, Ralf Kühn, Jana Hartmann, Rosa M. Karl, Arthur Konnerth, Thomas Korn, Wolfgang Wurst, Doron Merkler, Stefan F. Lichtenthaler, Fabiana Perocchi and Thomas Misgeld (*equal contribution)

C.F., L.T., T.M. conceived and designed the study, drafted the article (Fecher et al., 2019) and revised the article (Fecher et al., 2019) with input from all co-authors.

L.T. generated the GFP-OMM knock in vector; optimized Cpt1a immunofluorescence staining in mouse tissue; performed, analyzed and interpreted mitochondrial transport, NMJ characterization, oxygen consumption measurements and corresponding immunocaptures from cerebellar astrocytes and Purkinje cells.

S.A.M. performed, acquired and analyzed mass spectrometry experiments.

S.F.L. advised on and interpreted mass spectrometry experiments.

N.S. performed and acquired electron microscopy data.

J.W., F.P. advised on study design, oxygen consumption measurements and Ca^{2+} uptake assay.

S.H. advised on and acquired flow cytometry data.

T.K. advised on and interpreted flow cytometry experiments.

O.O., R.K. generated *Rosa26* GFP-OMM chimera.

W.W. advised on *Rosa26* knock in strategy.

I.W. performed immunofluorescence staining in human specimens.

D.M. advised on and provided human specimens.

J.H., R.M.K., A.K. provided input on single-cell characterization and electrophysiology (not included in this thesis); A.K. provided the Pvalb:GFP and APP/PS1 mouse model.

C.F. wrote this thesis and generated shown figures;
characterized the MitoTag expression across Cre lines, the $Rmdn3^{tm1a}$ and Mcu^{tm1c} mouse models; designed the immunocapture protocol and performed most isolations; analyzed and interpreted the mass spectrometry data; performed, analyzed and interpreted the flow cytometry experiments, western blot experiments, Ca^{2+} uptake assay, immunofluorescence staining in mouse and other species; analyzed electron microscopy data; acquired and analyzed immunofluorescence staining in human specimens.

Munich, the Caroline Fecher

Lausanne, the Laura Trovò, PhD

Munich, the Prof. Thomas Misgeld, Dr.med

Acknowledgements

„Der Weg ist das Ziel.“

(German expression
likely originated from the teachings of Confucius,
Chinese philosopher, 551 – 479 BC)

Without a doubt, it has been quite a long journey from my first interest in science and biology during my final high school years until the completion of this Doctor of Philosophy.

I am grateful for all the support from my parents who always believed in my choices and supported them to their best efforts – even now, as I am starting a new journey to my postdoctoral training at Washington University in St. Louis, MO despite these present troublesome waters that all of us experience.
With my successful doctorate ending in Munich, this new adventure will start; however, mitochondrial biology and its diversity are going to be constants in my life.

I am sincerely grateful to my mentors, Fabiana Perocchi and Thomas Misgeld that provided me with a scientific environment, in which I could grow my potential to the fullest. This project was not an easy one, but through teamwork and many great collaborators, we have accomplished a truly new insight into a unique area of biology – in my opinion.

I am also deeply grateful to Laura Trovò, who is a great teammate and supported this project in many ways, as well as to my former mentors, Alma Zernecke-Madsen, Robert Blum and Wim Vandenberghe from whom I learned a lot during my training.

Finally, I am grateful for all the amazing scientific and social moments that I experienced during my time in the Misgeld laboratory, the Graduate School of Systemic Neurosciences and wider Neuroscience community in Munich.

Thank you to all of you! and especially to …

Alexandra, G., Antoneta, G., Bogdan, M., Cathy, S., Doug, C., Eleni, P., Fabiana, P., Franziska, A., Gabi, P., Grace, W., Kristine, K., Kristina, W., Laura, H., Laura, T., Leanne, G., Magdalena, G., Mahyar, V., Manuela, B., Marina, H., Marion, E., Martina, S., Monika, L., Monika, S., Natalia, M., Nebi, B., Nic, S., Pedro, G., Peter, E., Pui Shee, L., Rachel, T., Roberta, M., Sebi, T., Selin, K., Shabab, H., Stavros, V., Tatjana, K., Tim, C., Thomas, M., Tobias, H., Yan, X., Yi-Heng, T., Yvonne, H., Wenke, B., the GSN team, the CiPSM gender team and the SyNergy team.

… and my our paths cross again in the future.

Munich, August 3rd 2020

Eidesstattliche Versicherung/Affidavit

Hiermit versichere ich an Eides statt, dass ich die vorliegende Dissertation

MITOCHONDRIAL DIVERSITY PROBED IN MOUSE CEREBELLUM ELUCIDATES
CELL TYPE-SPECIFIC FINE-TUNING OF MITOCHONDRIAL BIOLOGY

selbstständig angefertigt habe, mich außer der angegebenen keiner weiteren Hilfsmittel bedient und alle Erkenntnisse, die aus dem Schrifttum ganz oder annähernd übernommen sind, als solche kenntlich gemacht und nach ihrer Herkunft unter Bezeichnung der Fundstelle einzeln nachgewiesen habe.

I hereby confirm that the dissertation

MITOCHONDRIAL DIVERSITY PROBED IN MOUSE CEREBELLUM ELUCIDATES
CELL TYPE-SPECIFIC FINE-TUNING OF MITOCHONDRIAL BIOLOGY

is the result of my own work and that I have only used sources or materials listed and specified in the dissertation.

München, den 4. August 2020
Munich, August 4th, 2020

Caroline Fecher
Unterschrift / *Signature*